

STATEMENT

I hereby declare that the matter embodied in the thesis entitled: “**CFD Simulation of Multiphase Reactors**” is the result of investigations carried out by me at the Process Engineering and Environmental Technology Division of the National Institute for Interdisciplinary Science and Technology (*Formerly, Regional Research Laboratory*), CSIR, Trivandrum under the supervision of Dr. S. Savithri and the same has not been submitted elsewhere for a degree.

In keeping with the general practice of reporting scientific observations, due acknowledgement has been made wherever the work described is based on the findings of other investigators.

(Panneerselvam R.)



**National Institute for Interdisciplinary
Science & Technology**

(Formerly Regional Research Laboratory)
(Council of Scientific & Industrial Research) India
Industrial Estate P.O., Pappanamcode, Trivandrum – 695 019



Dr. S. Savithri
Scientist

Tel: +91 471 2515264; Fax: +91 471 2490186
E-mail: sivakumarsavi@gmail.com

March 11, 2008

CERTIFICATE

This is to certify that the work embodied in the thesis entitled:
“**CFD Simulation of Multiphase Reactors**” has been carried out by
Mr. Panneerselvam R. under my supervision at the Process
Engineering and Environmental Technology Division of the National
Institute for Interdisciplinary Science and Technology (*Formerly,*
Regional Research Laboratory), CSIR, Trivandrum and the same has
not been submitted elsewhere for a degree.

(S. Savithri)

Thesis Supervisor

ACKNOWLEDGEMENTS

I am dedicating this thesis to late Dr. G. D. Surender (Retired Director Grade Scientist 'G', NIIST) and I wish to express my deepest gratitude to him for defining clearly the research area from time to time, valuable guidance, suggestions. His constant encouragement rendered me to put all my efforts and concentration into this work. His sound knowledge in science and technology, sheer determination, wisdom, and insightful suggestions were the key factors that always helped me to remain focussed.

I express my sincere gratitude to Dr. S. Savithri, who is my mentor and she is the person who introduced me to the wonderful world of CFD. Her presence in my life is quite significant. She has been actively involved in my work and has always been available for advice and patient hearing every time. She was always there for me whenever I wanted help and she gave me complete freedom on all fronts. The successful completion of this investigation and subsequent thesis would not have been possible without her constant support and guidance. I am very much indebted to her for whatever I have achieved in my research tenure. Her contribution to this thesis, however, does not only encompass her role as an academic supervisor, but include her ongoing love, care and support personally without which this journey may never have been completed.

I wish to express my warm and sincere thanks to Dr. Roschen Sasikumar, Head, Computational Modeling and Simulation section (CMS), NIIST, for her support during the course of this research work. I also wish to express my sincere thanks to Dr. P. P. Thomas (former head), Mr. P. Raghavan (present head) of Process Engineering and Environmental Technology Division for their support during the course of this research work.

I owe my gratitude to Dr. Elizabeth Jacob, Scientist, Dr. C. H. Suresh, Scientist and Dr. Vijayalakshmi, CMS, NIIST, for their support and friendly attitude during my tenure at NIIST.

I wish to place on record my sincere thanks to Dr. B. C. Pai, Acting Director, NIIST for his support and encouragement during the course of this research work. I would like to extend my sincere thanks to Prof. T.K.Chandrashekar, former Director, NIIST for the support right from the beginning of this research work.

I am always grateful to Dr. T. R. Sivakumar, for his help and valuable suggestions provided to me throughout my research tenure and also for finding time to read through the manuscripts and the draft of the thesis in spite of his tight schedule.

I wish to express my gratitude to Dr. U. Shyamaprasad, Convener, Research committee and Prof. G. Madhu, Division of Safety & Fire Engineering, School of Engineering, CUSAT for their help in connection with my CUSAT registration and matters dealing with CUSAT.

I express my sincere thanks to NIIST Scientists, Dr. R.M.Pillai (Retired Scientist 'G'), Dr. C.S. Bhat, Dr. U.T.S. Pillai, Dr. P. Shanmugam, Dr. A. Srinivasan, Dr. S. Ananthkumar, Dr. T.P.D. Rajan, Dr. A. Srinivasan, Dr. M. Sundarrajan, Mr. Nithyanandam vasagam (CLRI), Mr. P. Anand (IICT), Mr. R. S. Praveenraj, Mr. Moni for their advice and support given to me during the course of this research work.

I wish to place on record my sincere thanks to Mr. K.R. Prasad (Retired Tech. officer) and Ms. K.S. Geetha, (former Ph.D. student of Dr. G. D. Surender) for their technical discussions.

I would like to thank Mrs Rani Surender, Mr. Vikram J Surender for their support and encouragement given to me throughout my research tenure.

I am really proud of being a part of this CMS section and I could not even imagine how the past 4 years have been spent in this section. I would like to appreciate the love, affection and care extended by all my CMS friends Jijoy Joseph, Alex Andrews, Jomon Mathews, M. Manoj, Neetha Mohan, M.J.Ajitha, P.K.Sajith, A. Ali Fathima Sabirneeza, Fareed Basha and my special acknowledgement to all my young CMS friends J.R. Rejitha, P.Rahul, P.K.Binumon, P.B. Shaija and K.S. Sandhya.

I express my sincere thanks to Ani K. John and M.S. Manju NIIST for the technical discussions and the help given to me during the course of this research work.

I would always cherish my long wonderful time with my NIIST friends, Bala, Suresh, Babu, Gokul, Prabhu, Selvakumar, Sureshkannan, Thirumalai, Sabari, Darani, Naren, Kauseelan, Sudhakar, Ravi, Sreeja, Saravanan, Jeeva, Tennavan, Jaganathan, Vinod, Neson.

I am always grateful to my friend, Prakash R. Kotecha (Post-Doctoral Fellow, IIT Chichago) whose timely help turned me to a person whatever I am today. I would always enjoy my long friendship with him since our UG days. I would also like to thank my postgraduate friends M. Saravanankumar (BPCL, Cochin), C. Saravanakumar (Invensys, Hyderabad), S. Saravanan (IOCL, Delhi) for being part of my most cheerful moments.

I would like to thank A. Subramani (IIT Madras), Pounrajan (Caterpillar Pvt. Ltd.,) B.N.Murthy (UIC, Bombay) for their helpful discussion on CFD

I am thankful to Council of Scientific and Industrial Research (CSIR), New Delhi for providing Senior Research Fellowship to carry out this research work.

At this juncture I fail to find appropriate words to express my gratitude towards my parents, brothers, sisters, uncles and all family members. They have always showered upon me their love, affection, faith and support and their complete belief in me is something which I can never forget in my life. They have supported me in all my decisions. Special thanks to my Anna R. Sivakumar, for his encouragement and untiring support given to me throughout my life.

I would also like to thank everybody who has played their role in making me complete this thesis on time. Finally, I would like to thank God, Almighty for everything.

Panneerselvam R.

CONTENTS

Page No.

STATEMENT.....	i
CERTIFICATE.....	ii
ACKNOWLEDGEMENT.....	iii
CONTENTS.....	v
PREFACE.....	x
LIST OF TABLES.....	xx
LIST OF FIGURES.....	xxii
LIST OF SYMBOLS.....	xxviii

CHAPTER 1: INTRODUCTION.

1.1. Background	1
1.2. Objectives of This Investigation	12
1.3. Outline of Thesis	13

CHAPTER 2: CFD MODELING OF MULTIPHASE FLOWS

2.1. Introduction	15
2.2. Eulerian–Eulerian Model.....	17
2.3. Eulerian–Lagrangian Model.....	23
2.4. Volume of fluid (VOF) approach.....	29
2.5. Overview of ANSYS CFX Package.....	31
2.5.1. Pre-Processor.....	32
2.5.2. Solver.....	34
2.5.3. Post-Processor.....	36

CHAPTER 3: CFD SIMULATION OF HYDRODYNAMICS OF LIQUID–SOLID FLUIDISED BED CONTACTOR

3.1. Introduction.....	37
3.2. CFD model.....	40
3.3. Numerical simulation.....	44

3.3.1. Flow Geometry and Boundary conditions.....	44
3.4. Results and Discussion.....	46
3.4.1. Comparison between 2D and 3D simulation.....	47
3.4.2. Grid resolution study.....	47
3.4.3. Effect of time step.....	47
3.4.4. Effect of drag force models.....	49
3.4.5. Effect of inlet feed condition.....	50
3.4.6. Comparison of solid holdup between experimental and CFD results.....	51
3.4.7. Solid motion in liquid fluidised bed.....	52
3.4.8. Effect of column diameter.....	53
3.4.9. Effect of particle size and density.....	55
3.4.10. Effect of liquid superficial velocity.....	56
3.4.11. Turbulence parameters.....	57
3.4.12. Computation of solid mass balance.....	59
3.4.13. Computation of various energy flows.....	60
3.5. Conclusions.....	67

CHAPTER 4: CFD SIMULATION OF SOLID SUSPENSION IN LIQUID–SOLID MECHANICAL AGITATED CONTACTOR

4.1. Introduction.....	68
4.2. CFD model.....	76
4.2.1. Model Equations.....	76
4.2.2. Interphase momentum transfer.....	78
4.2.3. Closure law for turbulence.....	79
4.2.4. Closure law for solids pressure.....	81
4.3. Numerical simulation.....	81
4.4. Results and Discussion.....	85
4.4.1. Single phase flow	85
4.4.2. Solid liquid flows	87
4.4.2.1. Off-bottom suspension.....	89
4.4.2.1.1. Effect of impeller type.....	90

4.4.2.2. Solid distribution.....	93
4.4.3. Power Number comparison	98
4.5. Conclusions.....	99
CHAPTER 5: CFD SIMULATION OF GAS–LIQUID–SOLID FLUIDISED BED CONTACTOR.	
5.1. Introduction.....	100
5.2. Computational flow model	106
5.2.1. Closure law for turbulence	107
5.2.2. Closure law for solid pressure.....	108
5.2.3. Closure law for interphase momentum exchange.....	109
5.2.3.1. Liquid–solid interphase drag force ($F_{D,ls}$).....	110
5.2.3.2. Gas–liquid interphase drag force ($F_{D,gl}$).....	111
5.2.3.3. Gas–solid interphase drag force ($F_{D,gs}$).....	112
5.3. Numerical methodology.....	113
5.4. Results and Discussion.....	115
5.4.1. Comparison between 2D and 3D simulation.....	117
5.4.2. Effect of interphase drag force model on gas–liquid phase.....	119
5.4.3. Mean bubble size for CFD simulation.....	120
5.4.4. Solid phase hydrodynamics.....	121
5.4.5. Gas and liquid hydrodynamics	128
5.4.6. Computation of solid mass balance.....	132
5.4.7. Computation of various energy flows	134
5.5. Conclusions.....	141
CHAPTER 6: CFD SIMULATION OF SOLID SUSPENSION IN GAS–LIQUID–SOLID MECHANICAL AGITATED CONTACTOR	
6. 1. Introduction.....	142
6.2. Experimental methodology	145
6.3. CFD modeling.....	150
6.3.1. Models equations.....	151
6.3.2. Interphase momentum transfer.....	151

6.3.3. Closure law for turbulence.....	154
6.3.4. Closure law for solids pressure.....	155
6.4. Numerical methodology.....	156
6.5. Results and Discussion.....	159
6.5.1. Solid–liquid flows in an agitated contactor.....	159
6.5.2. Gas–liquid flows in an agitated contactor	165
6.5.2.1. Gross flow field characteristics.....	166
6.5.3. Gas–Liquid–Solid flows in an agitated contactor.....	167
6.5.3.1. Flow field.....	168
6.5.3.2. Liquid phase mixing.....	171
6.5.3.3. Solid suspension studies.....	173
6.5.3.3.1. Effect of Impeller design	175
6.5.3.3.2. Effect of particle size	179
6.5.3.3.3. Effect of air flow rate	180
6.6. Conclusions.....	185

CHAPTER 7: A COMPARITIVE STUDY OF HYDRODYNAMICS AND MASS TRANSFER IN GAS-LIQUID-SOLID MECHANICAL AGITATED CONTACTOR AND FLUIDISED BED CONTACTOR USING CFD

7.1. Introduction.....	186
7.2. Experimental details	187
7.2.1. Mechanically agitated contactor	187
7.2.1.1. Hydrodynamics.....	187
7.2.1.2. Mass transfer.....	188
7.2.2. Fluidized bed contactor.....	189
7.2.2.1. Hydrodynamics.....	199
7.2.2.2. Mass transfer.....	192
7.3. CFD model for hydrodynamics simulation.....	192
7.4. Numerical simulations.....	194
7.5. Results and Discussions	195
7.5.1. Hydrodynamic parameters.....	195
7.5.1.1. Gas holdup.....	196

7.5.1.2. Mean bubble size.....	197
7.5.1.3. Interfacial area.....	198
7.5.2. Mass transfer parameters.....	202
7.6. Conclusions.....	204
CHAPTER 8: CONCLUSIONS AND FUTURE WORK	
8.1. Conclusions.....	206
8.1.1. Mechanically agitated contactor.....	206
8.1.2. Fluidised bed reactor.....	207
8.1.3. Comparison of reactors.....	207
8.2. Scope for Future work	209
REFERENCES.....	210
LIST OF PUBLICATIONS.....	225

PREFACE

1. Introduction

Multiphase reactors are being widely used in chemical, biochemical, petrochemical, and pharmaceutical industries. Most of the multiphase reactors of interest in industrial practice are packed-bed reactors, trickle bed reactors, mechanically agitated reactors, slurry bubble column reactors, fluidised bed reactors and loop reactors. Conversion of mineral ores to value added products by hydrometallurgical processing route is another area where multiphase reactors are extensively used but less understood. This is due to the complex multiphase reactions occurring between different phases in such reactors. NIIST (CSIR) has been involved in the development of a process for production of synthetic rutile from ilmenite by modifying the existing Becher's process. The main processes involved in the modified Becher's process are metallisation of ilmenite in a rotary kiln, in which the iron (II) and Iron (III) content of the ilmenite is reduced to metallic iron at about 1050–1100°C using Coal as both reductant and fuel. The second step is removal of metallic iron from reduced ilmenite by an accelerated corrosion reaction using aerated condition in a liquid contacting electrolyte, which is carried out in a mechanically agitated contactor and followed by liquid phase oxidation of Fe^{2+} along with hydrolysis and precipitation of Fe^{3+} ion as oxides. The disadvantages of using this type of mechanically agitated reactor are high energy consumption and breakage of particles due to non uniform energy dissipation. Hence investigations have been directed towards development of an alternate reactor viz. fluidised bed reactor for leaching and rusting processes. The major advantages of using gas–liquid–solid fluidised bed reactor for leaching and rusting processes are near uniform energy dissipation, higher

mass transfer rates. Moreover, the same reactor can be used both for rusting and for separation and hence act as a multifunctional reactor. But for development of such an alternate reactor, a fundamental knowledge of the various complex mechanisms like hydrodynamics, mass transfer and heat transfer occurring in these type of reactors is essential. At present, the understanding of these reactors is far from complete because of the complex interactions among the phases and also due to insufficient quantitative information about flow patterns, phase holdups, solids mixing and circulation. Thus, there is a need to quantify the performance of such multiphase reactors in terms of flow patterns, phase holdups, solids mixing and circulation and transport phenomena. For this reason, Experimental Fluid Dynamics (EFD) and Computational Fluid Dynamics (CFD) techniques have been promoted as useful tools for understanding multiphase reactors for precise design and scale up. Experimental fluid dynamics (EFD) is nothing but to get physics through the instrumentation. In recent years, computational fluid dynamics (CFD) has emerged, as a powerful tool for the study of fluid dynamics of multiphase processes within each of the process equipments. Two models are widely used for describing the hydrodynamics of multiphase system, i.e., the Euler–Euler model and Euler–Lagrange model. Euler–Euler fluid model treats all the phases to be continuous and fully interpenetrating. Owing to the continuum representation of the particle phases, Eulerian models require additional closure laws to describe the rheology of particles. The Euler–Lagrange model on the other hand adopts a continuum description for fluid phase and tracks the dispersed solids phase by applying Newton’s Law of motion for each individual particle. As the volume fraction of solids phase increases Euler–Lagrange model becomes more computationally intensive.

Hence the objective of this research work is directed towards understanding the complex hydrodynamics of mechanically agitated reactors and fluidised bed reactors using multiphase CFD. The CFD simulations are based on Eulerian formulation where each phase is treated as continuum and interpenetrating and appropriate closure laws are used. Based on CFD predictions, the performance of the both the reactors are compared in terms of hydrodynamics and mass transfer. For the hydrodynamics, the investigations are based on the solids suspension characteristics and for mass transfer, the investigations are based on gas-liquid mass transfer coefficient in both the reactors. The lay out of the thesis is as follows:

The first chapter gives a detailed introduction to multiphase reactors and their classification which is followed by the scope and objectives of the present investigation. In the second chapter, various types of CFD techniques used for simulating multiphase flows are described in detail. Detailed investigations on the two phase hydrodynamics of liquid–solid flows in mechanically agitated reactor and fluidised bed reactor using multiphase flow CFD approach is presented in chapter three and four. The fifth and sixth chapters of the thesis deals with the investigations of CFD simulations of hydrodynamics of gas–liquid–solid flows in mechanically agitated and fluidised bed reactor. The detailed investigations on gas–liquid mass transfer characteristics in gas–liquid–solid mechanically agitated reactor and fluidised bed reactor using CFD simulation is presented in chapter seven. This is followed by the overall comparison of performance of mechanically agitated and fluidised bed reactor in terms of hydrodynamics and mass transfer. Conclusions based on the present investigations and scope and suggestions for the future course of work in this

field is presented in the last chapter. The following sections gives a brief summary of the work carried out in this research work.

2. CFD Simulation of Hydrodynamics of Liquid–Solid Fluidised Bed

Liquid–solid fluidised beds continue to attract increasing attention due to their inherent versatility for several industrial applications in hydrometallurgical, biochemical, environmental and chemical process industries.

In this present work, CFD simulation have been performed to predict the flow pattern of solids and liquid motion in liquid fluidised bed for various design and operating conditions by employing the multifluid Eulerian–Eulerian approach. The data of Limtrakul et al. (2005) is used for validating the CFD simulation results. They have used non invasive techniques such as computer tomography (CT), computer-aided radioactive particle tracking (CARPT) to measure solid holdup, solid motion and turbulence parameters in two liquid fluidised beds of plexiglas columns: 0.1 m i.d. with 2 m height and 0.14 m i.d. with 1.5 m height. The liquid phase is chosen as water. The solid phase is chosen as glass beads of size 1 and 3 mm with a density of 2900 kg /m³ and 2500 kg/m³ respectively. They also used acetate beads of 3 mm size with a density of 1300 kg /m³. Adequate agreement was demonstrated between CFD simulation results and experimental findings reported by Limtrakul et al. (2005). The predicted flow pattern demonstrates that the time averaged solid velocity profile exhibits axisymmetric with downward velocity at the wall and maximum upward velocity at the center of the column and higher value of solid holdup at the wall and lower value of that at the center. CFD model has been further extended to compute solid mass balance in the center and wall regions and energy flows due to various

contributing dissipation mechanisms such as friction, liquid phase turbulence and mean flow. The result obtained shows a deviation in the range of 10–15% between center and wall region for solid flow balance calculations. In the computation of energy flows, the energy difference observed is in the range of 2–9%

In the present study, the influence of various interphase drag models on solid motion in liquid fluidised bed was studied. The drag models proposed by Gidaspow, (1994); Syamlal and O'Brien, (1988), and Di Felice, (1994) can qualitatively predict the flow pattern of solid motion inside the fluidised bed, in which the model proposed by Gidaspow gives the best agreement with experimental data. To identify the CFD methodology to enhance the accuracy of numerical simulation comparison between 2D and 3D simulation, the effect of grid sensitivity, time step sensitivity and effect of inlet feed conditions were investigated and a comprehensive CFD methodology was established to model the liquid–solid fluidised bed.

3. CFD Simulation of Solid Suspension in Liquid–Solid Mechanically Agitated Contactor

Liquid–Solid mixing in mechanically agitated contactors is a widely used operation in the chemical industries, mineral processing, wastewater treatment and biochemical processes. Solid suspension in mechanically agitated contactors is important wherein, the solid particles are moving in the liquid phase and hence increase the rate of mass and/or heat transfer between the particles and the liquid. One of the main criteria which is often used to investigate the solid suspension is the critical impeller speed at which solid are just suspended. Zwietering (1956) was the

first author who proposed a correlation for minimum impeller speed for just suspension condition of solids.

The objective of this work is to carry out the CFD simulation based on Eulerian multi-fluid approach for the prediction of the critical impeller speed for solid suspension in mechanically agitated reactor. CFD Simulations are carried out using the commercial package ANSYS CFX-10. The CFD simulations are validated qualitatively with literature experimental data (Micheletti et al., 2003; Spidla et al., 2005a) for solid-liquid agitated reactors in terms of axial profiles of solid distribution in liquid-solid stirred suspension. A good agreement was found between the CFD prediction and experimental data. The CFD predictions are compared quantitatively with literature experimental data (Spidla et al., 2005a) in terms of critical impeller speed based on the criteria of standard deviation method and cloud height in a mechanically agitated contactor. An adequate agreement was found between CFD predictions and experimental data. After the validation, the CFD simulations have been extended to study the effect of impeller design (DT, PBTD and A315 Hydrofoil), impeller speed and particle size (200–650 μm) on the solid suspension in liquid-solid mechanically agitated contactor.

4. CFD Simulation of Hydrodynamics of Gas-Liquid-Solid Fluidised Bed

Three-phase reactors are used extensively in chemical, petrochemical, refining, pharmaceutical, biotechnology, food and environmental industries. Depending on the density and volume fraction of particles, three-phase reactors can be classified as slurry bubble column reactors and fluidised bed reactors. In slurry bubble column reactors, the density of the particles are slightly higher than the liquid

and particle size is in the range of 5–150 μm and volume fraction of particles is below 0.15. Hence, the liquid phase along with particles can be treated as a homogenous liquid with mixture density. But in fluidised bed reactors, the density of particles are much higher than the density of the liquid and particle size is normally large (above 150 μm) and volume fraction of particles varies from 0.6 (packed stage) to 0.2 (close to dilute transport stage). In this study, the focus is on understanding the complex hydrodynamics of three-phase fluidised beds containing coarser particles of size above 1 mm.

In this work, CFD simulation of hydrodynamics of gas–liquid–solid fluidised bed was studied for different operating conditions by employing the multifluid Eulerian–Eulerian approach. The CFD model prediction have been validated with experimental data for mean and turbulent parameters of solid phase reported by Kiared et al. (1999) and gas and liquid phase hydrodynamics in terms phase velocities and holdup reported by Yu et al. (1988, 2001). The CFD simulation results showed good agreement with experimental data for solid phase hydrodynamics in terms of mean and turbulent velocities reported by Kiared et al. (1999) and for gas and liquid phase hydrodynamics in terms of phase velocities and holdup reported by Yu and Kim (1988, 2001). The predicted flow pattern shows that the averaged solid velocity profile with lower downward velocity at the wall and higher upward velocity at the center of the column. CFD simulation exhibits single solid circulation cell for all operating conditions, which is consistent with the observations reported by various authors. Based on the predicted flow field by CFD model, the focus has been on the computation of the solid mass balance and computation of various energy flows in fluidised bed reactors. The result obtained shows a deviation in the range of 8–21%

between center and wall region for solid mass flow balance calculations. In the computation of energy flows, the energy difference observed is in the range of 10–19% for the case of fluidised bed column of diameter 0.1 m, and in the range of 1–3%, for the fluidised bed column of diameter 0.254 m.

The influence of various interphase drag models for gas–liquid interaction on gas holdup in gas–liquid–solid fluidised bed are also studied in this work. The drag models proposed by Tomiyama (1998), gives the best agreement with experimental data. To identify the CFD methodology to enhance the accuracy of numerical simulation comparison between 2D and 3D simulation are also investigated and a comprehensive CFD methodology is established to predict the flow behaviour of gas–liquid–solid fluidised bed.

5. CFD Simulation of Solid Suspension in Gas–Liquid–Solid Mechanical Agitated Contactor

Mechanically agitated reactor involving gas, liquid and solid phases have been widely used in the chemical industries and in mineral processing, wastewater treatment and biochemical industries. This is one of the widely used unit operations because of its ability to provide excellent mixing and contact between the phases. In these types of reactors, the agitator plays the dual role of keeping the solids suspended, while dispersing the gas uniformly as bubbles. An important consideration in the design and operation of these agitated reactors is the determination of the state of just suspension, at which point no particles reside on the vessel bottom for more than 1 to 2s. Such a determination is critical to enhance the performance of the reactor, because until such a condition is achieved the total surface area of the

particles is not efficiently utilized. Hence, it is essential to determine the minimum impeller speed required for the state of complete off bottom suspension of the solids called the critical impeller speed. The critical impeller speed for gas–liquid–solid mechanically agitated reactors mainly depend on several parameters such as particle settling velocity, impeller design, impeller diameter, sparger design, and its location.

In this present work, multi-fluid Eulerian–Eulerian approach along with standard k- ϵ turbulence model has been used to study solid suspension in gas–liquid–solid agitated contactor. The results obtained from CFD simulations are validated qualitatively with literature experimental data (Guha et al., 2007; Spidla et al., 2005; Aubin et al., 2004) in terms of axial and radial profiles of solid velocity in liquid–solid suspension and liquid velocity in gas–liquid dispersion for different operating conditions. A good agreement was found between the CFD prediction and experimental data. For gas–liquid–solid flows, the CFD predictions are compared quantitatively with our experimental data in the terms of critical impeller speed for just suspended conditions based on the criteria of standard deviation method and cloud height in a mechanically agitated contactor. An adequate agreement was found between CFD prediction and experimental data. The numerical simulation has further been extended to study the effect of impeller design (DT, Pitched blade turbine), impeller speed, particle size (125–230 μm) and air flow rate (0–1vvm) on the critical impeller speed for solid suspension in gas–liquid–solid mechanically agitated contactor.

6. A Comparative Study of Hydrodynamics and Mass Transfer in Gas–Liquid–Solid Mechanically Agitated and Fluidised Bed Contactors using CFD

Since the main aim of the thesis is the comparison of mechanically agitated reactor and fluidised bed reactor in terms of hydrodynamics and mass transfer, this chapter is focused on a comparative study of mechanically agitated reactors and fluidised bed reactor. The hydrodynamic parameters like gas hold up and power consumption obtained by CFD simulations explained in the previous chapters are compared for both the type of reactors. Similarly for comparing mass transfer characteristics of both the reactors, the mass transfer coefficient obtained by CFD simulation is used in the present study.

For gas holdup prediction, fluidised bed contactor gives a range of 0.03–0.07 at lower P/V values (300–700 W/m³) whereas mechanically agitated contactor with DT and PBTD gives same range of gas holdup (0.03–0.1) at higher P/V range of 1000–3000 W/m³. For interfacial area prediction, the fluidised bed contactor gives between 100 and 250 m²/m³ for P/V varying between 300 and 700 W/m³ whereas mechanically agitated contactor gives between 50 and 150 m²/m³ for P/V varying between 1000 and 4000 W/m³. For gas–liquid mass transfer coefficient ($k_L a$)_s prediction, fluidised bed contactor gives in the range of 0.05–0.2 s⁻¹ at lower P/V varying between 300 and 700 W/m³ whereas mechanically agitated contactor with DT and PBTD gives same range of ($k_L a$)_s (0.05–0.2 s⁻¹) at higher P/V range of 1000–3000 W/m³.

For the various operating conditions, fluidised bed contactor gives the best performance at low total power consumption per unit volume of contactor (P/V) compared to mechanically agitated contactor with DT and PBTD in terms of gas holdup, interfacial area and gas–liquid mass transfer coefficient ($k_L a$)_s prediction.

LIST OF TABLES

Table No.	Caption	Page No.
1.1	List of various industrial sectors that involve Multiphase reactor technology	2
3.1	Standard values of the parameters used in the Turbulence model	42
3.2	Simulation process conditions	44
3.3	Simulation model parameters	44
3.4	Comparison of bed expansion and solid holdup prediction from different drag force models and experimental data	49
3.5	Comparison of bed expansion and solid holdup on the type of velocity profiles at the inlet	50
3.6	Parameters employed in the CFD simulation	51
3.7	Experimental validation of average solid holdup predicted by the CFD	52
3.8	Comparison of inversion points for different operating conditions	56
3.9	Mass Balance of solid in the liquid fluidised bed	60
3.10	Various energy flows in the liquid fluidised bed	65
4.1	Empirical correlations for critical impeller speed from the literature	69
4.2	Literature reviews on the CFD modeling of solid suspension in stirred vessel	74
4.3	Reactor configuration and process parameter	82
4.4	Effect of impeller type on quality of suspension (particle size of 350 μm with solid loading of 10 vol. %)	93
4.5	Experimental and predicted values of Power number	98

5.1	Literature survey on CFD modeling of three-phase reactors	103
5.2	Physical and process parameters for simulation	116
5.3	Solid mass balance in three-phase fluidised bed	134
5.4	Various energy flows in three-phase fluidised bed	140
6.1	Empirical correlations in the literature for the critical impeller speed in the presence of gas	145
6.2	Values of critical impeller speed	150
6.3	Tank design parameters and physical properties	156
6.4	Gross Characteristics of gas–liquid Stirred Vessel	167
6.5	Energy dissipation rate obtained by CFD simulation for different type of impellers (particle size = 230 μm & particle loading = 30 wt. %)	171
6.6	Effect of impeller type on quality of suspension (gas flow rate =0.5 vvm, particle size = 230 μm & particle loading = 30 wt %)	177
6.7	Effect of particle size on quality of suspension (gas flow rate =0.5 vvm & particle loading = 30 wt %)	179
6.8	Effect of air flow rate on quality of suspension for different type of impellers (particle size = 230 μm & particle loading = 30 wt. %)	181
6.9	Reported values of constant ‘a’ of Equation (6.34) along with CFD prediction	184
7.1	Model parameters for the CFD simulations	194
7.2	Process parameters for the CFD simulations	195

LIST OF FIGURES

Figure No.	Caption	Page No.
1.1	Schematic diagram of mechanically agitated contactor for rusting reaction	5
1.2	Schematic representation of the rusting process in a mechanically agitated reactor	7
1.3	Schematic diagram of circulating fluid bed reactor for rusting reaction	10
3.1	(a) 2D (b) 3D mesh of liquid fluidised bed	45
3.2	Comparison of 2D and 3D Simulation, time averaged solid holdup from (a) 2D (b) 3D simulation, time averaged solid velocity from (c) 2D Simulation (d) 3D simulation	47
3.3	Influence of mesh sensitivity on the time averaged axial solid velocity at superficial liquid velocity of 0.07 m/s	48
3.4	Influence of time sensitivity studies on the solid holdup (a) 0.01 s (b) 0.005s (c) 0.001s	48
3.5	Influence of different drag force models on the time averaged axial solid velocity of fluidised at a superficial liquid velocity of 0.07 m/s	49
3.6	Azimuthally averaged solid holdup profile obtained by CT scan and CFD simulation, 0.14 m diameter column, 0.003 m glass beads $U_1=0.07$ m/s	52
3.7	Typical time averaged azimuthally averaged axial solid velocity profile	53
3.8	Axial solid velocity profiles as a function of radial position at a superficial velocity of 0.07 m/s	54
3.9	Effect of column size for 0.003 m glass beads at $U_1= 0.07$ m/s	54
3.10	(a) Effect of particle type (U_1 for glass beads =0.007 m/s, U_1 for acetate=0.024 m/s) and (b) Effect of particle size (U_1 for 3 mm	55

	=0.007 m/s, U_1 for 1mm =0.024 m/s) on axial solid velocity	
3.11	Effect of superficial liquid velocity on time averaged axial solid velocity	57
3.12	(a) Variation of radial rms velocities along the radial position (b) Variation of axial rms velocities along the radial position	58
3.13	Variation of Reynolds shear stress along the radial position	59
4.1	Flow regimes of liquid–solid stirred reactor (Kraume, 1992)	68
	Typical geometry, impeller and mesh used for CFD simulation	
4.2	(a) Pitched blade Turbine (PBTD) (b) Rushton Turbine (DT) (c) A315 hydrofoil	83
4.3	Axial profiles of normalized radial mean velocity at $r/T = 0.224$, $Re = 20\ 000$	86
4.4	Radial profiles of normalized radial mean velocity at $z/T = 0.33$, $Re = 20\ 000$	87
4.5	Radial profiles of normalized axial mean velocity at $z/T = 0.33$, $Re = 20,000$	87
4.6	Effect of drag force models on axial solid concentration for case of radial type impeller	89
4.7	Standard deviation values obtained from CFD with respect to impeller rotational speed for different types of impeller (particle size of 350 μm with solids loading of 10 vol. %)	91
4.8	Cloud height predicted by CFD simulation for PBTD impeller at different rotational speeds (particle size of 350 μm with solid loading of 10 vol. %) (a) 4.0 rps (b) 4.45 rps (d) 5 rps	92
4.9	Cloud height predicted by CFD simulation for A315 hydrofoil impeller at different rotational speeds (particle size of 350 μm with solid loading of 10 vol. %) (a) 3.5 rps (b) 4.1 rps (c) 4.7 rps	92
4.10	Normalized Axial concentration profiles for an overall solid holdup of 9.2% and 655 μm glass particles at critical impeller speed of $N_{js} = 988$ rpm	94

4.11	Contours of solid volume fraction and axial solid concentration profiles at just suspended speed N_{js} (a) DT (b) PBDP (c) A315 Hydrofoil	95
4.12	Normalized Axial concentration profiles for an overall solid holdup of 10% and 350 μm glass particles at critical impeller speed of $N_{js} = 267$ rpm	96
4.13	Effect of particle size on axial solid concentration profiles, (solid holdup of 9.2 vol. % glass particle of size 200, 360, 655 μm)	97
5.1	(a) 2D; (b) 3D mesh of fluidised bed	115
5.2	Comparison of 2D and 3D simulation on the (a) averaged axial solid velocity at gas superficial velocity of 0.069 m/s and liquid superficial velocity of 0.065 m/s (b) averaged gas holdup at gas superficial velocity of 0.04 m/s and liquid superficial velocity of 0.06 m/s	118
5.3	Effect of different drag models on averaged gas holdup at gas superficial velocity of 0.04 m/s and liquid superficial velocity of 0.06 m/s	119
5.4	Effect of mean bubble size on the averaged gas holdup at gas superficial velocity of 0.04 m/s and liquid superficial velocity of 0.06 m/s	120
5.5	Time and azimuthal averaged solid circulation pattern (a) experimental data of Larachi et al. (1996) (b) CFD simulation	122
5.6	(a) Axial solid velocity (b) radial solid velocity profiles as a function of radial position at a gas superficial velocity of 0.069 m/s and liquid superficial velocity of 0.065 m/s	123
5.7	Effect of superficial gas velocity on the axial solid velocity as a function of radial position at liquid superficial velocity of 0.065 m/s	125
5.8	Instantaneous snapshots of solid velocity vectors for gas superficial velocity of 0.069 m/s and liquid superficial velocity of 0.065 m/s	126
5.9	(a) Axial solid turbulent velocity; (b) radial solid turbulent velocity; (c) shear stress profiles of solid along the radial direction at superficial gas velocity of 0.032 m/s and superficial	127

	liquid velocity of 0.065 m/s	
5.10	Radial distribution of gas holdup at liquid superficial liquid velocity $U_l = 0.06$ m/s and gas superficial liquid velocity $U_g = 0.04$ m/s at axial position of 0.325 m	129
5.11	Radial distribution of bubble velocity at liquid superficial liquid velocity $U_l = 0.06$ m/s and gas superficial liquid velocity $U_g = 0.04$ m/s	130
5.12	Radial distribution of liquid velocity at liquid superficial liquid velocity $U_l = 0.06$ m/s and gas superficial liquid velocity $U_g = 0.04$ m/s	131
5.13	Instantaneous snapshots of gas velocity vectors for gas superficial velocity of 0.04 m/s and liquid superficial velocity of 0.06 m/s	132
6.1	Experimental setup used for the present study	148
6.2	Prediction of critical impeller speed from graphical plot of N_{Re} vs. N_p	149
6.3	Computational grid of mechanically agitated three-phase contactor used in the present study (a) Tank (b) DT (c) PBTB	159
6.4	Axial profiles of various components of solid velocity for an overall solid holdup of 7% at 1200 RPM a) Radial component of solids velocity (b) Tangential component of solids velocity (c) Axial component of solids velocity	161
6.5	Radial profiles of various components of solid velocity for overall solid holdup of 7% at 1200 RPM a) Radial component of solids velocity (b) Tangential component of solids velocity (c) Axial component of solids velocity	163
6.6	Axial solid concentration profile for PBTB in solid-liquid stirred reactor (solids loading = 10% wt., impeller speed = 267 rpm, $r/R = 0.8$)	164
6.7	Radial profiles of dimensionless axial liquid velocity at various axial locations for the case of pitched blade turbine and downward pumping (impeller speed = 300 rpm, $z/T = 0.31$)	165
6.8	Radial profiles of dimensionless axial liquid velocity at various axial locations for the case of pitched blade turbine and upward pumping (impeller speed = 300 rpm, $z/T = 0.31$)	166

6.9	Solid flow pattern predicted by CFD simulation in gas–liquid–solid stirred reactor for the case of (a) DT (b) PBTD (gas flow rate =0.5 vvm, particle size = 230 μm & solids loading = 30 wt %)	169
6.10	Turbulence kinetic energy profile predicted by CFD simulation in gas–liquid–solid stirred reactor for the case of (a) DT (b) PBTD (gas flow rate =0.5 vvm, particle size = 230 μm & particle loading =30 wt %)	170
6.11	Mixing time variation with impeller speed	173
6.12	Variation of standard deviation values with respect to impeller speed for DT and PBTD	175
6.13	CFD prediction of cloud height with respect to impeller speed for DT (gas flow rate = 0.5 vvm, particle size =230 μm , & particle loading =30 wt %)	175
6.14	CFD prediction of cloud height with respect to impeller speed for PBTD (gas flow rate = 0.5 vvm, particle size =230 μm & particle loading =30 wt %)	176
6.15	Axial concentration profiles predicted by CFD simulation for different impellers of (a) DT (b) PBTD (gas flow rate = 0.5 vvm, particle size = 230 μm & particle loading = 30 wt %)	178
6.16	Effect of particle size on critical impeller speed for different impellers (gas flow rate = 0.5 vvm, & particle loading = 30 wt %)	180
6.17	Effect of air flow rate on Critical impeller speed for different impellers (particle size= 230 μm & particle loading = 30 wt %)	181
6.18	Effect of air flow rate on solid concentration distribution for DT by CFD simulations at the critical impeller speed (a) 0 vvm (b) 0.5 vvm (c) 1. 0 vvm (particle size =230 μm and particle loading = 30 wt. %)	182
6.19	Effect of gas flow rate on standard deviation value for different impeller speeds of DT (particle size =230 μm & particle loading = 30 wt. %)	183
7.1	A schematic diagram of the experimental setup for mechanically agitated contactor	188

7.2	A schematic diagram of the circulating fluidised bed contactor used for experiments	191
7.3	Contour plot of the fractional gas holdup, (a) mechanically agitated reactor with DT, (b) mechanically agitated contactor with PBTD, (c) Fluidised bed contactor	197
7.4	Contour plot of the mean bubble size (a) mechanically agitated contactor with DT, (b) mechanically agitated contactor with PBTD, (c) Fluidised bed contactor	198
7.5	Contour plot of the interfacial area (m^2/m^3) (a) mechanically agitated reactor with DT, (b) mechanically agitated contactor with PBTD, (c) Fluidised bed contactor	199
7.6	Gas holdup versus the total power consumption per unit volume of contactor (P/V)	200
7.7	Interfacial area versus the total power consumption per unit volume of contactor (P/V)	201
7.8	Gas-liquid mass transfer coefficient ($k_{L,a}$) _s prediction versus the total power consumption per unit volume of contactor for mechanically agitated and fluidized bed contactors	204

LIST OF SYMBOLS

Nomenclature

a	parameter in equation (3.41)
a	constant in equation (6.34)
a	interfacial area, m^2/m^3
A, B	coefficient used in equation (3.22)
Ar	Archimedes Number
c	solid compaction modulus (equation 3.7)
C	constant used in equation (3.27)
C_{avg}	average solid concentration
C_d, C_D	drag coefficient
C_D	drag coefficient in turbulent liquid
C_{D0}	drag coefficient in stagnant liquid
$C_{D,lg}$	drag coefficient between liquid and gas phase
$C_{D,ls}$	drag coefficient between liquid and solid phase
C_i	instantaneous solid concentration in equation (4.22)
C_i	concentration of oxygen at the gas–liquid interface in equation (7.4)
C_{O_2}	concentration of oxygen in liquid phase
$C_{O_2}^*$	saturation concentration of oxygen
C_{SO_3}	concentration of sulphite
C_{TD}	turbulent dispersion coefficient
$C_\mu, C_{\epsilon 1}, C_{\epsilon 2}$	constants used in turbulence equations
$C_{\mu p}$	coefficient in particle induced turbulence model

d_b	mean bubble diameter, m
d_p	mean particle diameter, m
D	column diameter, m (equation 3.30)
D	impeller diameter, m
D_C	diameter of center (core) region in fluidised bed column, m
D_L	diffusivity coefficient, m^2/s
D_p	particle diameter, m (equation 2.9)
E_{Bgl}	energy dissipated at the gas–liquid interface, W
E_{Bls}	energy dissipated at the solid-liquid interface, W
E_D	energy dissipation by the liquid phase, W
E_c	energy dissipated due to liquid phase turbulence, W
E_i	energy entering the fluidised bed by liquid and gas, W
E_{kg}	gas phase kinetic energy, W
E_{kl}	kinetic energy of liquid leaving the fluidised bed, W
E_{ks}	kinetic energy of the solids in the center region, W
E_o	Eotvos number
E_{out}	energy leaving the fluidised bed by the outflowing liquid, W
E_{Pg}	gas phase potential energy, W
E_{Pl}	potential energy of liquid leaving the fluidised bed, W
E_{PS}	potential energy of the solids in the center region, W

E_T	energy gained by the solid phase, W
f	ratio of the falling velocity to the terminal velocity of a single particle
F_D	drag force, N (equation 2.7)
$F_{D,ls}$	interphase drag force between liquid and solid phases, N
$F_{D,gs}$	interphase drag force between gas and solid phases, N
$F_{D,lg}$	interphase drag force between liquid and gas phases, N
F_G	force due to gravity, N (equation 2.7)
F_H	Basset force, N (equation 2.7)
F_L	lift force, N (equation 2.7)
F_P	force due to continuous phase pressure gradient, N (equation 2.7)
F_T	total drag force, N
F_{TD}	turbulent dispersion force, N
F_{VM}	virtual mass force, N (equation 2.7)
\vec{g}	acceleration vector due to gravity, m / s^2
$G(\epsilon_s)$	solid elastic modulus
G_0	reference elasticity modulus (equation 3.7)
H	expanded bed height, m
H_{cloud}	Cloud height, m
H, J, M	parameters in equation (5.30)
I	Unit vector
k	turbulence kinetic energy, m^2/s^2

k_L	liquid phase mass transfer coefficient,
$k_L a, k_{gl} a_g$	gas–liquid mass transfer coefficient, s^{-1}
$(k_L a)_s$	gas–liquid mass transfer coefficient in the presence of particles, s^{-1}
m	constant used in equation (3.27)
m_p	mass of particles, kg
m_{pk}	mass transfer between phase k and phase p
M_{ik}	momentum transfer between phases i, k
$M_{i,l}, M_{i,g}, M_{i,s}$	interphase force term for liquid, gas, and solid Phase
n	curvature of the velocity profile in equations (3.28), (5.42)
n	parameter in equation (3.40)
n	flow index of the power law model in equation (6.32)
n	number of sampling locations in equation (6.33)
n_b	number of bubbles
n_p	number of particles
N	impeller speed, rpm
N_{js}	critical impeller speed for just suspended, rpm
N_{jsg}	critical impeller speed in the presence of gas, rpm
N_p	power number
N_q	pumping number
P	liquid-phase pressure, $kg/ m s^2$
P	power in equation (6.30), W

P	number of locations in equation (5.38)
P_g	total power consumption, W
P_a	turbulence production due to viscous and buoyancy forces
Q_g	gas flow rate, vvm
r	radial position, m
r_{O_2}	rate of transfer of oxygen, kmol/m ³ s
r_{SO_3}	rate of oxidation of sulphite, kmol/m ³ s
R	radius of column, m
R_i	radius of inversion
Re	Reynolds number
Re_b	bubble Reynolds number
Re_p	particle Reynolds number
Re_t	Reynolds number based on particle terminal velocity
R_p	proportion of fluctuation velocity of gas and liquid phase (equation 5.12)
t	contact time, s
t_1, t_2	time interval for averaging
T	tank height, m
\bar{u}_k	local velocity vector of phase k, m/s
\bar{u}_g	local gas phase velocity vector, m/s
\bar{u}_l	local liquid phase velocity vector, m/s
\bar{u}_s	local solid phase velocity vector, m/s

U	superficial velocity, m/s
U_c	velocity vector of continuous phase m/s (equation 2.9)
U_g	gas superficial velocity, m/s
U_l	liquid superficial velocity, m/s
U_{mf}	minimum fluidisation velocity, m/s
U_p	velocity vector of particle, m/s (equation 2.9)
U_t	terminal setting velocity, m/s
U_{tip}	impeller tip velocity, m/s
v_s	time averaged solid velocity in the center region, m/s
V_{bs}	slip velocity between gas and liquid phase, m/s
V_g	superficial gas velocity, m/s
V_{in}	inlet superficial liquid velocity, m/s
V_l	superficial liquid velocity, m/s
V_l	liquid volume in equation (7.16), m ³
V_{max}	maximum velocity at center, m/s
V_p	volume of particle, m ³ (equation 2.8)
V_s	slip velocity between liquid and solid phase, m/s
$V_z(0)$	centerline axial solids velocity, m/s
$V_z(r)$	time averaged axial solid velocity, m/s
W	solid loading, kg
x	empirical coefficient in the Di Felice model (1994)
z	axial coordinate

Greek letters

α_1, α_2	empirical constants used in equations (3.28) and (5.42)
β	inter-phase drag coefficient, $\text{kg}/\text{m}^3 \text{ s}$
ϵ_k	volume fraction of phase k
$\epsilon_l, \epsilon_g, \epsilon_s$	liquid, gas and solid volume fractions
ϵ_{mf}	voidage at minimum fluidisation
$\bar{\epsilon}_s$	time-averaged solid holdup
ϵ_{sm}	maximum solid packing parameter
$\epsilon(\mathbf{r})$	time-averaged radial solid holdup profile
ϵ, ϵ_l	turbulence eddy dissipation, m^2/s^3
λ_k	bulk viscosity of k^{th} phase, $\text{kg}/\text{m s}^2$
μ_k	shear viscosity of k^{th} phase, kg/ms^2
$\mu_{\text{eff},g}$	gas phase effective viscosity, $\text{kg}/\text{m s}^2$
$\mu_{\text{eff},l}$	liquid phase effective viscosity, kg/ms^2
$\mu_{\text{eff},s}$	solid phase effective viscosity, kg/ms^2
μ_f	viscosity of continuous phase, $\text{kg}/\text{m s}^2$
μ_g	gas viscosity, $\text{kg}/\text{m s}^2$
μ_l	liquid viscosity, $\text{kg}/\text{m s}^2$
μ_{ref}	molecular viscosity of water at some reference temperature and pressure in equation. (5.32), kg/ms^2
μ_s	solid viscosity, $\text{kg}/\text{m s}^2$
μ_{tg}	gas induced turbulence viscosity, $\text{kg}/\text{m s}^2$

μ_{tp}	particle induced turbulence viscosity, kg /m s ²
μ_{ts}	solid induced turbulence viscosity, kg /m s ²
$\mu_{T,l}$	liquid phase turbulent viscosity, kg /m s ²
$\mu_{T,g}$	gas phase turbulent viscosity, kg /m s ²
$\mu_{T,s}$	solid phase turbulent viscosity, kg /m s ²
ρ_k	density of phase k, kg/ m ³
ρ_c	slurry density, kg/m ³
ρ_f	density of continuous phase, kg/m ³
ρ_g	gas density, kg/m ³
ρ, ρ_l	liquid density, kg/m ³
ρ_p	density of particle, kg/m ³ (equation 2.8)
ρ_s	solid density, kg/ m ³
$\Delta\rho$	density difference between liquid and gas, kg/m ³
∇P_s	solid pressure
ΔN_{js}	difference in critical impeller speed, rpm
σ	surface tension coefficient, kg s ²
σ	standard deviation value for solid suspension equations (4.22) and (6.33)
τ_k	viscous stress tensor of k th phase, kg/ m s ²
$\sigma_k, \sigma_\varepsilon,$	coefficient in turbulent parameters

Abbreviations

eff	effective
max	maximum
mf	minimum fluidisation
DT	disc turbine
PBTD	pitched blade turbine downward
PBTU	pitched blade turbine upward
rpm, RPM	revolutions per minute
vvm	volume of gas per volume of liquid per minute
2D	two dimensional
3D	three dimensional

Subscripts and superscripts

k, f ,q	phase
c	continuous phase
p	particle phase
g	gas phase
l	liquid phase
s	solid phase

Chapter 1

INTRODUCTION

Introduction

1.1. Background

All industrial chemical processes are designed to convert cheap raw materials to high value products through chemical reactions involving gas/liquid, gas/solid or gas/liquid/solid phases. A reactor in which such chemical transformations take place has to carry out several functions such as bringing reactants into intimate contact (to allow chemical reactions to occur), providing an appropriate environment (temperature and concentration fields, catalysts) for an adequate time and allowing for the removal of products. Handling systems involving two or more phases is common in areas from the processing of fuels and chemicals to the production of food, paper, pharmaceuticals and speciality materials. Typical examples of reactors involving multiphase flows are gas–liquid reactors like stirred reactors, bubble columns, gas–liquid–solid reactors like stirred slurry reactors, three-phase fluidised bed reactors *etc.*,

Some examples of multiphase reactor technology as cited by Dudukovic et al. (1999) include (1) the upgrading and conversion of petroleum feed stocks and intermediates; (2) the conversion of coal-derived chemicals or synthesis gas into fuels, hydrocarbons, and oxygenates; (3) the manufacture of bulk commodity chemicals that serve as monomers and other basic building blocks for higher chemicals and polymers; (4) the manufacture of pharmaceuticals or chemicals that are used in fine and speciality chemical markets as drugs or pharmaceuticals and (5) the conversion of undesired chemical or petroleum processing by-products into environmentally acceptable or recyclable products. The list of various types of industries that use multiphase reactor technology is shown in Table 1.1. The importance of multiphase reactor technology is clearly evident from the separate sessions dedicated to this topic

Introduction

in recent conferences like International Symposium on Multifunctional Reactor (ISMP-5), Gas–Liquid–Solid Reactor Engineering (GLS-8)).

Table 1.1. List of various industrial sectors that involve multiphase reactor technology

Industries	Examples
Synthesis and natural gas conversion	MeOH, DME, MTBE, paraffins, olefins and higher alcohols
Energy	coal, oil, gas and nuclear power plants
Bulk chemicals	aldehydes, alcohols, amines, acids, esters and inorganic acids
Fine chemicals and pharmaceuticals	dyes, fragrances, flavors and pharmaceuticals
Biomass conversion	syngas, methanol, ethanol, oils and high value added products
Petroleum refining	dewaxing, fuels, aromatics and olefins
Polymer and materials manufacture	polycarbonates, PPO, polyolefins, speciality plastics, semiconductors, <i>etc.</i>
Environmental remediation	De-NO _x , De-Sox, HCFCs, DPA and green processes
Hydrometallurgy	Refining of iron ore, ilmenite ore <i>etc.</i>

The development of multiphase reactor technology involves, initially development of either a new or an improved process which is often done in a laboratory scale and next is to select the practical and economical reacting system for the optimised process conditions with high performance. The performance may be expressed in the following way, *i.e.*, achieve a high selectivity and yield, reproduce the chemist's laboratory process on an industrial scale, high capacity and throughput, perform the reactions in a safe way and also fulfill the requirements of environmental

Introduction

regulations. The selection of multiphase reactor based on the systematic procedures is highly desirable and it should be based on a rational approach based on a reactor model. Such model must capture events on different scales and provides the ability to scale from laboratory to commercial process. Krishna and Sie (1994) proposed a strategy for multiphase reactor selection based on examining the particle scale phenomena, phase contacting pattern and flow, and the mixing pattern expected in a particular reactor from the point of view of their effect on chemical pathways and energy requirements of the process under consideration.

The refining and manufacture of value-added products of metal ores through hydro-metallurgical processing route is another area where multiphase reactor technology plays a major role. Typical example include refining iron containing ores like iron ore or ilmenite ore to value added products like sponge iron or synthetic rutile. During the last two decades, National Institute for Interdisciplinary Science & Technology (NIIST) (Formerly known as Regional Research Laboratory - Trivandrum) has been involved in development of an environmentally friendly process for the production of high grade synthetic rutile from ilmenite by modifying the existing Becher's process.

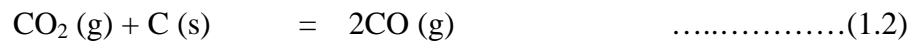
The environmentally friendly process for the manufacture of high grade synthetic rutile developed by NIIST consists of the following two major steps:

- 1) Metallisation (reduction of the ferrous and ferric oxide content in ilmenite to metallic iron) of ilmenite using a high volatile sub-bituminous coal as both fuel and reductant
- 2) Oxidative removal (accelerated corrosion) of metallic iron from the reduced ilmenite in an aerated solution containing an electrolyte, as hydrated iron

Introduction

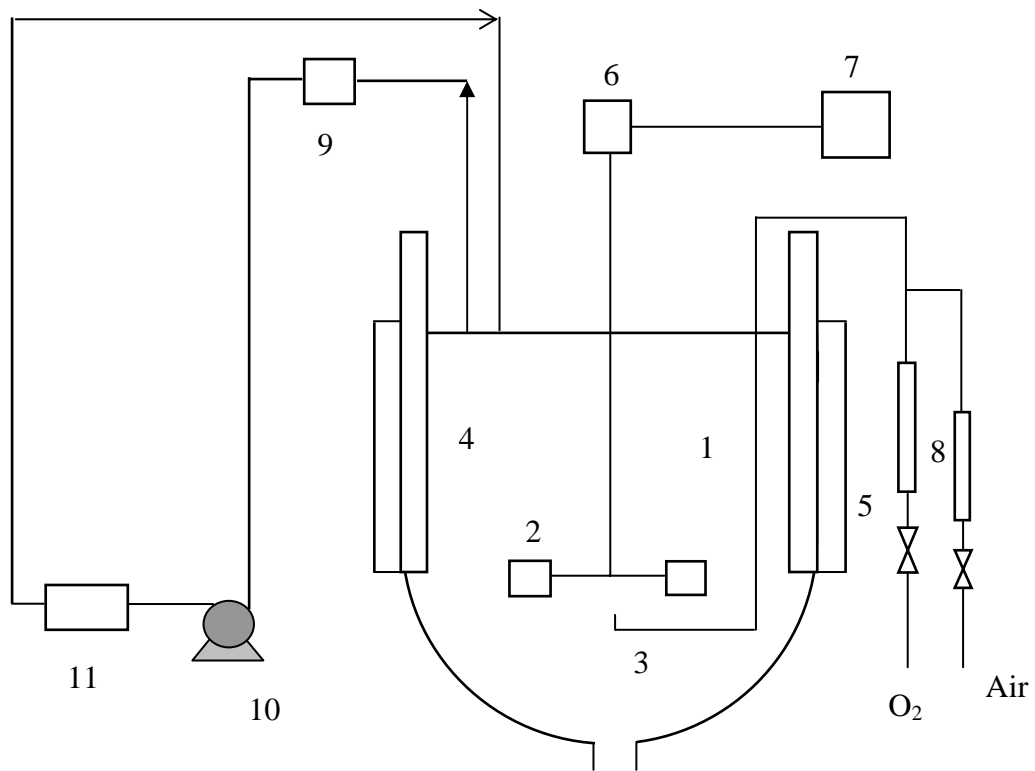
oxide (rust) and the separation of the hydrated iron oxide from rusted (beneficiated ilmenite) ilmenite.

The metallisation process is carried out in a rotary kiln, in which the iron (II) and iron (III) content of the ilmenite is reduced to metallic iron at about 1150°C using coal as both reductant and fuel. Overall reactions constituting the metallisation process can be represented as



During this step, reduced ilmenite particle consists of porous matrix of rutile covered on the surface with metallic iron.

The second major step is the removal of metallic iron from the surface of reduced ilmenite particles. The process of metallic iron removal from reduced ilmenite through the hydrometallurgical aeration leaching is popularly known as rusting reaction and is carried out by air sparging through slurry containing reduced ilmenite particles and liquid contacting electrolyte solution in a mechanically agitated reactor as a batch process. Figure 1.1 shows the schematic diagram of mechanically agitated contactor for rusting reaction.



- | | |
|----------------|--|
| 1. Reactor | 7. Power Meter |
| 2. Agitator | 8. Rotameters |
| 3. Gas Sparger | 9. Dissolved oxygen probe |
| 4. Baffles | 10. Pump |
| 5. Jacket | 11. Probe for pH temperature
and oxygen reduction potential |
| 6. D C Motor | |

Figure 1.1. Schematic diagram of mechanically agitated contactor for rusting reaction

The rusting process for removing metallic iron from metallised (reduced) ilmenite is an accelerated corrosion reaction carried out under aerated (oxygen enriched) condition in liquid containing electrolytes. The uniqueness and complexity of the process arises from the simultaneous but varying presence of four phases *viz.*, metallised ilmenite, hydrated iron oxide (rust), air bubbles and the liquid containing electrolytes. This is schematically depicted in Figure 1.2. The existence of interfaces

Introduction

between the phases is also depicted in the same figure highlighting the various resistances for the transfer of a gaseous species such as oxygen to the surface of a metallised ilmenite particle.

The mechanism of iron removal from metallised ilmenite can be represented as follows:

1. Reaction of solid surface

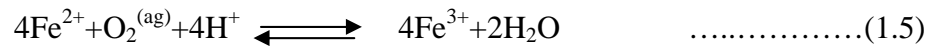
(a) Anodic reaction



(b) Cathodic reaction



If FeCl₂ is employed in the electrolyte, oxygen mass transfer rate enhancement occurs due to the reaction in the gas-liquid film;



followed by a cathodic reaction



at the solid-liquid interface depending on the red-ox potential and pH of the medium.

The reaction in the bulk liquid responsible for generation of the hydrated iron oxide are oxidation of ferrous ions given by



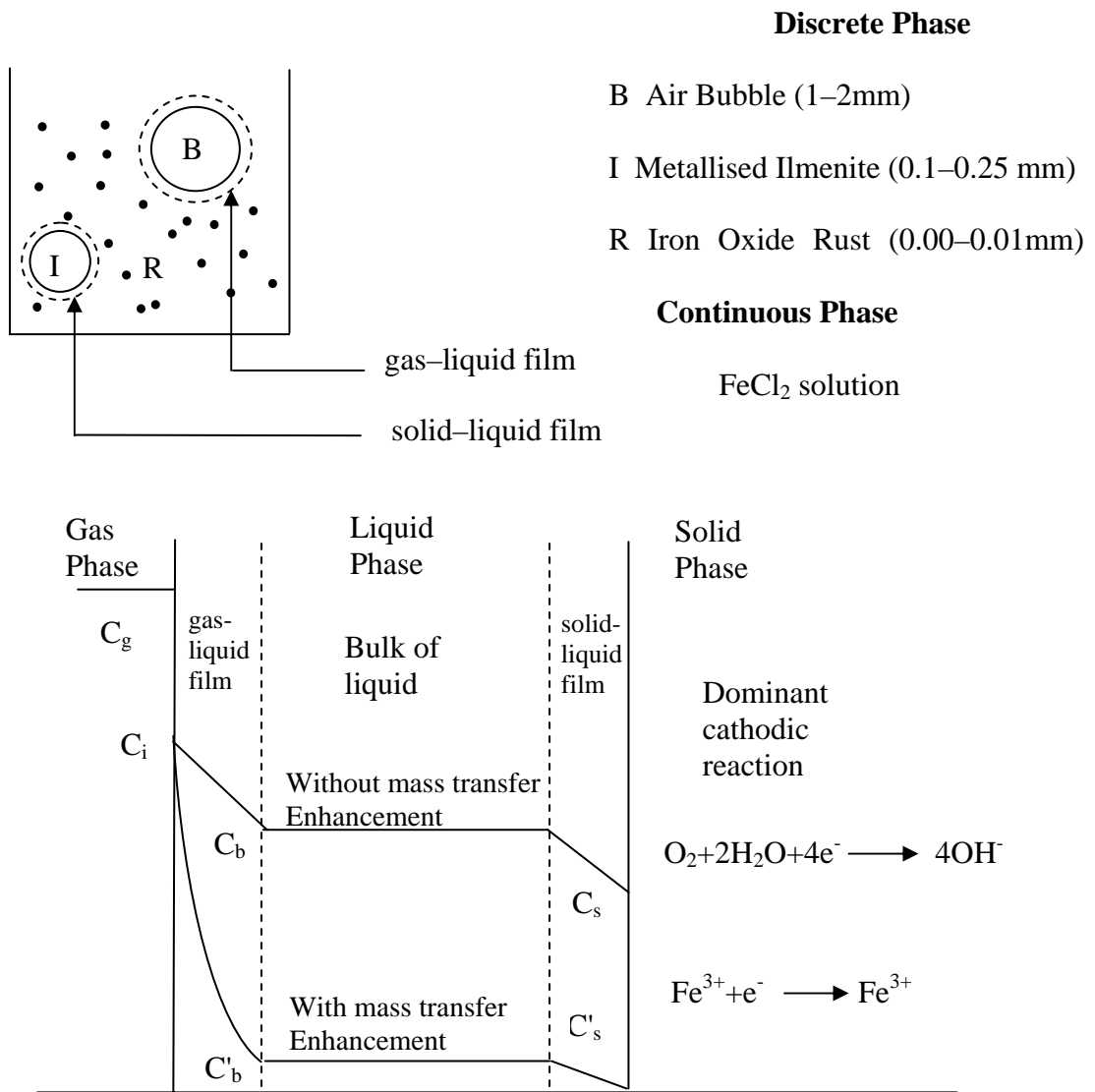


Figure 1.2. Schematic representation of the rusting process in a mechanically agitated reactor

The rate of metallic iron removal from metallised ilmenite in the corrosion environment is controlled by gas–liquid mass transfer, which was extensively studied by Geetha (1997), Geetha and Surender, (2001). The rates of mass transfer of oxygen depends on the size of air bubbles generated from the sparger, the impeller speed and the properties of the aqueous medium between metallised ilmenite and air bubble; namely, oxygen solubility viscosity, surface tension and oxygen diffusivity. It is

Introduction

important to note that the rusting process involves a slurry containing high solid content, typically in the range 20–40% by weight, with particle size in the range of 125–230 μm and density of 4200 kg/m^3 .

Eventhough the lab scale experiments showed higher degree of leaching of metallic iron from reduced ilmenite particles in the mechanically agitated reactor, the pilot plant trials showed lower degree of leaching. This may be due to the ineffective gas–liquid mass transfer at higher gas flow rates and higher solid content, particle breakage and also due to the scale up problems from lab scale to pilot scale. A significant problem with mechanically agitated reactors as multiphase reactors, as reported by Stitt (2002), is that the reactor may be mass transfer or heat transfer limited, and this can impact on operations by limiting productivity, and may affect both rate and selectivity. These problems are particularly acute during scale up. Geometric, bubble, mixing and kinetic lengths do not scale in proportion. This leads to uncertain changes in heat and mass transfer when scaling up the reactor from the laboratory to pilot /full scale.

Hence an investigation was carried out for finding an alternative multiphase phase reactor which can replace the traditionally used mechanically agitated reactor for rusting reaction. Based on the literature survey, it was concluded that gas–liquid–solid fluidised bed reactor provides a viable option to replace the traditionally used mechanically agitated reactors for achieving cost reduction and improvement (Epstein et al., 1981). Fluidised beds reactors provide many efficient properties such as good phase contact, minimum dead zone, excellent heat and mass transfer characteristics and high operational flexibility.

Introduction

A schematic diagram of the lab scale circulating fluidised bed reactor employed for rusting reactions is shown in Figure 1.3. It is a gas–slurry–solid fluidised bed operation in which coarse particles of metallic ilmenite is fluidised by concurrent flows of gas and slurry of rust with electrolyte liquid. The process comprises of subjecting metallised ilmenite particles to rusting reaction (accelerated corrosion) in a fluidised bed reactor with hydrated iron oxide (rust) and electrolyte liquid circulating through an external centrifugal pump. The oxygen required for the reaction is provided by venturi ejector aerator provided between the discharge of the centrifugal pump and the inlet of fluidised bed. Storage tanks are provided for electrolyte reaction medium, hydrated iron oxide slurry, dilute acid wash liquor and wash water, which are connected to the circulation loop through pipes. The TiO₂ enriched solids (beneficiated ilmenite) stays in the fluidised bed without undergoing external circulating till it is discharged from the bottom of the fluidised bed through the distributor as slurry. The various stages of rusting reaction, like washing and leaching of beneficiated ilmenite is carried out by appropriate liquid flow rate and the hydrated iron oxide is continuously separated as a wet cake and the liquor is returned to the reactor. This is an improved process for the removal and recovery of iron component from metallised ilmenite in a fluidised bed reactor with *in-situ* processing of metallised ilmenite (60–65 % TiO₂) upto the synthetic rutile (88–92%) stage in the same reactor, capable of carrying out the multifunctional tasks like iron removal from ilmenite beneficiate (rusting or accelerated corrosion), oxygen mass transfer, separation of hydrated iron oxide slurry, washing of beneficiated ilmenite with a mild acid followed by water.

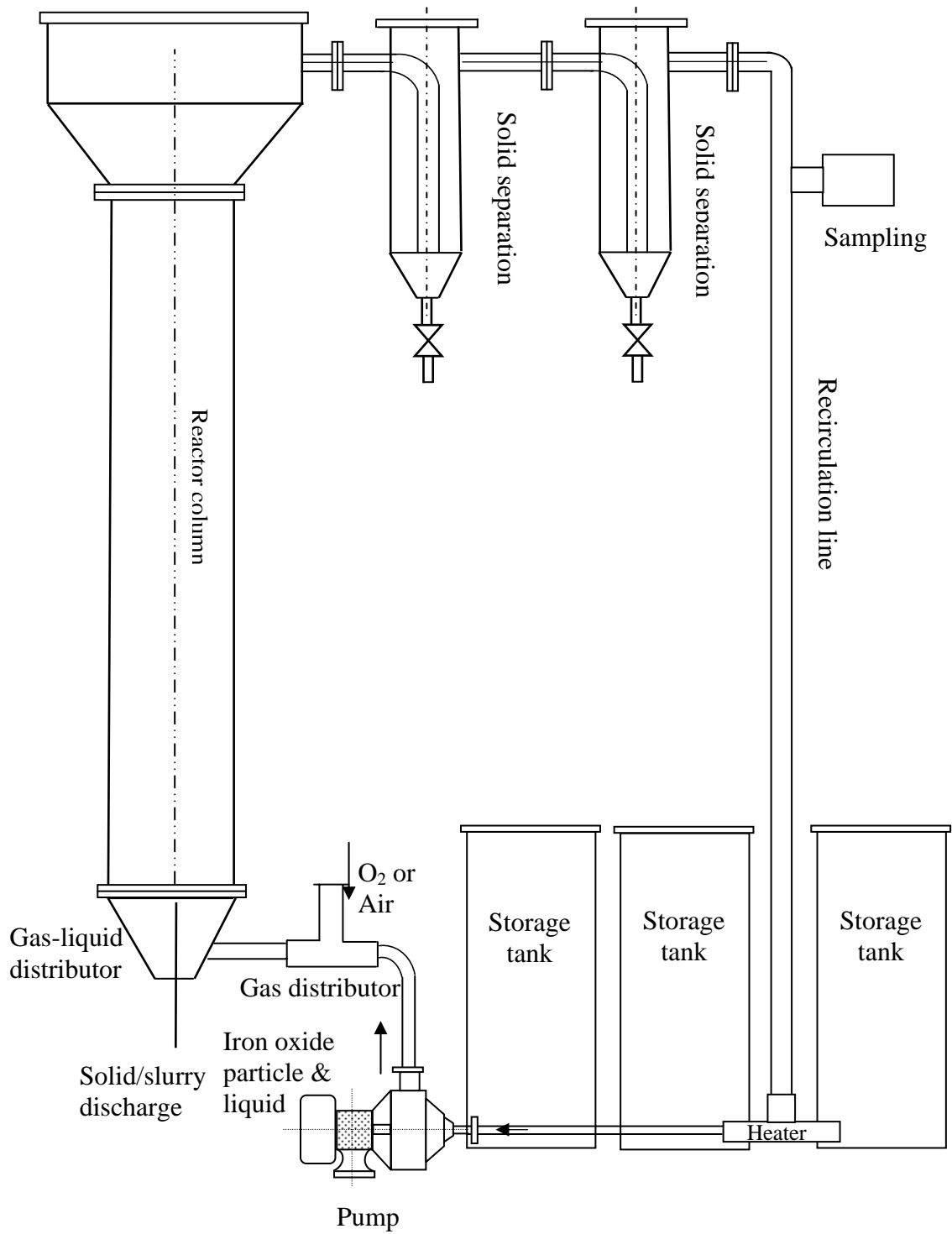


Figure 1.3. Schematic diagram of circulating fluid bed reactor for rusting reaction

Introduction

The main advantages of using circulating fluidised bed multi phase reactor are uniform distribution of fluid shear leading to reduced attrition between particles; less breakage of particles compared to mechanically agitated reactor and reduced capital and operating costs. Eventhough, the lab scale three-phase fluidised bed reactor gave excellent benefits, the scale-up problem from lab scale to pilot scale still remains. This is, because detailed knowledge of the solid circulation patterns is needed to prevent scale-up errors and to provide guidance in fluid bed reactor design.

Hence, an improved understanding of the fluid dynamics and transport processes in these multiphase reactors is very essential. This has forced many researchers and the practice engineers to resort to empirical relationships for design and scale up. But during the last two decades, there have been serious attempts by various researchers to reduce the state of empiricism. They have tried to understand the complex hydrodynamics of multiphase reactors by using two powerful tools *viz.*, Experimental Fluid Dynamics (EFD) and Computational Fluid Dynamics (CFD).

EFD is a technique to understand the flow structure of any multiphase reactor through the instrumentation. In recent years, various non-invasive methods have been developed for the measurement of the flow filed and holdup of phases in multiphase reactors, like tomography techniques based on the X-ray, Gamma ray and electron resistance tomography (ECT), and optical methods based on visible light i.e., laser doppler velocimetry (LDA), particle image velocimetry (PIV), computer automated radioactive particle tracking (CAPRT) methods.

CFD is an alternative tool which is based on solving the conservation equations for mass, momentum and energy using numerical methods in a computer. The application of CFD as a tool, for design and optimisation of reactors has grown in

Introduction

a rapid way because of the recent advances in numerical methods and computer hardware/ software. These CFD models can effectively be used to understand the complex flow phenomena in any reactor, which in turn can help in the better design of the reactor.

Both CFD and EFD techniques have led to better understanding of the detailed hydrodynamics in single phase flow systems. Eventhough, in this decade, there are more number of papers devoted for the case of gas–liquid, liquid–solid and gas–solid flows using these two techniques, only a handful of papers are available in the literature for gas–liquid–solid multiphase reactors.

Hence in this work, we have used computational fluid dynamics (CFD) tool to understand the complex hydrodynamics of the flow structures of three-phase system in both mechanically agitated contactor and fluidised bed reactor. Further, there is a need to quantify the performance of both these multiphase reactors in terms of flow patterns, phase holdups, solids mixing and circulation and transport phenomena. CFD models and simulations can effectively be used in understanding the extremely complex flow structures, which can then be used for scale up issues.

1.2. Objectives of this Investigation

Hence, in this investigation multiphase flow CFD simulation is used as a tool to develop validated computational models that accurately predict the various hydrodynamic flow behaviors of both liquid–solid and gas–solid–liquid mechanically agitated reactor and fluidised bed reactor under various process operating conditions. Further, the performance of both these reactors are carried out in terms of the following.

Introduction

- Hydrodynamics, by comparing power per volume (P/V) for solid suspension in liquid–solid and gas–liquid–solid fluidised bed and solid suspension in liquid–solid and gas–liquid–solid mechanically agitated reactor using CFD techniques.
- Transport phenomena, by comparing gas–liquid mass transfer in gas–liquid–solid fluidised bed and gas–liquid–solid mechanically agitated reactor using CFD techniques.

1.3. Outline of the Thesis

Chapter 1 gives the brief introduction to the subject of investigation, its relevance and scope of the present study. Chapter 2 gives a brief introduction to the CFD modeling of multiphase flows followed by the merits and demerits of different modeling approaches used in multiphase flow CFD. In the second chapter, various types of CFD techniques used for simulating multiphase flows are described in detail. This is followed by a brief introduction to ANSYS CFX software package which has been used in the present investigation.

Since development of a CFD model for three-phase system is quite complex, in terms of choosing the correct interphase momentum exchange mechanisms *etc.*, third and fourth chapter of this thesis is focused on developing a validated CFD simulation tool for the prediction of liquid solid flows in both the fluidised bed reactor and the mechanically agitated reactor. Detailed investigations on the two phase hydrodynamics of liquid–solid flows in fluidised bed reactor and mechanically agitated reactor using multiphase flow CFD approach is carried out and the validation of the CFD simulation is carried out for the experimental results reported in the literature in both these chapters.

Introduction

Chapters 5 and 6 of the thesis deal with the investigations of CFD simulations of hydrodynamics of gas–liquid–solid flows in mechanically agitated and fluidised bed reactor. The detailed investigations on gas–liquid mass transfer characteristics in gas–liquid–solid mechanically agitated reactor and fluidised bed reactor using CFD simulation is presented in Chapter 7. This is followed by the overall comparison of performance of mechanically agitated and fluidised bed reactor in terms of hydrodynamics and mass transfer. Conclusions based on the present investigations and scope and suggestions for the future course of work in this field is presented in the last Chapter.

Chapter 2

CFD MODELING OF MULTIPHASE FLOWS

2.1. Introduction

Computational Fluid Dynamics (CFD) is a body of knowledge and technique used to solve mathematical models of fluid dynamics on digital computers. The three major tasks involved in CFD are mathematical modeling of fluid flows, numerical solution of model equations and computer implementation of numerical techniques. CFD requires relatively few restrictive assumptions and gives a complete description of the flow field for all variables. Quite complex configurations can be treated and the methods are relatively easy to apply. It can incorporate a variety of processes simultaneously. CFD simulations serve as a bridge between the theory and reality. The detailed predicted flow field gives an accurate insight to the fluid behavior and can, sometimes, give information which cannot be obtained from experiments.

Computational Fluid Dynamics (CFD) is the science of predicting the fluid flow, heat transfer, mass transfer, chemical reactions and related phenomena by solving the mathematical equations that govern these processes using a numerical algorithm (that is, on a computer). CFD methods are based on the first principles of mass, momentum and energy conservation, as described by the Navier-Stokes equation. These methods involve the solution of conservation equations of mass, momentum, energy and species at thousands of locations within the flow domain. The computed solution provides flow variables such as velocity, pressure, temperature, density, concentration, *etc.*, within the domain.

There are two different approaches in deriving the governing equations. In the Eulerian approach, an arbitrary control volume in a stationary reference frame is used to derive the basic governing equations. In the Lagrangian approach, equations are

CFD Modeling of Multiphase Flows

derived by considering a control volume (material volume) such that the velocity of the control volume surface always equals the local fluid velocity.

When two or more phases move relative to each other in multiphase flow reactors, these phases exhibit different flow regimes. There are different ways of classifying these multiphase flows. The simplest classification is based on the thermodynamic state of phases like gas–solid, gas–liquid and gas–liquid–solid phases. Each component of these classes is then grouped according to the flow regimes which are generally classified as dispersed flows, mixed flows and separated flows. Dispersed multiphase flows occur in a number of industrially important reactors including stirred tank reactors, fluidised bed reactors, bubble column reactors, combustors and so on.

In CFD modeling of these dispersed multiphase flow processes, in general, there are three main issues:

- Definition of ‘phase’/flow regime/required resolution
- Formulation of governing equations
- Solution of governing equations

In dispersed flows, all the phases except one exist as dispersed (discontinuous) particles flowing through the continuous fluid. For many gas–liquid or gas–liquid–solid reactors, the liquid phase is a continuous phase in which gas bubbles and solid particles are dispersed (bubble column or stirred tank reactors). Since dispersed multiphase flows exhibit complex flow behavior, depending upon the situation one deals with, the coupling between the continuous phase and dispersed phase has to be considered while modeling multiphase flow process.

The simplest situation is a one way calculation, where the prediction of particle trajectories or distribution is sought in a known single-phase flow field. However, dispersed phase particles may influence the flow of the continuous phase and the level of interaction becomes especially complex for a turbulent flow field. When the size of the dispersed phase particle is very small or the mass loading of the particles is small, the influence of dispersed phase particles on the flow field of the continuous phase may be neglected. This is called one-way coupling. When the dispersed phase volume fraction is increased, the presence of dispersed phase will significantly affect the continuous phase flow field. This is called two-way coupling. If the particle number density is sufficiently large to allow direct particle–particle interactions, the modeler is faced with four-way coupling: continuous phase–dispersed phase particles–dispersed phase particles–continuous phase. It is essential to examine the extent of coupling between the dispersed and continuous phase to select an appropriate modeling approach.

There are three main approaches for modeling disperse multiphase flows:

- (a) Eulerian framework for all phases (without explicitly accounting for the interface between phases).
- (b) Eulerian framework for the continuous phase and Lagrangian framework for all the dispersed phases.
- (c) Volume of fluid approach (Eulerian framework for both the phases with reformulation of interface between the phases on volumetric basis).

2.2. Eulerian–Eulerian Model

The Eulerian–Eulerian approach models the flow of all phases in Eulerian framework on the interpenetrating continuum assumption. The discrete character of the underlying process is, therefore, averaged out to provide a model involving a

CFD Modeling of Multiphase Flows

continuum associated with the dispersed phase particles. This approach is the most difficult one to understand conceptually, requiring extensive modeling efforts. Various averaging issues will have to be addressed while formulating the governing equations in this approach. If modeled successfully, this approach can be applied to multiphase flow processes containing large volume fractions of dispersed phase. It may, therefore, be extended to the simulation of complex industrial multiphase reactors consisting of a large number of dispersed particles.

This is the most general model for multiphase flows. In this approach, each phase is treated as an interpenetrating continua. The phases share the same volume and penetrate each other in space and exchange mass, momentum and energy. Each phase is described by its distinctive physical properties and has its own velocity, pressure, concentration and temperature field. Conservation equations for each phase are derived based on the principles of mass, momentum and energy. The interphase transfer between the different phases is computed using empirical closure relations (van Wachem et al., 2003).

If the multiphase system has k phases, then the volume-averaged continuity equation for each phase is given by

$$\frac{\partial}{\partial t} (\epsilon_k \rho_k) + \nabla \cdot (\rho_k \epsilon_k \bar{u}_k) = \sum_{p=1}^n m_{pk} \dots\dots\dots(2.1)$$

where ρ_k is the density and ϵ_k is the volume fraction of k^{th} phase respectively and m_{pk} is the mass transfer from p^{th} to the k^{th} phase. The momentum balance for the phase k can be written as

$$\frac{\partial}{\partial t} (\rho_k \epsilon_k \bar{u}_k) + \nabla \cdot (\rho_k \epsilon_k \bar{u}_k \bar{u}_k) = - \epsilon_k \nabla P + \nabla \cdot (\epsilon_k \tau_k) + \rho_k \epsilon_k \bar{g} + M_{i,k} \dots\dots\dots(2.2)$$

CFD Modeling of Multiphase Flows

It should be noted that pressure, P , is regarded as being shared by all the phases and, therefore, appears in the governing equations of all phases. $M_{i,k}$ denotes the interphase momentum exchange terms between phase k and all other phases present in the system. τ_k is the viscous stress tensor of the k^{th} phase which is given by

$$\tau_k = \varepsilon_k \mu_k (\nabla \bar{u}_k + \nabla \bar{u}_k^T) + \varepsilon_k \left(\lambda_k - \frac{2}{3} \mu_k \right) \nabla \cdot \bar{u}_k \mathbf{I} \dots\dots\dots(2.3)$$

where μ_k and λ_k are the shear and bulk viscosity of phase k and \mathbf{I} is unit vector. When particle–particle interactions play a substantial role, it is necessary to introduce additional terms in the basic governing equations.

The Eulerian–Eulerian model is applicable for continuous–dispersed and continuous–continuous systems. For continuous–dispersed systems, the dispersed phase can be in the form of particles, drops or bubbles. The forces acting on the dispersed phase are modeled using empirical correlations and are included as part of the interphase momentum exchange terms. Drag, lift, gravity, buoyancy and virtual-mass effects are some of the forces that might be acting on the dispersed phase. These forces are computed for an individual particle and then scaled by the local volume fraction to account for multiple particles. If the dispersed phase is in the form of bubbles, then appropriate correlations for bubble distortion effects also are required. Correlations based on a single particle are not appropriate when the local volume fraction of the dispersed phase is high. Multi particle effects and corrections based on the presence of multiple particles in the vicinity of a single particle have to be applied.

This approach is more suitable for modeling dispersed multiphase systems where the dispersed phase volume fraction is greater than 10%. The accuracy of the Eulerian–Eulerian approach mainly depends on the empirical constitutive equations

CFD Modeling of Multiphase Flows

used. Although it requires significantly fewer computational recourses (which make it more effective for simulating the large individual reactions), it does not provide information about the hydrodynamics of individual bubbles and particles and thus has limitations in predicting certain discrete flow characteristics such as particle size effect, particle agglomeration or bubble coalescence and break up (Ranade, 2002).

In recent years, a number of simulation results have been presented on the hydrodynamics of multiphase reactors using Eulerian–Eulerian approach. Among these contributions, Lia and Salcudean (1987) simulated the bubble rise behavior using Eulerian–Eulerian approach and obtained good agreement between experimental and predicted velocity field. Ranade (1992) used Eulerian approach to investigate the flow field in a bubble column reactor. The same author (Ranade, 1997) later reported a new model (based on Eulerian approach) to include a radially varying slip velocity. Becker et al. (1994) simulated the 2D dynamic behavior of a relatively large laboratory bubble column with an Eulerian–Eulerian approach. The same case was the subject of study by Sokolichin and Eigenberger (1994). They used laminar flow conditions and concluded that unsteady-state simulations of gas liquid flow are essential in order to resolve the prevailing oscillating structures. The same authors (Sokolichin and Eigenberger, 1999), in a later communication, reported Eulerian simulation results with turbulent flow conditions in both 2D and 3D geometries. They inferred that it was not possible to reproduce the dynamic nature of bubble column using 2D simulations and emphasised the need for 3D dynamic simulation. Dudukovic and co-workers (Pan et al. 1999) used an Eulerian–Eulerian approach description to simulate the flow structures in a gas–liquid bubble column reactor. The simulated velocity field was compared with the experimental observations using

CFD Modeling of Multiphase Flows

radioactive particle tracking. Mudde and Simonin (1999) reported two and three-dimensional simulations of a meandering bubble plume using the Eulerian–Eulerian approach that included the k – ϵ turbulence model.

Krishna and co-workers (Krishna et al., 2000; van Baten and Krishna, 2002) used an Eulerian–Eulerian approach to simulate a bubble column reactor operating in the churn-turbulent regime. Because of varying size (1–5 cm) of bubbles in the churn-turbulent regime, the authors characterised the gas phase as two different phases – ‘small bubbles’ (1–6 mm) and ‘large bubbles’ (20–80 mm). Using 2D and 3D simulations, they obtained good agreement between the predicted and experimental gas holdup. Pflieger and co-workers (Pflieger et al. 1999; Pflieger and Becker 2001) carried out a transient three-dimensional Eulerian–Eulerian simulation of a bubble column reactor. They used the k – ϵ model to simulate the turbulent phenomena in the continuous phase. The dispersed phase was modeled using laminar flow conditions. The authors compared the dynamic and time-averaged prediction with the experimental data obtained from a 28.8 cm OD bubble column reactor and obtained good agreement for gas hold-up and velocity profiles. Buwa and Ranade (2004) have recently presented an extensive experimental investigation of a rectangular column with varying parameters such as sparger design, gas flow rate and coalescing properties. The plume oscillating period was shown to decrease with increasing gas flow rate. Although the period of oscillation was somewhat unpredicted, the 3D numerical simulations still exhibited reasonable agreement with experiments.

Gas–solid/gas–solid–liquid simulations with Eulerian–Eulerian approach is an emerging important research area in the last two decades. Gidaspow (1994) provided a comprehensive summary of the numerical models of gas–solid fluidised bed

CFD Modeling of Multiphase Flows

systems. Most of the effort was primarily focused on 2D simulations. Taghipour and co-workers (2005) have recently applied multi-fluid Eulerian model to simulate gas–solid fluidised bed. Comparison of their model predictions and experimental measurements on the time- averaged bed pressure drop, bed expansion, and qualitative gas–solid flow pattern has indicated reasonable agreement for different operating conditions. While there is an extensive literature on the two-phase flow model, studies of three-phase flow hydrodynamics are rather limited.

Hydrodynamics of bubble column slurry reactor was first investigated by Hillmer et al. (1994). Gidaspow et al. (1994) described a model for three-phase slurry hydrodynamics. Grevskott et al. (1996) developed a two-fluid model for three-phase bubble columns in cylindrical coordinates. They used a k – ϵ turbulence model and included bubble generated turbulence. Mitra-Majumdar et al. (1997) proposed a CFD model for examining the structure of three-phase flows through a vertical column. They suggested new correlations for the drag between the liquid and the bubbles and accounted for the particle effects on bubble motions. Recently, Wu and Gidaspow (2000) reported their simulation results for gas–liquid–slurry bubble column using the kinetic theory of granular flows for particle collisions. Padial et al. (2000) performed simulations of three-phase flows in a three dimensional draft-tube bubble column using a finite-volume technique. Gamwo et al. (2003) reported a CFD model for chemically active three-phase slurry reactors for methanol synthesis. van Baten et al. (2003) used Eulerian–Eulerian approach for three-phase bubble column. Slurry phase was assumed as a pseudo liquid phase (assuming uniform distribution of particles in liquid).

Rampure et al. (2003) studied both experimentally and computationally the effects of gas superficial velocity, H/D ratio and solid loading on the dynamic and time averaged flow behavior which provides a basis for further development of CFD models for three-phase systems. In spite of all these recent progresses in the applications of Eulerian–Eulerian approach for two and three-phase flows, experimental validation of these simulation results is still required.

2.3. Eulerian–Lagrangian model

In this approach, motion of the continuous phase is modeled using a conventional Eulerian framework. Depending on the degree of coupling (one-way, two-way or four-way), solutions of both phases interact with each other. For two-way or four-way coupling, an iterative solution procedure needs to be adopted. For four-way coupling, additional models to simulate particle–particle interactions have to be incorporated while simulating the trajectories of dispersed phase particles. In simple, one-way coupling, a continuous phase flow field can be obtained independent of the motion of the dispersed phase. Using such a flow field, the trajectories of dispersed phase particles can be obtained by solving the equations of motion for dispersed phase particles.

The continuous phase flow is described using the volume-averaged (overall) mass and momentum conservation equations:

The continuity equation for the continuous phase is

$$\frac{\partial}{\partial t}(\epsilon_f \cdot \rho_f) + \nabla \cdot (\rho_f \cdot \epsilon_f \cdot \bar{\mathbf{u}}_f) = 0 \quad \dots\dots\dots(2.4)$$

and the momentum balance equation is

$$\frac{\partial}{\partial t}(\rho_f \cdot \epsilon_f \cdot \bar{u}_f) + \nabla \cdot (\rho_f \cdot \epsilon_f \cdot \bar{u}_f \bar{u}_f) = -\epsilon_f \cdot \nabla P + \nabla \cdot \bar{\tau}_f + \rho_f \cdot \epsilon_f \cdot \mathbf{g} - \frac{\sum_{i=1}^K V_{s,i} \beta(\mathbf{u}_f - \mathbf{u}_{s,i}) \delta(\mathbf{x} - \mathbf{x}_{s,i})}{\sum_{i=1}^K V_{s,i}} \dots\dots\dots(2.5)$$

where the fluid phase stress tensor is defined as

$$\bar{\tau}_f = \epsilon_f \mu_f \left(\nabla \bar{\mathbf{u}}_f + \left(\nabla \bar{\mathbf{u}}_f \right)^T \right) + \epsilon_f \left(\lambda_f - \frac{2}{3} \mu_f \right) \nabla \cdot \bar{\mathbf{u}}_f \bar{\mathbf{I}} \dots\dots\dots(2.6)$$

where μ_f is fluid viscosity. The last term of equation (2.5) represents the interphase momentum transfer between the fluid phase and each individual particle, δ represents a pulse function, which is one, if its argument is zero and zero otherwise. The last term is to ensure that the interphase momentum transfer is only taken into account in the fluid-phase momentum equation at the location of the corresponding particle.

A general force balance over a single dispersed phase particle is written in Lagrangian reference frame. This force balance equates the particle inertia with forces acting on the particle using Newton's second law

$$m_p \frac{dU_p}{dt} = F_P + F_D + F_{VM} + F_L + F_H + F_G \dots\dots\dots(2.7)$$

Here m_p and U_p represent the mass and velocity vector of the particle, respectively. The right-hand side represents the total force acting on the dispersed phase particle. The sum of forces due to continuous phase pressure gradient, F_p , and due to gravity, F_G , can be written as

$$F_P + F_G = V_P \nabla P - \rho_p V_P \mathbf{g} \dots\dots\dots(2.8)$$

CFD Modeling of Multiphase Flows

where p is pressure in the continuous phase and V_p is the volume of the particle. The drag force, F_D , can be written as

$$F_D = -\frac{\pi}{8} C_D \rho_C D_P^2 |U_P - U_C| (U_P - U_C) \dots\dots\dots(2.9)$$

where the subscript C denotes the continuous phase and P denotes the particulate phase. The drag force has been studied extensively. The drag coefficient, C_D , depends on the flow regime (particle Reynolds number) and the properties of the continuous phase. Several empirical correlations have been proposed for the estimation of the drag coefficient. For a single rigid sphere, the drag coefficient is usually approximated by the correlation proposed by Schiller and Naumann (1935):

$$C_D = \begin{cases} \frac{24}{Re} (1 + 0.15 Re^{0.687}) & \text{if } Re_p < 1000 \\ 0.44 & \text{if } Re_p > 1000 \end{cases} \dots\dots\dots(2.10)$$

where Re_p is the particle Reynolds number

$$Re_p = \frac{\rho_C d_p |U_p - U_C|}{\mu_C} \dots\dots\dots(2.11)$$

$|U_p - U_C|$ represents the slip velocity between the continuous phase and dispersed phase. Apart from the drag force, there are three other important forces acting on a dispersed phase particle, namely lift force, virtual mass force and Basset history force. When the dispersed phase particle is rising through the non-uniform flow field of the continuous phase, it will experience a lift force due to vorticity or shear in the continuous phase flow field. Auton (1983) showed that the lift force is proportional to the vector product of the slip velocity and the curl of the liquid velocity and acts in a

CFD Modeling of Multiphase Flows

direction perpendicular to both, the direction of slip velocity and the direction of the curl of the continuous phase velocity field.

When a dispersed phase particle accelerates relative to the continuous phase, some part of the surrounding continuous phase is also accelerated. This extra acceleration of the continuous phase has the effect of added inertia or ‘added mass’ or virtual mass force. There may be some additional forces, such as Basset force (due to development of a boundary layer around the dispersed phase particles), thermophoretic force (due to large temperature gradient) and Brownian force. The Basset force denoted by F_H in equation (2.7) is relevant only for unsteady flows and in most cases, its magnitude is much smaller than the interphase drag force. Basset force involves a history integral, which is time-consuming to evaluate. Moreover, Basset force decays as t^{-n} with $n > 2$ (Mei, 1993) for an intermediate time. Therefore, it is very often neglected while integrating the equation of motion of the particle. Picart et al. (1982) discussed specific conditions under which the Basset term may be neglected. For most reactor engineering flows, the other two forces *viz.*, thermophoretic and Brownian forces, are also quite small compared to some of the terms discussed earlier.

Basically different approaches have been made to simulate a large number of dispersed phase particles, i.e., hard sphere approach, soft sphere approach and Monte Carlo techniques. In a hard sphere approach, particles are assumed to interact through instantaneous binary collisions. This means particle interaction times are much smaller than the free flight time and, therefore, hard particle simulations are event (collision) driven. In a soft sphere approach, particles are allowed to overlap slightly. The contact forces are then calculated from the deformation history of the contact,

CFD Modeling of Multiphase Flows

using say a linear spring/dashpot model. In Monte Carlo simulations, a new overlap-free particle configuration is generated at each time step. The new configuration is accepted based on the change in the system energy.

The advantage of Eulerian–Lagrangian approach is that the dynamics of the individual bubbles or particles can be assessed; however, in the case of turbulent flows, it is necessary to simulate a very large number of particle trajectories to obtain meaningful averages. Eventhough this approach gives useful information about particle–particle interaction, it is still difficult to apply this approach for large industrial multiphase reactors. This is due to the fact that for large size reactors, the tracking process of thousands of particles becomes highly memory-intensive and this approach is, therefore, suitable for simulating multiphase flows containing a low (<10%) volume fraction of the dispersed phases (Ranade, 2002). In literature, many papers have been published on the hydrodynamic modeling of multiphase reactors with Eulerian–Lagrangian approach.

Grevet et al. (1982) were among the first researchers to theoretically investigate the bubble rise phenomenon using Eulerian–Lagrangian approach in a bubble plume. The authors obtained a reasonably good agreement with experimental observations. van Swaaij and co-workers (Delnoij et al. 1997a; Delnoij et al. 1997b) used the same approach to simulate bubble trajectories in a bubble column reactor. Using 2D simulation, they obtained good agreement with the experimental observations of Becker et al. (1994). Delnoij et al. (1999) reported a 3D simulation of bubble rise in a rectangular bubble column reactor. They studied the effect of aspect ratio of the bubble column reactor on the flow pattern. As expected, they observed significantly complex flow patterns with 3D simulations. Lain et al. (1999) developed

CFD Modeling of Multiphase Flows

an Eulerian–Lagrangian approach including the k - ε turbulence model. Their model, however, neglected the effect of phase volume fractions. In a recent effort (Lain et al., 2002) a similar approach was applied for turbulence modeling in a cylindrical bubble column reactor with 14 cm diameter and 65 cm height. Bubble source term was included for hydrodynamic modeling and numerical results were confirmed with the experimental measurements using the phase-Doppler anemometer.

More recently, by ignoring the bubble–bubble interactions, Lapin et al. (2002) reported their Eulerian–Lagrangian simulations for slender bubble columns. They observed that the flow moves downwards near the axis and rises close to the wall in the lower part of the column, but in the upper part, the opposite trend is observed. When one or more dispersed phases are present as solid particles, the implementation of an Eulerian–Lagrangian approach is still straightforward.

Tsuji et al. (1993) developed an alternate Eulerian–Lagrangian method that used the discrete element method (DEM) for the solid phase coupled with the Eulerian equations for the fluid phase and studied 2D fluidisation of particles by a jet of gas at the inlet. Li et al. (1999) performed a series of simulations of gas–liquid–solid flows in fluidised beds using Eulerian–Lagrangian approach. Their study, however, was limited to the consideration of only a single bubble rising in liquid–solid fluidised bed. The predicted bubble rise velocity and bubble size compared very well with experimental data.

More recently, Zhang and Ahmadi (2005) have used similar approach to study the transient characteristics of gas–liquid–solid phase flows in three-phase slurry reactors. In addition to considering the interactions between particle–particle,

bubble–bubble, and particle–bubble, bubble coalescence is also included and the effects of bubble size variation on the flow pattern was also included.

2.4. Volume of Fluid (VOF) Approach

The VOF is one of the simplest and conceptually simple approach. In this approach, the motion of all phases is modeled by formulating local, instantaneous conservation equations for mass, momentum and energy. Such local instantaneous conservation equations can be solved using appropriate jump boundary conditions at the interface. However, the interface between different phases may not remain stationary and imposing boundary conditions at such an interface becomes a very complicated moving boundary problem. To avoid this, instead of directly tracking the deforming and moving interface, the VOF approach tracks the motion of all the phases, from which motion of the interface is inferred indirectly. All the interfacial forces, therefore, have to be replaced by smoothly varying volumetric forces. If the shape and flow processes occurring near the interface are of interest, the VOF approach should be used.

In VOF approach, the tracking of the interface between the phases is accomplished by the solution of a continuity equation for the volume fraction of one (or more) of the phases. For the q^{th} phase, this equation has the following form:

$$\frac{d \epsilon_q}{dt} + \vec{v} \nabla \cdot \epsilon_q = 0 \quad \dots\dots\dots(2.12)$$

A single momentum equation, which is solved throughout the domain and shared by all the phases, is given by

$$\frac{\partial}{\partial t} (\rho \vec{v}) + \nabla \cdot (\rho \vec{v} \vec{v}) = -\nabla P + \nabla \cdot \bar{\tau}_r + \rho g + F \quad \dots\dots\dots(2.13)$$

Whenever the shape and flow processes occurring near the interface are of interest, the VOF approach is useful. Some interface related forces, such as surface or adhesion forces can be modeled accurately using this approach (van Wachem et al., 2003). The only drawback of VOF method is the so-called artificial (or numerical) coalescence of gas bubbles which occurs when their mutual distances is less than the size of the computational cell, which also make this approach memory intensive for simulation of dispersed multiphase flows in large equipment (Ranade 2002). The first VOF type approach was suggested by Hirt and Nichols (1981). Although this scheme is still considered one of the simplest and well known methods for volume tracking, it performs badly due to large amount of smearing at the interface. The application of the so-called surface sharpening or reconstruction models, which are present in some commercial CFD codes, can somewhat prevent the smearing of the interface.

Hydrodynamic modeling of multiphase reactors with VOF is so far limited. The motion of single bubble in liquid is relatively well understood and extensive experimental data on shape and terminal velocity are available in the literature (Clift et al., 1978). Using these experimental data, 2D VOF simulations have been carried out for a single bubble rising in a stagnant fluid by many researchers (Krishna and van Baten, 1999; Essemiani et al., 2001; Liu et al., 2005) and few simulations have been carried out in three-dimensions (Olmos et al., 2001; van Sint Annaland et al., 2005). The rise trajectories of bubbles, their size and shape, rise velocity; effect of fluid properties on bubble dynamics and gas holdup were largely discussed. Among these studies, the efficiency of VOF approach was proved for the calculation of air bubble terminal velocities and shapes in stagnant water by Rudman (1997) and Krishna and van Baten (1999). For a precise prediction of ellipsoidal bubble properties, a three-

CFD Modeling of Multiphase Flows

dimensional system with sufficient small grid scales was considered by Olmos et al. (2001) and small spherical bubbles were simulated using two-dimensional axisymmetric models. Chen et al. (2004) has applied level set formulation of VOF to simulate bubble motion for two and three-phase fluidised bed. More recent studies (Bertola et al., 2004) predict the influence of bubble diameter and gas holdup on the hydrodynamics of bubble column reactor using VOF approach. Even though VOF simulations have shown significant improvements, there are still a lot of problems to be sorted out before implementing VOF simulations for large scale dispersed multiphase flow simulation.

2.5. Overview of ANSYS CFX Package

Since in the present work, the main emphasis is on understanding the complex flow structure of multiphase flow reactors using CFD as a tool, we have not attempted to develop an in-house code. Instead we have used one of the available commercial CFD code for our study in this thesis. There are many general purpose commercial software codes available in the market like, ANSYS CFX, FLUENT, STAR-CD, CHAM *etc.*, Ranade (2002) in his book has devoted a separate chapter discussing in length about the capabilities of these commercial codes. For our investigations we have used ANSYS CFX software package.

The major modules available in ANSYS CFX are shown in Figure 2.1

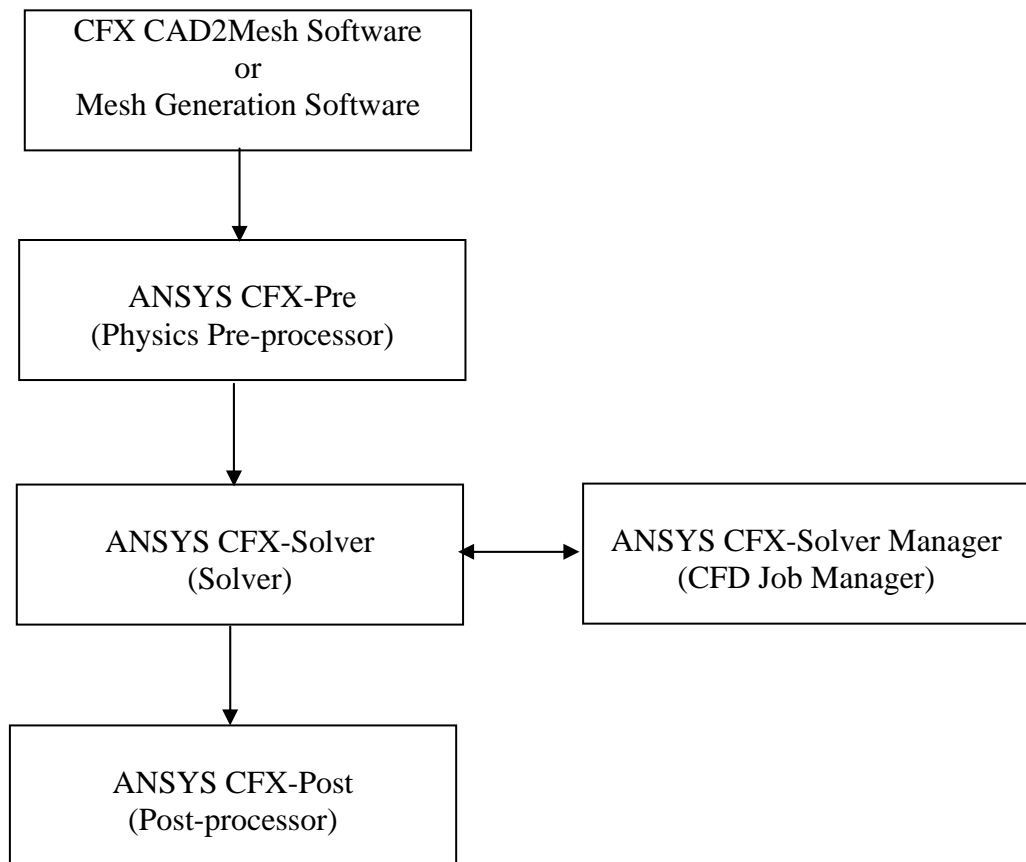


Figure 2.1. Modules of ANSYS CFX Software Package

2.5.1. Pre-Processor

In the preprocessor module the following tasks are carried out:

- a) Creation of geometry under investigation (Geometry);
- b) Dividing the geometry into smaller non-overlapping control volumes or meshing (Meshing);
- c) Defining the material properties, inlet and outlet conditions and specifications of boundary and initial conditions (ANSYS CFX-Pre);
- d) Setting up of the governing equations (ANSYS CFX-Pre).

CFD Modeling of Multiphase Flows

The ANSYS Workbench for CFD Applications module from ANSYS, Inc. offers a viable alternative approach for creating the geometry. The meshing application within the ANSYS Workbench environment provides access to swept, hex-dominant, tetrahedral and prism meshing technologies in a single location that can be applied on a part-by-part basis. ANSYS ICEMCFD meshing tools are available that include mesh editing capabilities as well as structured hexahedral meshing. After users have completed meshing, ANSYS CFX-Pre offers a modern, consistent and intuitive interface for the definition of complex CFD problems. ANSYS CFX-Pre can read one or more meshes from a variety of sources. Once meshes have been loaded, the user also has greater flexibility in assigning meshes to domains. In ANSYS CFX-10 multiple meshes can be put into a single domain, or a single mesh can be split into multiple domains, depending on the demands of the physics of the problem. Users are guided through physics definition by moving along the 'Define' toolbar, which presents the key steps in problem set-up. Existing cases may be loaded directly from CFX-5 DEF or RES files, ensuring consistent problem definition no matter how the problem may have been modified.

The creation and modification of physics objects is presented through a user interface with tabbed panels providing easy access to model details. The evolving problem definition is displayed in the object selector, which shows the key objects that can be selected to access any part of the problem definition. Errors or inconsistencies that occur during the problem setup/modification are shown through color coding in the object selector, or via descriptive messages in the Physics Message panel. Double-clicking in any one of the location will automatically open a panel to correct the problem.

CFD Modeling of Multiphase Flows

Once the problem definition is complete, hitting the 'Go' button will write a definition file for the CFX-5 solver.

2.5.2. Solver

Solving the governing conservation equations quickly and efficiently is a vital aspect of any CFD code. ANSYS CFX-10 uses a unique solution strategy, based on coupled multigrid solver technology, that surpasses existing CFD methods in speed and robustness. It produces accurate solutions to the linear algebraic equations with fast and reliable convergence.

The salient features of the ANSYS CFX solver are

- Fully automatic and requires no user input.
- Fully scalable achieving linear increase in CPU time with problem size.
- Representative of true physics.
- Easy to set up in both serial and parallel.
- Insensitive to mesh aspect ratio; so it reliably converges even with high refinement of boundary layer.

ANSYS CFX-10 radically improves the performance of the solver by solving the full hydrodynamic system of equations simultaneously across all grid nodes. This technique provides a robust and reliable solver, which requires far fewer iterations to converge. The coupled solver delivers better performance on all types of problems, but is particularly powerful in flows where inter-equation coupling is significant. The second important aspect of the ANSYS CFX-10 solver is its multigrid approach. While the coupled aspect of the solver deals with local effects, the multigrid solver effectively deals with the long distance or 'long wavelength' effects. This approach automatically generates a cascade of successively coarser grids, which allows the

CFD Modeling of Multiphase Flows

solution information to propagate rapidly across the entire computational domain. The solutions on the coarser meshes are used to accelerate the original fine grid solution. Also, iterations performed on the coarse mesh are proportionally less expensive than finer grid iterations, so it is clear that these accelerations are also economical. The ANSYS CFX-10 solver provides high memory efficiency. One million unstructured tetrahedral mesh element problems can be run in 400 MB RAM. The software intelligently uses the memory available in order to dynamically optimise the balance of resource usage against computational speed. The advanced numeric of ANSYS CFX-10's default "High-Resolution" discretisation delivers both of these. This adaptive numeric scheme locally adjusts the discretisation to be as close to Second-Order as possible, while ensuring the physical boundedness of the solution.

ANSYS CFX-10 has a large number of physical models like heat transfer, multiphase flow etc., to provide accurate simulation of a wide variety of industrial applications. Accurate simulation is enhanced because almost all the physical models inter operate with each other and in conjunction with all element types, across all grid interfaces, connection types, using the coupled multigrid solver, in parallel, with accurate numerics.

2.5.3. Post-Processor

Post-processing is a key step in the CFD analysis process. The large quantities of data generated by the solver must be clearly presented and help the analyst make valuable engineering decisions about their application. A good post-processing tool should allow the user to not only examine qualitative flow visualisation, but also to extract quantitative numbers for performance comparison and prediction. ANSYS

CFD Modeling of Multiphase Flows

CFX Post is a powerful graphical and quantitative post-processing tool that allows users to quickly extract useful information from ANSYS CFX-10. It's intuitive user interface makes it easy to use even for the casual user. In the standard interactive mode, ANSYS CFX Post also easily execute post-processing session files in batch mode to quickly reproduce the output for a series of runs.

ANSYS CFX Post provides flexible and accurate quantitative post-processing of ANSYS CFX-10 results. CFX-Post enables the full power of the CFX Expression Language within the post-processor, and extends it with a range of post-processing specific functions such as exact mass flow, area, length and volume-based integrals and averages of any quantity. Expressions can also be used to define new variables for the presentation of user specified quantities.

Chapter 3

CFD Simulation of Hydrodynamics of Liquid-Solid Fluidised Bed

3.1. Introduction

Liquid–solid fluidised beds continue to attract increasing attention due to their inherent versatility for several industrial applications in hydrometallurgical, biochemical, environmental and chemical process industries (Epstein, 2003). Due to advantages such as the absence of high shear zones and uniform distribution of solids, liquid–solid fluidised beds provide a viable option to replace mechanically agitated reactors for achieving cost reduction and improvements in product quality. However, due to the lack of information on various design and operating aspects of liquid–solid fluidised beds, it is likely that their introduction to large scale applications may not be realised as soon as desirable. Significant contributions have been made by several authors (Kiared et al., 1997; Limtrakul et al., 2005) to improve the understanding of the hydrodynamics of liquid–solid fluidised beds through experimental and theoretical investigations.

In comparison to reactors such as bubble column reactors, the flow patterns of solids in liquid fluidised beds is not yet fully understood in terms of circulation patterns and energy dissipation. Circulation phenomena of solids have been observed to be dominant in liquid fluidised beds due to non uniform solid holdup profiles and solid velocity profiles. For this reason, computational fluid dynamics (CFD) has been promoted as a useful tool for understanding multiphase reactors (Dudukovic et al., 1999) for reliable design and scale up.

Hydrodynamics and solids expansion in liquid fluidised beds have been extensively studied by several authors (Richardson and Zaki, 1954; Latif and Richardson, 1972; Gibilaro et al., 1986) and reviewed by Di Felice (1995). Kiared et al. (1997) investigated the motion of solids in liquid fluidised beds using non-invasive

CFD Simulation of Hydrodynamics of Liquid-Solid Fluidised Bed

radioactive particle tracking technique. According to their investigation, in the fully developed region of the bed, the flow structure consisted of a core and an annulus in which the solids underwent distinct upward and downward movements. Yang and Renken (2003) developed a more accurate relationship linking the apparent drag force, the effective gravitational force and the voidage to propose a generalised correlation for liquid particle interaction which is applicable for intermediate regime. This correlation along with Richardson and Zaki equation is applicable for laminar, intermediate and turbulent regimes. Recently, Limtrakul et al. (2005) have reported comprehensive experimental results for solid holdup and solids velocity profiles in liquid fluidised beds using non-invasive gamma ray based techniques. The non-invasive measurement techniques such as computer tomography (CT), computer-aided radioactive particle tracking (CARPT) are used for the prediction of phase holdup and solid velocity profiles respectively of liquid–solid fluids beds. This study provides the data needed for CFD validation. Based on the experimental observations, they have reported that the time-averaged solid holdup distribution is axisymmetric with high value at the wall and low value at the center and the average solid holdup can be predicted reasonably well with the modified Richardson-Zaki equation (Garside and Al-Dibouni, 1977).

Roy and Dudukovic (2001) have carried out experimental investigations on the fluid dynamics of liquid–solid risers using non-invasive flow methods and created a database for solids holdup distribution, the solids instantaneous and ensemble-averaged velocity patterns, as well as the solids residence time distribution in the riser. They used this database for validating their two fluid Euler–Euler CFD model. Cheng and Zhu (2005) developed a CFD model for simulating the hydrodynamics of

CFD Simulation of Hydrodynamics of Liquid-Solid Fluidised Bed

liquid–solid circulating fluidised bed reactor. They included turbulence and kinetic theory of granular flow in the governing equations to model the high Reynolds number two phase flows with strong particle–particle interactions and used FLUENT 4.5.6 for their CFD simulations. They reported strong non-uniformities in flow structure for the larger particle system. Doroodchi et al. (2005) used CFD approach to investigate the influence of inclined plates on the expansion behavior of solids in a liquid fluidised bed containing two different sized particles. Their model is based on the solution of Eulerian multiphase equations with two different particle sizes with continuous phase of water. The hindered settling behavior was included in their model via the inclusion of a volume fraction dependent drag law. The authors validated their computational model with their own experiments performed with ballotini particles demonstrating a significant increase in particle sedimentation rate due to introduction of inclined plates into the conventional fluidised bed. However, comparatively less information is available regarding CFD modeling of the solids flow pattern in a liquid–solid fluidised beds in contrast to the extensive knowledge of gas–solid fluidised beds and bubble column reactors.

In this chapter, the flow pattern of solids and liquid motion in liquid fluidised beds are simulated using CFD for various design and operating conditions. The data of Limtrakul et al. (2005) is chosen for the purpose of validating the numerical results obtained through CFD. The liquid fluidised beds used in the experimental study of Limtrakul et al. (2005) are two plexiglas columns: 0.1 m i.d. with 2 m height and 0.14 m i.d. with 1.5 m height. The liquid phase is chosen as water. The solid phase is chosen as glass beads of size 1 and 3 mm with a density of 2900 kg/m^3 and 2500 kg/m^3 respectively. They also used acetate beads of 3 mm size with a density of

1.3kg/m³

The present work also aims to evaluate the influence of various interphase drag force models, inlet boundary condition, grid resolution, time step sensitivity as well as a comparison between 2D and 3D simulation on the predictive capabilities of the numerical investigation. Based on the flow pattern of solids motion predicted by CFD, a solid mass balance in the center and wall regions of the fluidised bed and various energy flows are computed.

3.2. CFD Model

The simulation of liquid fluidised bed was performed by solving the governing equations of mass and momentum conservation using ANSYS CFX software. A multi-fluid Eulerian model, which considers the conservation of mass and momentum of fluid and solid phases, was applied.

Continuity equations:

Liquid phase

$$\frac{\partial}{\partial t}(\epsilon_l \rho_l) + \nabla \cdot (\rho_l \epsilon_l \vec{u}_l) = 0 \quad \dots\dots\dots(3.1)$$

Solid phase

$$\frac{\partial}{\partial t}(\epsilon_s \rho_s) + \nabla \cdot (\rho_s \epsilon_s \vec{u}_s) = 0 \quad \dots\dots\dots(3.2)$$

where ϵ_l, ϵ_s are the volume fractions of liquid and solid phase respectively which satisfy the relation

$$\epsilon_l + \epsilon_s = 1 \quad \dots\dots\dots(3.3)$$

\vec{u}_l, \vec{u}_s are the liquid and solid phase velocities respectively and ρ_l, ρ_s are the liquid

CFD Simulation of Hydrodynamics of Liquid-Solid Fluidised Bed

and solid phase densities respectively.

Momentum equations:

Liquid phase

$$\frac{\partial}{\partial t}(\rho_l \cdot \epsilon_l \cdot \bar{u}_l) + \nabla \cdot (\rho_l \cdot \epsilon_l \cdot \bar{u}_l \bar{u}_l) = -\epsilon_l \cdot \nabla P + \nabla \cdot (\epsilon_l \mu_{\text{eff},l} [\nabla \bar{u}_l + (\nabla \bar{u}_l)^T]) + \rho_l \epsilon_l \bar{g} + \bar{F}_{D,ls}$$

.....(3.4)

Solid phase

$$\frac{\partial}{\partial t}(\rho_s \cdot \epsilon_s \cdot \bar{u}_s) + \nabla \cdot (\rho_s \cdot \epsilon_s \cdot \bar{u}_s \bar{u}_s) = -\epsilon_s \cdot \nabla P - \nabla P_s + \nabla \cdot (\epsilon_s \mu_{\text{eff},s} (\nabla \bar{u}_s + (\nabla \bar{u}_s)^T)) + \rho_s \cdot \epsilon_s \cdot \bar{g} - \bar{F}_{D,ls}$$

.....(3.5)

where P is the pressure, which is shared by all the phases, μ_{eff} is the effective viscosity, ∇P_s is the collisional solids stress tensor that represent the additional stresses in solid phase due to particle collisions, g is the gravity vector, and the last term ($F_{D,ls}$) represents interphase drag force between the liquid and solid phases.

The most popular constitutive equation for solids pressure is due to Gidaspow (1994) viz.,

$$\nabla P_s = G(\epsilon_s) \nabla \epsilon_s$$

.....(3.6)

where $G(\epsilon_s)$ is the elasticity modulus and it is given as

$$G(\epsilon_s) = G_0 \exp(c(\epsilon_s - \epsilon_{sm}))$$

.....(3.7)

as proposed Bouillard et al. (1989), where G_0 is the reference elasticity modulus and is set to 1 Pa, c is the compaction modulus which is set to 100 for the present simulation and ϵ_{sm} is the maximum packing parameter.

For the continuous phase (liquid phase) the effective viscosity is calculated as

$$\mu_{\text{eff},l} = \mu_l + \mu_{T,l} + \mu_{tp}$$

.....(3.8)

where μ_l is the liquid viscosity, $\mu_{T,l}$ is the liquid phase turbulence viscosity or shear

CFD Simulation of Hydrodynamics of Liquid-Solid Fluidised Bed

induced eddy viscosity, which is calculated based on the k-ε model of turbulence as

$$\mu_{T,l} = c_\mu \rho_l \frac{k^2}{\varepsilon} \dots\dots\dots(3.9)$$

where the values of k and ε come directly from the differential transport equations for the turbulence kinetic energy and turbulence dissipation rate, μ_{tp} represents the particle induced turbulence and is given by the equation proposed by Sato et al. (1981) as

$$\mu_{tp} = c_{\mu b} \rho_s \varepsilon_s d_s |\bar{u}_s - \bar{u}_l| \dots\dots\dots(3.10)$$

The values used for constants in the turbulence equations are summarised in Table 3.1.

Table 3.1. Standard values of the parameters used in the Turbulence model

C_μ	σ_k	σ_ε	$C_{\varepsilon 1}$	$C_{\varepsilon 2}$	$C_{\mu b}$
0.09	1.0	1.3	1.44	1.92	0.6

The interphase drag force, which is generally, computed from the knowledge of the drag coefficient C_D , particle Reynolds number and solids volume fraction is given by

$$\bar{F}_{D,ls} = C_{D,ls} \frac{3}{4} \rho_l \frac{\varepsilon_s}{d_p} |\bar{u}_s - \bar{u}_l| (\bar{u}_s - \bar{u}_l) \dots\dots\dots(3.11)$$

where $C_{D,ls}$ is the interphase drag coefficient.

The following drag models are used for representing the drag coefficient between solid and liquid phases.

Drag model 1: Gidaspow (1994)

$$C_{D,ls} = \frac{150 \varepsilon_s^2 \mu_l}{\varepsilon_l d_p^2} + \frac{1.75 \varepsilon_s \rho_l (u_s - u_l)}{\varepsilon_l d_p} \quad (\varepsilon_l < 0.8) \dots\dots\dots(3.12)$$

$$C_{D,ls} = \frac{3}{4} Cd \rho_l \frac{\varepsilon_s}{d_p} (\bar{u}_s - \bar{u}_l) f(\varepsilon_l) \quad (\varepsilon_l > 0.8) \dots\dots\dots(3.13)$$

CFD Simulation of Hydrodynamics of Liquid-Solid Fluidised Bed

where

$$C_D = \frac{24}{Re_p} (1 + 0.15 Re_p^{0.687}), \quad Re_p \leq 1000 \quad \dots\dots\dots(3.14)$$

$$C_D = 0.44, \quad Re_p \geq 1000 \quad \dots\dots\dots(3.15)$$

and $f(\epsilon_1) = \epsilon_1^{-2.65} \quad \dots\dots\dots(3.16)$

Drag model 2: Di Felice (1994)

$$C_D = \frac{3}{4} C_d \rho_l \frac{\epsilon_s}{d_p} (\bar{u}_s - \bar{u}_1) f(\epsilon_1) \quad \dots\dots\dots(3.17)$$

where

$$f(\epsilon_1) = \epsilon_1^{-x} \quad \dots\dots\dots(3.18)$$

where x is given

$$x = 3.7 - 0.65 \exp \left[-\frac{1}{2} (1.5 - \log_{10} Re_p)^2 \right] \quad \dots\dots\dots(3.19)$$

Drag model 3: Syamlal and O'Brien (1988)

$$C_D = \frac{3}{4} \frac{C_d}{f^2} \frac{\rho_l |u_s - u_1|}{d_p} \epsilon_1 \epsilon_s \quad \dots\dots\dots(3.20)$$

and $C_d = (0.63 + 4.8 \sqrt{f/Re_t})^2 \quad \dots\dots\dots(3.21)$

where f is the ratio of the falling velocity of a superficial to the terminal velocity of a single particle and is given by Kmiec (1982) as

$$f = 0.5 \left(A - 0.06 Re_t + \sqrt{(0.06 Re_t)^2 + 0.12 Re_t (2B - A) + A^2} \right) \quad \dots\dots\dots(3.22)$$

where

$$A = \epsilon_1^{4.14} \quad \dots\dots\dots(3.23)$$

$$B = \begin{cases} \epsilon_1^{2.65}, & \epsilon_s < 0.15, \\ 0.8 \epsilon_1^{1.28}, & \epsilon_s \geq 0.15. \end{cases} \quad \dots\dots\dots(3.24)$$

3.3. Numerical Simulation

ANSYS CFX software code is used for simulating the hydrodynamics of liquid–solid fluidised bed. Tables 3.2 and 3.3 summarise the model parameters/conditions used for the simulation of solid motion in liquid fluidised beds.

Table 3.2. Simulation process conditions

Description	Value
2-D and 3-D simulation	column Diameter 0.14 m, height 1.5 m
Grid size	coarse mesh with 25000 nodes finer mesh with 40000 nodes
Time step	0.001–0.01 s
Inlet boundary	fully developed velocity profile uniform inlet velocity
Column diameter	diameter : 0.1 m , 0.14 m
Particle size	1 mm, 3 mm
Particle density	1300–2500 kg/m ³
Superficial liquid velocity	0.07–0.13 m/s

Table 3.3. Simulation model parameters

Solid	Glass beads	
Density (kg/m ³)	2500	
Size (mm)	3	1
U_{mf} (m/s)	0.0412	0.014
Solid holdup (-)	0.683	0.593
Bed voidage (-)	0.317	0.417
Initial bed height (m)	0.369	0.366

3.3.1. Flow Geometry and Boundary conditions

Figure 3.1 depicts typical numerical mesh used for simulation. The upper section of the simulated geometry, or freeboard, was considered to be occupied by liquid only. Inlet boundary conditions were employed at the bottom of the bed to specify a uniform liquid inlet velocity. The liquid is introduced at all the computational cells of the bottom of the column. Pressure boundary condition was employed at the top of the freeboard. This implies outlet boundary conditions on

CFD Simulation of Hydrodynamics of Liquid-Solid Fluidised Bed

pressure, which was set at a reference value of 1.013×10^5 Pa. The lateral walls were modeled using the no-slip velocity boundary conditions for the liquid phase and the free slip assumption for the solid phase.

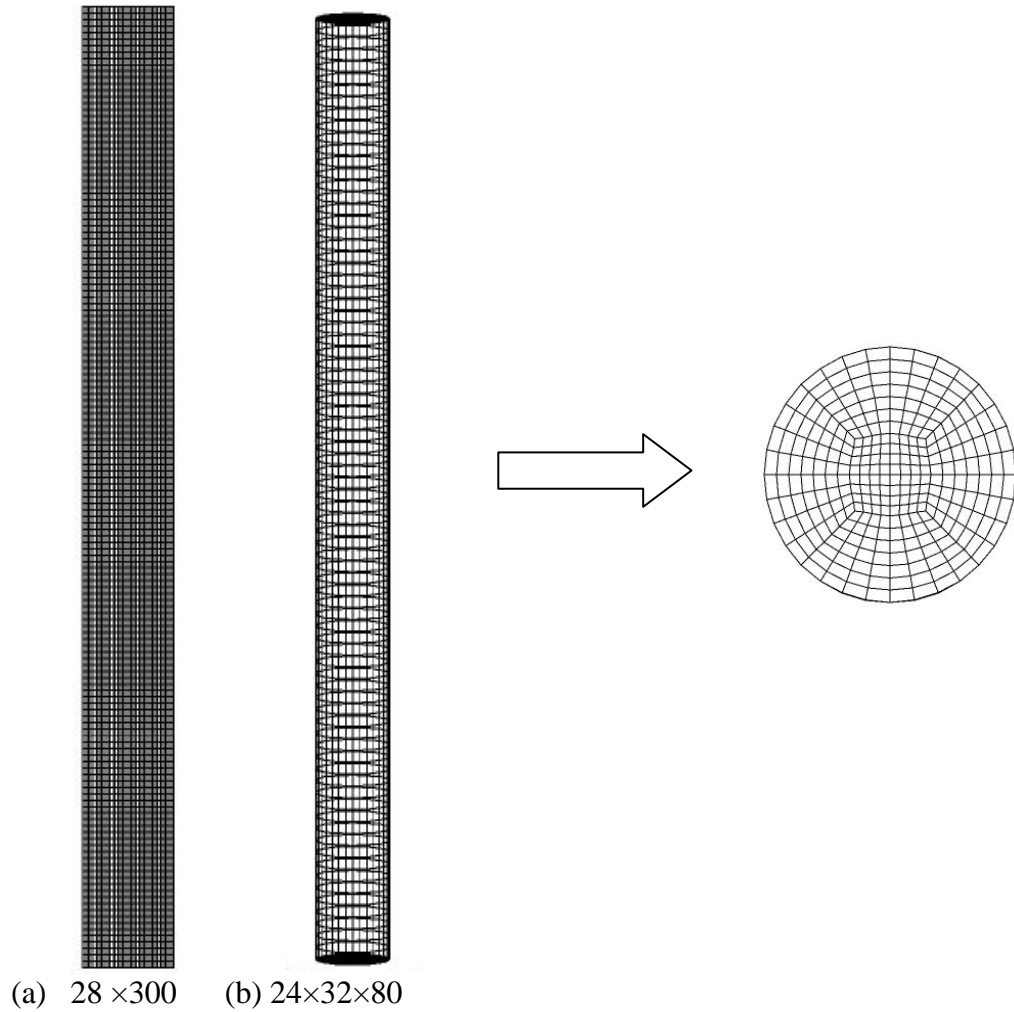


Figure 3.1. (a) 2D (b) 3D mesh of liquid fluidised bed

The numerical simulations of the discrete governing equations were achieved by finite volume method. Pressure-velocity coupling was achieved by the SIMPLE algorithm. The governing equations were solved using the advanced coupled multi-grid solver technology of ANSYS CFX. The second order equivalent to high-resolution discretisation scheme of momentum, volume fraction of phases, turbulent

CFD Simulation of Hydrodynamics of Liquid-Solid Fluidised Bed

kinetic theory and turbulence dissipation rate was chosen. During the simulations, the standard values of under relaxation factors were used. For time dependent solution the second order implicit time discretisation was used. The simulations were carried out till the system reached the pseudo steady state. Once the fully developed quasi-steady state is reached, the time averaged quantities are calculated. For all the simulations, the time averaged quantities are performed in the time interval 50–150s. The axial and azimuthal average is then performed along the axial direction within the middle section of the column. The convergence criteria for all the numerical simulation is based on monitoring the mass flow residual and the value of $1.0e-04$ is set as converged value. This convergence is monitored as a function of number of iterations at each time.

3.4. Results and Discussion

3.4.1. Comparison between 2D and 3D simulation

Figure 3.2 provides a comparison of time averaged solid holdup and solid velocity obtained through 2D and 3D CFD simulation. From Figures 3.2(b) & 3.2(d) it is evident that 3D CFD simulation provides a more accurate prediction of solid motion involving the core–annulus pattern and hence only 3D simulation was chosen for further studies in this work.

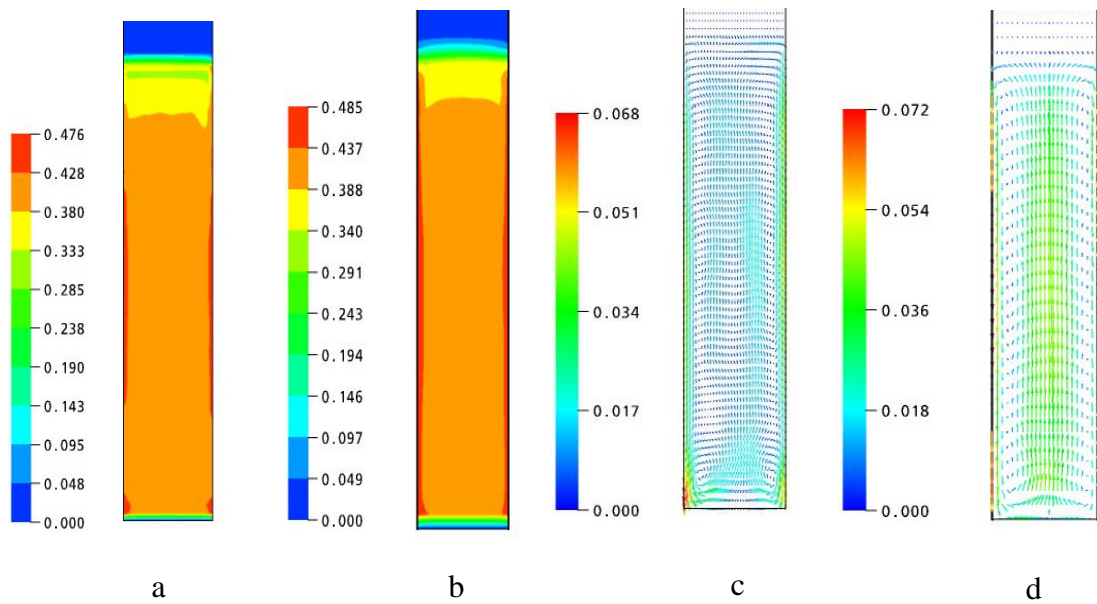


Figure 3.2. Comparison of 2D and 3D Simulation, time averaged solid holdup from (a) 2D (b) 3D simulation, time averaged solid velocity from (c) 2D Simulation (d) 3D simulation

3.4.2. Grid resolution study

Two type of meshes were used in this study i.e., mesh 1 contains a medium mesh of around 25000 nodes and mesh 2 contains 40000 nodes. The simulation was performed using a liquid superficial velocity of 0.07 m/s. Figure 3.3 illustrates the effect of different meshes on time averaged axial solid velocity. It shows that both meshes are giving the same pattern of axial solid velocity and there is not much difference in prediction of solid velocity profiles. So, in order to reduce the computational time, medium mesh was used for further simulation.

3.4.3. Effect of time step

Time dependent simulations were performed with time step in the range of 0.01–0.001 sec. The various time steps viz., 0.01, 0.005 and 0.001 sec were used for testing the accuracy of solution. Figure 3.4 shows the predicted solid volume fraction

CFD Simulation of Hydrodynamics of Liquid-Solid Fluidised Bed

at 5 sec for different time step of 0.01, 0.005 and 0.001 s. It can be shown that there is not much variation of solid holdup prediction for the time step values 0.005s and 0.001s. A computational time a value of 0.005 s was set as the time step for the simulation studies in this work.

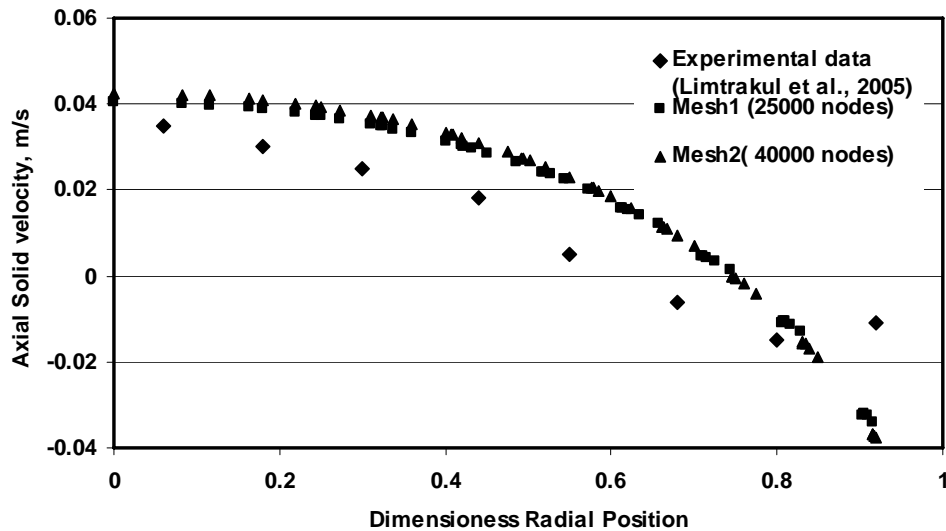


Figure 3.3. Influence of mesh sensitivity on the time averaged axial solid velocity at superficial liquid velocity of 0.07 m/s.

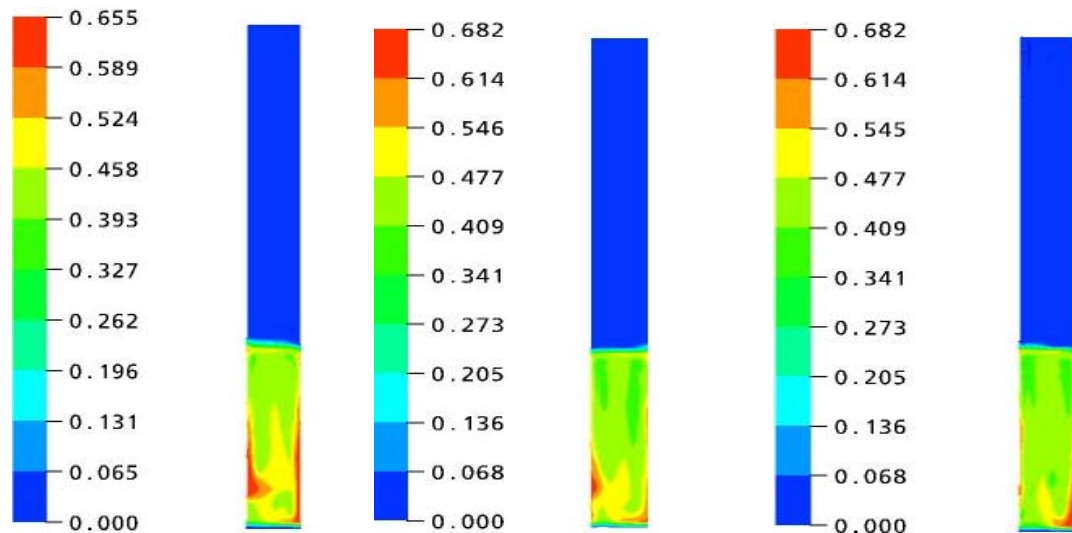


Figure 3.4. Influence of time sensitivity studies on the solid holdup (a) 0.01 s (b) 0.005s (c) 0.001s

3.4.4. Effect of drag force models

Figure 3.5 shows the effect of drag force models proposed by Gidaspow (1994), Di Felice (1994) and Syamlal and O'Brien (1988) by comparing the variation of axial solid velocity against dimensionless radius position. Table 3.4 depicts the influence of drag force models by comparing the bed expansion and solid holdup with experimental data reported by Limtrakul et al. (2005).

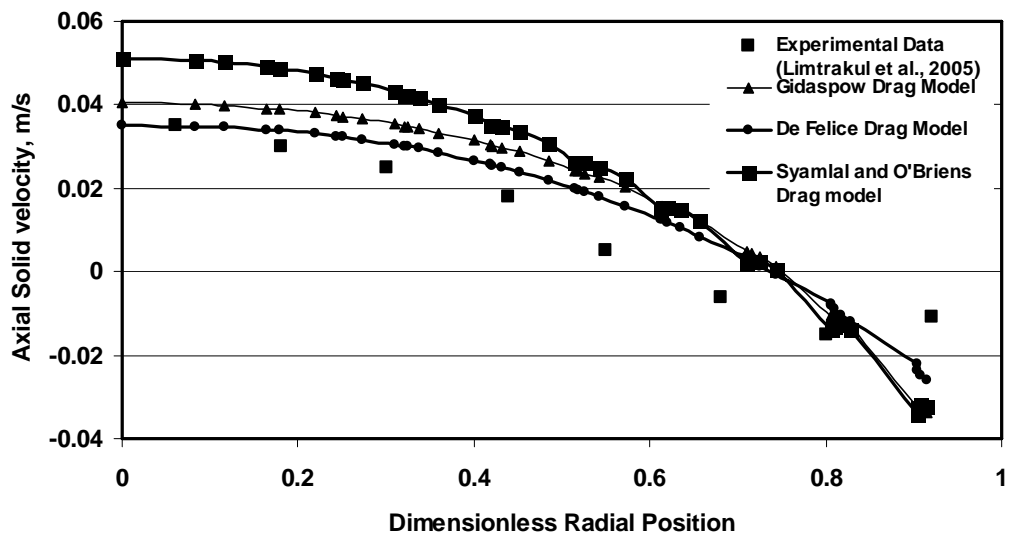


Figure 3.5. Influence of different drag force models on the time averaged axial solid velocity of fluidised at a superficial liquid velocity of 0.07 m/s.

Table 3.4. Comparison of bed expansion and solid holdup prediction from different drag force models and experimental data

Drag force Model	Bed Expansion			Solid holdup		
	Experimental	CFD	Error (%)	Experimental	CFD	Error (%)
Gidaspow (1994)		0.59	+0.7	0.43	0.43	-0.7
Di Felice (1994)	0.586	0.68	+16.0	0.43	0.36	-15.8
Syamlal and O'Brien (1988)		0.58	-1.0		0.43	0.23

CFD Simulation of Hydrodynamics of Liquid-Solid Fluidised Bed

Eventhough the models proposed by Syamlal and O'Brien and Gidaspow match closely with the experimental data of Limtrakul et al. (2005) (average error of 0.2–0.7% for solid holdup), the drag model proposed by Syamlal and O'Brien overpredicts the axial solid velocity profiles. Based on these observations the Gidaspow drag model was used in the present study.

3.4.5. Effect of inlet feed condition

The effect of two types of inlet velocity profiles ($V_{in} = V_{max} (1-r/R)^{1/7}$, uniform velocity profile) of liquid feed was evaluated with the experimental results in the present study. Table 3.5 presents the effect of different inlet conditions on bed expansion and solid holdup. The fully developed inlet profile gives lower bed expansion and higher solid holdup than the velocity profiles assuming uniform velocity as shown in Table 3.5.

Table 3.5. Comparison of bed expansion and solid holdup on the type of velocity profiles at the inlet

Type of feed inlet conditions	Bed Expansion			Solid holdup		
	Experimental	CFD	Error (%)	Experimental	CFD	Error (%)
Fully developed velocity profile	0.586	0.5	+14.7	0.43	0.49	-15.8
Uniform velocity profile		0.59	-0.68		0.42	+0.7

Table 3.6 gives the CFD model parameters used in the numerical investigation.

Table 3.6. Parameters employed in the CFD simulation

Description	Method used
Mode of simulation	3D
Grid size	25000 nodes
Time step	0.005 s
Drag model	Gidaspow Model
Inlet boundary	Uniform inlet velocity

3.4.6. Comparison of solid holdup between experimental and CFD results

Figure 3.6 shows the time averaged solid holdup as a function of dimensionless radial position along with the experimental results reported by Limtrakul et al. (2005). The solid holdup is defined as the volume fraction of the solid phase in the liquid–solid mixture. The solid holdup profile predicted by the CFD simulation matches closely with experimental data at the center of the column and varies at the wall region of the column with an average error of 2.6 %. The enhanced deviation at the wall may be due to wall effects which have not been explicitly considered in the present study. Table 3.7 shows the averaged solid holdup obtained by the experimental and the CFD simulation at various operating conditions. It is observed that the solid holdup obtained from the CFD simulation is able to predict the experimental results reported by Limtrakul et al. (2005) with an average error of 2–14 %.

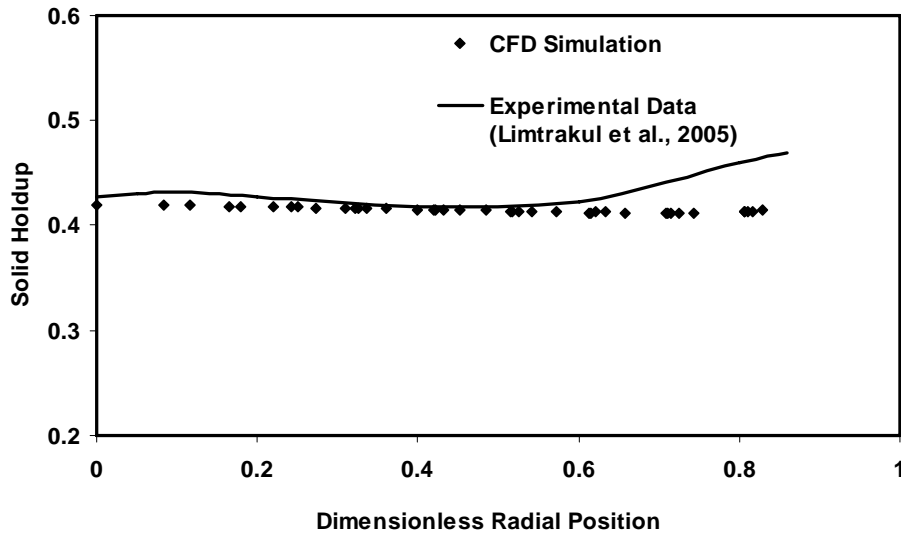


Figure 3.6. Azimuthally averaged solid holdup profile obtained by CT scan and CFD simulation, 0.14 m diameter column, 0.003 m glass beads $U_1=0.07$ m/s

Table 3.7. Experimental validation of average solid holdup predicted by the CFD

Column size (m)	Superficial Liquid velocity (m/s)	Solid particle	Holdup from Experimental Data (Limtrakul et al., 2005)	Holdup from the present CFD simulation	Error (%)
0.14	0.07	Glass beads (3mm)	0.44	0.42	+4.5
		Glass beads (1mm)	0.51	0.48	+5.9
0.1	0.1	Glass beads (3mm)	0.35	0.3	+14.3
	0.13	Glass beads (3mm)	0.25	0.255	-2.0
	0.065	Glass beads (3mm)	0.48	0.43	+10.4

3.4.7. Solid motion in liquid fluidised bed

Experimental studies of solid motion reported by Limtrakul et al. (2005) show that multiple solids cell circulations patterns exist for all conditions of liquid fluidised

CFD Simulation of Hydrodynamics of Liquid-Solid Fluidised Bed

bed operations. However CFD simulation exhibits only a single solid circulation cell which is also in agreement with the observations of Roy et al. (2005) in a liquid–solid riser. Figure 3.7 shows the vector plot of time averaged solid velocity on the different planes at typical operating conditions ($U_1=0.07$ m/s) for glass beads. The existence of a single recirculation cell with solids ascending along the column at the center and descending along the wall is evident from the simulation results. CFD simulation of axial solid velocity at various dimensionless radial positions is depicted in Figure 3.8. The agreement between the experimental and simulation results is quite satisfactory.

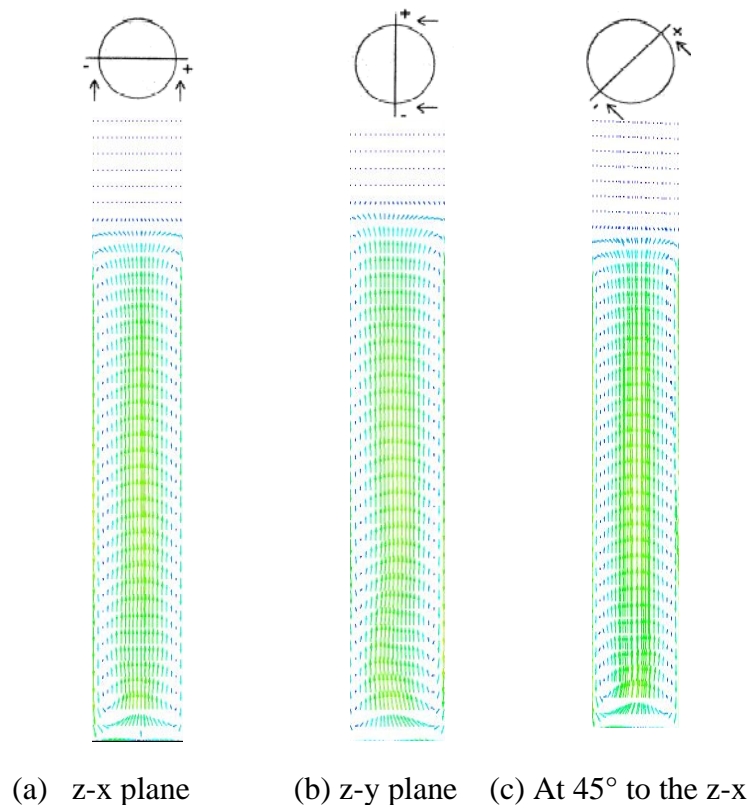


Figure 3.7. Typical time averaged azimuthally averaged axial solid velocity profile

3.4.8. Effect of Column Diameter

In this work, two columns of 0.1 m and 0.14 m in diameter are used to study the effect of column diameter. The simulation results of the effect of column diameter

CFD Simulation of Hydrodynamics of Liquid-Solid Fluidised Bed

on axial solid velocities are compared with the experimental results in Figure 3.9 and it shows that the axial solid velocities increase with increase in column diameter, at superficial liquid velocity of 0.07 m/s

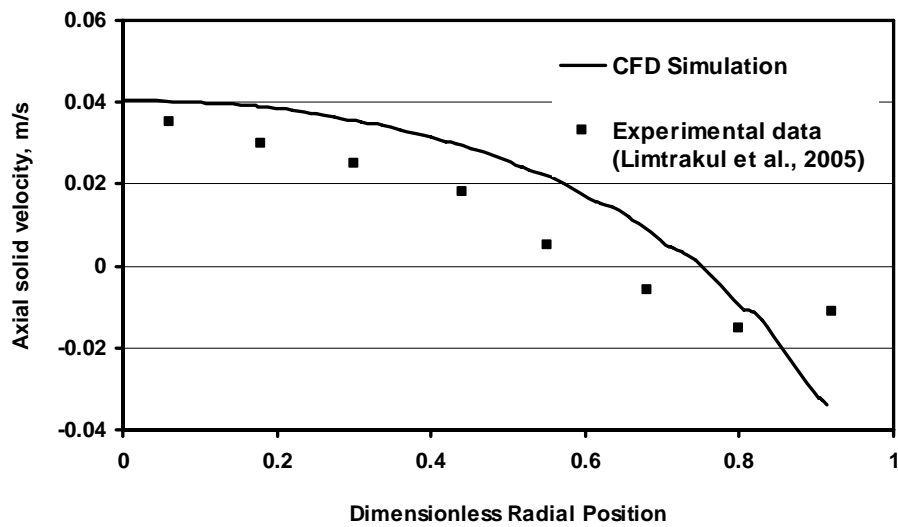


Figure 3.8. Axial solid velocity profiles as a function of radial position at a superficial velocity of 0.07 m/s

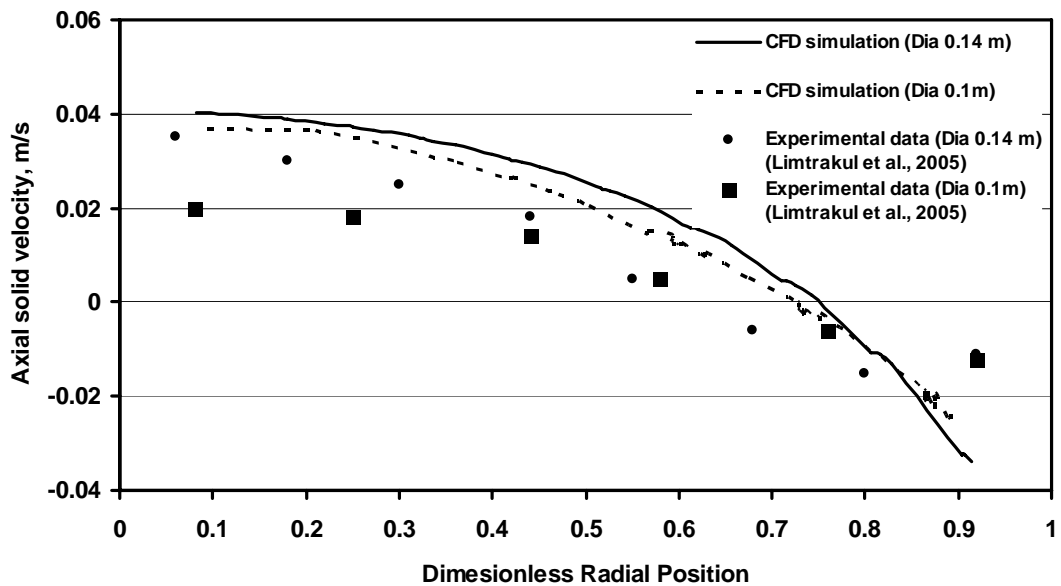
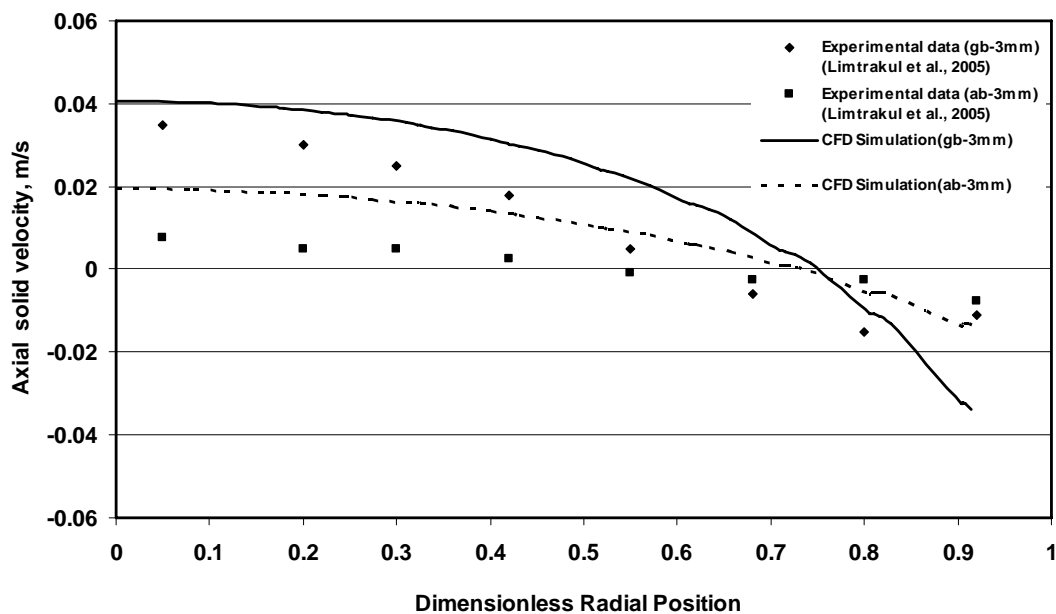


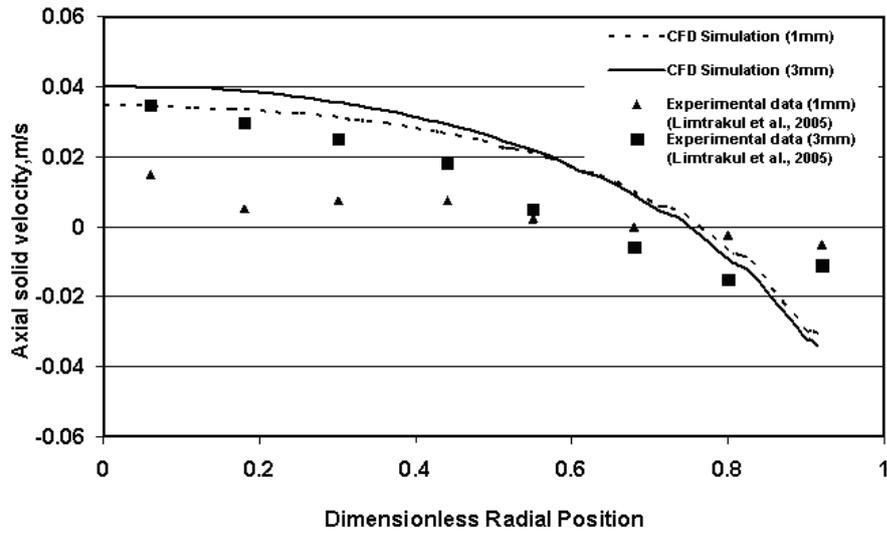
Figure 3.9. Effect of column size for 0.003 m glass beads at $U_1= 0.07$ m/s

3.4.9. Effect of Particle size and density

Acetate beads ($\rho_s = 1300 \text{ kg/ m}^3$) and glass beads ($\rho_s = 2500 \text{ kg/ m}^3$) with particle sizes, 0.001m and 0.003 m were used to study the effect of particle size and density. Figure 3.10 (a, b) shows that the axial solid velocities increase with increase in particle diameter and density leading to larger inversion point (the point at which axial solid velocity is zero) for both CFD simulation and the experimental results reported by Limtrakul et al. (2005). Table 3.8 depicts the comparison of the inversion points for different operating conditions. The smaller size particle of 1 mm glass beads has a smaller value of inversion point compared to that of glass beads of 3 mm size. Song and Fan (1986) mentioned that due to higher value of apparent viscosity of slurry, the inversion point is reduced for systems with particles having smaller sizes.



(a)



(b)

Figure 3.10. (a) Effect of particle type (U_1 for glass beads =0.007 m/s, U_1 for acetate=0.024 m/s) and (b) Effect of particle size (U_1 for 3 mm =0.007 m/s, U_1 for 1mm =0.024 m/s) on axial solid velocity

Table 3.8. Comparison of inversion points for different operating conditions

Column Diameter	Solid properties	Inversion Points	
		Experimental (Limtrakul et al., 2005)	CFD Simulation
0.14 m	Glass beads (2500 kg/m ³ ,3mm)	0.72	0.77
	Glass beads (2900 kg/m ³ ,1mm)	0.62	0.69
	Acetate beads (1300 kg/m ³ ,3mm)	-	0.64
0.1m	Glass beads (2500 kg/m ³ ,3mm)	-	0.72

3.4.10. Effect of liquid superficial velocity

The increase in superficial liquid velocity increases the energy input to the system, leading to enhanced bed expansion and solid motion. Figure 3.11 shows the

CFD Simulation of Hydrodynamics of Liquid-Solid Fluidised Bed

effect of liquid superficial velocity on the time averaged axial solid velocity. The CFD predictions of axial solid velocity give the same pattern as that obtained from the experimental data.

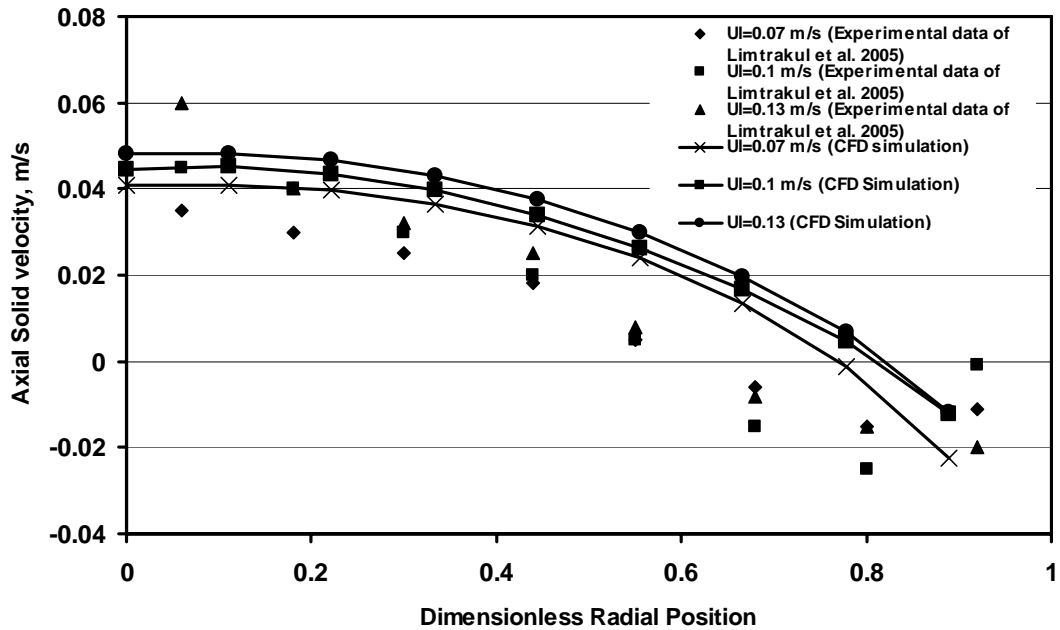


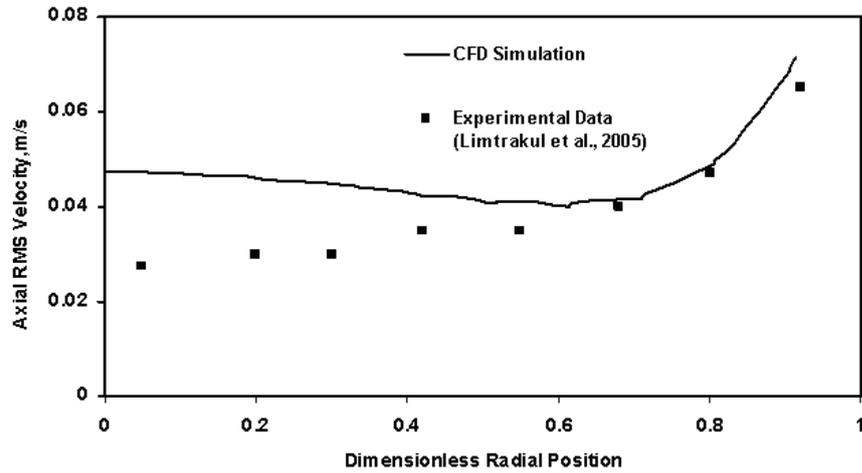
Figure 3.11. Effect of superficial liquid velocity on time averaged axial solid velocity

3.4.11. Turbulence parameters

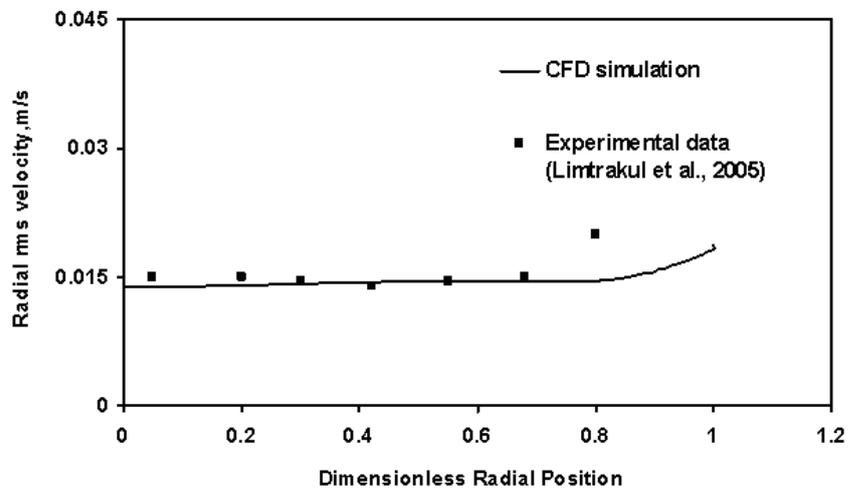
To further validate the CFD simulation results, a comparison of the turbulence parameters viz., turbulence intensities, and shear stress profiles with the experimental data provided by Limtrakul et al. (2005) was made. Figure 3.12 shows the root-mean-square (rms) axial (u_r') and radial (u_r') velocities of solids along the radial position. Figures 3.12a and b show that the axial RMS velocities are roughly twice those of the corresponding radial components. Similar to the observations made by Devanathan et al. (1999) in gas–liquid bubble columns systems and Roy et al. (2005) in liquid–solid

CFD Simulation of Hydrodynamics of Liquid-Solid Fluidised Bed

riser. A typical comparison of the experimental and the simulation results is depicted in Figures 3.12 and 3.13.



(a)



(b)

Figure 3.12. (a) Variation of radial rms velocities along the radial position
(b) Variation of axial rms velocities along the radial position

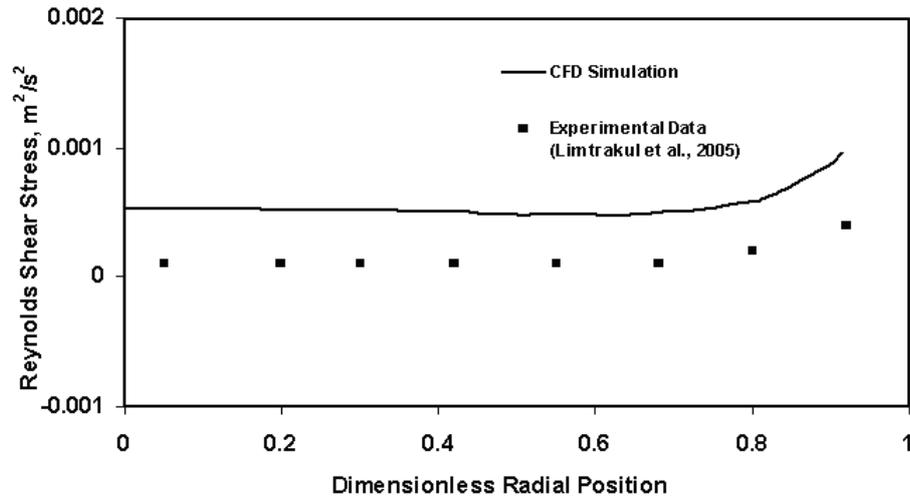


Figure 3.13. Variation of Reynolds Shear stress along the radial position

3.4.12. Computation of solids mass balance

Based on the validation of CFD model predictions discussed earlier, a mass balance of solids in the center and wall region was computed to verify the conservation of solid mass in the liquid–solid fluidised bed i.e. the net solid volume flow rate in center region should equal the net solid volume flow rate in the wall region represented mathematically as

$$\text{Solid upflow rate in the core region} = 2\pi \int_0^{R_i} r \epsilon(r) V_z(r) dr \quad \dots\dots\dots(3.25)$$

$$\text{Solid downflow rate in the annular region} = 2\pi \int_{R_i}^R r \epsilon(r) V_z(r) dr \quad \dots\dots\dots(3.26)$$

where $\epsilon(r)$ is the time averaged radial solid holdup profile and $V_z(r)$ is the time averaged axial solid velocity and R_i is the radius of inversion, defined as the point at which the axial solids velocity is zero. The radial solid holdup profile at each of the operating conditions proposed by Roy et al. (2005) is given by

$$\epsilon_s(r) = \bar{\epsilon}_s \frac{m+2}{m+2+2C} \left[1 + C \left(\frac{r}{R} \right)^m \right] \quad \dots\dots\dots(3.27)$$

Similarly an expression that has been observed to describe the radial profile of the

CFD Simulation of Hydrodynamics of Liquid-Solid Fluidised Bed

axial solids velocity (Roy et al., 2005) is

$$V_z(r) = V_z(0) + \alpha_1 \left(\frac{r}{R}\right)^n - \alpha_2 \left(\frac{r}{R}\right)^{n\alpha_1/\alpha_2} \dots\dots\dots(3.28)$$

In equation 3.28, $V_z(0)$ is the centerline axial solids velocity, and α_1 and α_2 are empirical constants determined through curve fitting. The exponent n defines the curvature of the velocity profile.

The net volumetric solid flow rates computed from equations (3.26) and (3.27) are shown in Table 3.9. The relative deviation of volumetric solid flow between core and wall region is observed in the range of 10–15%. This finding may be compared with observation of Kiared et al. (1997) who investigated the net solid flow rate in the center and wall region and obtained the relative deviation for volumetric mass rate in the range of 23–27 %.

Table 3.9. Mass balance of solid in the liquid fluidised bed

Column Size (m)	Liquid superficial velocity(m/s)	Solid particle	Volumetric flow rate of solid in center (m ³ /s)	Volumetric flow rate of solid in wall (m ³ /s)	Relative deviations (in %)
	0.07	Glass beads (3mm)	1.614E-05	1.86E-05	13.1
	0.07	Glass beads (1mm)	1.236E-05	1.506E-05	17.9
0.14	0.1	Glass beads (3mm)	8.303E-06	8.563E-06	3.0
	0.13	Glass beads (3mm)	6.3507E-06	5.629E-06	12.8
	0.024	Acetate beads (3mm)	5.3572E-06	5.339E-06	0.03

3.4.13. Computation of various energy flows

It is informative to investigate the various energy flows into the two-phase fluidised bed and make an order-of-magnitude estimate of the various terms in the

CFD Simulation of Hydrodynamics of Liquid-Solid Fluidised Bed

energy flows. Extensive work has been carried out by Joshi (2001) to understand the energy transfer mechanism in gas–liquid flows in bubble column reactors. A similar attempt is made in this work. In liquid–solid fluidised beds, the input energy from liquid is distributed to the mean flow of the liquid and the solid phases. Also, a part of the input energy is used for liquid phase turbulence and some part of the energy gets dissipated due to the friction between the liquid and solid phases. Apart from these energy dissipation factors, some of the other energy losses due to solid fluctuations, collisions between particles, between particles and column wall are also involved in two-phase reactors. Since the present CFD simulation is based on Eulerian–Eulerian approach, these modes of energy dissipation could not be quantified. Hence, these terms are neglected in the energy calculation.

In general, the difference between the input and output energy should account for the energy dissipated in the system. Thus, the energy difference in this work is calculated as

$$\begin{aligned} \text{Energy difference} = & \text{Energy entering the fluidised bed } (E_i) - \text{Energy leaving the} \\ & \text{fluidised bed by the liquid } (E_{out}) - \text{Energy gained by the solid} \\ & \text{phase } (E_T) - \text{Energy dissipated by the liquid phase turbulence} \\ & (E_c) - \text{Energy dissipated due to friction at the liquid–solid} \\ & \text{interface } (E_{Bis}) \end{aligned} \dots\dots\dots(3.29)$$

Energy entering the fluidised bed (E_i) by the incoming liquid and gas

The energy entering the fluidised bed due to the incoming liquid and gas flow is given by

$$E_i = \frac{\pi}{4} D^2 H g V_1 (\epsilon_s \rho_s + \epsilon_l \rho_l) \dots\dots\dots(3.30)$$

where D is the diameter of the column, H is the expanded bed height, V_1 is superficial

CFD Simulation of Hydrodynamics of Liquid-Solid Fluidised Bed

liquid velocity, ϵ_l, ϵ_s are the liquid and solid volume fractions respectively and ρ_l, ρ_s are the liquid and solid densities respectively.

Energy leaving the fluidised bed (E_{out}) by the outflowing liquid

The liquid leaving the bed possess both potential energy and kinetic energy by virtue of its expanded bed height and are given as

$$E_{Pl} = \frac{\pi}{4} D^2 H V_l \rho_l g \dots\dots\dots(3.31)$$

$$E_{kl} = \frac{1}{2} \rho_l \frac{\pi}{4} D^2 V_l^3 \dots\dots\dots(3.32)$$

$$E_{out} = E_{Pl} + E_{kl} \dots\dots\dots(3.33)$$

Energy gained by the solid phase (E_T)

The solid flow pattern in the present study shows a single circulation pattern, as depicted in Figure 3.7. The energy gained by the solids for its upward motion in the center region is the sum of the potential energy and kinetic energy of the solids in the center region and are given by

$$E_{PS} = \rho_s g H \frac{\pi}{4} D_c^2 v_s \dots\dots\dots(3.34)$$

$$E_{KS} = \frac{1}{2} \rho_s \frac{\pi}{4} D_c^2 v_s^3 \dots\dots\dots(3.35)$$

$$E_T = E_{PS} + E_{KS} \dots\dots\dots(3.36)$$

where v_s is the time averaged solid velocity in the center region, and D_c is the diameter of the center region.

Energy dissipation due to liquid phase turbulence (E_c)

Since k- ϵ model for turbulence is used in this work, the energy dissipation rate per unit mass is given by the radial and axial variation of ϵ . Hence, the energy dissipated due to liquid phase turbulence is calculated as

CFD Simulation of Hydrodynamics of Liquid-Solid Fluidised Bed

$$E_e = \int_0^R \int_0^H \int_0^{2\pi} \varepsilon \, dr \, dz \, d\theta \quad \dots\dots\dots(3.37)$$

Energy dissipation at the liquid–solid interface (E_{Bls})

The net rate of energy dissipated between liquid–solid phases is calculated based on the drag force and slip velocity between liquid and solid and is summed over all the particles.

For a single particle at an infinite expanded state ($\epsilon=1$), the interaction can be represented as the sum of drag and buoyancy forces. Hence, the force balance for a single particle is

$$mg = \text{drag} + \text{buoyancy}$$

$$\frac{\pi}{6}d_p^3(\rho_s - \rho_l) = C_d \frac{\pi}{4}d_p^2(U_1 - U_s)|U_1 - U_s| \frac{\rho_l}{2} \quad \dots\dots\dots(3.38)$$

For multiple particles, the above equation can be written as

$$\frac{\pi}{6}d_p^3(\rho_s - \rho_l)f(\epsilon) = C_d \frac{\pi}{4}d_p^2(U_1 - U_s)|U_1 - U_s| \frac{\rho_l}{2} \quad \dots\dots\dots(3.39)$$

Lewis et al. (1952), Wen and Yu (1966); and Kmiec (1981) presented the above equation in the form of

$$\frac{\pi}{6}d_p^3(\rho_s - \rho_l)\epsilon^n = C_d \frac{\pi}{4}d_p^2(U_1 - U_s)|U_1 - U_s| \frac{\rho_l}{2} \quad \dots\dots\dots(3.40)$$

where $n = 4.65$ (Lewis et al.), $n = 4.7$ (Wen and Yu) and $n = 4.78$ (Kmiec).

Yang and Renken (2003) developed an equilibrium force model for liquid–solid fluidised bed and derived an empirical correlation for equilibrium between forces to account for laminar, turbulent and intermediate region as given by

$$C_d \frac{\pi}{4}d_p^2(U_1 - U_s)|U_1 - U_s| \frac{\rho_l}{2} = \frac{\pi}{6}d_p^3(\rho_s - \rho_l)(a \epsilon^{4.78} + (1-a)\epsilon^{2.78}) \quad \dots\dots\dots(3.41)$$

$$a = 0.7418 + 0.9674Ar^{-0.5} \qquad 1 < Re_t < 50, \qquad 24 < Ar < 3000$$

CFD Simulation of Hydrodynamics of Liquid-Solid Fluidised Bed

$$a=0.7880-0.00009Ar^{0.625} \quad 50 < Re_t < 500, \quad 3000 < Ar < 10^5$$

The total drag force is thus equal to the product of drag force for single particle and multiplied by the total number of particles namely,

$$F_T = \frac{\pi}{4} D^2 H \epsilon_s g(\rho_s - \rho_l) (a \epsilon^{4.78} + (1-a) \epsilon^{2.78}) \dots\dots\dots(3.42)$$

The rate of energy transferred to the solid from liquid motion is computed from equations (3.41) and (3.42) as

$$E_B = \frac{\pi}{4} D^2 H \epsilon_s g(\rho_s - \rho_l) (a \epsilon^{4.78} + (1-a) \epsilon^{2.78}) V_s \dots\dots\dots(3.43)$$

where V_s is the slip velocity.

The values calculated for these terms along with the energy difference (in terms of %) are presented in Table 3.10. It can be observed that energy difference is in the range of 2–9% for various operating conditions. This can be attributed to the fact that the energy losses due to particle–particle collisions and particle–wall collisions are not included in this present energy calculation. It can also be seen from Table 3.10 that the energy required for solid motion is more around 70–80% of total energy dissipation of fluidised bed.

3.5. Conclusions

CFD simulation of hydrodynamics and solid motion in liquid fluidised bed were carried out by employing the multi-fluid Eulerian approach. Adequate agreement was demonstrated between the CFD simulation results and the experimental findings reported by Limtrakul et al. (2005) using non invasive techniques to measure solid holdup, solid motion and turbulence parameters. The predicted flow pattern demonstrates that the time averaged solid velocity profile exhibits axisymmetric with downward velocity at the wall and maximum upward velocity at the center of the column and higher value of solid holdup at the wall and lower value of that at the center. The CFD simulation exhibits a single solid circulation cell for all the operating conditions, which is consistent with the observations reported by various authors. Based on the predicted flow field by CFD model, the focus has been on the computation of the solid mass balance and computation of various energy flows in fluidised bed reactors. The result obtained shows a deviation in the range of 10–15% between center and wall region for solid flow balance calculations. In the computation of energy flows, the energy difference observed is in the range of 2–9%

In the present study, the influence of various interphase drag models on solid motion in liquid fluidised bed was studied. The drag models proposed by Gidaspow (1994), Syamlal and O'Brien (1994), and Di Felice (1988) can qualitatively predict the flow pattern of solid motion inside the fluidised bed, in which the model proposed by Gidaspow gives the best agreement with experimental data.

Table 3.10. Various energy flows in the liquid fluidised bed

Column Size (m)	U_1 (m/s)	Solid type	E_i (Eqn.3.30)	E_{out} (Eqn.3.33)	E_T (Eqn.3.36)	E_e (Eqn. 3.37)	E_B (Eqn.3.43)	Difference (in %)
0.14	0.07	Glass beads (3mm)	10.05	6.11	2.66	0.13	0.44	7.06
	0.07	Glass beads (1mm)	8.58	4.32	3.34	0.05	0.07	9.3
	0.1	Glass beads (3mm)	18.35	12.65	3.76	0.2	1.18	3.05
	0.13	Glass beads (3mm)	27.09	19.59	3.73	0.36	1.95	5.4
	0.024	Acetate beads (3mm)	1.97	1.72	0.18	4e-04	0.02	2.3
0.1	0.07	Glass beads (3mm)	10.16	6.18	2.52	0.14	0.48	8.26

CFD Simulation of Hydrodynamics of Liquid-Solid Fluidised Bed

To identify the CFD methodology to enhance the accuracy of numerical simulation comparison between 2D and 3D simulation, the effect of grid sensitivity, time step sensitivity and effect of inlet feed conditions were investigated and a comprehensive CFD methodology was established to model the liquid–solid fluidised bed.

Chapter 4

CFD Simulation of Solid Suspension in Liquid-Solid Mechanically Agitated Contactor

4.1. Introduction

Mechanical agitation is the most widely used unit operation for liquid–solid mixing in the chemical industries, mineral processing, wastewater treatment and biochemical process industries. The typical process requirement in this type of reactor is for the solid phase to be suspended for the purpose of dissolution, reaction, or to provide feed uniformity. Since the suspension of solids is an intensive energy consuming operation, the main challenge is the ability to maintain the solid suspension at the lowest cost. The challenge is in understanding the fluid dynamics in the reactor and relating this knowledge to design.

Mechanically agitated reactors involving solid–liquid flows exhibit three suspension states: complete suspension, homogeneous suspension and incomplete suspension, as depicted in Figure 4.1 (Kraume, 1992)

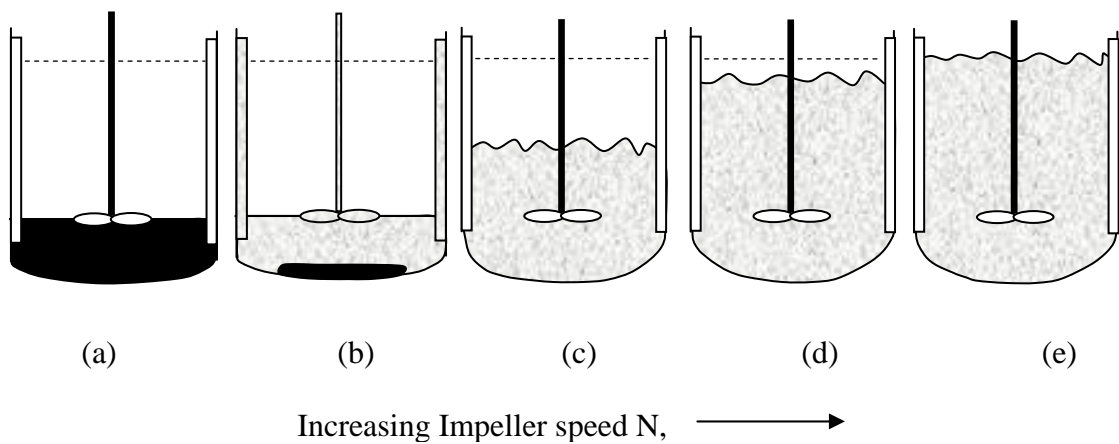


Figure 4.1. Flow regimes of liquid–solid stirred reactor (Kraume, 1992)

A suspension is considered to be complete if no particle remains at rest on the bottom of the tank for more than 1 or 2 sec. One of the main criteria which is often used to investigate the solid suspension is the critical impeller speed (N_{js}) at which

CFD Simulation of Liquid-Solid Mechanically Agitated Contactor

solids are just suspended (Zwietering, 1958). A homogeneous suspension is the state of solid suspension, where the local solid concentration is constant throughout the entire region of column. An incomplete suspension is the state, where the solids are deposited at the bottom of reactor. Zwietering (1958) is the first author, who proposed a correlation for the minimum impeller speed for complete suspension of solids on the basis of dimensional analysis of the results obtained from over a thousand experiments. Table 4.1 shows empirical correlations developed by various authors for the determination of critical impeller speed from their own experimental data.

Table 4.1. Empirical correlations for the critical impeller speed from the literature

Authors	Experimental system used	Empirical Correlation
Zweitering (1958)	Impeller type = Propeller, Disc and 2-paddle T = 0.154–1.0 m D = 0.06–0.26 m C = 0.051E-02–0.076E-02 m Particle density = 2500 kg /m ³ Dp = 125–850 μm Solid loading = 0.34–3.4 wt %	$N_{js} = \frac{S\gamma^{0.1} dp^{0.2} \left(\frac{g\Delta\rho}{\rho_1} \right)^{0.45}}{D^{0.85}} x^{0.13}$
Nienow (1968)	Impeller type = 6-DT T = 0.14m D = 0.0364, 0.049, 0.073 Dp = 153–9000 μm Particle density = 530–1660 kg/m ³ Solid loading = 0.1–1.0 wt %	$N_{js} = \frac{(\Delta\rho/\rho_1)^{0.43} dp^{0.21}}{D^{2.25}} x^{0.12}$
Narayanan et al. (1969)	Impeller type = 8-Paddle T = 0.114, 0.141 m D = 0.036–0.057 m Particle density = 140–1600 kg/m ³ Dp = 106–600 μm Solid loading = 2.5–20 wt %	$N_{js} = \frac{0.9v}{2T-D} \left(\frac{T}{D} \right)^2$ $v = \sqrt{\left(2g(\rho_p - \rho_1) \left(\frac{2dp}{3\rho_p} + \frac{X_s H_{sl}}{\rho_p + H_{sl}\rho_1} \right) \right)}$
Raghava Rao et al. (1988)	Impeller type = 6-DT, 6-PTD, 6-PDU	

CFD Simulation of Liquid-Solid Mechanically Agitated Contactor

	<p>T = 0.3–0.15 m D = 0.175–0.58 m C = 0.5T– 0.167T W/D = 0.25–0.4 Particle density = 1520 kg/m³ Solid loading = 0–50 wt % Dp = 100–2000 μm</p>	$N_{js} = \frac{f\gamma^{0.1} \left(\frac{g\Delta\rho}{\rho_1} \right)^{0.45} X^{0.1} dp^{0.11} T^{0.31}}{D^{1.16}}$
Takahashi et al. (1993)	<p>T = 0.1–0.58 m Impeller type = 6-DT D = 0.05–0.29 m C = 0.0125–0.0725 m Dp = 50–5000 μm Particle density = 1049–3720 kg/m³ Solid concentration = 0.1–2 vol. %</p>	$N_{js} \propto \frac{\mu^{0.1} \left(\frac{g\Delta\rho}{\rho_1} \right)^{0.34} X^{0.22} dp^{0.023}}{D^{0.54}}$ $N_{js} \propto \frac{\mu^{0.1} \left(\frac{g\Delta\rho}{\rho_1} \right)^{0.38} X^{0.17} dp^{0.05}}{D^{0.6}}$
Rieger and Dittl et al. (1994)	<p>Impeller type = pitched six blade turbines with 45° T = 0.2, 0.3, 0.4 m D = T/3 C = 0.5D Dp = 0.18–6 mm Particle density = 1243 kg/m³ Solid concentration = 2.5, 10 vol. %</p>	$N_{js} \propto (\Delta\rho/\rho_1)^{0.5} D^{-0.5}$ $N_{js} \propto (\Delta\rho/\rho_1)^{0.5} d_p^{0.3} D^{-0.8}$ $N_{js} \propto \Delta\rho^{0.42} \rho_1^{-0.58} \mu^{0.16} D^{-0.73}$ $N_{js} \propto \Delta\rho^{0.42} \rho_1^{-0.58} \mu^{0.16} d_p^{0.25} D^{-0.99}$
Ibrahim & Nienow (1996)	<p>Impeller type = 6-DT, 6-FDT, 6-PDT T = 0.292, 0.33 m D = 0.065–0.102 Particle density = 2500 kg/m³ Dp = 110 μm Solid concentration = 0.5 vol %</p>	$N_{js} = \frac{S\gamma^{0.1} dp^{0.2} \left(\frac{g\Delta\rho}{\rho_1} \right)^{0.45}}{D^{0.85}} X^{0.13}$
Armenante & Nagamine (1998)	<p>Impeller type = 6-DT, 6-FBT, 6-PTD, HE-3 T = 0.188–0.584 m D = 0.0635–0.203m Particle density = 2500 kg/m³ Dp = 60–300 μm Solid concen. = 0.5 vol %</p>	$N_{js} = \frac{S\gamma^{0.1} dp^{0.2} \left(\frac{g\Delta\rho}{\rho_1} \right)^{0.45}}{D^{0.13}} X^{0.13}$

CFD Simulation of Liquid-Solid Mechanically Agitated Contactor

Bujalski et al. (1999)	Impeller type = A310, A315 T= 0.29 m D= 0.10–0.12 m Particle density=1350–500kg/m ³ Dp = 100–1000 μm Solid concentration = 0–40%	$N_{js} = \frac{S\gamma^{0.1} dp^{0.2} \left(\frac{g\Delta\rho}{\rho_1}\right)^{0.45}}{D^{0.85}} X^{0.13}$
Sharma & Shaikh (2003)	Impeller type: 4,6-PTD T= 0.15–1.21 m D= 0.0535-0.348 m Particle density=1390–635kg/m ³ Dp = 130–850 μm Solid concentration =1.55–2 vol.%	$N_{js} = \frac{S\gamma^{0.1} dp^{0.2} \left(\frac{g\Delta\rho}{\rho_1}\right)^{0.45}}{D^{-2.0}} X^{0.13}$
Dohi et al. (2004)	Impeller type = Maxblend, PTD Fullzone,Pfaudler T= 0.2–0.8 m D= 0.42T–0.53T m Particle density = 2500 kg/m ³ Dp = 187–810 μm Solid concentration =0–30 by vol%	$N_{js} = \frac{S\gamma^{0.1} dp^{0.2} \left(\frac{g\Delta\rho}{\rho_1}\right)^{0.45}}{D^{-0.85}} X^{0.13}$

Another criterion which is also used for assessing the quality of solids suspension is the degree of homogeneity of suspension. Einkenkel (1979), suggested the variance of solid concentration as a measure of homogeneity of the solids suspension, which is defined as

$$\sigma^2 = \frac{1}{n} \sum_1^n \left(\frac{C}{\bar{C}} - 1\right)^2 \dots\dots\dots(4.1)$$

Bohnet and Niesmak (1980) used the square root of variance, which corresponds to the standard deviation of the concentration profile (σ). Kraume, (1992) used another measure to evaluate the homogeneity of suspension which is based on the cloud height. The suspension is said to be homogeneous when the solid concentration is uniform throughout the tank. When the slurry height or cloud height becomes equal to 0.9H, the state of suspension is said to be homogeneous where H refers to the height

CFD Simulation of Liquid-Solid Mechanically Agitated Contactors

of the reactor. Eventhough the suspended slurry height or cloud height is not an absolute measure of homogeneity, it may be useful for comparing the identical slurries.

During the last few decades, various models have been proposed for quantifying the solid suspension from the theoretical power requirement. Kolar (1967) presented a model for solid suspension based on energy balance, that all the power is consumed for suspending the solids and that the stirred tank is hydrodynamically homogeneous. Baldi et al. (1978) proposed a new model for complete suspension of solids where it is assumed that the suspension of particles is due to turbulent eddies of certain critical scale. Further it is assumed that the critical turbulent eddies that cause the suspension of the particles being at rest on the tank bottom have a scale of the order of the particles size, and the energy transferred by these eddies to the particles is able to lift them at a height of the order of particle diameter. Since their hypothesis related the energy dissipation rate for solid suspension to the average energy dissipation in the vessel by employing modified Reynolds number concept, it gave good insight into the suspension process compared to other approaches.

Chudacek (1986) proposed an alternative model for the homogeneous suspension based on the equivalence of particle settling velocity and mean upward flow velocity at the critical zone of the tank which leads to the constant impeller tip speed criterion, but this is valid only under conditions of geometric and hydrodynamic similarity. Shamlou and Koutsakos (1989) introduced a theoretical model based on the fluid dynamics and the body force acting on solid particles at the state of incipient motion and subsequent suspension. Rieger and Ditzl (1994) developed a dimensionless

CFD Simulation of Liquid-Solid Mechanically Agitated Contactor

equation for the critical impeller speed required for complete suspension of solids based on the inspection analysis of governing fluid dynamic equations. They observed four different hydrodynamic regimes based on the relative particle size and Reynolds number values.

Since most of the present knowledge on solid suspension is based on simplified models and empirical correlations it cannot account for the complex manner in which various parameters interact with the complex flow field. Eventhough in the recent past, both invasive and non invasive experimental measurement techniques have been reported in the literature, significant improvements of the design capability and reliability can be expected from advances in computational fluid dynamics (CFD) techniques (Dudukovic et al., 1999). CFD simulations offer the only cost-effective means to acquire the detailed information on flow and turbulence fields needed for realistic distributed-parameter process simulations. Table 4.2 shows the various studies related to CFD modeling of solid suspension in such mechanically agitated contactors in the recent past.

Hence, the objective of this work is to develop a validated CFD simulation tool based on Eulerian multi-fluid approach for the prediction of the solid suspension in a solid–liquid mechanically agitated contactor. CFD simulations are carried out using the commercial package ANSYS CFX-10. After the validation, the CFD simulations have been extended to study the effects of impeller design, impeller speed and particle size on the solid suspension behavior.

CFD Simulation of Liquid-Solid Mechanically Agitated Contactor

Table 4.2. Literature review on the CFD modeling of solid suspension in stirred vessel

Authors	Experiment details	Details of modeling	Conclusions
Micale et al. (2000)	Tank dia : 0.154 m Tank height : 0.154 m Impeller type : Rushton turbine Impeller dia : 0.051 m, Impeller clearance : 0.051 m Particle density : 2480 kg/m ³ Particle diameter: 355–425 μm	Two modeling approaches viz. Settling velocity model (SVM) and Multi-fluid model (MFM) is used for simulating the hydrodynamics of multiphase flows. Inner – Outer approach method for impeller representation, Brucato et al., (1998) drag model for liquid–particle interaction, k-ε turbulence model for liquid phase turbulence.	They concluded that both models gave acceptable agreement when compared with the experimental data of one dimensional axial concentration profile, but SVM model is applicable to simulation of low values of volume fraction of solids and MFM model gives good comparison with experimental data up to 4% by volume of solids.
Sha et al. (2001)	Tank dia : 0.15m Tank height : 0.15 m Impeller type: 6 blade 45 ⁰ Pitched turbine Impeller dia : 0.051 m Impeller clearance : 0.051 m Particle density : 2600 kg/m ³ Particle diameter: 50–900 μm Solid concn. : 5 vol.%	Multi-fluid model is used along with k-ε turbulence model. Sliding grid method for impeller rotation. Multiple particle effects on the drag force is also included, the non-drag forces of virtual mass, lift, wall lubrication and turbulence dispersion force are also included in their simulation.	They considered six different size particles as six different phases along with continuous phase in their simulation and the solid volume fraction distribution of different sizes of particles are studied. The predicted volume fraction distribution of solid phase agreed sufficiently with the experimental data.
Barrue et al. (2001)	Tank dia : 1.5 m Tank height : 2.424 m Impeller type : Propeller Impeller dia : 1.026 m, 0.907 m Particle density : 2420 kg/m ³ Particle diameter: 50 μm Solid concn. : 26% by v/v	Eulerian–Eulerian method, Black box method for impeller representation, Syamlal and O'Brien's drag model for liquid–particle interaction, kinetic theory of granular flow was	Numerical and experimental solids distributions showed remarkable agreement. They concluded that the homogeneity of suspension increases with increasing rotational speed and also for their high solid

CFD Simulation of Liquid-Solid Mechanically Agitated Contactor

			used for solid phase description, k-ε turbulence model for liquid phase turbulence.	concentration, increase of the mean concentration increases the homogeneity of the vessel.
Kee and Tan (2002)	T: 0.24 m, 0.29 m, 0.192 m Impeller type: A310, Rushton Particle size: 250–150 μm Solid loading: 14.1–13.5% Particle density : 2160, 2600 kg/m ³		Eulerian–Eulerian method, sliding grid method for impeller representation, Eulerian granular multiphase model, k-ε turbulence model for liquid phase turbulence.	Using CFD they proposed a new criteria for critical impeller speed by observing the transient profiles of solid volume fraction at the base of the vessel. At N _{js} and higher impeller speed, solid volume fraction at the bottommost rows should attain steady state value 50% of initial volume fraction.
Montante and Magelli (2005)	Impeller type: Multiple Rushton, Pitched blade turbine Tank dia: 23.2 cm, 48 cm, 49 cm Impeller diameter : T/3 Impeller clearance : T/2 Lower impeller clearance : T/2 Particle size : 137, 327, 675 μm Density of solid : 2450 kg/m ³		Eulerian–Eulerian method, Sliding grid method for impeller rotation, Schiller and Naumaan drag model for liquid–solid interaction, k-ε turbulence model for liquid phase turbulence.	They concluded that an Eulerian–Eulerian model with a suitable correction of the particle drag coefficient provides a solid concentration distribution that is in very good agreement with the experimental data provided that the liquid flow field is correctly simulated. They also observed that the mixture model for turbulence is the most proper of turbulence models and also the Granular modification of the Eulerian model for the solid phase provides a slight improvement in the predictions with respect to the Eulerian model in the lower part of the vessel.

CFD Simulation of Liquid-Solid Mechanically Agitated Contactor

Ochieng and Lewis (2006)	Impeller type : 4 blade Hydrofoil (MixtecA735) Tank dia : 0.38 m Impeller dia : 0.33 T Impeller clearance : 0.15 T Impeller speed : 200-700 rpm Solid vol. frac.: 1-20 % w/w Particle size : 150-1000 μm Solid density : 8903 kg/m^3	Eulerian based polydisperse multiphase simulation, sliding grid method for impeller rotation, Gidaspow's drag model for liquid-solid interaction, k- ϵ turbulence model for liquid phase turbulence, and Lopez de Bertodano model for turbulent dispersion force.	They concluded that influence of turbulent dispersion force and solid pressure on solid suspension increases with an increase in solid loading. Low solid loading may be scaled up on the basis of the impeller tip speed. Axial concentration distribution decreases with particle size and loading.
Khopkar et al. (2006)	Published experimental data of Yamazaki et al. (1986) and Godfrey and Zhu (1994), For Yamazaki et al. (1986) Tank dia : 0.3 m Impeller type : Rushton Turbine Impeller dia : 0.1 m Impeller clearance : 0.1 m Particle size : 150& 264 μm Solid density : 2470 kg/m^3 For Godfrey and Zhu (1994) Tank dia : 0.3 m Impeller type : 4-PBTD Impeller dia : 0.052 m Impeller clearance : 0.1 m Particle size : 390& 655 μm Solid density : 2480 kg/m^3	Eulerian-Eulerian multi-fluid approach, k- ϵ turbulence model with mixture properties for liquid phase turbulence Multiple frame of reference approach for the impeller rotation.	After validating the CFD model with the experimental results of Yamazaki et al. (1986) and Godfrey and Zhu (1994), the model was used to understand the influence of particle size. They also observed that for higher solid loading and larger particle Reynolds's number and the proportionality constant used in Brucato et al., (1998) need to be reduced for reasonable prediction of suspension quality. 10 times lower value of the proportionality constant is used in their work.

4.2. CFD Modeling

4.2.1. Model equations

The liquid-solid flows in the mechanically agitated contactor are simulated using Eulerian multi-fluid approach. Each phase is treated as a different continua which interacts with other phases everywhere in the computational domain. The motion of each phase is governed by the respective Reynolds averaged mass and

CFD Simulation of Liquid-Solid Mechanically Agitated Contactor

momentum conservation equations. The governing equations for each phase are given below:

Continuity equation:

$$\frac{\partial}{\partial t}(\epsilon_k \rho_k) + \nabla \cdot (\rho_k \epsilon_k \bar{u}_k) = 0 \quad \dots\dots\dots(4.2)$$

where ρ_k is the density and ϵ_k is the volume fraction of phase $k = s$ (solid), l (liquid) and the volume fraction of the two phases satisfy the following condition:

$$\epsilon_l + \epsilon_s = 1 \quad \dots\dots\dots(4.3)$$

Momentum Equations:

Liquid phase (continuous phase)

$$\frac{\partial}{\partial t}(\rho_l \epsilon_l \bar{u}_l) + \nabla \cdot (\rho_l \epsilon_l \bar{u}_l \bar{u}_l) = - \epsilon_l \nabla P + \nabla \cdot (\epsilon_l \mu_{eff,l} (\nabla \bar{u}_l + (\nabla \bar{u}_l)^T)) + \rho_l \epsilon_l \bar{g} + \bar{F}_{D,ls} + \bar{F}_{TD} \quad \dots\dots\dots(4.4)$$

Solid phase (dispersed solid phase)

$$\frac{\partial}{\partial t}(\rho_s \epsilon_s \bar{u}_s) + \nabla \cdot (\rho_s \epsilon_s \bar{u}_s \bar{u}_s) = - \epsilon_s \nabla P - \nabla P_s + \nabla \cdot (\epsilon_s \mu_{eff,s} (\nabla \bar{u}_s + (\nabla \bar{u}_s)^T)) + \rho_s \epsilon_s \bar{g} - \bar{F}_{D,ls} - \bar{F}_{TD} \quad \dots\dots\dots(4.5)$$

where P is the pressure, which is shared by both the phases, μ_{eff} is the effective viscosity. The second term on the RHS of the solid phase momentum equation (4.5) accounts for additional solids pressure which arise due to solids collision and last term (F_D) in both the momentum equations (4.4) and (4.5) represents the drag force that arise due to the momentum exchange mechanisms between the different phases.

4.2.2. Interphase momentum transfer

There are various interaction forces such as the drag force, the lift force and the added mass force etc. during the momentum exchange between the different phases. But the main interaction force is due to the drag force which is caused by the slip between the different phases. Recently, Khopkar et al. (2003, 2005) studied the influence of different interphase forces and reported that the effect of the virtual mass force is not significant in the bulk region of agitated reactors and the magnitude of the Basset force is also much smaller than that of the interphase drag force. Further they also reported that the turbulent dispersion terms are significant only in the impeller discharge stream. Very little influence of the virtual mass and lift force on the simulated solid holdup profiles was also reported by Ljungqvist and Rasmuson (2001). Hence based on their recommendations and also to reduce the computational time, only the interphase drag force is considered in this work. In our CFD simulation, the solid phase is treated as a dispersed phase and the liquid phase is treated as continuous. Hence the drag force exerted by the dispersed phase on the continuous phase is calculated as follows:

The drag force between the liquid and solid phases is represented by the equation

$$\vec{F}_{D,ls} = C_{D,ls} \frac{3}{4} \rho_l \frac{\epsilon_s}{d_p} |\vec{u}_s - \vec{u}_l| (\vec{u}_s - \vec{u}_l) \dots\dots\dots(4.6)$$

where the $C_{D,ls}$ is drag coefficient, which can be calculated using one of the following drag force models

(i) Wen and Yu (1966)

$$C_{D,ls} = \frac{24}{Re_p} \left(1 + 0.15 Re_p^{0.687} \right) \dots\dots\dots(4.7)$$

(ii) Brucato et al. (1998)

$$\frac{C_{D,ls} - C_{D0}}{C_{D0}} = 8.67 \times 10^{-4} \left(\frac{d_p}{\lambda} \right)^3 \dots\dots\dots(4.8)$$

(iii) Pinelli et al. (2001)

$$\frac{C_{D0}}{C_{D,ls}} = \left(0.4 \tanh \left(\frac{16\lambda}{d_p} - 1 \right) + 0.6 \right)^2 \dots\dots\dots(4.9)$$

where d_p is the particle size and λ is the Kolmogorov length scale, C_{D0} is the drag coefficient in the stagnant liquid which is given as

$$C_{D0} = \frac{24}{Re_p} \left(1 + 0.15 Re_p^{0.687} \right) \dots\dots\dots(4.10)$$

where Re_p is the particle Reynolds number.

The only other non drag force considered in the present work is the turbulent dispersion force. This turbulent dispersion force is the result of the turbulent fluctuations of liquid velocity which approximates a diffusion of the dispersed phase from higher region to lower region. The importance of modeling of turbulent dispersion force in liquid–solid stirred tank was also highlighted in the literature by few authors (Ljungqvist and Rasmuson, 2001; Barrue et al., 2001). The following equation for the turbulent dispersion force derived by Lopez de Bertodano (1992), is used for the present simulation and is given by

$$\bar{F}_{TD} = -C_{TD} \rho_1 k_1 \nabla \epsilon_1 \dots\dots\dots(4.11)$$

where C_{TD} is a turbulent dispersion coefficient, and is taken as 0.1 for the present investigation.

4.2.3. Closure law for turbulence

In the present study, the standard k-ε turbulence model for single phase flows has been extended for turbulence modeling of two phase flows in mechanically

CFD Simulation of Liquid-Solid Mechanically Agitated Contactor

agitated contactors. The corresponding values of k and ε are obtained by solving the following transport equations for the turbulence kinetic energy and turbulence dissipation rate.

$$\frac{\partial(\epsilon_1 \rho_1 k_1)}{\partial t} + \nabla \cdot \left(\epsilon_1 \left(\rho_1 \bar{u}_1 k_1 - \left(\mu + \frac{\mu_{tl}}{\sigma_k} \right) \Delta k_1 \right) \right) = \epsilon_1 (P_1 - \rho_1 \epsilon_1) \quad \dots\dots\dots(4.12)$$

$$\frac{\partial(\epsilon_1 \rho_1 \epsilon_1)}{\partial t} + \nabla \cdot \left(\epsilon_1 \rho_1 \bar{u}_1 \epsilon_1 - \left(\mu + \frac{\mu_{tl}}{\sigma_\epsilon} \right) \Delta \epsilon_1 \right) = \epsilon_1 \frac{\epsilon_1}{k_1} (C_{\epsilon 1} P_1 - C_{\epsilon 2} \rho_1 \epsilon_1) \quad \dots\dots\dots(4.13)$$

where $C_{\epsilon 1}=1.44$, $C_{\epsilon 2}=1.92$, $\sigma_k=1.0$, $\sigma_\epsilon=1.3$ and P_1 , the turbulence production due to viscous and buoyancy forces, is given by

$$P_1 = \mu_{tl} \nabla \bar{u}_1 \cdot (\nabla \bar{u}_1 + \nabla \bar{u}_1^T) - \frac{2}{3} \nabla \cdot \bar{u}_1 (3\mu_{tl} \nabla \cdot \bar{u}_1 + \rho_1 k_1) \quad \dots\dots\dots(4.14)$$

For the continuous phase (liquid phase) the effective viscosity is calculated as

$$\mu_{eff, l} = \mu_l + \mu_{T, l} + \mu_{tg} + \mu_{ts} \quad \dots\dots\dots(4.15)$$

where μ_l is the liquid viscosity, $\mu_{T, l}$ is the liquid phase turbulence viscosity or shear induced eddy viscosity, which is calculated based on the k - ε model as

$$\mu_{T, l} = c_\mu \rho_1 \frac{k^2}{\varepsilon} \quad \dots\dots\dots(4.16)$$

μ_{ts} represents the solid phase induced turbulence viscosity and is given by

$$\mu_{ts} = c_{\mu p} \rho_1 \epsilon_s d_p |\bar{u}_s - \bar{u}_l| \quad \dots\dots\dots(4.17)$$

where $C_{\mu p}$ has a value of 0.6.

For solid phase the effective viscosity is calculated as

$$\mu_{eff, s} = \mu_s + \mu_{T, s} \quad \dots\dots\dots(4.18)$$

where $\mu_{T, s}$ is the turbulence viscosity of the solid phase. The turbulent viscosity of the solids phase is related to the turbulence viscosity of the liquid phase by the equation

$$\mu_{T,s} = \frac{\rho_s}{\rho_l} \mu_{T,l} \dots\dots\dots(4.19)$$

4.2.4. Closure law for solids pressure

The solids phase pressure gradient results from normal stresses resulting from particle–particle interactions, which become very important when the solid phase fraction approaches the maximum packing. This solid pressure term is defined based on the concept of elasticity, which is described as a function of elasticity modulus and solid volume fraction. The most popular constitutive equation for solids pressure, as given by Gidaspow (1994), is

$$\nabla P_s = G(\epsilon_s) \nabla \epsilon_s \dots\dots\dots(4.20)$$

where $G(\epsilon_s)$ is the elasticity modulus and it is given as

$$G(\epsilon_s) = G_0 \exp(c(\epsilon_s - \epsilon_{sm})) \dots\dots\dots(4.21)$$

as proposed by Bouillard et al. (1989), where G_0 is the reference elasticity modulus, c is the compaction modulus and ϵ_{sm} is the maximum packing parameter.

4.3. Numerical Simulation

In this work, the commercial CFD software package ANSYS CFX-10 is used for the steady state hydrodynamic simulation of liquid–solid flows in the mechanically agitated contactor. We have considered three different reactor configurations for the validation purpose of the CFD simulation. The details of the reactor geometries, impeller types and the operating process conditions, physical parameters used for CFD simulation are given in Table 4.3. Steady state simulations are performed for different types of impellers, agitation speeds and particle sizes.

CFD Simulation of Liquid-Solid Mechanically Agitated Contactor

Due to the symmetry of the geometry, only one-half of the agitated contactor is considered as the computational domain, and is discretised using block structured grids which allows finer grids in regions where higher spatial resolutions are required. The blocks are further divided into finer grids. Around 200,000 total computational nodes are created using the structured hexa mesh option of ICEMCFD in order to get the grid independent solution for the flow. Figure 4.2 depicts a typical mesh used for the numerical simulation in this work.

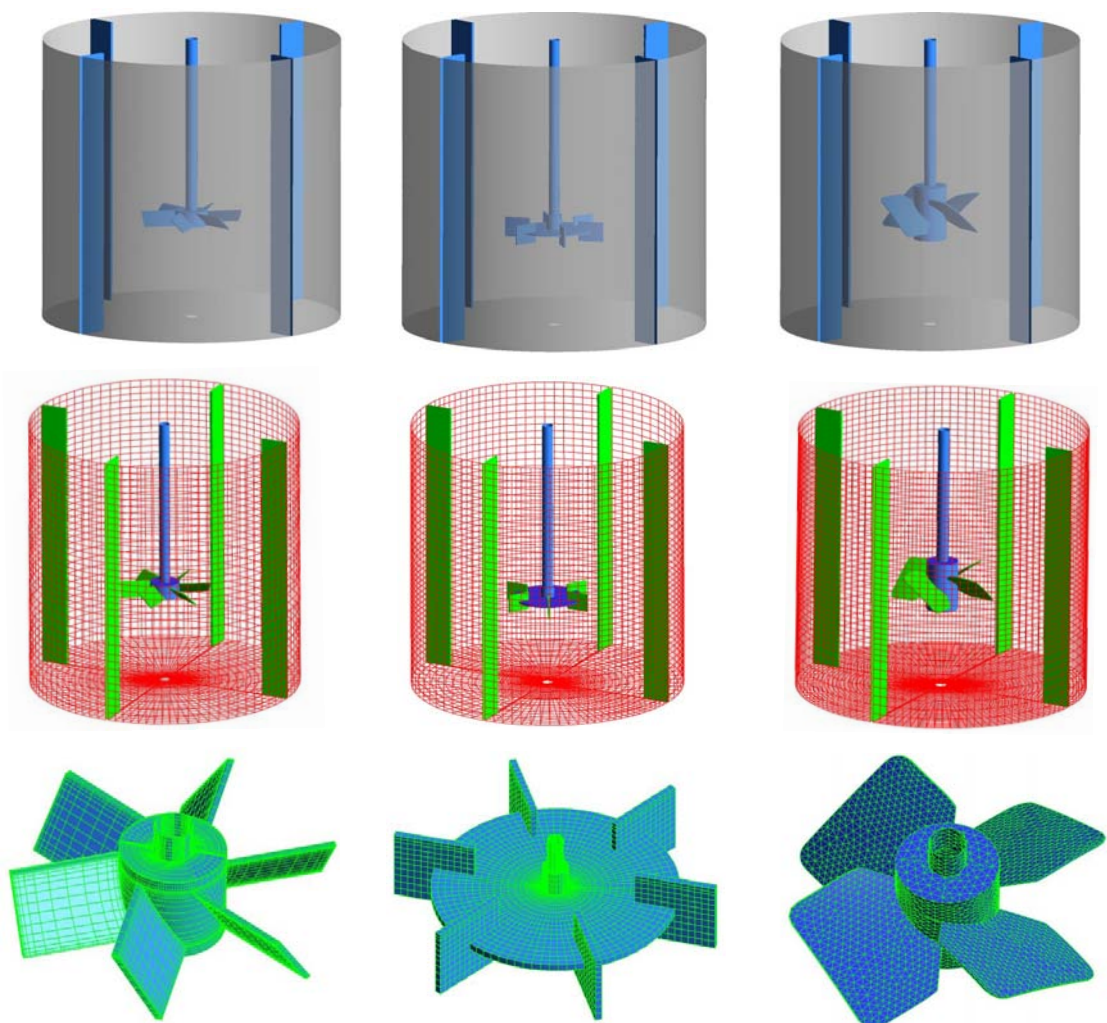
Table 4.3. Reactor configuration and process parameter

Reference	Impeller type	Geometry	Physical Properties	Operating conditions
Michelletti et al. (2003)	6-DT	T=H=0.29 m D/T=1/3, C/T=1/3	Liquid: $\rho = 1000 \text{ kg/m}^3$, Solid: $\rho = 2470 \text{ kg/m}^3$, $d_p = 655 \text{ }\mu\text{m}$	Solid conc. =7 vol% $N_{js}=1200 \text{ rpm}$
Michelletti and Yianneskis (2004)	6-DT	T=H=0.0805 m D=0.027 m, C/T=1/3	Liquid: $\rho = 1000 \text{ kg/m}^3$, Solid: $\rho = 1060 \text{ kg/m}^3$, $d_p = 186 \text{ }\mu\text{m}$	$N = 2500 \text{ rpm}$
Spidla et al.(2005 a, b)	6-PBTD and 4-A315	T=H=1.0 m D/T=1/3, C/T=1/3	Liquid: $\rho = 1000\text{kg/m}^3$, Solid: $\rho = 2500\text{kg/m}^3$, $d_p = 350 \text{ }\mu\text{m}$	Solid conc. =10 vol% $N_{js} = 267 \text{ rpm}$

During the last few decades, different numerical approaches have been proposed to predict the interaction of the rotating impeller blades and the stationary baffles of mixing tank. In the simplest approach, the flow field in the stirred tank is treated as stationary without resolving the geometry of impeller and the induced periodic vortical flow structure. This is mostly done by specifying the velocities and turbulence properties which are obtained from experiment at outer cylindrical surface

CFD Simulation of Liquid-Solid Mechanically Agitated Contactor

of the region swept by the impeller. The second method is the multiple frame of reference (MFR) approach. It was originally introduced by Luo et al., (1994). This is a steady state method in which the whole solution domain is divided into two regions i.e., inner region of impeller is resolved using a rotating frame and the outer region of tank is resolved using the stationary frame.



(a) Pitched blade Turbine (PBT) (b) Rushton Turbine (DT) (c) A315 Hydrofoil

Figure 4.2. Typical geometry, impeller and mesh used for CFD simulation

CFD Simulation of Liquid-Solid Mechanically Agitated Contactor

The transformation of conservation equation into a rotating system yields additional terms in the momentum equation namely the centrifugal and Coriolis force. Another approach called inner-outer approach was introduced by Brucato et al., (1994). It is basically similar to the multiple frame of reference approach. The difference between these two methods is that, there is a small overlap between the calculation domain of the two regions and a large number of outer iterations are required to ensure continuity across the interface between the two parts. The third approach is the sliding grid approach. This method was first applied to the flow in a stirred tank by Perng and Murthy (1993). In this approach, the inner region is rotated during computation. The shape and the rotation of the impeller are therefore represented exactly. Because the grid of the inner region is made to rotate and slide along the interface with the outer region, this is fully transient and is considered as a more accurate method, but it is also much more time consuming compared to MFR. The final approach is the snapshot method. This was originally developed by Ranade (1997). In this method the solution domain is divided into an inner region, in which the time derivative term is approximated using a spatial derivative and in the outer region, in which the time derivative term is neglected. The boundary between the inner and outer region need to be selected in such a way that, the predicted results are not sensitive to its actual location.

For the present simulation, we have used the MFR approach for simulating the impeller rotation. In the MFR approach, the computational domain is divided into an impeller zone (rotating reference frame) and a stationary zone (stationary reference frame). The interaction of inner and outer regions is accounted by a suitable coupling

CFD Simulation of Liquid-Solid Mechanically Agitated Contactor

at the interface between the two regions where the continuity of the absolute velocity is implemented. The boundary between the inner and the outer region is located at $r/R=0.6$. No-slip boundary conditions are applied on the tank walls and shaft. The free surface of tank is considered as the slip boundary condition. Initially the solid particles are distributed in a homogeneous way inside the whole computational domain. The discrete algebraic governing equations are obtained by the element based finite volume method. The second order equivalent to high-resolution discretisation scheme is applied for obtaining algebraic equations for momentum, volume fraction of individual phases, turbulent kinetic energy and turbulence dissipation rate. Pressure–velocity coupling was achieved by the Rhie-chow algorithm (1982).

The governing equations are solved using the advanced coupled multi grid solver technology of ANSYS CFX-10. The criteria for convergence is set as 1×10^{-4} for the RMS residual error for all the governing equations. The RMS (Root Mean Square) residual is obtained by taking all of the residuals throughout the domain, squaring them, taking the mean, and then taking the square root of the mean for each equation.

4.4. Results and Discussion

4.4.1. Single phase flow

Initially only the liquid flow (single phase) simulation of mechanically agitated contactor was carried out to obtain the liquid phase flow field and this was validated with the experimental data of Michelletti and Yianneskis (2004). They carried out the measurements in a cylindrical vessel of diameter $T = 0.0805$ m and

CFD Simulation of Liquid-Solid Mechanically Agitated Contactor

height equal to the tank diameter. A six bladed Ruston Turbine of diameter $D=T/3$ with a clearance of $C=T/3$ is used. Figure 4.3 shows good agreement between the predicted and measured axial profiles of mean radial velocity at r/T of 0.224. Both experiments and simulation results gave a maximum velocity of $0.55 V_{tip}$ where V_{tip} (πDN) is the blade tip velocity.

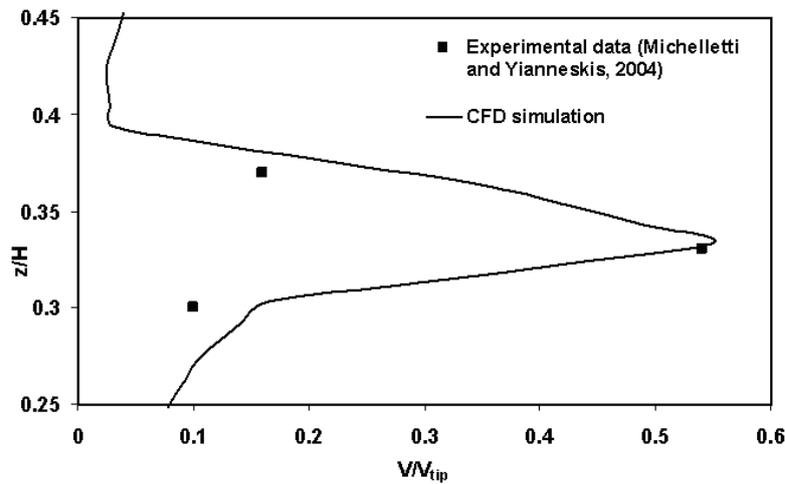


Figure 4.3. Axial profiles of normalised radial mean velocity at $r/T = 0.224$, $Re = 20\ 000$

Similarly the radial profile of normalised mean radial velocity and mean tangential velocity is compared with the experimental data of Michelletti and Yianneskis (2004), which is shown in Figures 4.4 and 4.5. The comparison shows good agreement between experiments and simulation.

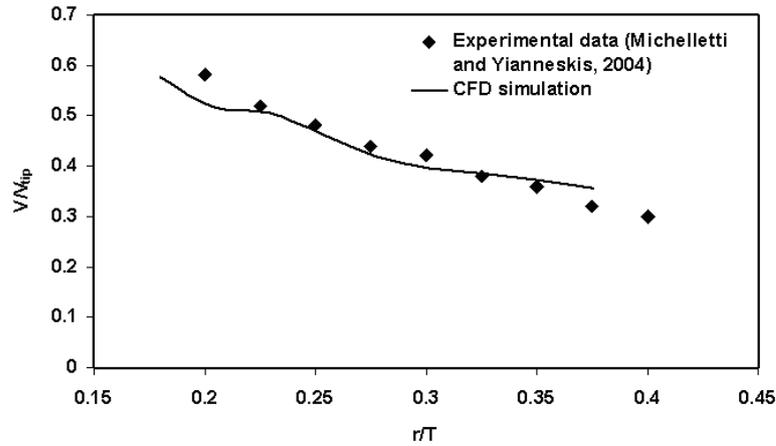


Figure 4.4. Radial profiles of normalised radial mean velocity at $z/T = 0.33$, $Re = 20000$

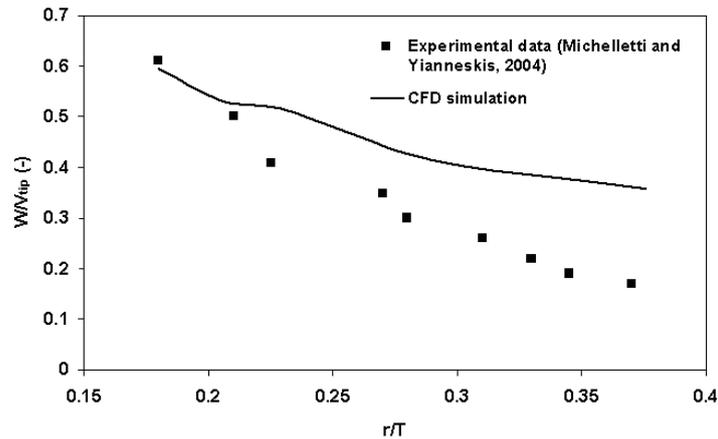


Figure 4.5. Radial profiles of normalised mean tangential velocity at $z/T = 0.33$, $Re = 20000$

4.4.2 Solid-liquid flows

CFD simulation of liquid-solid mechanically agitated contactor is undertaken in this study to verify quantitatively the solid suspension characteristics since this is the vital parameter for predicting the performance of this type of reactor. One way of checking the quality of solid suspension is by evaluating the extent of off-bottom

CFD Simulation of Liquid-Solid Mechanically Agitated Contactor

suspension i.e., critical impeller speed for just suspended state. Another way is to map the radial and axial concentration profiles of solids in such reactors to determine the extent of solid distribution i.e., solid suspension height.

Since the interphase drag force model is a critically important parameter for obtaining correct predictions for the solid distribution, we have considered three different interphase drag force models as given by equations (4.7), (4.8) & (4.9) in this work. The first drag model was by Wen and Yu (1966), in which drag force was calculated using equation (4.7) where the free stream turbulence is not taken into account. The other drag force models are due to Brucato et al. (1998) and Pinelli et al. (2001) where, they included the effect of free turbulence, and the turbulent drag force is calculated from the correlations, as given by equations (4.8) and (4.9), respectively. The experimental data reported by Micheletti et al. (2003) for a solid–liquid stirred tank reactor with a Rushton turbine impeller (DT) is taken for CFD validation. They characterised the particle distribution in a stirred tank using a conductivity probe and measured the axial distribution of solids at a solids loading of 9.2% at an impeller speed of 988 RPM. Comparison of experimental data for the local normalised concentration C_v/C_{avg} of solid volume fraction with different interphase drag force models in the midway plane at $r/T = 0.35$ is shown in Figure 4.6.

As can be expected, when Wen and Yu (1966) drag force correlation was used, the simulated normalised axial solid concentration values deviated much from the experimental predictions. Also the simulated axial solid concentration values were the highest at the bottom of the contactor. The values predicted by Brucato et al. (1998) drag model are closer to the experimental values for normalized axial solid

concentration compared to Pinelli et al. (2001) drag model and hence for further simulations, we have used Brucato et al. (1998) drag force correlation for simulating the solid liquid flows in the mechanically agitated contactor.

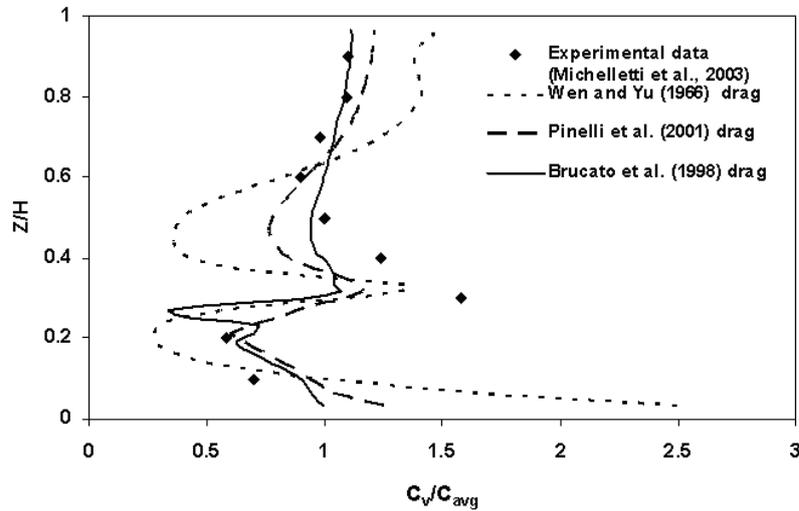


Figure 4.6. Effect of drag force models on axial solid concentration for case of radial type impeller

4.4.2.1. Off-bottom suspension

Generally Zwietering criteria (the impeller speed at which the particles do not remain stationary at the bottom of the vessel for more than 2 s) is used for characterising the off-bottom suspension. But incorporating Zwietering criteria is difficult in the Eulerian–Eulerian approach of the present CFD simulation. Hence the method proposed by Bohnet and Niesmak (1980), which is based on the value of standard deviation, is used in the present study for the prediction of critical impeller speed. This standard deviation method was also successfully employed for liquid–solid suspension by Khopkar et al. (2006). It is defined as

$$\sigma = \sqrt{\frac{1}{n} \sum_{i=1}^n \left(\frac{C_i}{C_{avg}} - 1 \right)^2} \dots\dots\dots(4.22)$$

CFD Simulation of Liquid-Solid Mechanically Agitated Contactor

where n is the number of sampling locations which is used for measuring the solid holdup. The increase in the degree of homogenisation (better suspension quality) is manifested in the reduction in the value of the standard deviation. The standard deviation is broadly divided into three ranges based on the quality of suspension. For uniform suspension the value of the standard deviation σ is found to be smaller than 0.2 ($\sigma < 0.2$), for just suspended condition the value of the standard deviation is between 0.2 and 0.8 ($0.2 < \sigma < 0.8$) and for an incomplete suspension the standard deviation value is greater than 0.8 ($\sigma > 0.8$).

But it is very difficult to exactly find the critical impeller speed required for the just suspended state from the values of the standard deviation. These difficulties were also cited in literature (Khopkar et al., 2006, van der Westhuizen et al., 2008). Hence we have also used another criterion which is based on the solid suspension height i.e., cloud height ($H_{\text{cloud}} = 0.9H$) along with the standard deviation method. Kraume (1992) used these two criteria to determine the critical impeller speed in liquid–solid suspension. For the present study, both these criteria have been used to evaluate the quality of solid suspension and to determine the critical impeller speed.

4.4.2.1.1. Effect of impeller type

CFD simulations have been carried out for the reactor configuration of Spidla et al. (2005a) for three different impeller types. Figure 4.7 shows the variation of the standard deviation values with respect to the impeller speed for DT, PBTD and A315 hydrofoil impeller. The standard deviation value decreases with an increase in impeller speed for all the impellers. Figure 4.8 depicts the predicted cloud height for

CFD Simulation of Liquid-Solid Mechanically Agitated Contactor

various impeller rotational speeds (4.0, 4.45, and 5.0 rps) for the PBTD impeller. Figure 4.9 depicts the predicted cloud height for various impeller rotational speeds (3.5, 4.1, and 4.7 rps) for the A315 hydrofoil impeller. It can be seen clearly from these figures that there is an increase in the cloud height with an increase in the impeller speed. Similar observations were also reported by Khopkar et al. (2006). The values of the standard deviation and cloud height obtained by CFD simulation along with experimental values for the three types of impellers are presented in Table 4.4. Based on these two criteria, it is found that the critical impeller speed required for 6-PBTD is 4.45 rps which agrees very well with the experimental observation. It has to be noted again that both these criteria have to be satisfied for the determination of the critical impeller speed.

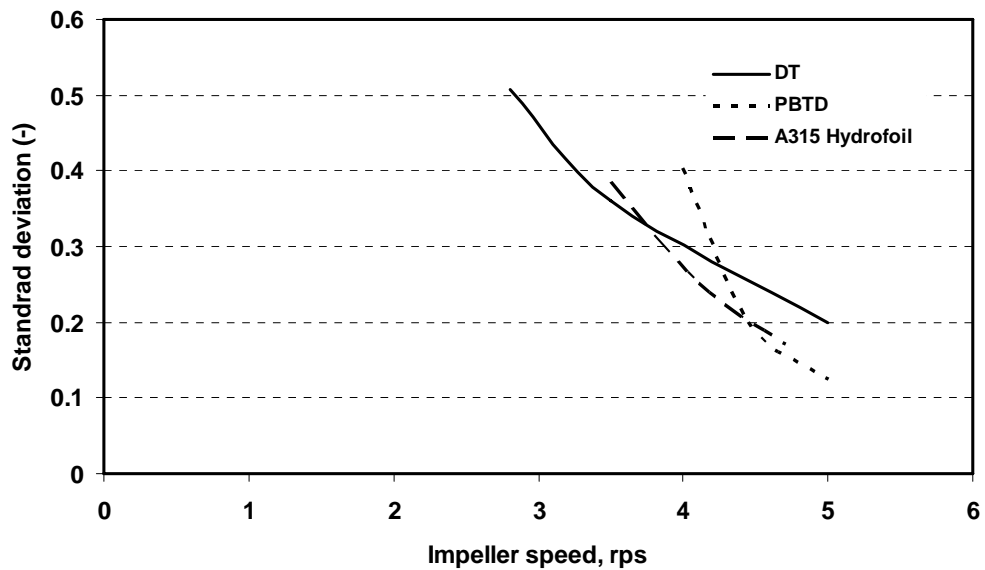
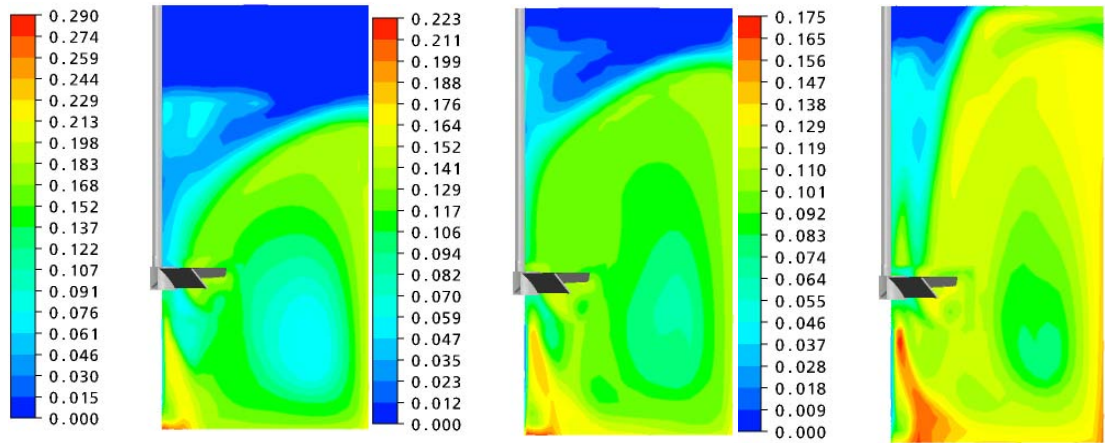
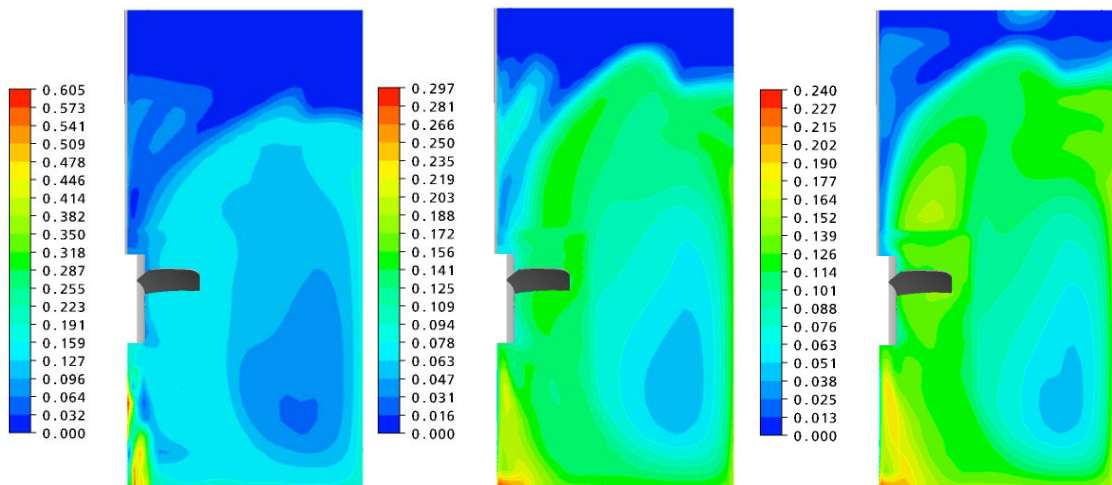


Figure 4.7. Standard deviation values obtained from CFD with respect to impeller rotational speed for A315 hydrofoil impeller (particle size of 350 μm with solids loading of 10 vol. %)



(a) 4 rps ($H_s/H=0.8$) (b) 4.45 rps ($H_s/H=0.9$) (c) 5 rps ($H_s/H=1.0$)

Figure 4.8. Cloud height predicted by CFD simulation for PBTD impeller at different rotational speeds (particle size of 350 μm with solid loading of 10 vol. %)



(a) 3.5 rps ($H_s/H=0.8$) (b) 4.1 rps ($H_s/H=0.88$) (c) 4.7 rps ($H_s/H=1.0$)

Figure 4.9. Cloud height predicted by CFD simulation for A315 hydrofoil impeller at different rotational speeds (particle size of 350 μm with solid loading of 10 vol. %)

Table 4.4. Effect of impeller type on the quality of suspension (particle size of 350 μm with solid loading of 10 vol. %)

Type of impeller	Critical impeller speed, rps		Standard deviation, σ	Cloud height
	Experimental (rps)	CFD (rps)		
DT	-	3.5	0.36	0.90
PBTD	4.45	4.45	0.21	0.91
A315 hydrofoil	-	4.1	0.25	0.88

4.4.2.2. Solid distribution

During the last few decades, various authors have investigated the solid distribution in mechanically agitated contactor in terms of the axial and/or radial profiles experimentally. Therefore, in the present work, attention has been focused on the study of axial solid distribution in mechanically agitated contactor using CFD simulation. The axial solid concentration profiles reported by Michelletti et al. (2003) and Spidla et al. (2005a) have been considered for the validation of CFD results. The effect of various type of impellers and particle size are also investigated in this work

Rushton turbine of radial type impeller (DT) has been widely characterised in terms of solid–liquid dispersion. The radial flow impeller generates two circular loops above and below the impeller and a radial jet of solids flow in the impeller stream. CFD simulations of this impeller are performed using the experimental data of Michelletti et al. (2003). The operating conditions used are solid loading of 9.2 vol. % with 655 μm glass particles at the critical impeller speed of 988 rpm. The normalised

CFD Simulation of Liquid-Solid Mechanically Agitated Contactor

axial solid concentration profile along the normalised axial direction obtained from CFD simulation is compared with the experimental data and is shown in Figure 4.10.

The axial solid concentrations have been made normalised by dividing the local solid concentration by the average solid concentration. It can be seen that the axial variation of the axial solid concentration agrees well with the experimental results. But, there is a discrepancy between numerical simulations and experimental results qualitatively near the impeller region.

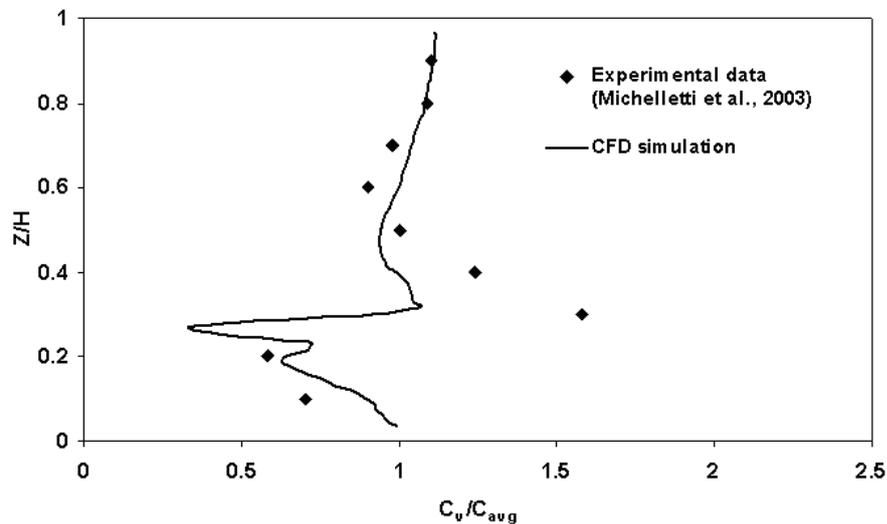


Figure 4.10. Normalised axial concentration profiles for an overall solid holdup of 9.2% and 655 μm glass particles at critical impeller speed of $N_{js} = 988$ rpm

Similarly, the predicted solid holdup distribution (at mid-baffle plane) and flow fields of solids for the 6 blade DT impellers are shown in Figure 4.11 (a). It can be seen from Figure 4.11 (a) that the predicted solid holdup distribution shows the accumulation of the solid particles around the central axis at the bottom of the vessel.

CFD Simulation of Liquid-Solid Mechanically Agitated Contactor

However, in both the circulation loops, there is a uniform distribution of the solid particles.

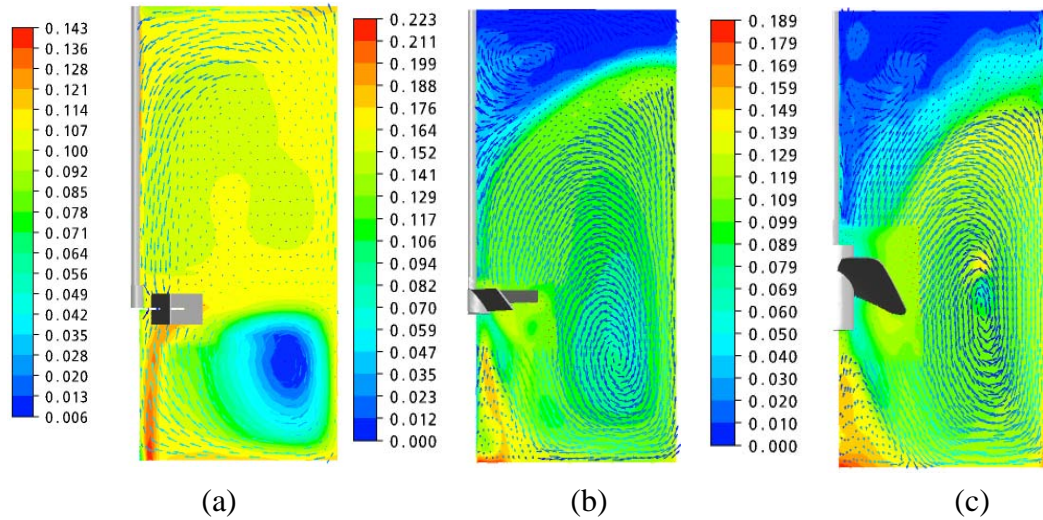


Figure 4.11. Contours of solid volume fraction and axial solid concentration profiles at just suspended speed N_{js} (a) DT (b) PBDP (c) A315 Hydrofoil

The axial type impellers with downward pumping (PBTD and A315 hydrofoil) generate a flow field where the discharge stream produced by the impeller proceeds towards the bottom of the tank, and then it hits the bottom wall, then proceeds up along the tank wall. For PBTD, CFD simulations have been performed using the experimental data of Spidla et al. (2005a). The impeller geometry and the tank details are given in Table 4.3. The solid loading is 10 vol. % and particle size chosen is 350 μm for the simulation. In order to compare the simulated solid concentration profiles with the experimental profiles reported by Spidla et al. (2005a), the local solid concentration along the reactor height is plotted at $r/R= 0.8$, in Figure 4.12. A good comparison exists between the CFD prediction and the experimental results for the axial solid concentration.

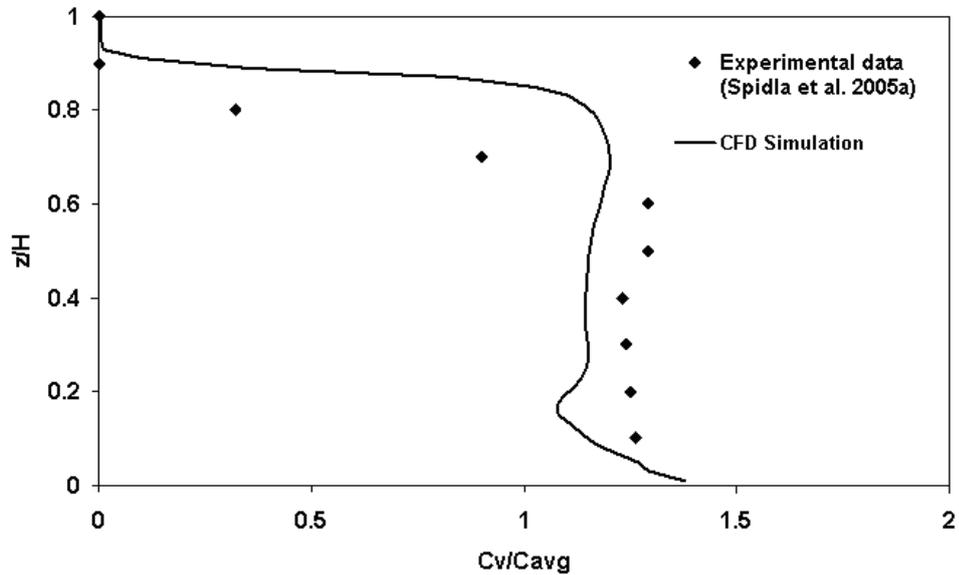


Figure 4.12. Normalised axial concentration profiles for an overall solid holdup of 10 vol. % and 350 μm glass particles at critical impeller speed of $N_{js} = 267$ rpm

The predicted solid holdup distribution for PBTD is shown in Figure 4.11 (b). It can be clearly seen that the solid particles are completely absent near the top surface, indicating the presence of clear liquid layer above the level of the suspension. For A315 hydrofoil impeller, the experimental operating process parameters of Spidla et al. (2005b) have been used. Since the experimental data for local axial solid concentration is not available, only the predicted solid holdup distribution is plotted in Figure 4.11 (c).

To study the effect of particle size on the axial solid concentration, CFD simulations have been carried out for three different particle sizes *viz.*, 200 μm , 360 μm and 655 μm for the solid loading of 9.2 % by vol., and the impeller chosen is 6 blade Rushton turbine impeller. For each particle size, the critical impeller speed was

CFD Simulation of Liquid-Solid Mechanically Agitated Contactor

determined and the simulation runs are made with the corresponding critical impeller speed. The critical impeller speed for the three particle sizes are 200, 360 and 655 μm . The critical impeller speed for solid suspension increases with an increase in the particle size for a fixed set of operating conditions and impeller configuration. This is due to the fact that with increase in the particle size, the terminal settling velocity increases. This settling velocity of particle causes sedimentation which in turn affects the solids suspension.

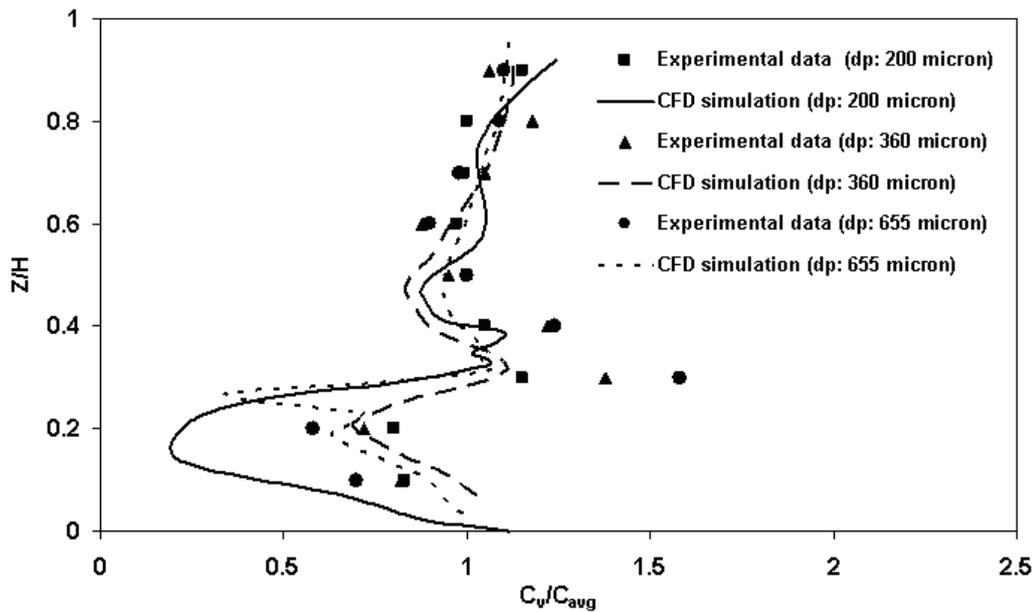


Figure 4.13. Effect of particle size on axial solid concentration profiles, (solid holdup of 9.2 vol. % glass particle of size 200, 360, 655 μm)

The axial solid concentration values obtained from CFD simulation are plotted in Figure 4.13 along with the experimental values. It can be seen clearly that, the agreement is quite good except at the impeller region.

4.4.3. Power Number comparison

The comparison of different types of impellers with regard to their suspension ability is investigated in terms of power number. The power consumption is calculated as the product of torque on the impeller blades and the angular velocity. This is then used for the estimation of power number which is expressed as follows:

$$N_p = 2\pi NT / \rho_s N^3 D^5 \dots\dots\dots(4.23)$$

where torque (*T*) exerted on all blades was computed from the total momentum vector, which is computed by summing the cross products of the pressure and viscous forces vectors for each facet on the impeller with the moment vector.

The predicted values of power number are compared with experimental data and are shown in Table 4.5. It can be observed that the values predicted by CFD simulations agrees reasonably well with the experimental values. It can also be seen from the table that the suspension performance in terms of power number is different for different impeller designs. The lowest power consumption was observed for A315 hydrofoil impeller and highest for Rushton turbine impeller. This indicates that the impeller which directs the flow downward having mainly axial component and has the least power number is most energy efficient.

Table 4.5. Experimental and predicted values of Power number

Impeller type	Power number	
	Experimental	CFD
6-Rushton turbine	6.0	5.1
6-PBTD	1.67	1.55
4- A315 Hydrofoil downward	1.5	1.37

4.5. Conclusions

1. In this chapter, Eulerian multi-fluid approach along with standard k- ϵ turbulence model has been used to study the solid suspension in liquid–solid mechanically agitated contactor.
2. The results obtained from CFD simulations are validated qualitatively with literature experimental data (Michelletti et al., 2003; Michelletti and Yianneskis 2004, Spidla et al., 2005a) in terms of axial profiles of solid distribution in liquid–solid stirred suspension. A good agreement was found between the CFD prediction and experimental data.
3. CFD predictions are compared quantitatively with literature experimental data (Spidla et al., 2005a) in the terms of critical impeller speed based on the criteria of standard deviation method and cloud height in a mechanically agitated contactor. An adequate agreement was found between CFD prediction and the experimental data.
4. The numerical simulation has further been extended to study the effect of impeller design (DT, PBTD and A315 Hydrofoil), impeller speed and particle size (200–650 μm) on the solid suspension in liquid–solid mechanically agitated contactor.

Chapter 5

CFD Simulation of Hydrodynamics of Gas-Liquid-Solid Fluidised Bed

5.1. Introduction

Three-phase reactors are used extensively in chemical, petrochemical, refining, pharmaceutical, biotechnology, food and environmental industries. Depending on the density and volume fraction of particles, three-phase reactors can be classified as slurry bubble column reactors and fluidised bed reactors. In slurry bubble column reactors, the density of the particles are slightly higher than the liquid and particle size is in the range of 5–150 μm and volume fraction of particles is below 0.15 (Krishna et al., 1997). Hence, the liquid phase along with particles can be treated as a homogenous liquid with mixture density. But in fluidised bed reactors, the density of particles are much higher than the density of the liquid and the particle size is normally large (above 150 μm) and volume fraction of particles varies from 0.6 (packed stage) to 0.2 (close to dilute transport stage). In this study, the focus is on understanding the complex hydrodynamics of three-phase fluidised beds containing coarser particles of size above 1 mm. Most of the previous studies related to three-phase fluidised bed reactors have been directed towards the understanding the complex hydrodynamics, and its influence on the phase holdup and transport properties. Recent research on fluidised bed reactors focuses on the following topics:

(a) Flow structure quantification

The quantification of flow structure in three-phase fluidised beds mainly focuses on local and globally averaged phase holdups and phase velocities for different operating conditions and parameters. In literature, Rigby et al. (1970); Muroyama and Fan (1985); Lee and De Lasa (1987); Yu and Kim (1988) investigated bubble phase holdup and velocity in three-phase fluidised beds for various operating conditions using experimental techniques like electroresistivity

CFD Simulation of Gas-Liquid-Solid Fluidised bed Contactor

probe and optical fiber probe. Larachi et al. (1996) and Kiared et al. (1999) investigated the solid phase hydrodynamics in three-phase fluidised bed using radio active particle tracking. Recently Warsito and Fan (2001, 2003) quantified the solid and gas holdup in three-phase fluidised bed using the electron capacitance tomography (ECT).

(b) Flow regime identification

Muroyama and Fan (1985) developed the flow regime diagram for air–water–particle fluidised bed for a range of gas and liquid superficial velocities. Chen et al. (1995) investigated the identification of flow regimes by using pressure fluctuations measurements. Briens and Ellis (2005) used spectral analysis of the pressure fluctuation for identifying the flow regime transition from dispersed to coalesced bubbling flow regime based on various data mining methods like fractal and chaos analysis, discrete wake decomposition method etc. Fraguío et al. (2006) used solid phase tracer experiments for flow regime identification in three-phase fluidised beds.

(c) Advanced modeling approaches

Eventhough a large number of experimental studies have been directed towards the quantification of flow structure and flow regime identification for different process parameters and physical properties, the complex hydrodynamics of these reactors are not well understood due to complicated phenomena such as particle–particle, liquid–particle and particle–bubble interactions. For this reason, Computational Fluid Dynamics (CFD) has been promoted as a useful tool for understanding multiphase reactors (Dudukovic et al., 1999) for precise design and scale up. Basically two approaches are used namely; the Euler–Euler formulation

CFD Simulation of Gas-Liquid-Solid Fluidised bed Contactor

based on the interpenetrating multi-fluid model, and the Euler–Lagrangian approach based on solving Newton’s equation of motion for the dispersed phase.

Recently, several CFD models based on Eulerian multi-fluid approach have been developed for gas–liquid flows (Kulkarni et al., 2007; Cheung et al., 2007) and liquid–solid flows (Roy et al., 2001) and gas–solid flows (Jiradilok et al., 2007). Some of the authors (Matonis et al., 2002; Feng et al., 2005; Schallenberg et al., 2005) have extended these models to three-phase flow systems. Comprehensive list of literature on modeling of these reactors are tabulated in Table 1. Most of these CFD studies are based on steady state, 2D axisymmetric, Eulerian multi-fluid approach. But in general, three-phase flows in fluidised bed reactors are intrinsically unsteady and are composed of several flow processes occurring at different time and length scales. The unsteady fluid dynamics often govern the mixing and transport processes and is inter-related in a complex way with the design and operating parameters like reactor and sparger configuration, gas flow rate and solid loading. Also, there is scarcely any report focusing on hydrodynamic studies related to 3D transient simulation with high solid content on fluidised bed reactors in literature.

Hence, in this work a 3D transient model is developed to simulate the local hydrodynamics of a gas–liquid–solid three-phase fluidised bed reactor using the CFD method. Since simulation of hydrodynamics of three-phase fluidised beds based on Euler–Lagrangian are computationally intensive, an Eulerian multi-fluid approach is used in the present study and simulations are carried out using the commercial package ANSYS CFX-10. The first aim of this work is to capture the dynamic characteristics of gas–liquid–solid flows using Eulerian multi-fluid approach and validate the same for two sets of fluidised bed reactors for which extensive

CFD Simulation of Gas-Liquid-Solid Fluidised bed Contactor

experimental results are reported in the literature. The first set of experimental data is of Kiared et al. (1999) for the solid phase hydrodynamics and the second set of experimental data is of Yu and Kim (1988 & 2001) for liquid and gas phase hydrodynamics. After the validation of the proposed CFD model, the computation of the solid mass balance and various energy flows in fluidised bed reactors are carried out.

Table 5.1. Literature survey on CFD modeling of three-phase reactors

Authors	Multiphase approach	Models used	Parameter studied
Bahary (1994)	Multi-fluid Eulerian approach for three-phase fluidised bed	Gas phase was treated as a particulate phase having 4 mm diameter and a kinetic theory granular flow model applied for solid phase. They have simulated both symmetric and axisymmetric mode.	Verified the different flow regimes in the fluidised bed and compared the time averaged axial solid velocity with experimental data.
Grevskott et al. (1996)	Two fluid Eulerian–Eulerian model for three-phase bubble column	The liquid phase along with the particles is considered pseudo-homogeneous by modifying the viscosity and density. They included the bubble size distribution based on the bubble induced turbulent length scale and the local turbulent kinetic energy level.	Studied the variation of bubble size distribution, liquid circulation and solid movement.
Mitra-Majumdar et al. (1997)	2D axisymmetric , multi-fluid Eulerian approach for three-phase bubble column	Used modified drag correlation between the liquid and the gas phase to account for the effect of solid particles and between the solid and the liquid phase to account for the effect of gas	Examined axial variation of gas holdup and solid holdup profiles for various range of liquid and gas superficial velocities and solid

CFD Simulation of Gas-Liquid-Solid Fluidised bed Contactor

		bubbles. A $k-\varepsilon$ turbulence model was used for the turbulence and considered the effect of bubbles on liquid phase turbulence.	circulation velocity.
Jianping and Shonglin (1998)	2D, Eulerian–Eulerian method for three-phase bubble column	Pseudo-two-phase fluid dynamic model. $k_{sus}-\varepsilon_{sus}-k_b-\varepsilon_b$ turbulence model was used for turbulence.	Validated local axial liquid velocity and local gas holdup with experimental data.
Padial et al. (2000)	3D, multi-fluid Eulerian approach for three-phase draft-tube bubble column	The drag force between solid particles and gas bubbles was modeled in the same way as that of drag force between liquid and gas bubbles.	Simulated gas volume fraction and liquid circulation in draft tube bubble column.
Matonis et al. (2002)	3D, multi-fluid Eulerian approach for slurry bubble column	Kinetic theory granular flow (KTGF) model for describing the particulate phase and a $k-\varepsilon$ based turbulence model for liquid phase turbulence.	Studied the time-averaged solid velocity and volume fraction profiles, normal and shear Reynolds stress and compared with the experimental data.
Feng et al. (2005)	3D, multi-fluid Eulerian approach for three-phase bubble column	The liquid phase along with the solid phase considered as a pseudo-homogeneous phase in view of the ultrafine nanoparticles. The interface force model of drag, lift and virtual mass and $k-\varepsilon$ model for turbulence are included.	Compared the local time averaged liquid velocity and gas holdup profiles along the radial position.
Schallenberg et al. (2005)	3D, multi-fluid Eulerian approach for three-phase bubble column	Gas–liquid drag coefficient based on single bubble rise, which is modified for the effect of solid phase. Extended	Validated local gas and solid holdup as well as liquid velocities with the experimental data.

CFD Simulation of Gas-Liquid-Solid Fluidised bed Contactor

		$k-\varepsilon$ turbulence model to account for bubble-induced turbulence. The interphase momentum between two dispersed phases is included.	
Li et al. (1999)	2D, Eulerian–Lagrangian model for three-phase fluidisation	The Eulerian fluid dynamic (CFD) method, the dispersed particle method (DPM) and the volume-of-fluid (VOF) method are used to account for the flow of liquid, solid, and gas phases, respectively. A continuum surface force (CSF) model, a surface tension force model and Newton’s third law are applied to account for the interphase couplings of gas–liquid, particle–bubble and particle–liquid interactions, respectively. A close distance interaction (CDI) model is included in the particle–particle collision analysis, to consider the liquid interstitial effects between colliding particles.	Investigated single bubble rising velocity in a liquid–solid fluidised bed and the bubble wake structure and bubble rise velocity in liquid and liquid–solid medium are simulated.
Zhang and Ahmadi (2005)	2D, Eulerian–Lagrangian model for three-phase slurry reactor	The interactions between bubble–liquid and particle–liquid are included. The drag, lift, buoyancy, and virtual mass forces are also included. Particle–particle and bubble–bubble interactions are accounted for by the hard sphere model approach. Bubble coalescence is also included in the model.	Studied transient characteristics of gas, liquid, and particle phase flows in terms of flow structure and instantaneous velocities. The effect of bubble size on variation of flow patterns are also studied.

5.2. Computational flow model

In the present work, an Eulerian multi-fluid model is adopted where gas, liquid and solid phases are all treated as continua, interpenetrating and interacting with each other everywhere in the computational domain. The pressure field is assumed to be shared by all the three phases, in proportion to their volume fraction. The motion of each phase is governed by respective mass and momentum conservation equations.

Continuity equation:

$$\frac{\partial}{\partial t}(\epsilon_k \rho_k) + \nabla \cdot (\rho_k \epsilon_k \bar{u}_k) = 0 \quad \dots\dots\dots(5.1)$$

where ρ_k is the density and ϵ_k is the volume fraction of phase $k = g$ (gas), s (solid), l (liquid) and the volume fraction of the three phases satisfy the following condition

$$\epsilon_l + \epsilon_g + \epsilon_s = 1 \quad \dots\dots\dots(5.2)$$

Momentum equations:

For liquid phase:

$$\frac{\partial}{\partial t}(\rho_l \epsilon_l \bar{u}_l) + \nabla \cdot (\rho_l \epsilon_l \bar{u}_l \bar{u}_l) = - \epsilon_l \nabla P + \nabla \cdot (\epsilon_l \mu_{eff,l} [\nabla \bar{u}_l + (\nabla \bar{u}_l)^T]) + \rho_l \epsilon_l g + M_{i,l} \quad \dots\dots\dots(5.3)$$

For gas phase:

$$\frac{\partial}{\partial t}(\rho_g \epsilon_g \bar{u}_g) + \nabla \cdot (\rho_g \epsilon_g \bar{u}_g \bar{u}_g) = - \epsilon_g \nabla P + \nabla \cdot (\epsilon_g \mu_{eff,g} [\nabla \bar{u}_g + (\nabla \bar{u}_g)^T]) + \rho_g \epsilon_g g - M_{i,g} \quad \dots\dots\dots(5.4)$$

For solid phase:

$$\frac{\partial}{\partial t}(\rho_s \epsilon_s \bar{u}_s) + \nabla \cdot (\rho_s \epsilon_s \bar{u}_s \bar{u}_s) = - \epsilon_s \nabla P - \nabla P_s + \nabla \cdot (\epsilon_s \mu_{eff,s} [\nabla \bar{u}_s + (\nabla \bar{u}_s)^T]) + \rho_s \epsilon_s g - M_{i,s} \quad \dots\dots\dots(5.5)$$

CFD Simulation of Gas-Liquid-Solid Fluidised bed Contactor

where P is the pressure and μ_{eff} is the effective viscosity. The second term on the R.H.S of solid phase momentum equation (5.5) is the term that accounts for additional solid pressure due to solid collisions. The terms $M_{i,l}$, $M_{i,g}$, and $M_{i,s}$ of the above momentum equations represent the interphase force term for liquid, gas and solid phase respectively.

5.2.1. Closure law for Turbulence

The effective viscosity of the liquid phase is calculated by the following equation

$$\mu_{\text{eff},l} = \mu_l + \mu_{T,l} + \mu_{tg} + \mu_{ts} \dots\dots\dots(5.6)$$

where μ_l is the liquid viscosity, $\mu_{T,l}$ is the liquid phase turbulence viscosity or shear induced eddy viscosity, which is calculated based on the k- ϵ model of turbulence as

$$\mu_{T,l} = c_{\mu} \rho_l \frac{k^2}{\epsilon} \dots\dots\dots(5.7)$$

where the values of k and ϵ are obtained directly from the differential transport equations for the turbulence kinetic energy and turbulence dissipation rate. μ_{tg} and μ_{ts} represent the gas and solid phase induced turbulence viscosity respectively and are given by the equations proposed by Sato et al. (1981) as

$$\mu_{tg} = c_{\mu p} \rho_l \epsilon_g d_b |\vec{u}_g - \vec{u}_l| \dots\dots\dots(5.8)$$

$$\mu_{ts} = c_{\mu p} \rho_l \epsilon_s d_p |\vec{u}_s - \vec{u}_l| \dots\dots\dots(5.9)$$

The standard values used for constants in the turbulence equations are $C_{\epsilon 1} = 1.44$, $C_{\epsilon 2} = 1.92$, $C_{\mu} = 0.09$, $C_{\mu p} = 0.6$, $\sigma_k = 1.0$ and $\sigma_{\epsilon} = 1.3$. The effective viscosity of gas and solid phases are calculated as

$$\mu_{\text{eff},g} = \mu_g + \mu_{T,g} \dots\dots\dots(5.10)$$

$$\mu_{\text{eff, s}} = \mu_s + \mu_{\text{T, s}} \dots\dots\dots(5.11)$$

where $\mu_{\text{T,g}}, \mu_{\text{T,s}}$ are the turbulence viscosity of gas and solid phases respectively. The turbulent viscosity of the gas phase is related to the turbulence viscosity of the liquid phase by the correlation proposed by Schijnung (1983) as

$$\mu_{\text{T,g}} = \frac{\rho_g}{\rho_l} R_p^2 \mu_{\text{T,l}} \dots\dots\dots(5.12)$$

where R_p is defined as the proportion of the fluctuation velocity of the gas and liquid phase. Grienberger and Hofmann (1992) reported that the value of R_p is between 1 and 2. Jakobsen et al. (1997) proposed the following equations for the turbulent viscosity of dispersed phases and these equations are used in the present work:

$$\mu_{\text{T,g}} = \frac{\rho_g}{\rho_l} \mu_{\text{T,l}} \dots\dots\dots(5.13)$$

$$\mu_{\text{T,s}} = \frac{\rho_s}{\rho_l} \mu_{\text{T,l}} \dots\dots\dots(5.14)$$

5.2.2. Closure law for Solid pressure

The solid phase pressure gradient results from normal stresses resulting from particle–particle interactions, which become very important when the solid phase fraction approaches the maximum packing. In literature, two closure models are used. The first model is the constant viscosity model (CVM), where the solid phase pressure is defined only as a function of the local solid porosity using empirical correlations and the dynamic shear viscosity of the solid phase is assumed constant. Second model is based on the kinetic theory of granular flow (KTGF) which is based on the application of the kinetic theory of dense gases to particulate assemblies. Eventhough

CFD Simulation of Gas-Liquid-Solid Fluidised bed Contactor

this model gives more insight in terms of particle–particle interactions, CVM is used in this work based on the following observation.

Recently Patil et al. (2005) compared the performance of both the models for gas–solid fluidised beds and reported that both KTGF model and CVM give similar predictions in terms of bubble rise velocity and bubble size when compared to the experimental data. They also observed that the KTGF model does not account for the long term and multi particle–particle contacts (frictional stresses) and underpredicts the solid phase viscosity at the wall as well as around the bubble and therefore overpredicts the bed expansion. These frictional stresses are usually implemented via a relatively simple semi-empirical closure model. Moreover, KTGF model is more computationally expensive. The constitutive equation for CVM model, as given by Gidaspow (1994), is

$$\nabla P_s = G(\epsilon_s) \nabla \epsilon_s \dots\dots\dots(5.15)$$

where $G(\epsilon_s)$ is the elasticity modulus and it is given by

$$G(\epsilon_s) = G_0 \exp(c(\epsilon_s - \epsilon_{sm})) \dots\dots\dots(5.16)$$

as proposed Bouillard et al. (1989), where G_0 is the reference elasticity modulus, c is the compaction modulus and ϵ_{sm} is the maximum packing parameter.

5.2.3. Closure law for Interphase Momentum exchange

The interphase momentum exchange terms M_i are composed of a linear combination of different interaction forces between different phases such as the drag force, the lift force and the added mass force, etc., and is generally represented as

$$M_i = M_D + M_L + M_{VM} \dots\dots\dots(5.17)$$

CFD Simulation of Gas-Liquid-Solid Fluidised bed Contactor

In a recent review, the effect of various interfacial forces have been discussed by Rafique et al. (2004). They reported that the effect of added mass can be seen only when high frequency fluctuations of the slip velocity occur and they also observed that the added mass force are much smaller than the drag force in bubbly flow. In most of the previous studies, lift force has been applied to 2D simulation of gas–liquid flows. But, it has been often omitted in 3D simulation of bubble flows. The main reason for this is the lack of understanding about the complex mechanism of lift forces in 3D gas–liquid flows (Bunner and Tryggvason, 1999). Also depending on the bubbles size, a negative or positive lift coefficient is used in the literature in order to obtain good agreement between simulation and experiment. Recently Sokolichin et al. (2004) suggested that the lift force should be omitted as long as no clear experimental evidence of their direction and magnitude is available and neglecting the lift force can still lead to good comparison with experimental data as reported by Pan et al. (1999, 2000). Hence, only the drag force is included for interphase momentum exchange in the present CFD simulation. In the present work, the liquid phase is considered as a continuous phase and both the gas and the solid phases are treated as dispersed phases. The interphase drag force between the phases is discussed below.

5.2.3.1. Liquid–solid interphase drag force ($F_{D,ls}$)

$$F_{D,ls} = C_{D,ls} \frac{3}{4} \rho_l \frac{\epsilon_s}{d_p} |\bar{u}_s - \bar{u}_l| (\bar{u}_s - \bar{u}_l) \dots\dots\dots(5.18)$$

where $C_{D,ls}$, is the drag coefficient between liquid and solid phases and is obtained by Gidaspow’s drag model (1994) as

$$C_{D,ls} = \frac{150 \epsilon_s^2 \mu_l}{\epsilon_l d_p^2} + \frac{1.75 \epsilon_s \rho_l (\bar{u}_l - \bar{u}_s)}{\epsilon_l d_p} \quad (\epsilon_l < 0.8) \quad \dots\dots\dots(5.19)$$

$$C_{D,ls} = \frac{3}{4} C_D \epsilon_s \rho_l \frac{(\bar{u}_l - \bar{u}_s)}{d_p} f(\epsilon_l) \quad (\epsilon_l > 0.8) \quad \dots\dots\dots(5.20)$$

where C_D is the drag coefficient proposed by Wen and Yu (1966) and is given as

$$C_D = \frac{24}{Re_p} (1 + 0.15 Re_p^{0.687}), \quad Re_p \leq 1000 \quad \dots\dots\dots(5.21)$$

$$C_D = 0.44, \quad Re_p > 1000 \quad \dots\dots\dots(5.22)$$

Here particle Reynolds number is defined as

$$Re_p = \frac{\rho_l d_p |\bar{u}_l - \bar{u}_s|}{\mu_l} \quad \dots\dots\dots(5.23)$$

$$\text{and} \quad f(\epsilon_l) = \epsilon_l^{-2.65} \quad \dots\dots\dots(5.24)$$

5.2.3.2. Gas-Liquid interphase drag force ($F_{D,gl}$)

$$F_{D,lg} = C_{D,lg} \frac{3}{4} \rho_l \frac{\epsilon_g}{d_b} |\bar{u}_g - \bar{u}_l| (\bar{u}_g - \bar{u}_l) \quad \dots\dots\dots(5.25)$$

$C_{D,lg}$ is the drag coefficient between liquid and gas phases. The most widely used drag correlations in the literature are by Tomiyama (1998) and Grace (1973).

Tomiyama drag model (1998):

$$C_{D,lg} = \text{Max} \left\{ \min \left(\frac{24}{Re_b} (1 + 0.15 Re_b^{0.687}), \frac{74}{Re_b} \right), \frac{8}{3} \frac{Eo}{Eo + 4} \right\} \epsilon_l^{-0.5} \quad \dots\dots\dots(5.26)$$

where the bubble Reynolds number (Re_b) and Eotvos number (Eo) are defined as

$$Re_b = \frac{|\bar{u}_l - \bar{u}_g| d_b}{\nu_l} \quad \dots\dots\dots(5.27)$$

$$Eo = \frac{g(\rho_l - \rho_g) d_b^2}{\sigma} \quad \dots\dots\dots(5.28)$$

Grace drag model (1973):

$$C_{D,lg} = \text{Max} \left\{ \frac{24}{\text{Re}_b} (1 + 0.15 \text{Re}_b^{0.687}), \text{Min} \left(\frac{8}{3}, \frac{4gd_b \Delta \rho}{3U_T^2 \rho_1} \right) \right\} \epsilon_1^2 \dots\dots\dots(5.29)$$

where the terminal velocity U_T is given by

$$U_T = \frac{\mu_1}{\rho_1 d_b} M^{-0.149} (J - 0.857) \dots\dots\dots(5.30)$$

$$M = \frac{\mu_1^4 g \Delta \rho}{\rho_1^2 \sigma^3} \dots\dots\dots(5.31)$$

$$J = \begin{cases} 0.9H^{0.7521} & 2 < H \leq 59.3 \\ 3.42H^{0.441} & H > 59.3 \end{cases} \dots\dots\dots(5.32)$$

$$H = \frac{4}{3} \text{Eo} M^{0.149} \left(\frac{\mu_1}{\mu_{\text{ref}}} \right)^{-0.14} \dots\dots\dots(5.33)$$

where $\mu_{\text{ref}} = 0.0009 \text{ kg m}^{-1} \text{ s}^{-1}$

5.2.3.3. Gas–Solid interphase drag force ($F_{D,gs}$)

The momentum exchange between the two dispersed phases viz, gas and solid phases have to be taken into account for CFD simulation of three-phase flows, since the particles in the vicinity of bubbles tend to follow the bubbles (Schallenberg et al., 2005; Mitra-Majumdar et al., 1997). Eventhough the drag force between the continuous phase and the dispersed phase is discussed widely in the literature, the interaction between dispersed bubbles and dispersed solids in liquid–solid–gas three-phase flows has not been modeled so far in the literature. Since the two dispersed phases are assumed to be continua in our simulation, it is reasonable to model the drag force between solid particles and bubbles in the same way as that between the continuous and the dispersed phase. Similar approach have also been used by Padijal

CFD Simulation of Gas-Liquid-Solid Fluidised bed Contactor

et al. (2000); Schallenberg et al. (2005); Wang et al. (2006). The equation used for drag force in the present simulation is the same as that of Wang et al. (2006). This interaction force is implemented as an additional source term in the momentum equations of the gas and the solid phase through a user defined function in CFX and is given as

$$F_{D,gs} = C_{D,gs} \frac{3}{4} \rho_g \frac{\epsilon_g \epsilon_s}{d_p} |\bar{u}_s - \bar{u}_g| (\bar{u}_s - \bar{u}_g) \dots\dots\dots(5.34)$$

$$C_{D,gs} = \frac{24}{Re} (1 + 0.15 Re_p^{0.687}), \quad Re_p \leq 1000 \dots\dots\dots(5.35)$$

$$C_{D,gs} = 0.44, \quad Re_p \geq 1000 \dots\dots\dots(5.36)$$

5.3. Numerical Methodology

The model equations described above are solved using the commercial CFD software package ANSYS CFX-10. Two fluidised bed reactors are considered for the present simulation studies: (a) cylindrical plexiglas column of diameter 0.1 m and height 1.5 m (Kiared et al., 1999), (b) cylindrical plexiglas column of diameter 0.254 m and height 2.5 m (Yu and Kim, 1988, 2001). Figure 5.1 depicts the typical numerical mesh used for this simulation. ‘O’ type structured hexagonal elements containing height to diameter ratio of four is generated using ICEM CFD. The governing equations are discretised using element based finite volume method (Raw, 1994) and for spatial discretisation of the governing equations, high-resolution discretisation scheme is applied which accounts for accuracy and stability. For time discretisation of the governing equations, a second order backward Euler scheme with time step of 0.001s is used.

CFD Simulation of Gas-Liquid-Solid Fluidised bed Contactor

The discretised equations are solved using the advanced coupled multi-grid solver technology of CFX-10 (Raw, 1994) where pressure velocity coupling is based on the Rhie-Chow algorithm (Rhie and Chow, 1982). The convergence criteria for all the numerical simulations are based on monitoring the mass flow residual and the value of 1.0e-04 was set as converged value. Inlet boundary condition is a uniform liquid and gas velocity at the inlet, and the outlet boundary condition is the pressure boundary condition, which is set as 1.013×10⁵ Pa. Wall boundary conditions are no-slip boundary conditions for the liquid phase and free slip boundary conditions for the solid phase and gas phase. Initial conditions are ε_s =0.59 and ε_l =0.41 up to the static bed height of column and ε_g =1.0, ε_s = 0 and ε_l = 0 in the freeboard region. The simulations are carried out till the system reached the quasi-steady state. i.e., the averaged flow variables are time independent; this can be achieved by monitoring the gas holdup. Once the fully developed quasi-steady state is reached, the averaged quantities in terms of time, axial and azimuthal directions are calculated as

Time averaged-velocity

$$\langle \bar{u}(r, \theta, z) \rangle = \frac{\int_{t_1}^{t_2} \bar{u}(r, \theta, z, t) dt}{\int_{t_1}^{t_2} dt} \dots\dots\dots(5.37)$$

where \bar{u} is local instantaneous velocity.

Azimuthally and axially averaged time-averaged velocity

$$U(r) = \frac{\int_0^z \int_0^{2\pi} \langle \bar{u}(r, \theta, z) \rangle P(r, \theta, z) d\theta dz}{\int_0^z \int_0^{2\pi} P(r, \theta, z) d\theta dz} \dots\dots\dots(5.38)$$

where P is number of locations .

CFD Simulation of Gas-Liquid-Solid Fluidised bed Contactor

For all the simulations, the time-averaged quantities are obtained for the time interval between $t_1=10s$ and $t_2=20s$.

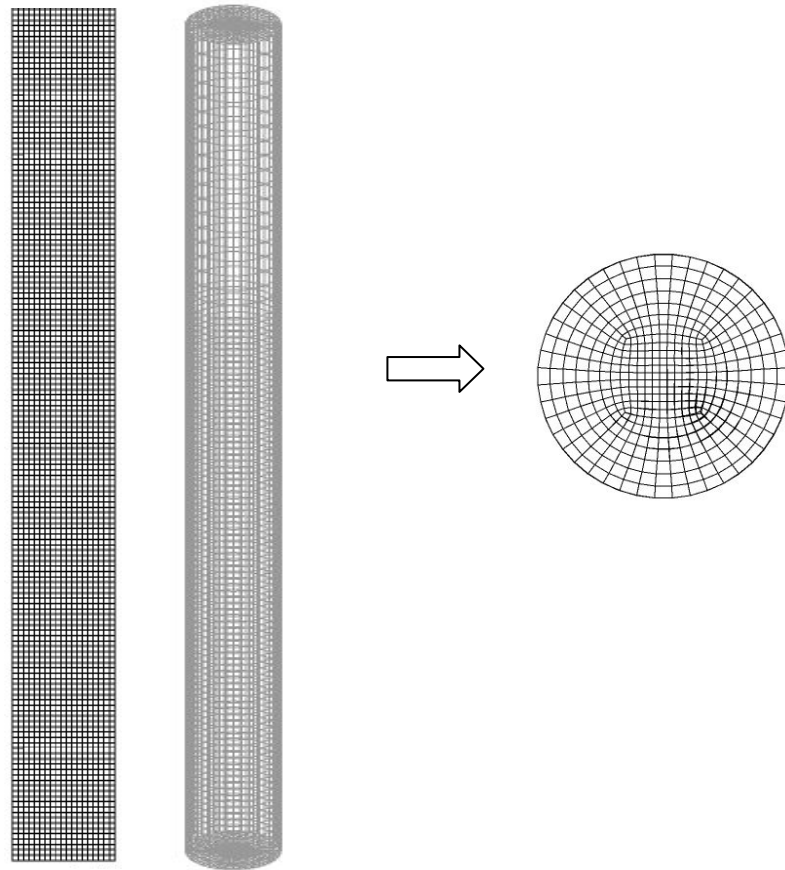


Figure 5.1. (a) 2D (20×280); (b) 3D (24×16×80) mesh of the reactor

5.4. Results and Discussion

The first goal of this work is to predict and validate the dynamic characteristics of gas–liquid–solid flows. The results obtained using the present CFD simulation is compared with two sets of experimental data. The first set of experimental data is that of Kiared et al. (1999) where the time-averaged solids flow in the fully developed region of a cylindrical gas–liquid–solid fluidised bed are

CFD Simulation of Gas-Liquid-Solid Fluidised bed Contactor

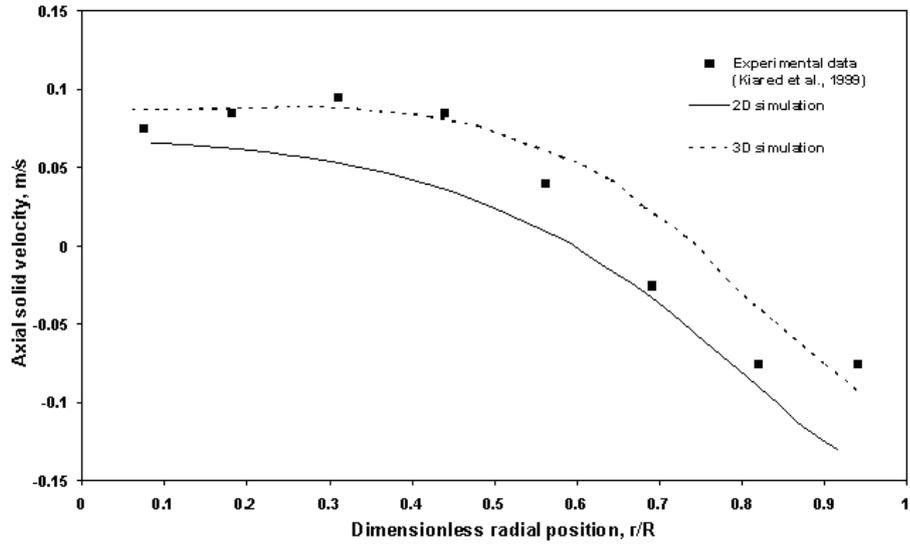
provided by using a noninvasive radioactive particle tracking technique (RPT). The second set of experimental data used for validation is that of Yu and Kim (1988, 2001) where the radial profiles of gas-phase holdup and local liquid velocity in a three-phase fluidised bed are obtained by optical fiber probe. The dimensions of the fluidised bed columns, the physical properties of phases and the process parameters used for the present simulation are presented in Table 5.2.

Table 5.2. Physical and process parameters for simulation

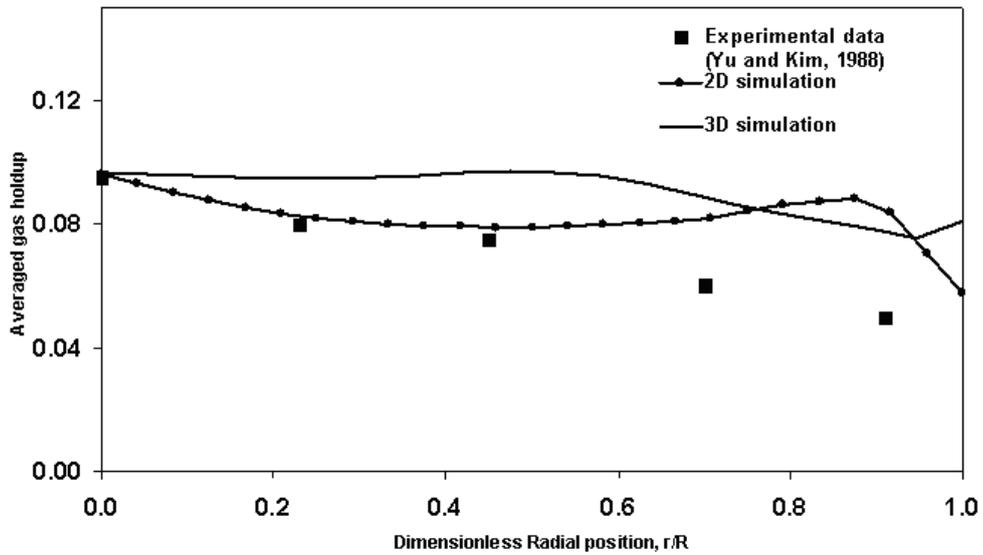
	Kiared et al.(1999)	Yu and Kim (1988, 2001)
Diameter of column (m)	0.1	0.254
Height of column (m)	1.5	2.5
Liquid phase	Water	Water
Solid phase	Glass beads	Glass beads
Gas Phase	Air	Air
Density of solid (kg/m ³)	2475	2500
Mean particle Size (mm)	3	2.3
Mean bubble size (mm)	2	13
Initial bed height (m)	0.35	0.39
Initial solid holdup	0.59	0.60
Initial bed voidage	0.41	0.40
Superficial gas velocity U_g (m/s)	0.032, 0.069, 0.11	0.01, 0.04
Superficial liquid velocity U_l (m/s)	0.065	0.06

5.4.1. Comparison between 2D and 3D simulation

Figure 5.2(a) compares the axial solid velocity obtained through 2D and 3D CFD simulation with the experimental data of Kiared et al. (1999). For this simulation, the liquid superficial velocity is taken as 0.065 m/s and the gas superficial velocity used is 0.069 m/s. It can be clearly seen that the 3D simulation gives a more accurate prediction for axial solid velocity when compared with the reported experimental results (Kiared et al., 1999) than that of 2D simulation. Figure 5.2(b) shows a similar comparison between the simulated radial variation of the gas holdup and the experimental results of Yu and Kim (1988). For this simulation, the liquid superficial velocity is taken as 0.06 m/s and the gas superficial velocity used is 0.04 m/s. The deviation of the simulated results from the experimental results are calculated as follows:
$$\text{Dev} = \frac{\sum_{i=1}^N (X_{z,\text{sim}_i} - X_{z,\text{exp}_i})^2}{N}$$
 where X_{z,sim_i} stands for the axial solid velocity values obtained through simulation and X_{z,exp_i} stands for the axial solid velocity values obtained through experiments at a particular radial position and N denotes the total number of observations. The deviation values for 2D and 3D simulation are $1.25\text{e-}03$ and $5.0\text{e-}04$ respectively. Thus, it can be clearly seen that the 3D simulation provides a more accurate prediction than that of 2D simulation and hence for further studies, 3D CFD simulation is carried out.



(a)



(b)

Figure 5.2. Comparison of 2-D and 3-D simulation on the (a) averaged axial solid velocity at gas superficial velocity of 0.069 m/s and liquid superficial velocity of 0.065 m/s (b) averaged gas holdup at gas superficial velocity of 0.04 m/s and liquid superficial velocity of 0.06 m/s

5.4.2. Interphase drag force model for gas–liquid phases

In literature, the most widely used drag models for the gas–liquid interphase are Grace drag model (1973) and Tomiyama drag model (1998). 3-D CFD simulations are carried out using both the drag models. The process conditions used for this simulation are liquid superficial velocity of 0.06 m/s and gas superficial velocity of 0.04 m/s. The solid phase consists of glass beads of diameter 2.3 mm. The gas holdup profile obtained by CFD simulation along with the experimental result of Yu and Kim (1988) is plotted in Figure 5.3. It can be observed that the results predicted by CFD simulation based on Tomiyama drag model (1998) are closer to the experimental results than that of results obtained by Grace drag model (1973). When the drag model of Tomiyama (1998) is used, the drag force between the gas and the liquid phase is increased. This increased drag force reduces the bubble velocity and hence increases the bubble residence time in the column. This leads to an increase in the gas holdup. For further CFD simulations, Tomiyama drag model (1998) is used for gas–liquid interphase drag.

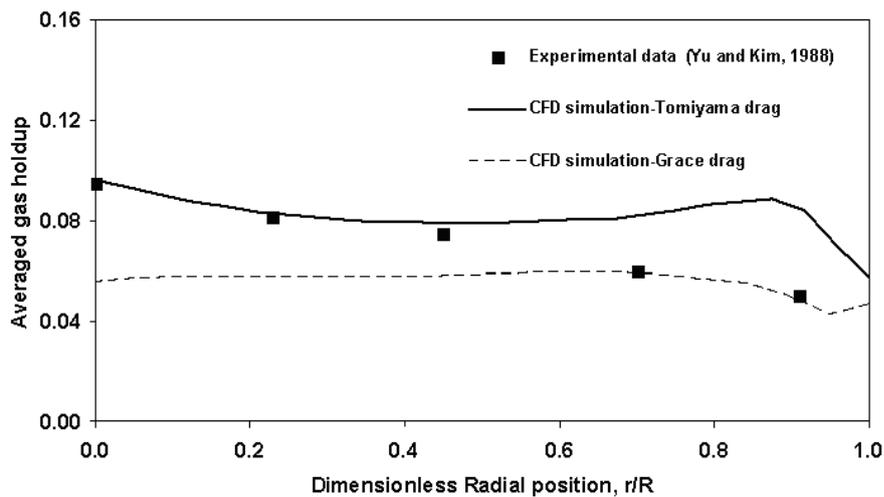


Figure 5.3. Effect of different drag models on averaged gas holdup at gas superficial velocity of 0.04 m/s and liquid superficial velocity of 0.06 m/s

5.4.3. Mean Bubble size for CFD simulation

The prediction of bubble size distribution in three-phase fluidised beds is quite complex because the bubble breakup and coalescence due to bubble–particle interaction are not well understood. Also, there is not much information available to model these phenomena in the literature. Further, a transient 3D simulation with a bubble size distribution requires an enormous amount of CPU time. Hence, a mean bubble size is assumed in the present study. An appropriate mean bubble size is chosen by matching the gas holdup profile obtained by CFD simulation with that of the experimental results of Yu and Kim (1988). For 3D CFD simulation, we have considered three different bubble sizes (5 mm, 13 mm and 17 mm), where the liquid superficial velocity is chosen as 0.06 m/s and the gas superficial velocity is chosen as 0.04 m/s. The solid phase considered is glass beads of size 2.3 mm. The predicted results are shown in Figure 5.4.

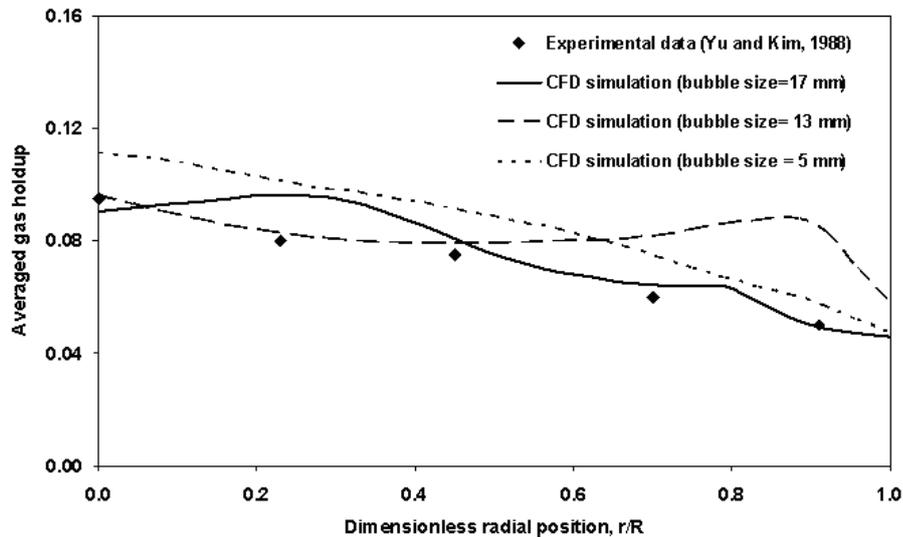


Figure 5.4. Effect of mean bubble size on the averaged gas holdup at gas superficial velocity of 0.04 m/s and liquid superficial velocity of 0.06 m/s

CFD Simulation of Gas-Liquid-Solid Fluidised bed Contactor

It can be seen that the gas holdup profiles along the radial direction are quite good for bubbles of size 13 mm and 17 mm. However, for 5 mm bubbles the predicted gas holdup is higher than the experimental observation and this may be because smaller bubbles spend more time in the column than larger size bubbles. Hence, for further CFD simulation a mean bubble size of 13 mm for the fluidised bed of diameter 0.254 m (Yu and Kim, 1988) and a mean bubble size of 2 mm for the fluidised bed of diameter 0.1 m (Kiared et al., 1999) is used.

5.4.4. Solid phase hydrodynamics

According to Chen et al. (1994) and Larachi et al. (1996), the dynamic solids flow structure in three-phase fluidised beds shows a single circulation pattern, where there is a central fast bubble flow region in which the solids move upward and a relatively bubble free wall region where the solids flow downwards. The present transient CFD simulation also shows a similar pattern for solids flow structure as depicted in Figure 5.5. The process conditions used for this simulation is $U_g = 0.11$ m/s and $U_l = 0.065$ m/s. Roy et al. (2005) also observed this type of single solid circulation pattern in a liquid-solid riser and we also observed a similar pattern in our own studies (Chapter 3) in a liquid-solid fluidised bed.

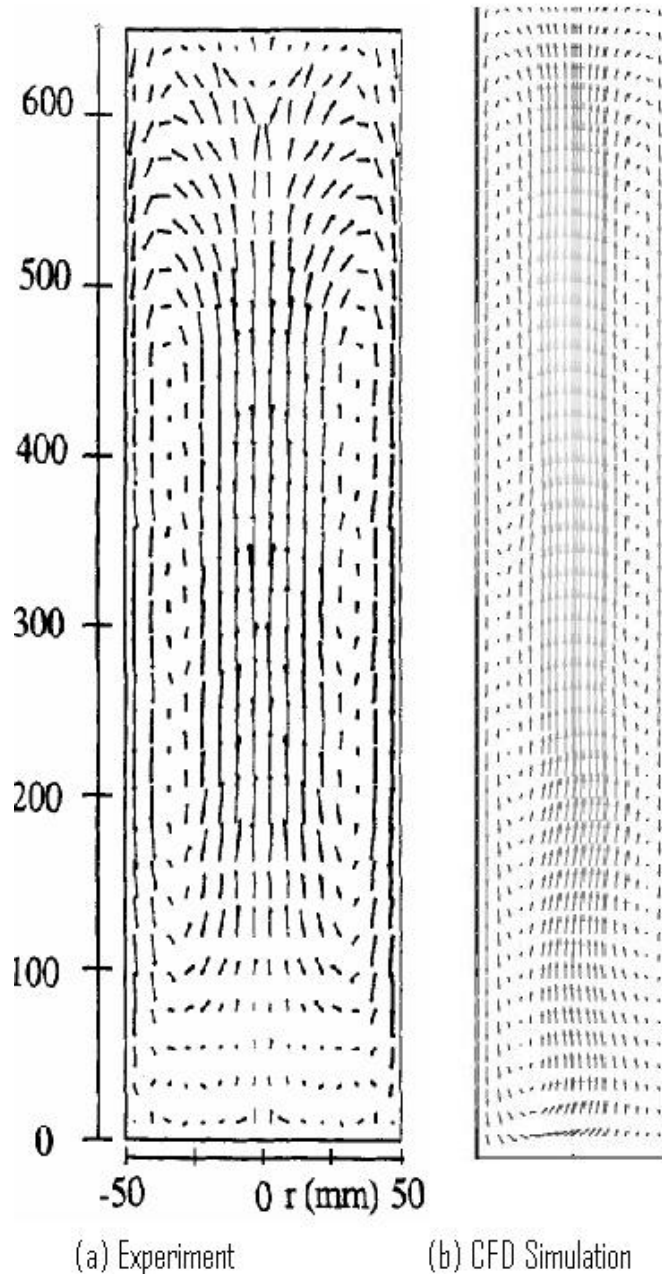
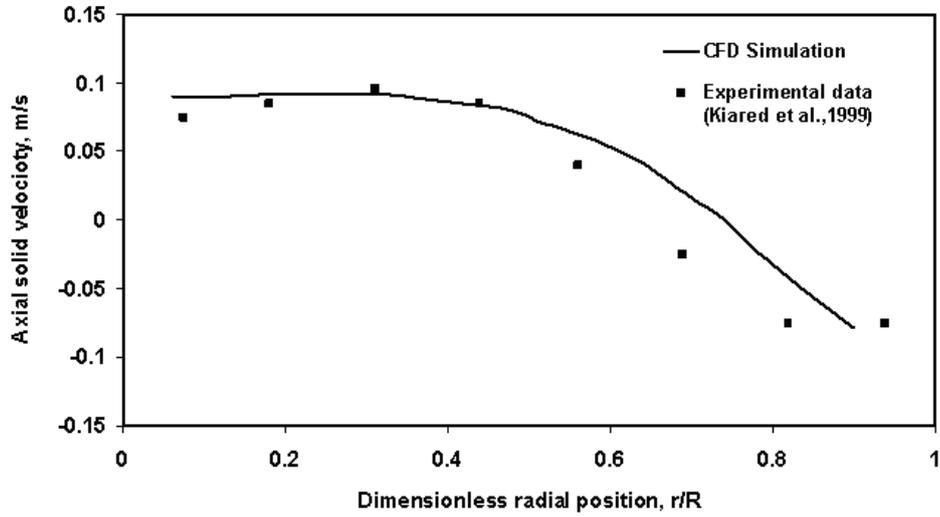
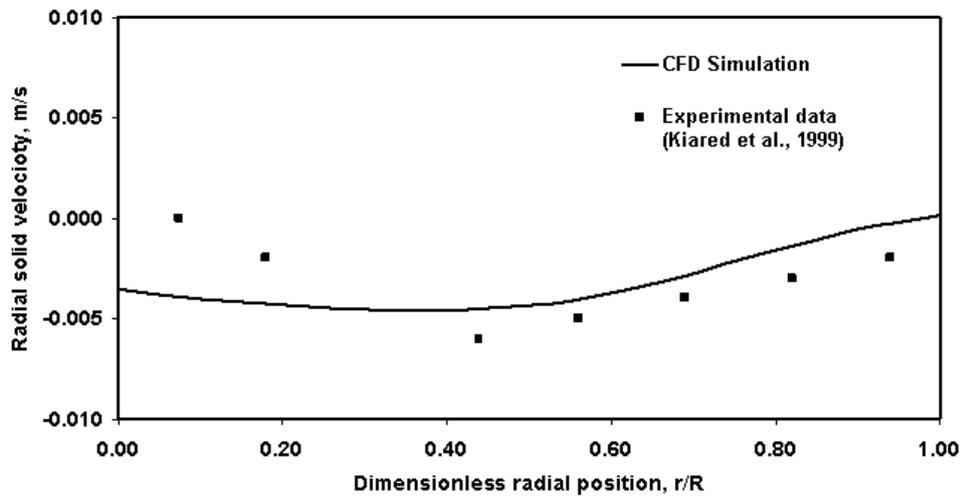


Figure 5.5. Time and azimuthally averaged solid circulation pattern (a) experimental data of Larachi et al. (1996) (b) present CFD simulation



(a)



(b)

Figure 5.6. (a) Axial solid velocity (b) radial solid velocity profiles as a function of radial position at a gas superficial velocity of 0.069 m/s and liquid superficial velocity of 0.065 m/s

CFD Simulation of Gas-Liquid-Solid Fluidised bed Contactor

The variation of time and spatially averaged axial and radial solid velocities along with the experimental data obtained by Kiared et al. (1999) with respect to the dimensionless radial position is shown in Figure 5.6 (a, b). For this simulation, the solid phase chosen is glass beads of size 3 mm, the liquid superficial velocity used is 0.065 m/s, the gas superficial velocity used is 0.069 m/s and the bubble size chosen is 2 mm. It can be observed that the agreement between the experimental and simulated results is good. It can also be observed that the axial solid velocity is higher in the central region where the solid particles move upward (positive velocity) and is lower in the wall region where the solid particles move downward (negative velocity). The flow reversal (where the sign changes) occurs at the dimensionless radial position of 0.74. According to the experimental observation of Kiared et al. (1999), the flow reversal occurs at $r/R \gg 0.70$. The maximum velocity observed for axial solid velocity is around 0.1m/s in the upward motion and is around 0.075 m/s in the downward motion. The radial solid velocity shows a flat profile (Figure 5.6b) where the values are almost near zero and this pattern agrees with the advectionless radial flow that is reported by other investigators on the liquid or solids behavior in bubble columns (Dudukovic et al., 1991), and in three-phase fluidised beds (Larachi et al., 1996). Also, the magnitude of the axial solid velocity is much higher than the radial solid velocity. This is in close agreement with experimental data reported by the Kiared et al. (1999).

The effect of gas superficial velocity on the time and spatially averaged axial solid velocity along with the experimental data of Kiared et al. (1999) is shown in Figure 5.7. The gas superficial velocities chosen for the present CFD simulation are 0.032, 0.069, 0.11 m/s. The liquid superficial velocity is 0.065 m/s and the particle

CFD Simulation of Gas-Liquid-Solid Fluidised bed Contactor

size is 3 mm, and the bubble size chosen is 2 mm. The increase in the gas superficial velocity leads to coalesced bubble flow regime, which in turn increases the axial solid velocity whereas the lower gas superficial velocity corresponds to the dispersed flow regime where the axial solid velocity are relatively flatter. The peak axial velocity of the solid increases from 0.1 m/s to 0.22 m/s when the gas superficial velocity increases from 0.069 to 0.11 m/s. The agreement between the simulation and experiments are closer for higher gas superficial velocities as evident from Figure 5.7.

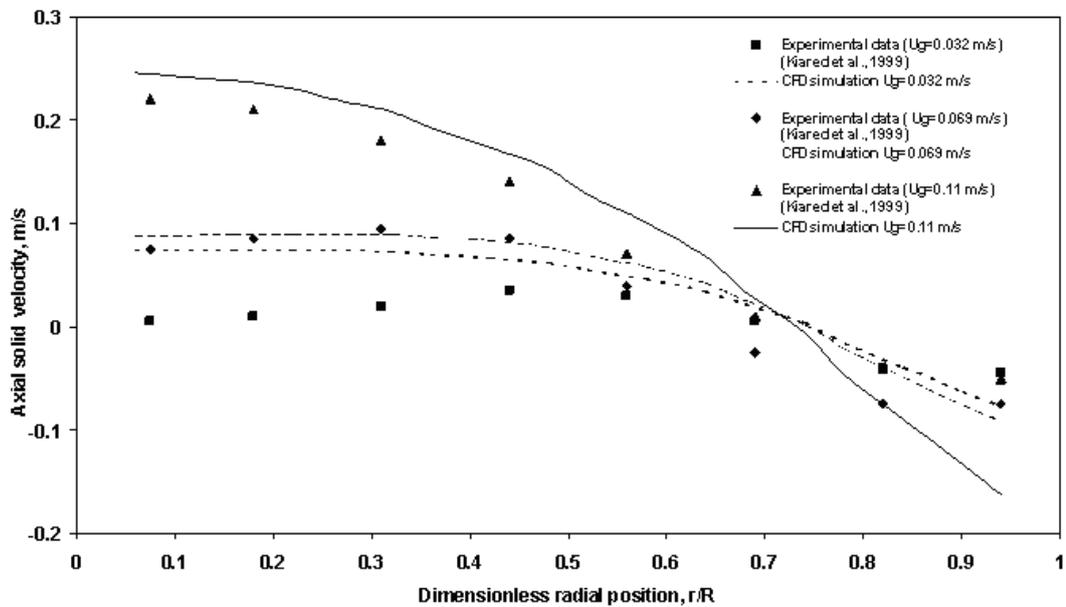
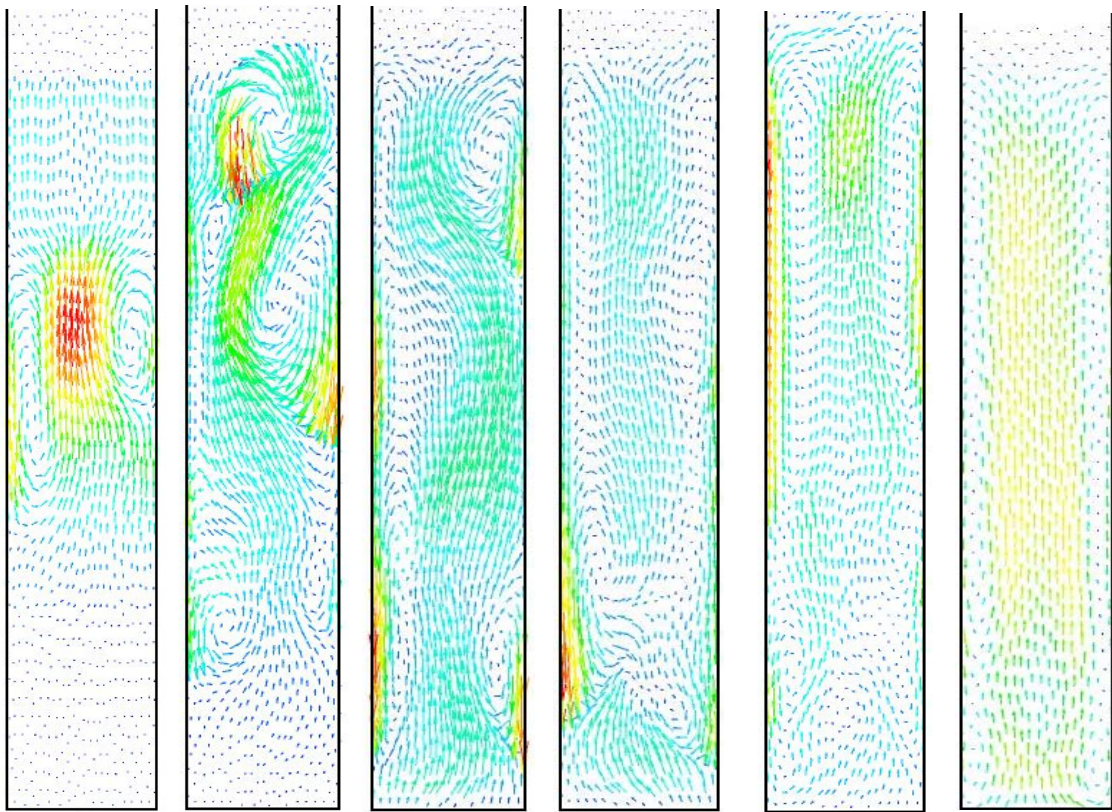


Figure 5.7. Effect of superficial gas velocity on the axial solid velocity as a function of radial position at liquid superficial velocity of 0.065 m/s

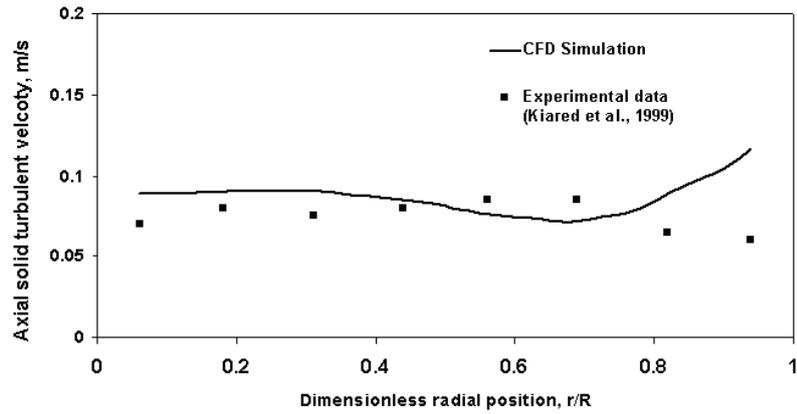
CFD Simulation of Gas-Liquid-Solid Fluidised bed Contactor



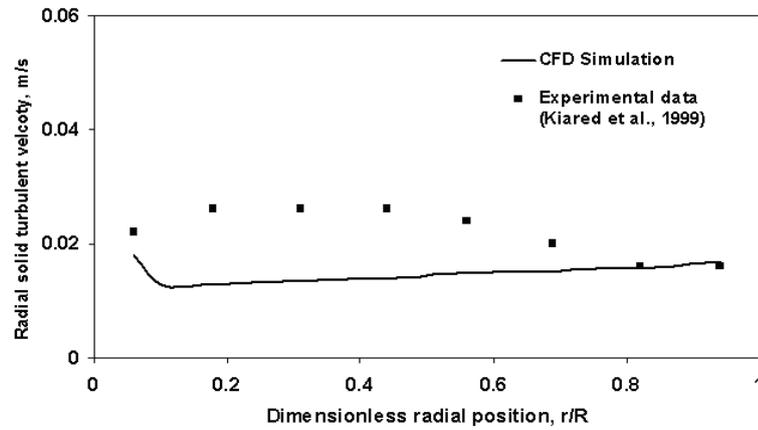
(a) 2s (b) 4s (c) 6s (d) 9s (e) 14s (f) Time average

Figure 5.8. Instantaneous snapshots of solid velocity vectors for gas superficial velocity of 0.069 m/s and liquid superficial velocity of 0.065 m/s

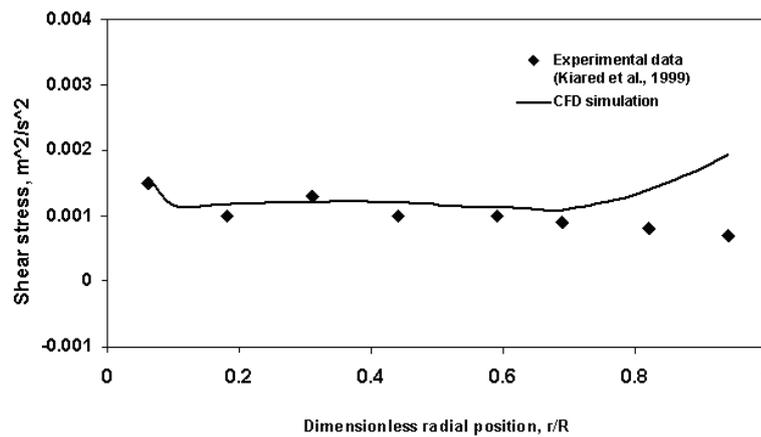
According to Kiared et al. (1999), the flow structure of solids corresponds to the transition regime or vortical–spiral flow regime for gas superficial velocity of 0.069 m/s and a liquid superficial velocity of 0.065 m/s. The flow structure of solids predicted by CFD simulation for these conditions at various time intervals are shown in Figure 5.8. The simulated flow profile shows clearly the vortical–spiral flow regime, which is characterised by a descending flow region, vortical–spiral flow region and central plume region.



(a)



(b)



(c)

Figure 5.9. (a) Axial solid turbulent velocity; (b) radial solid turbulent velocity; (c) shear stress profiles of solid along the radial direction at superficial gas velocity of 0.032 m/s and superficial liquid velocity of 0.065 m/s

CFD Simulation of Gas-Liquid-Solid Fluidised bed Contactor

Figure 5.9(a–c) shows the time and spatially averaged axial and radial solid turbulent fluctuating velocities and shear stress along dimensionless radial position at a superficial gas velocity of 0.032 m/s and a superficial liquid velocity of 0.065 m/s. The particle size is 3 mm and the bubble size is 2 mm. The simulated results are compared with the experimental results of Kiared et al. (1999). It can be observed that the agreement is quite good except at the wall region. It can be seen clearly that the axial turbulent solid velocity is the weak function of radial position and the maximum value occurs almost near the flow reversal radial location whereas the maximum radial solid turbulent fluctuating velocity occurs near the center. Also, the axial turbulent solid velocities are roughly twice that of the corresponding radial components. This is in line with the observations made by Devanathan et al. (1990) in gas–liquid bubble column and Roy et al. (2005) in a liquid–solid riser.

5.4.5. Gas and Liquid Hydrodynamics

The results obtained for the gas and liquid hydrodynamics in three-phase fluidised bed by the present CFD simulation are validated with the reported experimental data of Yu and Kim (1988). The experimental set up of Yu and Kim (1988) is a fluidised bed column of diameter 0.254 m and height 2.5 m. The operating conditions chosen for this simulation are gas superficial velocity of 0.04 m/s; liquid superficial velocity of 0.06 m/s. The solid particle size is 2.3 mm and the gas bubble size is 13 mm. Figure 5.10 shows the comparison of time averaged gas holdup profile along the dimensionless radial direction between CFD simulation and the experimental data of Yu and Kim (1988) at the axial position of 0.325 m. The gas holdup profile predicted by CFD simulation matches closely with the experimental

CFD Simulation of Gas-Liquid-Solid Fluidised bed Contactor

data reported by Yu and Kim (1988) at the center region of the column and slightly varies at the wall region of the column. This may be due to the effect of wall on the gas holdup. The gas hold up profile decreases with increase in radial position.

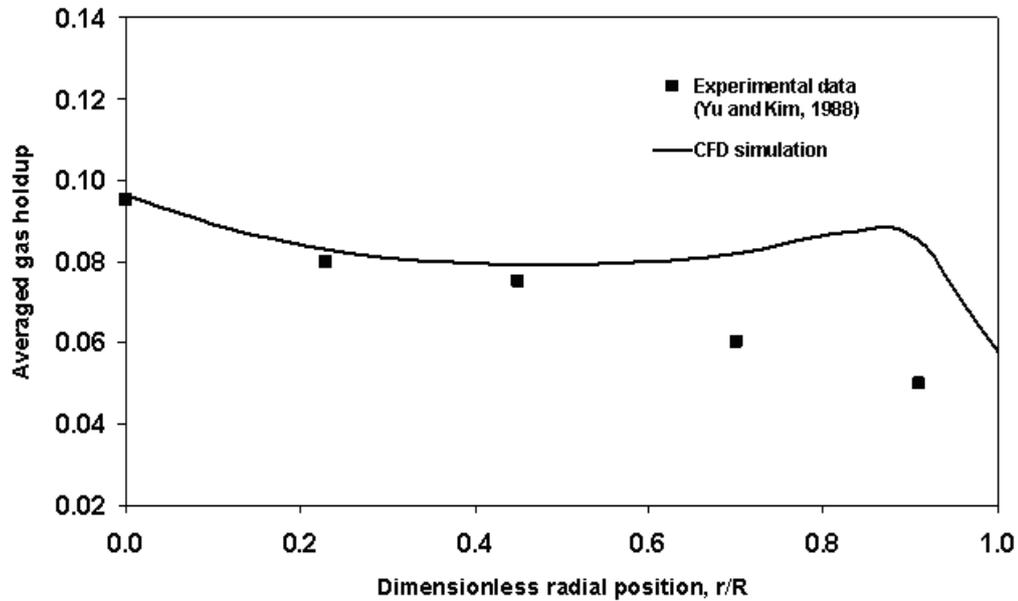


Figure 5.10. Radial distribution of gas holdup at liquid superficial liquid velocity $U_l=0.06$ m/s and gas superficial liquid velocity $U_g=0.04$ m/s at axial position of 0.325 m

Figure 5.11 shows the comparison between the CFD simulation and the experimental data (Yu and Kim, 1988) for bubble velocity profiles along the nondimensional radial direction. The predicted bubble velocity profile matches closely with the experimental data at the wall region of the column and slightly varies at the center region of the column. This may be because the bubbles coalescence leads to larger bubbles at the center region, which have faster rise velocities. This phenomenon can be accommodated only if we assume a bubble size distribution,

CFD Simulation of Gas-Liquid-Solid Fluidised bed Contactor

which is not included in the present CFD simulation. Further, it is observed that the bubble velocity decreases with increase in radial distance.

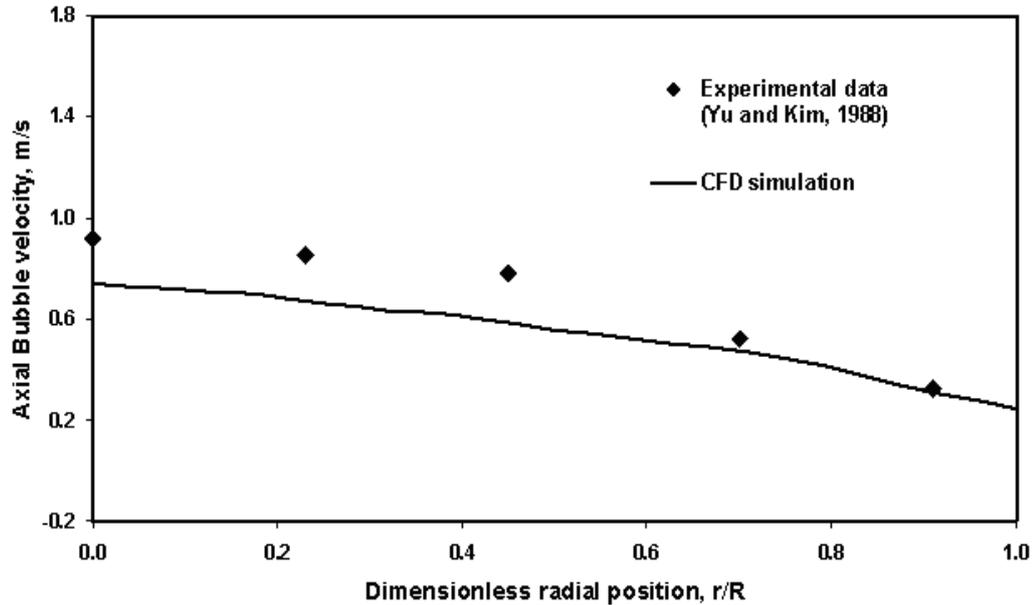


Figure 5.11. Radial distribution of bubble velocity at liquid superficial liquid velocity $U_l=0.06$ m/s and gas superficial liquid velocity $U_g = 0.04$ m/s

The time-averaged liquid velocity profile along the radial direction obtained by CFD simulation along with the experimental data reported by Yu and Kim (2001) is shown in Figure 5.12. The liquid velocity profile predicted by CFD simulation matches closely with the experimental prediction at the wall region of the column and slightly varies at the center region of the column, as in the case of bubble velocity prediction. The liquid velocity is maximum at the center of the column and there is a reverse flow at the wall region of the column. This recirculating flow is induced by the radial nonuniformity of gas phase holdup and bubble rising velocity. The radial location at which the flow direction is changing from upward to downward is around 0.75–0.80 and this value agrees very well with the experimental observation of Yu and Kim (2001).

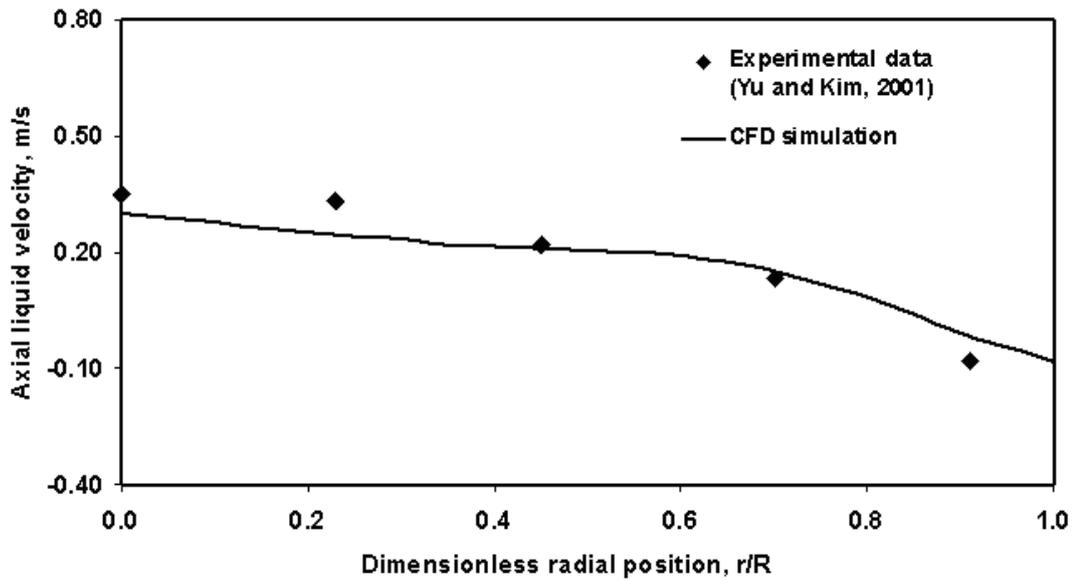


Figure 5.12. Radial distribution of axial liquid velocity at liquid superficial liquid velocity $U_l=0.06$ m/s and gas superficial liquid velocity $U_g = 0.04$ m/s

The flow structure of the gas phase in the gas–liquid–solid fluidised bed predicted by CFD simulation at a gas superficial velocity of 0.04 m/s and a liquid superficial velocity of 0.06 m/s at various time intervals are shown in Figure 5.13. The experimental studies show that for the above operating conditions, the flow regime correspond to that of coalesced bubble flow regime. The simulation results depicted in Figure 5.13 shows a vortical–spiral regime or coalesced flow regime, which is characterised by a descending flow region, vortical–spiral flow region and a central plume region. The present simulation accurately reproduces the central bubble plume region, which moves periodically from side to side of the fluidised bed.

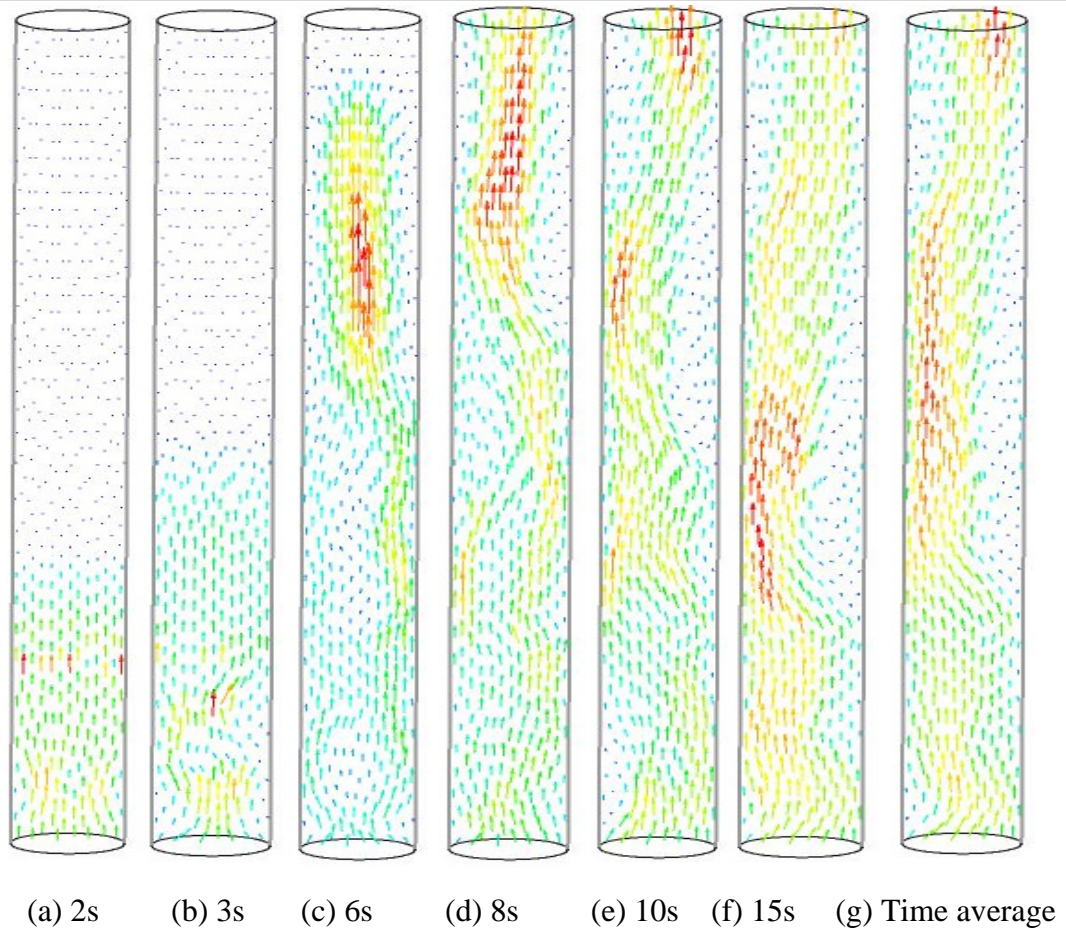


Figure 5.13. Instantaneous snapshots of gas velocity vectors for gas superficial velocity of 0.04 m/s and liquid superficial velocity of 0.06 m/s

5.4.6. Computation of solids mass balance

It is instructive to check the overall mass balance (continuity) of the solids in the fluidised bed column by estimating solid mass flow rate using the predicted flow field of solids by CFD simulation. The predicted flow field of solids shows a single circulation pattern. Hence, the net solid volume flow rate in center region should be equal to the net solid volume flow rate in the wall region. These quantities are represented mathematically as

CFD Simulation of Gas-Liquid-Solid Fluidised bed Contactor

Solid up flow rate in the center region

$$= 2\pi \int_0^{R_i} r \epsilon_s (r) V_z (r) dr \dots\dots\dots(5.39)$$

Solid down flow rate in the wall region

$$= 2\pi \int_{R_i}^R r \epsilon_s (r) V_z (r) dr \dots\dots\dots(5.40)$$

In the above equations, $\epsilon_s (r)$ is the time averaged radial solid holdup profile and $V_z(r)$ is the time averaged axial solid velocity and R_i is the radius of inversion, defined as the point along the radial direction at which the axial solids velocity is zero. The numerical values of the radial profiles of solid holdup and axial solids velocity obtained by CFD simulation for each of the operating conditions is fitted to the functions given by equations 5.41 and 5.42 as proposed by Roy et al. (2005)

$$\epsilon_s (r) = \bar{\epsilon}_s \frac{m + 2}{m + 2 + 2C} \left[1 + C \left(\frac{r}{R} \right)^m \right] \dots\dots\dots(5.41)$$

$$V_z (r) = V_z (0) + \alpha_1 \left(\frac{r}{R} \right)^n - \alpha_2 \left(\frac{r}{R} \right)^{n\alpha_1/\alpha_2} \dots\dots\dots(5.42)$$

where $V_z (0)$ is the centerline axial solids velocity, and m , C , n , α_1 and α_2 are empirical constants. The volumetric solid flow rates computed from equations 5.39 and 5.40 are shown in Table 5.3. The deviation is defined as the ratio of difference between upward and downward solid flow rate to the upward solid flow rate. It can be observed that this ratio is in the range of 8–21%, which is increasing with the increase in the gas superficial velocity. This may be due to the elutriation of solids by the gas phase when the superficial gas velocities are higher.

Table 5.3. Solid mass balance in three-phase fluidised bed

Column Size (m)	Liquid superficial velocity (m/s)	Gas superficial velocity (m/s)	Volumetric flow rate of solid in center (m ³ /s)	Volumetric flow rate of solid in wall (m ³ /s)	Deviation (%)
		0.032	1.34e-05	1.22e-05	9
0.10	0.065	0.069	1.61e-05	1.33e-05	18
		0.11	2.39e-05	1.86e-05	22

5.4.7. Computation of various energy flows

It is informative to investigate the various energy flows into the three-phase fluidised bed and make an order-of-magnitude estimate of the various terms in the energy flows. Extensive work has been carried out by Joshi (2001) to understand the energy transfer mechanism in gas–liquid flows in bubble column reactors. A similar attempt is made in this work.

In gas–liquid–solid fluidised beds, the input energy from the gas and liquid is distributed to the mean flow of the liquid, gas, and the solid phases. Also, a part of the input energy is used for liquid phase turbulence and some part of the energy gets dissipated due to the friction between the liquid and solid phases and the gas and liquid phases. Apart from these energy dissipation factors, some of the other energy losses due to solid fluctuations, collisions between particles, between particles and column wall are also involved in three-phase reactors. Since the present CFD simulation is based on Eulerian–Eulerian approach, these modes of energy dissipation could not be quantified. Hence, these terms are neglected in the energy calculation. In general, the difference between the input and output energy should account for the

CFD Simulation of Gas-Liquid-Solid Fluidised bed Contactor

energy dissipated in the system. Thus, the energy difference in this work is calculated as

$$\begin{aligned} \text{Energy difference} = & \text{Energy entering the fluidised bed } (E_i) - \text{Energy leaving the} \\ & \text{fluidised bed by the liquid and gas phase } (E_{out}) - \text{Energy} \\ & \text{gained by the solid phase } (E_T) - \text{Energy dissipated by the liquid} \\ & \text{phase turbulence } (E_e) - \text{Energy dissipated due to friction at the} \\ & \text{liquid–solid interface } (E_{Bls}) - \text{Energy dissipated due to friction} \\ & \text{at the gas–liquid interface } (E_{Blg}) \dots\dots\dots(5.43) \end{aligned}$$

The corresponding equations for each of these terms are given below:

Energy entering the fluidised bed (E_i) by the incoming liquid and gas

The energy entering the fluidised bed due to the incoming liquid and gas flow is given by

$$E_i = \frac{\pi}{4} D^2 H g (V_l + V_g) (\epsilon_s \rho_s + \epsilon_l \rho_l + \epsilon_g \rho_g) \dots\dots\dots(5.44)$$

where D is the diameter of the column, H is the expanded bed height, V_l is superficial liquid velocity, V_g is the gas superficial velocity, $\epsilon_l, \epsilon_g, \epsilon_s$ are the liquid, gas and solid volume fractions, respectively and ρ_l, ρ_g, ρ_s are the liquid, gas and solid densities, respectively.

Energy leaving the fluidised bed (E_{out}) by the outflowing liquid and gas

The liquid and the gas leaving the bed possess both potential energy and kinetic energy by virtue of its expanded bed height and are given as

$$E_{pl} = \frac{\pi}{4} D^2 H V_l \rho_l g \dots\dots\dots(5.45)$$

CFD Simulation of Gas-Liquid-Solid Fluidised bed Contactor

$$E_{pg} = \frac{\pi}{4} D^2 H V_g \rho_g g \dots\dots\dots(5.46)$$

$$E_{kl} = \frac{1}{2} \rho_l \frac{\pi}{4} D^2 V_l^3 \dots\dots\dots(5.47)$$

$$E_{kg} = \frac{1}{2} \rho_g \frac{\pi}{4} D^2 V_g^3 \dots\dots\dots(5.48)$$

$$E_{out} = E_{pl} + E_{pg} + E_{kl} + E_{kg} \dots\dots\dots(5.49)$$

Energy gained by the solid phase (E_T)

The solid flow pattern in the present study shows a single circulation pattern, as depicted in Figure 5.5. The energy gained by the solids for its upward motion in the center region is the sum of the potential energy and kinetic energy of the solids in the center region and are given by

$$E_{ps} = \rho_s g H \frac{\pi}{4} D_C^2 v_s \dots\dots\dots(5.50)$$

$$E_{ks} = \frac{1}{2} \rho_s \frac{\pi}{4} D_C^2 v_s^3 \dots\dots\dots(5.51)$$

$$E_T = E_{ps} + E_{ks} \dots\dots\dots(5.52)$$

where v_s is the time-averaged solid velocity in the center region, and D_C is the diameter of the center region.

Energy dissipation due to liquid phase turbulence (E_e)

Since k-ε model for turbulence is used in this work, the energy dissipation rate per unit mass is given by the radial and axial variation of ε. Hence, the energy dissipated due to liquid phase turbulence is calculated as

$$E_e = \int_0^R \int_0^H \int_0^{2\pi} \epsilon \, dr \, dz \, d\theta \dots\dots\dots(5.53)$$

CFD Simulation of Gas-Liquid-Solid Fluidised bed Contactor

Energy dissipation at the liquid–solid interface (E_{Bls})

The net rate of energy dissipated between liquid–solid phases is calculated based on the drag force and slip velocity between liquid and solid and is summed over all the particles.

For a single particle at an infinite expanded state ($\epsilon = 1$), the interaction can be represented as the sum of drag and buoyancy forces. Hence, the force balance for a single particle is

$$mg = \text{drag} + \text{buoyancy}$$

$$\frac{\pi}{6}d_p^3(\rho_s - \rho_l) = C_d \frac{\pi}{4}d_p^2(U_1 - U_s)|U_1 - U_s| \frac{\rho_l}{2} \dots\dots\dots(5.54)$$

For multiple particles, the above equation can be written as

$$\frac{\pi}{6}d_p^3(\rho_s - \rho_l)f(\epsilon) = C_d \frac{\pi}{4}d_p^2(U_1 - U_s)|U_1 - U_s| \frac{\rho_l}{2} \dots\dots\dots(5.55)$$

Wen and Yu (1966) presented the above equation in the form of

$$\frac{\pi}{6}d_p^3(\rho_s - \rho_l)(1 - \epsilon_s)^{4.78} = C_d \frac{\pi}{4}d_p^2(U_1 - U_s)|U_1 - U_s| \frac{\rho_l}{2} \dots\dots\dots(5.56)$$

The total drag force is thus equal to the drag force for single particle multiplied by the total number of particles namely,

$$F_T = n_p F_D \dots\dots\dots(5.57)$$

$$F_T = \frac{\pi}{4} \frac{D^2 H \epsilon_s}{\pi/6 d_p^3} \frac{\pi}{6} d_p^3 (\rho_s - \rho_l) (1 - \epsilon_s)^{4.78} \dots\dots\dots(5.58)$$

$$F_T = \frac{\pi}{4} D^2 H \epsilon_s g (\rho_s - \rho_l) (1 - \epsilon_s)^{4.78} \dots\dots\dots(5.59)$$

The net rate of energy dissipated between liquid–solid phase is computed from equation (5.59) as

CFD Simulation of Gas-Liquid-Solid Fluidised bed Contactor

$$E_{Bls} = \frac{\pi}{4} D^2 H \epsilon_s g (\rho_s - \rho_l) (1 - \epsilon_s)^{4.78} V_s \dots\dots\dots(5.60)$$

where V_s is the slip velocity between liquid and solid phase and ρ_s is the solid density.

Energy dissipation at the gas-liquid interface (E_{Bgl})

The net rate of energy dissipated between gas-liquid phases is calculated based on the total drag force between gas and liquid.

Force balance for single bubble in liquid-solid medium

$$mg = \text{buoyancy} + \text{drag}$$

$$\frac{\pi}{6} d_b^3 g \rho_g = \frac{\pi}{6} d_b^3 g (\rho_s \epsilon_s + \rho_l \epsilon_l) + F_D \dots\dots\dots(5.61)$$

$$F_D = \frac{\pi}{6} d_b^3 g (\rho_c - \rho_g) \dots\dots\dots(5.62)$$

where $\rho_c = \rho_s \epsilon_s + \rho_l \epsilon_l$ is the slurry density

For swarm of bubbles, the effective drag force is

$$F_D = \frac{\pi}{6} d_b^3 g (\rho_c - \rho_g) (1 - \epsilon_g) \dots\dots\dots(5.63)$$

The total drag force is thus equal to the drag force for single bubble multiplied by the total number of bubbles namely

$$F_T = n_b F_D \dots\dots\dots(5.64)$$

$$F_T = \frac{\pi}{4} \frac{D^2 H \epsilon_g}{\pi / 6 d_b^3} \frac{\pi}{6} d_b^3 g (\rho_c - \rho_{gl}) (1 - \epsilon_g) \dots\dots\dots(5.65)$$

$$F_T = \frac{\pi}{4} D^2 H \epsilon_g g (\rho_c - \rho_{gl}) (1 - \epsilon_g) \dots\dots\dots(5.66)$$

The net rate of energy dissipated between gas-liquid phase is

$$E_{Bgl} = \frac{\pi}{4} D^2 H \epsilon_g g (\rho_c - \rho_g) (1 - \epsilon_g) V_{bs} \dots\dots\dots(5.67)$$

where V_{bs} is the slip velocity between gas and liquid phase and ρ_c is the slurry density.

CFD Simulation of Gas-Liquid-Solid Fluidised bed Contactor

The values calculated for these terms along with the energy difference (in terms of %) are presented in Table 5.4. It can be observed that the energy difference is in the range of 10–19% for the case of fluidised bed column of diameter 0.1 m, and is in the range of 1–3% for the fluidised bed column of diameter 0.254 m. It can be noted that the energy difference are less for larger fluidised bed column. This can be attributed to the fact that the energy losses due to particle–particle collisions and particle–wall collisions are much lower for larger fluidised bed columns than for smaller fluidised bed columns. It can also be seen that the energy dissipation rate at the gas–liquid interface is more compared to other dissipation mechanisms and shows around 20% of the energy input, which is in agreement with literature (Joshi, 1980).

Table 5.4. Various energy flows in three-phase fluidised bed

Column diameter (m)	U_g (m/s)	Particle size (glass beads)	E_i (Eqn. 5.44)	E_{out} (Eqn. 5.49)	E_T (Eqn. 5.52)	E_e (Eqn. 5.53)	E_{Bls} (Eqn. 5.60)	E_{Bgl} (Eqn. 5.67)	Difference (%)
	0.032	3 mm	5.46	2.403	0.7206	0.06	0.125	1.31	15.2
0.1	0.069	3 mm	7.79	2.805	0.844	0.08	0.20	2.4	18.7
	0.11	3 mm	10.39	3.208	1.606	0.48	0.25	2.86	19.0
0.254	0.01	2.3 mm	31.45	16.658	10.422	0.49	0.54	2.84	1.6
	0.04	2.3 mm	47.3	19.05	14.704	0.98	0.8	10.28	3.2

5.5. Conclusions

CFD simulation of hydrodynamics of gas–liquid–solid fluidised bed is carried out for different operating conditions by employing the Eulerian multi-fluid approach. The CFD simulation results showed good agreement with experimental data for solid phase hydrodynamics in terms of mean and turbulent velocities reported by Kiared et al. (1999) and for gas and liquid phase hydrodynamics in terms of phase velocities and holdup reported by Yu and Kim (1988, 2001). It can be seen clearly from the validation that multi-fluid Eulerian approach is capable of predicting the overall performance of gas–liquid–solid fluidised bed. The predicted flow pattern of the averaged solid velocity profile shows a higher upward velocity at the center region and a lower downward velocity at the wall region of the column. The CFD simulation exhibits a single solid circulation cell for all the operating conditions, which is consistent with the observations reported by various authors. Based on the predicted flow field by CFD model, the focus has been on the computation of the solid mass balance and computation of various energy flows in fluidised bed reactors. The result obtained shows a deviation in the range of 8–21% between center and wall region for solid flow balance calculations. In the computation of energy flows, the energy difference observed is in the range of 10–19% for the case of fluidised bed column of diameter 0.1 m, and in the range of 1–3%, for the fluidised bed column of diameter 0.254 m.

Chapter 6

CFD Simulation of Solid Suspension in Gas-Liquid-Solid Mechanically Agitated Contactor

6.1. Introduction

Mechanically agitated reactors involving gas, liquid, and solid phases have been widely used in chemical industries, mineral processing industries, wastewater treatment, and biochemical industries. This is one of the most widely used unit operations because of its ability to provide excellent mixing and contact between the phases. Despite their widespread use, the design and operation of these agitated reactors remain a challenging problem because of the complexity encountered due to the three-dimensional (3D) circulating and turbulent multiphase flow in the reactor. An important consideration in the design and operation of these agitated reactors is the determination of the state of full suspension, at which point no particles reside on the vessel bottom for a long time. Such a determination is critical to enhance the performance of the reactor, because until such a condition is achieved, the total surface area of the particles is not efficiently utilized.

Hence, it is essential to determine the minimum impeller speed required for the state of complete off-bottom suspension of the solids, called the critical impeller speed. It is denoted by N_{js} for solid suspension in the absence of gas and by N_{jsg} for solid suspension in the presence of gas. A considerable amount of research work has been carried out to determine the critical impeller speed starting with the pioneering work of Zwietering (1958). Since then, numerous papers on determination of critical impeller speed for different operating conditions and different types of impellers have been published (Bohnet and Niesmak, 1980; Chapman et al., 1983; Kraume, 1992) for liquid–solid stirred reactors, and a few of them (Zlokarnik and Judat, 1969; Chapman et al., 1983; Warmoeskerken et al., 1984; Nienow et al., 1985; Bujalski et al., 1988; Wong et al., 1987; Frijlink et al., 1990; Rewatkar et al., 1991; Dylag and Talaga,

1994; Dutta and Pangarkar, 1995; Pantula and Ahmed, 1998; Zhu and Wu, 2002) have been extended toward the development of correlations for the critical impeller speed for gas–liquid–solid stirred reactors.

According to the literature, in general, N_{jsg} is always greater than N_{js} . Zlokarnik and Judat (1969) have reported that approximately 30% higher impeller speed over N_{js} is required to ensure the resuspension of solid, when gas is introduced. This is due to the reduction in impeller pumping capacity. The reason for the reduction in impeller power in three-phase agitated reactors system has been extensively studied in the literature. Chapman et al. (1983) explained the decreased liquid pumping capacity and power input on the basis of the sedimentation phenomena. Warmoeskerken et al. (1984) explained the decrease in impeller power due to the formation of gas-filled cavities behind the impeller blades. Rewatkar et al. (1991) reported that the reduction in the impeller power in the three-phase system is due to the formation of solid fillet at the center and along the periphery of the vessel bottom and the formation of gas-filled cavities behind the impeller. Table 6.1 shows the empirical correlations developed by various authors for critical impeller speed for just suspended state of solids in the presence of gas.

The critical impeller speed for gas–liquid–solid mechanically agitated reactors depend on several parameters, such as particle settling velocity, impeller design, impeller diameters and sparger design, and its location. The selection of impeller type is an important consideration for simultaneous solid suspension and gas dispersion with minimum power requirement in such reactors. In the literature, various authors (Chapman et al., 1983; Frijlink et al., 1990; Rewatkar et al., 1991; Pantula and Ahmed, 1998) have studied the performance of different types of impellers for a solid

CFD Simulation of Gas-Liquid-Solid Mechanically Agitated Contactor

suspension in a stirred tank for various ranges of operating conditions and concluded that the pitched blade turbine with downward pumping (PBTD) is more favorable at lower gassing rates and disc turbine (DT) and pitched blade turbine with upward pumping (PBTU) are more favorable at higher gassing rate.

Although the available correlations in the literature are of great importance from an operational view-point, they do not provide a clear understanding of the physics underlying the system. From a physical standpoint, the state of suspension of solid particles in the reactor is completely governed by the hydrodynamics and turbulence prevailing in the reactor. Only a few studies (Guha et al., 2007; Spidla et al., 2005; Aubin et al., 2004) have been made to understand the complex hydrodynamics of such complicated stirred reactors. Although much experimental effort has been focused on developing correlations for just-suspension speed, a systematic experimental study to characterise the solid hydrodynamics in stirred slurry reactors can hardly be found in the literature.

For this reason, computational fluid dynamics (CFD) has been promoted as a useful tool for understanding multiphase reactors (Dudukovic et al., 1999) for precise design and scale up. The RANS-based CFD approach is the most widely used approach for the multiphase phase flow simulation of such reactors. In the literature, CFD based simulations have been used to predict the critical impeller speed for a solid suspension in a liquid–solid stirred tank reactor (Bakker et al., 1994; Micale et al., 2000; Barrue et al., 2001; Sha et al., 2001; Kee and Tan, 2002; Montante and Magelli et al., 2005; Khopkar et al., 2006; Guha et al., 2008) by employing the Eulerian–Eulerian approach, and this prediction have been extended to the case of gas–liquid–solid stirred tank reactors. Recently Murthy et al. (2007) carried out CFD

CFD Simulation of Gas-Liquid-Solid Mechanically Agitated Contactor

simulations for three-phase stirred suspensions. The effect of tank diameter, impeller diameter, type, location, size, solid loading and superficial gas velocity on the critical impeller speed was investigated by them using the standard deviation approach. The solid loading in their study varied from 2–15% by weight. But most of the industrial applications, especially hydrometallurgical applications, involve high density particles with high concentration. Moreover, it has been reported in the literature (Khopkar et al., 2006; van der Westhuizen and Deglon, 2007) that it is difficult to quantify the critical impeller just based on the standard deviation approach alone.

Table 6.1. Empirical correlations in the literature for the critical impeller speed in the presence of gas

References	Experimental system used	Empirical correlation
Chapman et al.(1983)	tank diameter = 0.29–1.83 m, Impeller type = DT, PBSD and PBTU and marine propeller impeller clearance = T/4 solid loading = 0.34–50 wt % particle density = 1050– 2900 kg /m ³ particle diameter = 100–2800 μm air flow rate = 0–32 mm/s sparger type = ring, pipe, conical and concentric rings	$\Delta N_{js} = N_{jsg} - N_{js}$ $= kQ_v$ where k=0.94
Nienow et al.(1985)	tank diameter = 0.45 m impeller type = Disc turbine impeller diameter = 0.225 m impeller clearance = 0.1125 m particle type = glass beads particle diameter = 440–530 μm	$\Delta N_{js} = N_{jsg} - N_{js}$ $= kQ_v$ where k=0.94
Wong et al.(1987)	tank diameter = 0.29 m impeller type = Propeller, Disc and Pitched turbine impeller diameter = 0.06–0.26 m impeller clearance = 0.051– 0.076 m particle density = 2514–8642 kg /m ³ particle diameter = 200–1200 μm	$\Delta N_{js} = N_{jsg} - N_{js}$ $= kQ_v$ where k=2.03 for DT, k=4.95 for PBSD

CFD Simulation of Gas-Liquid-Solid Mechanically Agitated Contactor

	air flow rate	= 0–2 vvm		
Rewatkar et al.(1991)	tank diameter	= 0.57–1.5 m,	$\Delta N_s = 132.7 V_{s\infty}^{0.5} D^{-1.67} T V_g$ where $\Delta N_s = N_{jsg} - N_{sp}$ N_{sp} = critical impeller speed for solid suspension in the presence of sparger N_{jsg} = critical impeller speed for suspension in gas-liquid-solid system $V_{s\infty}$ = terminal settling velocity of particle	
	impeller type	= RT, PBTB and PBTU		
	impeller diameter	= 0.175T–0.58T m		
	impeller clearance	= T/3		
	particle diameter	= 100–2000 μ m		
	air flow rate	= 0–32 mm/s		
	Solid loading	= 0.34–50 wt %		
	sparger type	= ring, pipe, conical and concentric rings		
Dylag et al.(1994)	tank diameter	= 0.3 m and ellipsoidal bottom	For DT	
	impeller type	= DT and PBTB	$\frac{N_{jsg} D^2 \rho_c}{\eta_c} = 18.95 \times 10^4 \left(\frac{v_g D \rho_g}{\eta_g} \right)^{0.15} X^{0.15} \left(\frac{d_p}{D} \right)^{0.20}$	
	impeller clearance	= 0.5D	For PBTB	
	particle density	= 2315 kg /m ³	$\frac{N_{jsg} D^2 \rho_c}{\eta_c} = 17.55 \times 10^4 \left(\frac{v_g D \rho_g}{\eta_g} \right)^{0.31} X^{0.15} \left(\frac{d_p}{D} \right)^{0.20}$	
	particle diameter	= 0.248–0.945 mm		
	air flow rate	= 1.5–22.5 mm/s		
	solid loading	= 2–30 wt %		

Hence, the objective of this work is to carry out the CFD simulation based on the Eulerian multi-fluid approach for the prediction of the critical impeller speed for high density solid particles with solid loading in the range of 10–30% by weight. CFD Simulations were carried out using the commercial package ANSYS CFX-10. Since any CFD simulation has to be validated first, the CFD simulations have been validated with those reported in the literature (Guha et al., 2007; Spidla et al., 2005; Aubin et al., 2004) for solid–liquid and gas–liquid agitated reactors. After the validation, the CFD simulations have been extended for gas–liquid–solid mechanically agitated contactor to study the effects of impeller design, impeller speed, particle size and gas flow rate on the prediction of critical impeller speed based on both the standard deviation approach and cloud height criteria, and the simulation results were compared with our experimental results.

6.2. Experimental Methodology

The mechanically agitated contactor that was used to carry out the experiments is shown in Figure 6.1. It was a baffled cylindrical tank with an internal diameter of 250 mm that was transparent so that the suspension of solids was easily visible. The bottom of the tank was elliptical in shape. The liquid depth was equal to the tank diameter. Two types of impellers were employed viz., six-bladed Rushton turbine of diameter 100 mm and four-bladed 45° pitched blade turbine of diameter 125 mm. The impeller off-bottom clearance is 62.5 mm. The vessel was fitted with four vertical baffles with a width of 25 mm and its height was equal to the height of liquid level in the contactor. The dimensions of the impellers chosen for this work are based on the observation of Chapman et al. (1983) and Pantula and Ahmed (1998) that the performance in terms of suspension quality at higher gas rates are much improved if larger diameter is employed. Similarly low clearance has been shown to enhance particle suspension capability (Nienow, 1968). For this experimental study, water ($\rho = 1000 \text{ kg/m}^3$) is used as the liquid phase, and ilmenite particles ($\rho = 4200 \text{ kg/m}^3$) in the size range of 120–250 μm is used as the solids phase. The gas phase considered was air and was introduced into the reactor by a pipe sparger with diameter of 10 mm, which is placed at a clearance of 25 mm from the center of the impeller. Fine stainless steel of wire mesh (0.2 mm opening) was wound around the outlet of the sparger. This was to prevent the suction of fines into the sparger. Agitation was carried out using a variable-speed DC motor and the speed of the agitation was noted using a tachometer. Power consumptions were computed using measured values of current and voltages. Other details of the present experiment study are available in the earlier published work (Geetha and Surender, 1997).

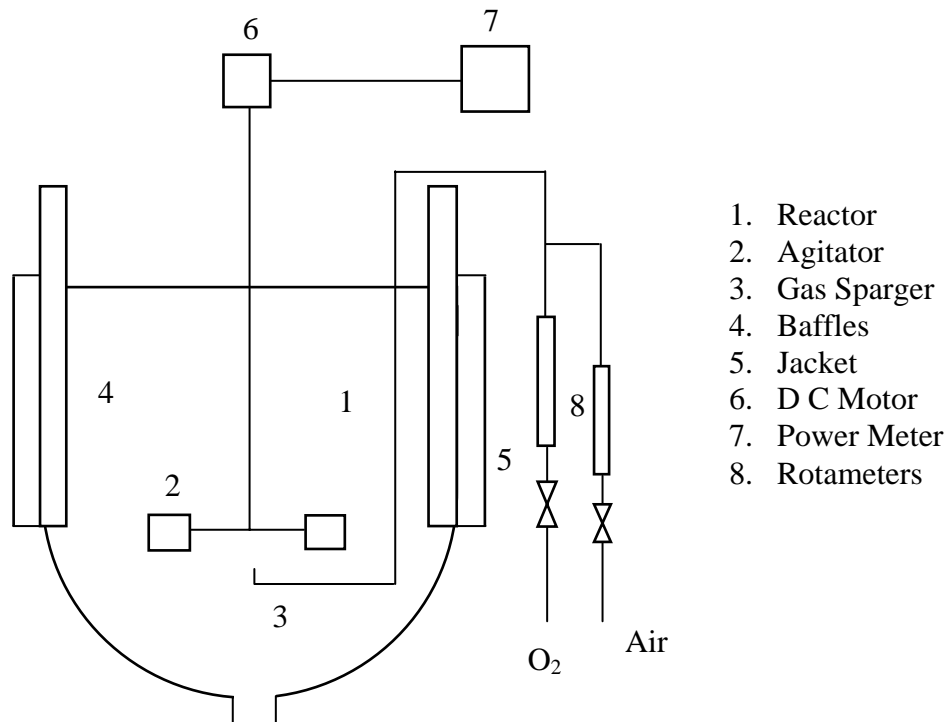


Figure 6.1. Experimental setup used for the present study

The experiments were carried out with different impeller types and different impeller speeds to determine the quality of solid suspension. The critical impeller speed of solid suspension were determined experimentally for four different solid loading rates, *viz.*, 10, 20, 30 and 40 % by weight. The critical impeller speed for solid suspension is predicted by observing visually that the solids remain at the tank bottom for not more than 2 seconds (Zwietering, 1958). Since visual method is reported to be not very accurate for higher solid loading rates, an alternate method based on the measurement of variation in impeller power consumption with respect to the impeller speed was also used to determine the critical impeller speed. The same method was adapted by Rewatkar et al. (1991) for determination of N_{js} and N_{jsg} for their reactors where the diameter of tank was ranging from 0.57 m to 1.5 m. In this

CFD Simulation of Gas-Liquid-Solid Mechanically Agitated Contactor

method, the graph of power number versus Reynolds number is plotted. Then the minimum value of the curve is taken as the critical impeller speed. This is shown in Figure 6.2.

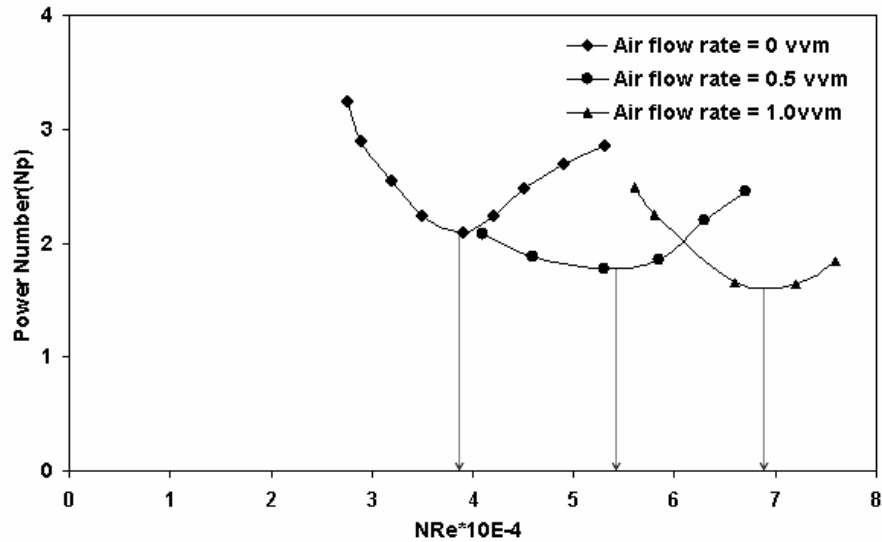


Figure 6.2. Prediction of critical impeller speed from the graphical plot of N_{Re} vs. N_p

and the value obtained for critical impeller speed by visual method, is also shown in Table 6.2. The error percentage was calculated as

$$\text{Error \%} = \left(\frac{\text{CIS}_{\text{visual}} - \text{CIS}_{\text{graphical}}}{\text{CIS}_{\text{visual}}} \right) \times 100$$

It can be observed that the percentage of error is in the range of 3–6% for various operating conditions. Since the deviation is not much between both the approaches and visual method is much easier, this method is used for the determination of critical impeller speed for further experimental conditions.

Table 6.2. Values of critical impeller speed

Particle size (μm)	Air flow rate (<i>vvm</i>)	Critical impeller speed, RPM		% of Error
		Visual method	Graphical method	
230	0	330	315	4.5
	0.5	428	415	3.0
	1.0	529	559	5.6

6.3. CFD Modeling

6.3.1. Model Equations

The gas–liquid–solid flows in mechanically agitated contactor are simulated using Eulerian multi-fluid approach. Each phase is treated as different continua that interact with other phases everywhere in the computational domain. The motion of each phase is governed by respective Reynolds averaged mass and momentum conservation equations. The governing equations for each phase are given below:

Continuity equation:

$$\frac{\partial}{\partial t}(\epsilon_k \rho_k) + \nabla \cdot (\rho_k \epsilon_k \bar{u}_k) = 0 \dots\dots\dots(6.1)$$

where ρ_k is the density and ϵ_k is the volume fraction of phase $k = g$ (gas), s (solid), l (liquid) and the volume fraction of the three phases satisfy the following condition:

$$\epsilon_l + \epsilon_g + \epsilon_s = 1 \dots\dots\dots(6.2)$$

Momentum equations:

Gas phase (dispersed fluid phase)

$$\frac{\partial}{\partial t}(\rho_g \cdot \epsilon_g \cdot \bar{u}_g) + \nabla \cdot (\rho_g \cdot \epsilon_g \cdot \bar{u}_g \bar{u}_g) = -\epsilon_g \cdot \nabla P + \nabla \cdot (\epsilon_g \mu_{\text{eff},g} [\nabla \bar{u}_g + (\nabla \bar{u}_g)^T]) + \rho_g \cdot \epsilon_g \cdot \bar{g} - \bar{F}_{D,lg}$$

.....(6.3)

Liquid phase (continuous phase)

$$\frac{\partial}{\partial t}(\rho_l \cdot \epsilon_l \cdot \bar{u}_l) + \nabla \cdot (\rho_l \cdot \epsilon_l \cdot \bar{u}_l \bar{u}_l) = -\epsilon_l \cdot \nabla P + \nabla \cdot (\epsilon_l \mu_{\text{eff},l} [\nabla \bar{u}_l + (\nabla \bar{u}_l)^T]) + \rho_l \cdot \epsilon_l \cdot \bar{g} + \bar{F}_{D,lg} + \bar{F}_{D,ls} + \bar{F}_{TD}$$

.....(6.4)

Solid phase (dispersed solid phase)

$$\frac{\partial}{\partial t}(\rho_s \cdot \epsilon_s \cdot \bar{u}_s) + \nabla \cdot (\rho_s \cdot \epsilon_s \cdot \bar{u}_s \bar{u}_s) = -\epsilon_s \cdot \nabla P - \nabla P_s + \nabla \cdot (\epsilon_s \mu_{\text{eff},s} [\nabla \bar{u}_s + (\nabla \bar{u}_s)^T]) + \rho_s \cdot \epsilon_s \cdot \bar{g} - \bar{F}_{D,ls} - \bar{F}_{TD}$$

.....(6.5)

where P is the pressure, which is shared by all the three phases, μ_{eff} is the effective viscosity. The second term on the RHS of solid phase momentum equation (6.5) accounts for additional solids pressure which arise due to solids collision and the last term (F_D) in all the momentum equations (6.3)–(6.5) represent the drag force that arise due to the momentum exchange mechanism between the different phases.

6.3.2. Interphase momentum transfer

There are various interaction forces such as the drag force, the lift force and the added mass force etc. during the momentum exchange between the different phases. But the main interaction force is due to the drag force caused by the slip between the different phases. Recently, Khopkar et al. (2003, 2005) studied the influence of different interphase forces and reported that the effect of the virtual mass force is not significant in the bulk region of agitated reactors and the magnitude of the

CFD Simulation of Gas-Liquid-Solid Mechanically Agitated Contactor

Basset force is also much smaller than that of the inter-phase drag force. Further they also reported that the turbulent dispersion terms are significant only in the impeller discharge stream. Very little influence of the virtual mass and lift force on the simulated solid holdup profiles was also reported by Ljungqvist and Rasmuson (2001). Hence based on their recommendations and also to reduce the computational time, only the interphase drag force is considered in this work. In our CFD simulation, both the gas and the solid phases are treated as dispersed phases and the liquid phase is treated as continuous. Hence the drag force exerted by the dispersed phase on the continuous phase is calculated as follows:

The drag force between the liquid and solid phases is represented by the equation

$$\vec{F}_{D,ls} = C_{D,ls} \frac{3}{4} \rho_l \frac{\epsilon_s}{d_p} |\vec{u}_s - \vec{u}_l| (\vec{u}_s - \vec{u}_l) \dots\dots\dots(6.6)$$

where the drag coefficient proposed by Brucato et al. (1998) is used.

$$\frac{C_{D,ls} - C_{D0}}{C_{D0}} = 8.67 \times 10^{-4} \left(\frac{d_p}{\lambda} \right)^3 \dots\dots\dots(6.7)$$

where, d_p is the particle size and λ is the Kolmogorov length scale, C_{D0} is the drag coefficient in stagnant liquid which is given as

$$C_{D0} = \frac{24}{Re_p} \left(1 + 0.15 Re_p^{0.687} \right) \dots\dots\dots(6.8)$$

where Re_p is the particle Reynolds number.

The drage force between the gas and liquid phases is represented by the equation

$$\vec{F}_{D,lg} = C_{D,lg} \frac{3}{4} \rho_l \frac{\epsilon_g}{d_b} |\vec{u}_g - \vec{u}_l| (\vec{u}_g - \vec{u}_l) \dots\dots\dots(6.9)$$

CFD Simulation of Gas-Liquid-Solid Mechanically Agitated Contactor

where the drag coefficient exerted by the dispersed gas phase on the liquid phase is obtained by the modified Brucato drag model (Khopkar et al., 2003), which accounts for interphase drag by microscale turbulence and is given by

$$\frac{C_{D,lg} - C_D}{C_D} = 6.5 \times 10^{-6} \left(\frac{d_p}{\lambda} \right)^3 \dots\dots\dots(6.10)$$

where C_D is the drag coefficient of single bubble in a stagnant liquid and is given by

$$C_D = \text{Max} \left(\frac{24}{\text{Re}_b} \left(1 + 0.15 \text{Re}_b^{0.687} \right), \frac{8}{3} \frac{\text{Eo}}{\text{Eo} + 4} \right) \dots\dots\dots(6.11)$$

where Eo is Eotvos number, Re_b is the bubble Reynolds number and they are given by

$$\text{Re}_b = \frac{|\bar{u}_l - \bar{u}_g| d_b}{\nu_l} \dots\dots\dots(6.12)$$

$$\text{Eo} = \frac{g(\rho_l - \rho_g) d_b^2}{\sigma} \dots\dots\dots(6.13)$$

The only other non drag force considered in the present work is of turbulent dispersion. This turbulent dispersion force is the result of the turbulent fluctuations of liquid velocity which approximates a diffusion of the dispersed phase from higher region to lower region. The importance of modeling of turbulent dispersion in liquid–solid stirred tank is also highlighted in the literature (Ljungqvist and Rasmuson, 2001; Barrue et al., 2001). The following equation for the turbulent dispersion force derived by Lopez de Bertodano (1992) is used for the present simulation and is given by

$$\vec{F}_{TD} = -C_{TD} \rho_l k_1 \nabla \epsilon_1 \dots\dots\dots(6.14)$$

where C_{TD} is a turbulent dispersion coefficient, and is taken as 0.1 for the present investigation.

6.3.3. Closure law for turbulence:

In the present study, the standard k-ε turbulence model for single phase flows has been extended for turbulence modeling of three phase flows in stirred reactors. The corresponding values of k and ε are obtained by solving the following transport equations for the turbulence kinetic energy and turbulence dissipation rate:

$$\frac{\partial(\epsilon_1 \rho_1 k_1)}{\partial t} + \nabla \cdot \left(\epsilon_1 \left(\rho_1 \bar{u}_1 k_1 - \left(\mu + \frac{\mu_{tl}}{\sigma_k} \right) \Delta k_1 \right) \right) = \epsilon_1 (P_1 - \rho_1 \epsilon_1) \quad \dots\dots\dots(6.15)$$

$$\frac{\partial(\epsilon_1 \rho_1 \epsilon_1)}{\partial t} + \nabla \cdot \left(\epsilon_1 \rho_1 \bar{u}_1 \epsilon_1 - \left(\mu + \frac{\mu_{tl}}{\sigma_\epsilon} \right) \Delta \epsilon_1 \right) = \epsilon_1 \frac{\epsilon_1}{k_1} (C_{\epsilon 1} P_1 - C_{\epsilon 2} \rho_1 \epsilon_1) \quad \dots\dots\dots(6.16)$$

where $C_{\epsilon 1}=1.44$, $C_{\epsilon 2}=1.92$, $\sigma_k=1.0$, $\sigma_\epsilon=1.3$ and P_1 , the turbulence production due to viscous and buoyancy forces, is given by

$$P_1 = \mu_{tl} \nabla \bar{u}_1 \cdot (\nabla \bar{u}_1 + \nabla \bar{u}_1^T) - \frac{2}{3} \nabla \cdot \bar{u}_1 (3\mu_{tl} \nabla \cdot \bar{u}_1 + \rho_1 k_1) \quad \dots\dots\dots(6.17)$$

For the continuous phase (liquid phase) the effective viscosity is calculated as

$$\mu_{eff,1} = \mu_1 + \mu_{T,1} + \mu_{tg} + \mu_{ts} \quad \dots\dots\dots(6.18)$$

where μ_1 is the liquid viscosity, $\mu_{T,1}$ is the liquid phase turbulence viscosity or shear induced eddy viscosity, which is calculated based on the k-ε model as

$$\mu_{T,1} = c_\mu \rho_1 \frac{k^2}{\epsilon} \quad \dots\dots\dots(6.19)$$

μ_{tg} and μ_{ts} represent the gas and solid phase induced turbulence viscosity respectively and are given by

$$\mu_{tg} = c_{\mu p} \rho_1 \epsilon_g d_b \left| \bar{u}_g - \bar{u}_1 \right| \quad \dots\dots\dots(6.20)$$

$$\mu_{ts} = c_{\mu p} \rho_1 \epsilon_s d_p \left| \bar{u}_s - \bar{u}_1 \right| \quad \dots\dots\dots(6.21)$$

where $C_{\mu p}$ has a value of 0.6.

For gas and solid phases the respective effective viscosities are calculated as

$$\mu_{\text{eff, g}} = \mu_{\text{g}} + \mu_{\text{T, g}} \dots\dots\dots(6.22)$$

$$\mu_{\text{eff, s}} = \mu_{\text{s}} + \mu_{\text{T, s}} \dots\dots\dots(6.23)$$

where $\mu_{\text{T,g}}$ and $\mu_{\text{T,s}}$ are the turbulence viscosity of gas and solid phases respectively.

The turbulent viscosity of the gas phase and the solids phase is related to the turbulence viscosity of the liquid phase and are given by equations (6.24) and (6.25)

(Jakobsen et al., 1997)

$$\mu_{\text{T,g}} = \frac{\rho_{\text{g}}}{\rho_{\text{l}}} \mu_{\text{T,l}} \dots\dots\dots(6.24)$$

$$\mu_{\text{T,s}} = \frac{\rho_{\text{s}}}{\rho_{\text{l}}} \mu_{\text{T,l}} \dots\dots\dots(6.25)$$

6.3.4. Closure law for solids pressure

The solids phase pressure gradient results from normal stresses resulting from particle–particle interactions, which become very important when the solid phase fraction approaches the maximum packing. This solid pressure term is defined based on the concept of elasticity, which is described as a function of elasticity modulus and solid volume fraction. The most popular constitutive equation for solids pressure as given by Gidaspow (1994) is

$$\nabla P_{\text{s}} = G(\epsilon_{\text{s}}) \nabla \epsilon_{\text{s}} \dots\dots\dots(6.26)$$

where $G(\epsilon_{\text{s}})$ is the elasticity modulus and it is given as

$$G(\epsilon_{\text{s}}) = G_0 \exp(c(\epsilon_{\text{s}} - \epsilon_{\text{sm}})) \dots\dots\dots(6.27)$$

as proposed by Bouillard et al. (1989), where G_0 is the reference elasticity modulus, c is the compaction modulus and ϵ_{sm} is the maximum packing parameter.

CFD Simulation of Gas-Liquid-Solid Mechanically Agitated Contactor

Table 6.3. Tank design parameters and physical properties

Reference	Impeller type	Geometry	Physical Properties	Operating conditions
Guha et al.(2007)	6-DT	T=H=0.2 m D/T=1/3, C/T=1/3	Liquid: $\rho = 1000 \text{ kg/m}^3$, Solid: $\rho = 2500 \text{ kg/m}^3$, $d_p = 300 \mu\text{m}$	Solid conc. =7 vol% $N_{js}=1200 \text{ rpm}$
Spidla et al.(2005)	6-PBTD	T=H=1.0 m D/T=1/3, C/T=1/3	Liquid: $\rho = 1000 \text{ kg/m}^3$, Solid: $\rho = 2500 \text{ kg/m}^3$, $d_p = 350 \mu\text{m}$	Solid conc. =10 vol% $N_{js}= 267 \text{ rpm}$
Aubin et al.(2004)	6-PBTD and 6-PBTU	T= H= 0.19 m, C=T/3 D=T/3	Liquid: $\rho=1000 \text{ kg/m}^3$, Gas: Air	$N= 300 \text{ rpm}$
Our experiment	6-DT and 4-PBTD	T=H=0.25 m For DT, D = 0.1m, For PBTD, D=0.125 m C/T=0.0625 m	Liquid: $\rho = 1000 \text{ kg/m}^3$, Solid: $\rho = 4200 \text{ kg/m}^3$, $d_p=125, 180, 230 \mu\text{m}$ Gas: Air	Solid conc. =30 wt% $N_{js} = 330\text{--}520 \text{ rpm}$ Air flow = 0–1.0 vvm

6.4. Numerical Methodology

In this work, the commercial CFD software ANSYS CFX-10 is used for the steady state hydrodynamic simulation of gas–liquid–solid flows in the mechanically agitated contactor. The details of the reactor geometry used for CFD simulation and the operating parameters are given in Table 6.3. Steady state simulations are performed for different types of impellers, agitation speeds, particle diameter, solid concentration, and superficial gas velocity. Due to the symmetry of geometry, only one-half of the agitated contactor is considered as the computational domain and is discretised using block structured grids, which allows finer grids in regions where higher spatial resolutions are required. The blocks are further divided into finer grids.

CFD Simulation of Gas-Liquid-Solid Mechanically Agitated Contactor

Around 200000 total computational nodes are created using the structured hexa mesh option of ICEM CFD in order to get the grid independent solution for the flow.

Figure 6.3 depicts a typical mesh used for the numerical simulation in this work.

During the last few decades, various approaches have been proposed in the literature for the simulation of impeller rotation. The most widely used approach in the literature is the multiple frame of reference (MFR) approach, in which the tank is divided into two regions: a rotating frame that encompasses the impeller and the flow surrounding it and a stationary frame that includes the tank, baffles, and the flow outside the impeller frame. The boundary between the inner and outer region have to be selected in such a way that the predicted results are not sensitive to its actual location. The other approach is the sliding grid approach, in which the inner region is rotated during computation and slide along the interface with the outer region. This method is fully transient and is considered as more accurate, but it requires more computational time when compared to MFR. Hence in this work, the MFR approach is used for simulating the impeller rotation. In the MFR approach, the computational domain is divided into an impeller zone (rotating reference frame) and a stationary zone (stationary reference frame). The interaction of inner and outer regions is accounted for by a suitable coupling at the interface between the two regions where the continuity of the absolute velocity is implemented. The boundary between inner and outer region is located at $r/R=0.6$. No-slip boundary conditions are applied on the tank walls and shaft. The free surface of tank is considered as the degassing boundary condition. Initially the solid particles are distributed in a homogeneous way inside the whole computational domain.

CFD Simulation of Gas-Liquid-Solid Mechanically Agitated Contactor

The bubble size distribution in the mechanically agitated reactor depends on the design and operating parameters and there is no experimental data available for bubble size distribution. It has been reported by Barigou and Greaves (1992) that their bubble size distribution is in the range of 3.5–4.5 mm for the higher gas flow rates used in their experiments. Also in the recent simulation study on a gas–liquid stirred tank reactor carried out by Khopkar et al. (2005) a single bubble size of 4 mm was assumed. Since the gas flow rates used in our experiments are also in the same range, a mean bubble size of 4 mm is assumed for all our simulations. Further, the validity of bubble size used in the CFD simulation is rechecked by calculating the bubble size based on the reported correlations in literature (Calderbank and Moo-Young, 1961) using the simulation results of gas holdup and power consumption values. The mean bubble size is calculated according to the following correlation as

$$d_b = 4.15 \left(\frac{(\rho \varepsilon)^{0.4} \rho^{0.2}}{\sigma^{0.6}} \right)^{-1} \varepsilon_g^{0.5} + 0.0009 \dots\dots\dots(6.28)$$

The value obtained for mean bubble size is around 3.7 mm. Hence for further simulations, the bubble size of 4 mm is used.

The discrete algebraic governing equations are obtained by element-based finite volume method. The second-order equivalent to high-resolution discretisation scheme is applied for obtaining algebraic equations for momentum, volume fraction of individual phases, turbulent kinetic energy, and turbulence dissipation rate. Pressure–velocity coupling was achieved by the Rhie-Chow algorithm (1994). The governing equations are solved using the advanced coupled multigrid solver technology of ANSYS CFX-10. The criteria for convergence is set as 1×10^{-4} for the rms (root mean square) residual error for all the governing equations. The rms

CFD Simulation of Gas-Liquid-Solid Mechanically Agitated Contactor

residual is obtained by taking all of the residuals throughout the domain, squaring them, taking the mean, and then taking the square root of the mean for each equation.

The simulations are carried out on the eight nodes, 32 processor AMD64 cluster with a clock speed of 2.55 GH and 8 GB memory for each node.

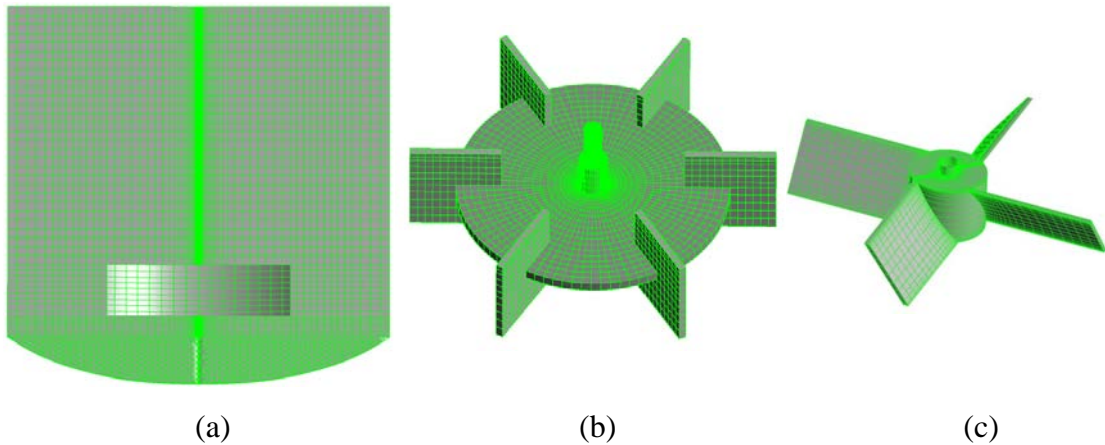


Figure 6.3. Computational grid of mechanically agitated three-phase contactor used in the present study (a) Tank (b) DT (c) PBT

6.5. Results and Discussion

6.5.1. Solid–liquid flows in an agitated contactor

Since any CFD model has to be validated first, we have carried out CFD simulations of gas–liquid and solid–liquid flows in mechanically agitated contactor.

The experimental results taken for validation of the CFD model are

- (a) The experimental data obtained by computer automated radioactive particle tracking (CARPT) technique by Guha et al. (2007) for the case of liquid–solid agitated contactor with a radial type impeller (DT)
- (b) The experimental data obtained by Spidla et al. (2005) using a conductivity probe for a pilot plant stirred vessel of 1m in diameter which is stirred with 6-pitched blade turbine (axial type impeller)

CFD Simulation of Gas-Liquid-Solid Mechanically Agitated Contactor

For the case of DT, Guha et al. (2007) characterised the solid hydrodynamics in a solid-liquid stirred tank reactor using computer automated radioactive particle tracking (CARPT) and measured axial and radial distribution of solid axial velocity for overall solid holdup of 7% at impeller speed of 1200 rpm. The variation of non-dimensional solid velocity components of axial, radial & tangential (U/U_{tip} , where $U_{tip} = \pi DN$) along the non-dimensional axial directions (z/T) are plotted in Figure 6.4 (a-c) for the case of DT at a radial position of $r/R = 0.5$. The experimental data plotted in Figure 6.4(a-c) corresponds to the data given by Guha et al. (2007). It can be observed that the axial variation of the axial component of solid velocity agrees well with the experimental results.

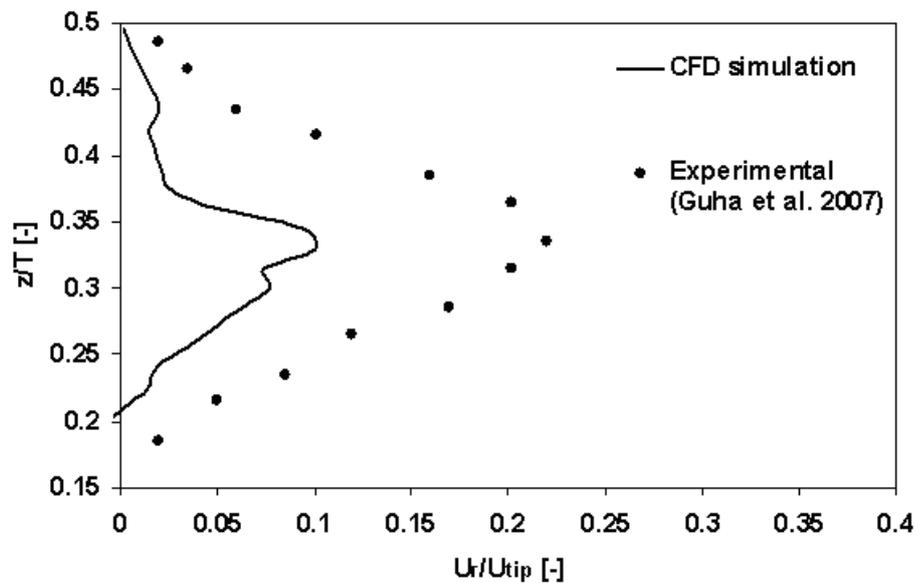


Figure 6.4 (a). Axial profiles of radial component of solid velocity

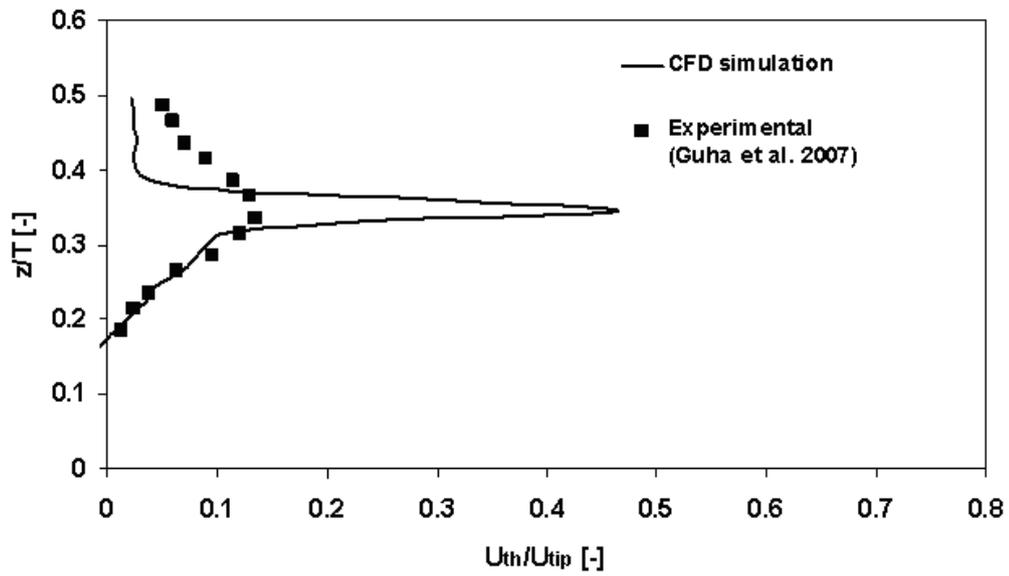


Figure 6.4 (b). Axial profile of the tangential component of the solids velocity

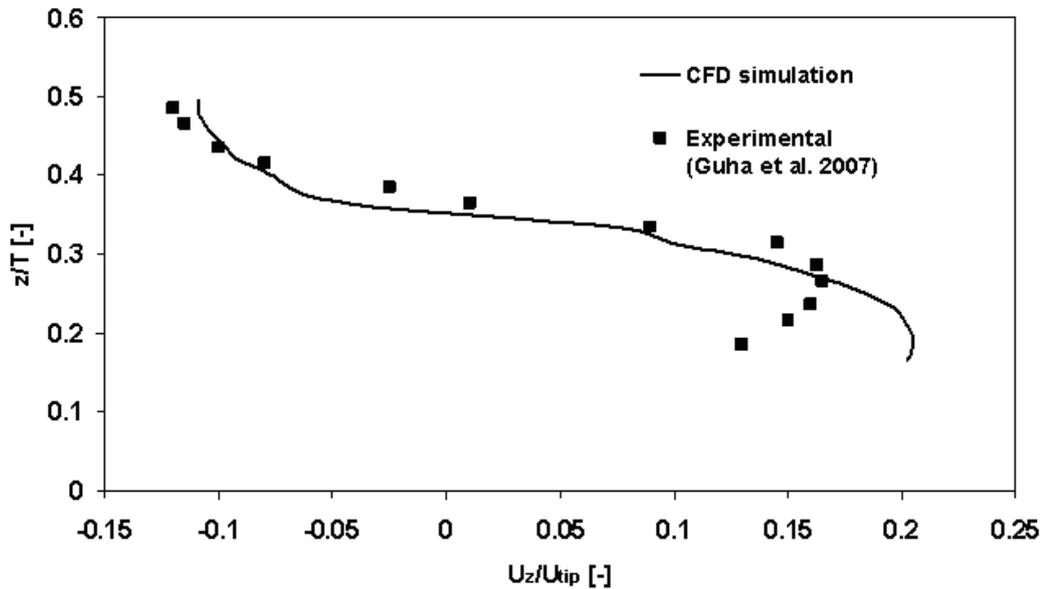


Figure 6.4(c). Axial profiles of the axial component of solid velocity

CFD Simulation of Gas-Liquid-Solid Mechanically Agitated Contactor

But for the other two components, even though there is a quantitative agreement between experimental and simulation results, there is a discrepancy between numerical simulations and experimental results qualitatively near the impeller region. This may be due to the fact that the mean velocity components of fluid mainly depend on the turbulent fluctuations and these turbulent fluctuations dominate mainly at the impeller region of stirred tank and the turbulence model used in the present study is not able to capture properly the strong turbulence near the impeller region.

Similarly non-dimensional radial profiles $((r-R_i)/(R-R_i))$, where R_i is the impeller radius) of various components of non-dimensional solid velocity at the axial position of $z/T=0.34$ is shown in Figure 6.5 (a-c).

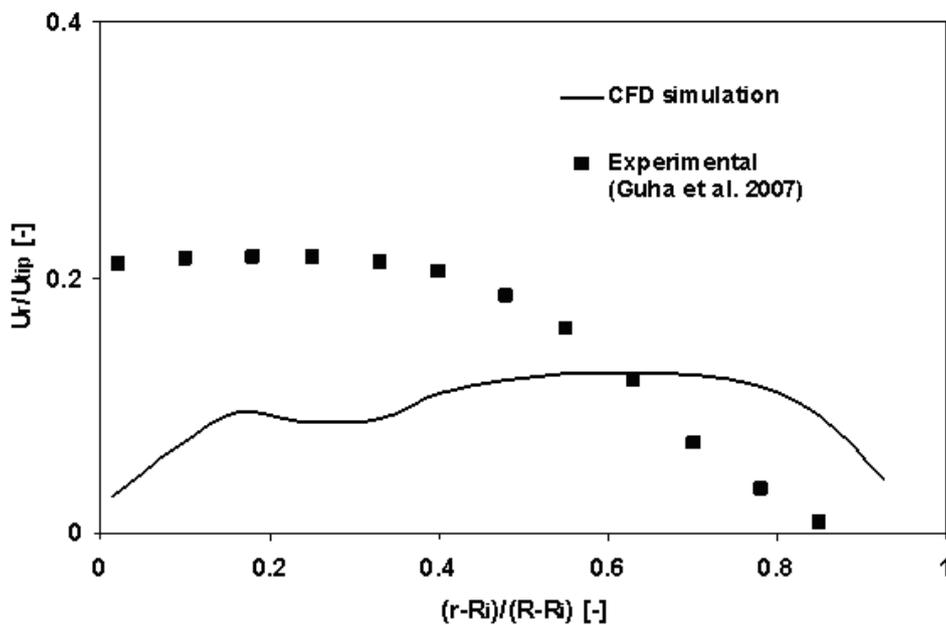


Figure 6.5 (a). Radial profiles of the radial component of the solids velocity

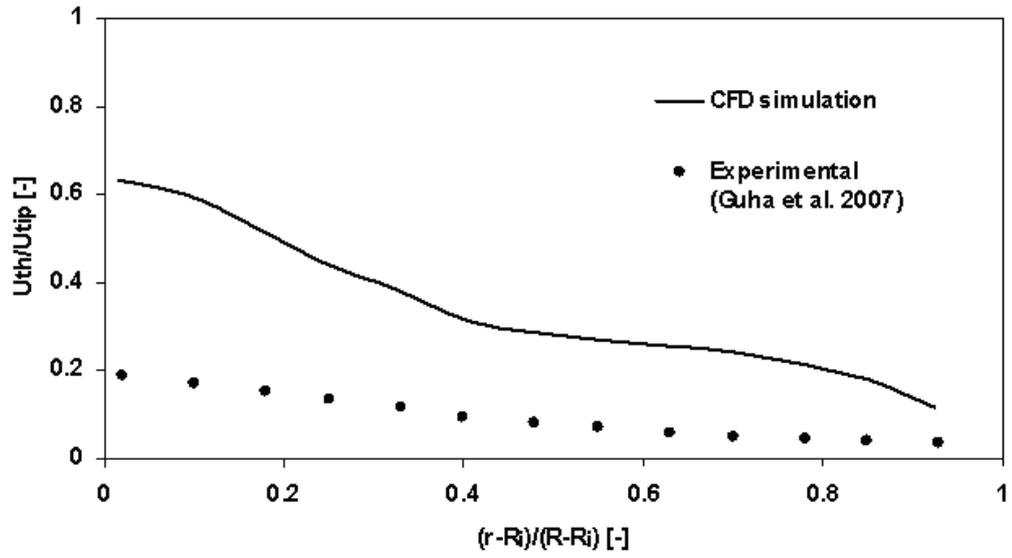


Figure 6.5 (b). Radial profiles of the tangential component of the solids velocity

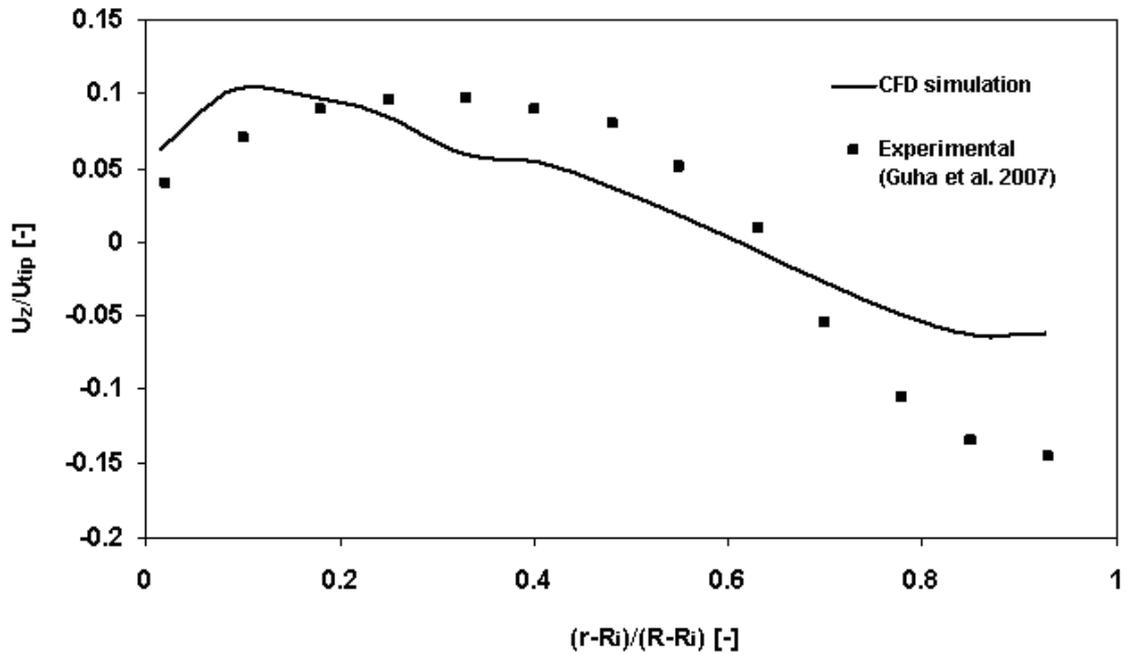


Figure 6.5 (c). Radial profiles of the axial component of the solids velocity

CFD Simulation of Gas-Liquid-Solid Mechanically Agitated Contactor

The same trend is observed in this case also. This type of discrepancy is confirmed by Guha et al. (2008) where they have carried out Large Eddy Simulation and Euler–Euler simulation of solid suspension in stirred tank reactor and concluded that there are major discrepancies in the prediction of solid velocities by both the numerical methods near the impeller region.

Similarly for the case of axial type impeller, experimental data of Spidla et al. (2005) have been used for the comparison of the axial solid distributions. They have presented detailed particle distribution data using a conductivity probe for a pilot plant stirred vessel of 1 m in diameter which is stirred with a six pitched blade turbine (PBTB). Figure 6.6 shows the comparison between the CFD simulation results and the experimental results for axial distribution of solid volume fraction at the radial position of $r/R=0.8$ for an overall solid holdup of 10% at the critical impeller speed of 267 rpm for the case of PBTB impeller. A good comparison exists between CFD prediction and experimental results for axial solid concentration.

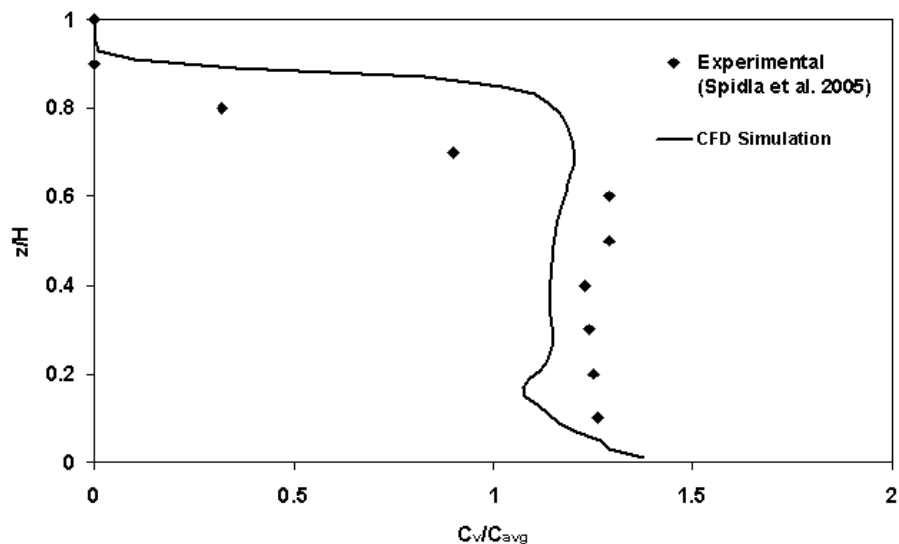


Figure 6.6. Axial solid concentration profile for PBTB in solid-liquid stirred reactor (solids loading = 10%, impeller speed =267 rpm, $r/R=0.8$)

6.5.2. Gas-liquid flows in an agitated contactor

For the case of gas-liquid flows in an agitated contactor, CFD model predictions of radial profiles of liquid velocity are validated with the experimental data of Aubin et al. (2004) for the pitched blade turbine with downward (PBTD) and upward (PBTU) pumping. They have used particle image velocimetry to investigate the liquid phase hydrodynamics. For the case of PBTD, the radial profile of the axial component of liquid velocity is shown in Figure 6.7 at the axial position $z/T = 0.31$. The impeller speed is taken as 300 rpm. Similar results are shown in Figure 6.8 for the case of PBTU with the same impeller speed. It can be seen clearly from both the figures that there exists excellent agreement between the CFD simulations and experimental data.

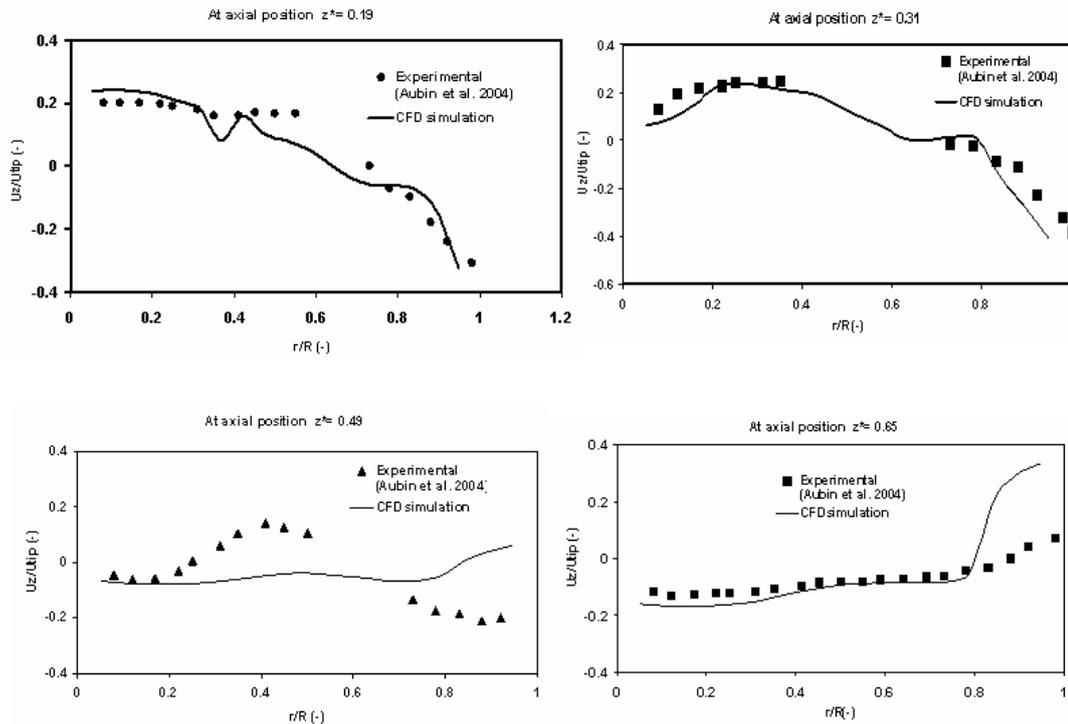


Figure 6.7. Radial profiles of dimensionless axial liquid velocity at various axial locations for the case of PBTD (impeller speed = 300 rpm, $z/T = 0.31$)

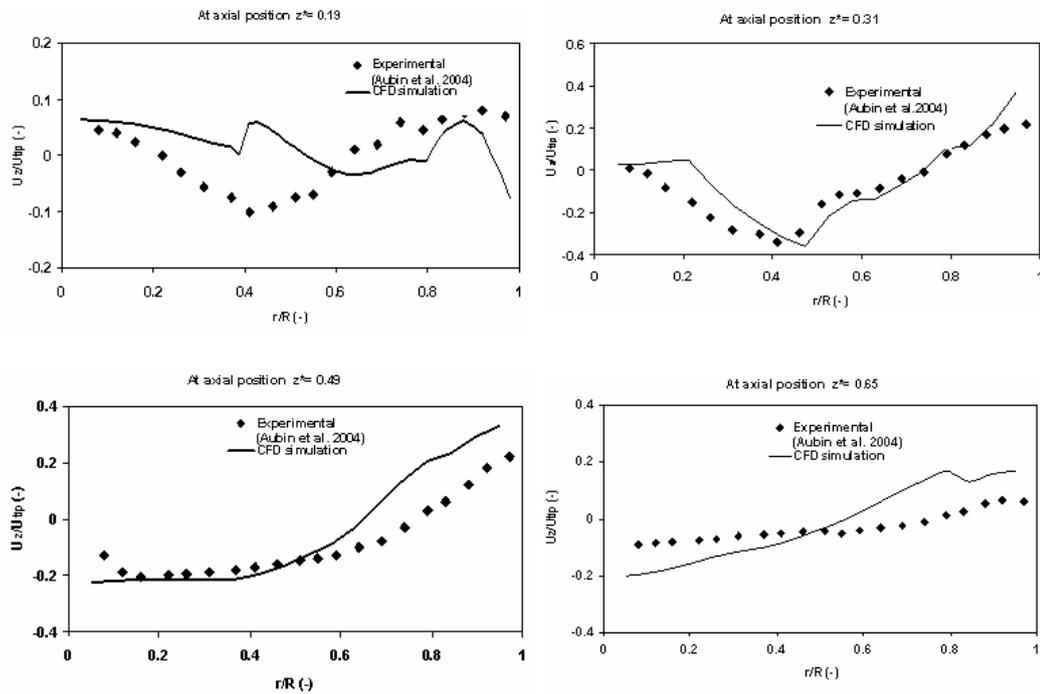


Figure 6.8. Radial profiles of dimensionless axial liquid velocity at various axial locations for the case of PBTU (impeller speed = 300 rpm, $z/T = 0.31$)

6.5.2.1. Gross flow field characteristics

The gross flow field characteristics of mechanically agitated reactor are generally characterised by power number, pumping number and pumping efficiency. Since the overall prediction of CFD is good, CFD simulation is used further to calculate these values. The pumping number (N_Q) and power number (N_P) are calculated as follows:

$$N_Q = \frac{2 \int \pi r U dr}{ND^3} \dots\dots\dots(6.29)$$

The limits of integration for the radial distance are from the surface of the shaft to the impeller radius and U is the axial liquid velocity.

$$N_p = P/\rho N^3 D^5 \dots\dots\dots(6.30)$$

CFD Simulation of Gas-Liquid-Solid Mechanically Agitated Contactor

The pumping efficiency is then calculated by the following equation

$$\text{Pumping efficiency} = N_Q/N_P \dots\dots\dots(6.31)$$

The Power draw (P) is determined from torque equation ($P = 2\pi NT$) and the total torque can be calculated from the torque acting on all the blades.

The predicted values of pumping number and power number are compared with experimental data and are shown in Table 6.4. It can be observed that the values predicted by CFD simulations agree reasonably well with the experimental values but the overall gas holdup predicted by CFD simulation is slightly varies with the experimental values. This may be because the gas holdup mainly depends on the bubble size distribution, which is not included in the present study.

Table 6.4. Gross Characteristics of Gas–liquid Stirred Vessel

Operating condition	Total gas holdup		Power number (N _p)		Pumping number (N _Q)		Pumping efficiency (N _Q /N _P)	
	Experimental (Aubin et al., 2004)	CFD	Experimental (Aubin et al., 2004)	CFD	Experimental (Sardeing et al., 2004)	CFD	Experimental	CFD
PBTD N =300 RPM	0.037	0.042	1.56	1.3	0.59	0.64	0.39	0.49
PBTU N =300 RPM	0.058	0.052	1.80	1.5	0.57	0.49	0.32	0.33

6.5.3. Gas–liquid–solid flows in an agitated contactor

In this section, CFD simulation has been used for simulating the hydrodynamics of gas–liquid–solid flows in an agitated contactor. Recently Murthy et al. (2007) have carried out detailed investigations on gas–liquid–solid stirred reactor

CFD Simulation of Gas-Liquid-Solid Mechanically Agitated Contactor

using CFD simulation for the case of lower solids concentration (2–15 wt.%) and for low-density particles. Their results clearly highlight the capability of CFD in predicting the gross characteristics of such three-phase systems. Also, only the standard deviation approach was used by these authors to characterise the critical impeller speed. In this work, we have carried out CFD simulation for the gas–liquid–solid mechanically agitated contactor with high density ilmenite particles as solids phase and with solid loading in the range of (10–30 wt.%).

Further, for the case of three-phase systems, experimental data for gas and solid holdup profile are very limited or not available. Therefore, the present simulations have been focused on the prediction of the critical impeller speed for gas–liquid–solid mechanically agitated contactor for different type of impellers, for various gas flow rates and different particle sizes. The critical impeller speed is determined from CFD simulation using both the standard deviation approach and cloud height criteria. The values obtained by CFD simulation for critical impeller speed is compared with our experimental data. Also the qualitative features of the flow pattern predicted by CFD simulation are presented in the following sections.

6.5.3.1. Flow field

The geometry chosen for this simulation is the reactor shown in Figure 6.1. The reactor dimensions and the physical properties of all the phases considered are given in Table 6.3.

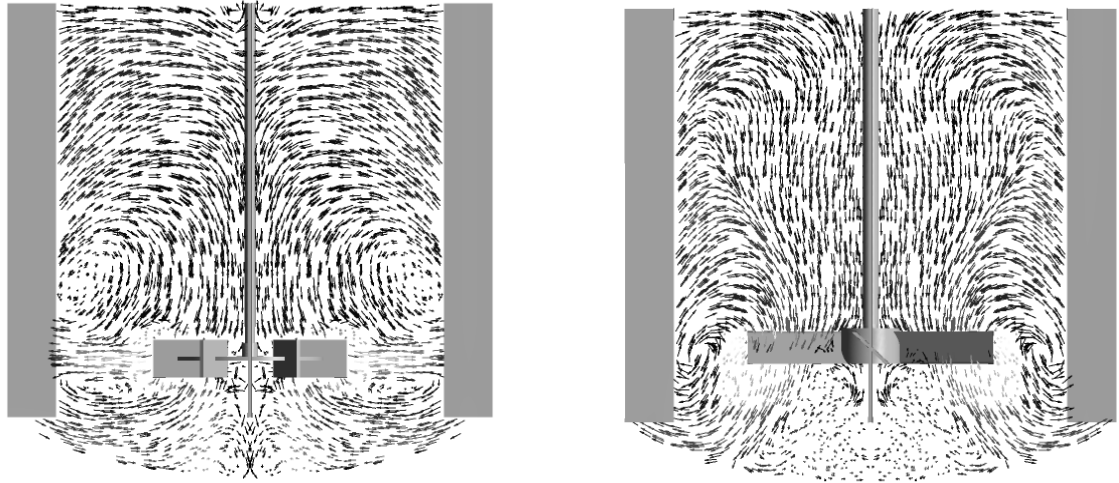


Figure 6.9. Solid flow pattern predicted by CFD simulation in gas-liquid-solid stirred reactor for the case of (a) DT (b) PBTD (gas flow rate =0.5 vvm, particle size = 230 μm & solids loading = 30 wt %)

The liquid phase chosen is water and the solid phase considered for the present study corresponds to high density ilmenite particles ($\rho_s = 4200 \text{ kg/m}^3$) with particle size 230 μm and with 30% solids loading by weight. The gas phase is air and the flow rate is taken as 0.5 vvm. Two types of impellers are considered for the simulation. One is axial type impeller (PBTD) and the other is radial type impeller (DT). Figures 6.9 (a & b) shows the solid velocity profile obtained for the two types of impellers where the impeller speed chosen for both the cases correspond to that of critical impeller speed. As can be seen clearly from Figure 6.9 (a) that, for the case of DT, there exists circular loops of solids above and below the impeller and there is a radial jet flow of solids flow in the impeller stream. For the case of PBTD impeller (Figure 6.9(b)), there is only one circulation loop for solids, where the solids move upward towards the surface of liquid and then turn downwards to the bottom. The flow field

CFD Simulation of Gas-Liquid-Solid Mechanically Agitated Contactor

pattern predicted by CFD simulations quantitatively agrees with the flow profiles reported in the literature.

The turbulence kinetic energy predicted by CFD simulation at the midbaffle plane for the case of DT and PBTD impellers shown in Figure 6.10. It can be clearly seen from Figures 6.10 (a & b) that DT impeller generates high intensity turbulence near the tip of the impeller blade which gets dissipated very quickly, whereas the PBTD impeller generates the medium intensity turbulence, which gives better distribution of turbulence over the entire vessel of stirred tank.

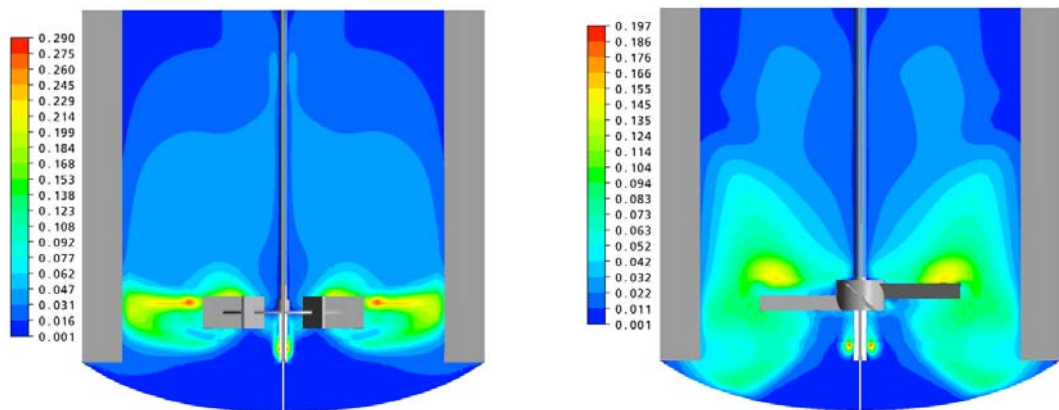


Figure 6.10. Turbulence kinetic energy profile predicted by CFD simulation in gas–liquid–solid stirred reactor for the case of (a) DT (b) PBTD (gas flow rate = 0.5 vvm, particle size = 230 μm & particle loading =30 wt %)

Since the energy dissipation rate plays an important role in solids suspension in agitated reactors, the energy dissipation rate obtained by CFD simulation for both DT and PBTD impellers with respect to the gas flow rate is shown in Table 6.5. The values presented in the table are generated at the critical impeller speed with a solid loading of 30% by weight. It can be observed from the results that the energy

CFD Simulation of Gas-Liquid-Solid Mechanically Agitated Contactor

dissipation rate is higher for the case of DT. It can also be seen from the table that under ungasged conditions (solid–liquid agitated reactors) the energy dissipation rate for DT impellers is approximately 1.5 times the energy dissipation rate for PBTD impellers. For the case of gas–liquid–solid agitated contactors, the energy dissipation rate increases with increase in gas flow rates. This increase in energy dissipation rate is slightly more for PBTD impellers (2 times) than for DT impellers (1.7 times). This may be due to instabilities due to large fluctuations in impeller power at the higher gas flow rate for PBTD and this observation is in agreement with those reported in literature (Nienow et al., 1985; Bujalski et al., 1988)

Table 6.5. Energy dissipation rate obtained by CFD simulation for different type of impellers (particle size = 230 μm & particle loading = 30 wt. %)

Air flow rate (vvm)	Energy dissipation rate, m^2/s^3	
	DT	PBTD
0	0.66	0.45
0.5	0.97	0.58
1.0	1.65	1.2

6.5.3.2. Liquid phase mixing

Generally the mixing performance is of crucial importance in turbulent mechanically agitated reactors. A global characterisation of such passive scalar mixing is the mixing time. Roughly speaking, it is the time to achieve complete (that is, over the whole vessel) homogenisation of an added passive scalar. It is generally defined as the time required to mix the added passive tracer with the contents of the tank until a certain degree of uniformity is achieved. But, usually the precise

CFD Simulation of Gas-Liquid-Solid Mechanically Agitated Contactor

definition of a certain degree of uniformity gives rise to little confusion. The definition of what is considered homogeneous varies from study to study. The degree of homogeneity considered in the present study is 95% which means that the concentration variations are smaller than 5% of the fully mixed concentration. The convection–diffusion equation for species transport equations for tracer addition to the stirred tank are solved till degree of mixing is achieved. The mixing time obtained from the CFD simulation are analysed based on a simplified model proposed by Kawase and Moo-Young (1989). They developed a correlation for mixing time in single-phase stirred tank reactors on the basis of Kolmogorov’s theory of isotropic turbulence. Their correlation for single phase system is a function of energy dissipation and is given as

$$\theta_m = 6.35 \times 2^{(5n-2)/3n} D_T^{2/3} \epsilon^{-1/3} = 12.7 D_T^{2/3} \epsilon^{-1/3} \dots\dots\dots (6.32)$$

In the above equation D_T is the diameter of the tank and ϵ is the energy dissipation rate and n is the flow index of the power law model. In this work, the extent of above correlation is examined for two- and three-phase systems by using the energy dissipation rate for the systems obtained from CFD simulation. Similar type of comparisons have also been reported in the literature (Kawase and Shimizu, 1997; Dohi et al., 1999). Figure 6.11 shows the comparison of liquid-phase mixing time for three-phase systems with the correlation given by equation (6.32) for both radial type (DT) and axial type impellers (PBTD). The deviation of the predicted values of mixing time by simulation from that of equation (6.32) is around 5% for DT and around 8 % for PBTD. It can also be seen from this figure that the value of mixing time decreases with an increase in impeller speed. This is due to the fact that eventhough, the suspension quality increases with an increase in impeller speed, more

amount of energy is spent at the solid–liquid interface and hence only less energy is available for liquid-phase mixing.

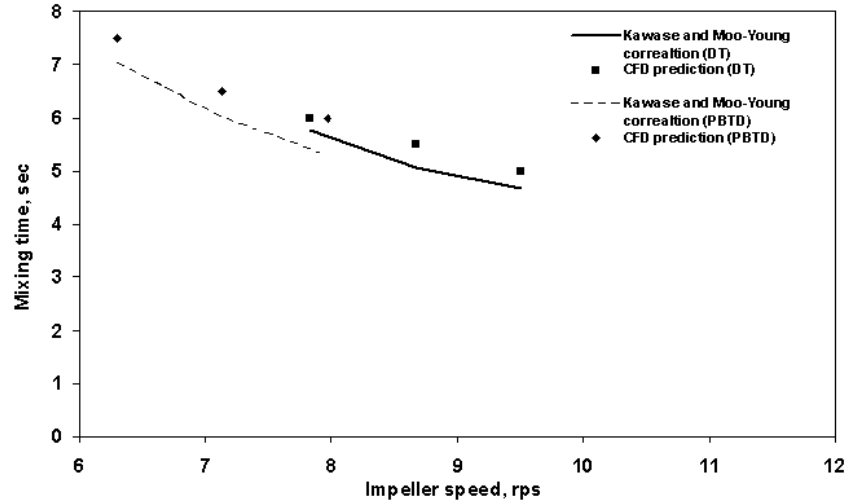


Figure 6.11. Mixing time variation with impeller speed

6.5.3.3. Solid suspension studies

CFD simulation of three-phase mechanically agitated contactor is undertaken in this study to verify quantitatively the solid suspension characteristics since the important consideration for design and operation of these types of reactors is the determination of the state of suspension. The quality of solid suspension is evaluated by the extent of off-bottom suspension i.e., critical impeller speed for just suspended state and extent of axial solid distribution i.e., solid suspension height. Generally Zwietering criteria (the impeller speed at which the particles do not remain stationary at the bottom of the vessel) is used for characterising the off-bottom suspension. But incorporating Zwietering criteria is difficult in the Eulerian–Eulerian approach of the present CFD simulation. Hence the method proposed by Bohnet and Niesmak (1980) which is based on the value of standard deviation is used in the present study for the

CFD Simulation of Gas-Liquid-Solid Mechanically Agitated Contactor

prediction of critical impeller speed. This standard deviation method was also successfully employed for liquid–solid suspension by various authors (Khopkar et al., 2006; Murthy et al., 2007). It is defined as

$$\sigma = \sqrt{\frac{1}{n} \sum_{i=1}^n \left(\frac{C_i}{C_{avg}} - 1 \right)^2} \dots\dots\dots(6.33)$$

where *n* is the number of sampling locations used for measuring the solid holdup.

The increase in the degree of homogenisation (better suspension quality) is manifested in the reduction of the value of standard deviation. The standard deviation is broadly divided into three ranges based on the quality of suspension. For uniform suspension the value of the standard deviation σ is found to be smaller than 0.2 ($\sigma < 0.2$), for just suspended condition the value of the standard deviation is between 0.2 & 0.8 ($0.2 < \sigma < 0.8$) and for an incomplete suspension the standard deviation value is greater than 0.8 ($\sigma > 0.8$). But it is very difficult to exactly find the critical impeller speed required for the just suspended state from the values of the standard deviation. These difficulties were also cited in the literature (Khopkar et al., 2006, van der Westhuizen et al., 2008). Hence we have used another criteria which is based on the solid suspension height i.e., cloud height ($H_{cloud} = 0.9H$) along with standard deviation method. Kraume (1992) used these two criteria to evaluate the critical impeller speed in liquid–solid suspension. For the present study, both these criteria have been used to evaluate the quality of solid suspension and to determine the critical impeller speed. Systematic investigation of solids suspension using CFD simulation has been carried out for different processing and operating conditions. The critical impeller speed obtained by CFD simulation based on these two criteria is validated with our experimental data.

6.5.3.3.1. Effect of impeller type

CFD simulations have been carried out for 6 blade Rushton turbine impeller (DT) and 4 blade pitched blade turbine with downward pumping (PBTD) at different impeller speeds. The air flow rate for this simulation is 0.5 vvm and the solid phase consists of ilmenite particles of size 230 μm and the solid loading is 30% by weight.

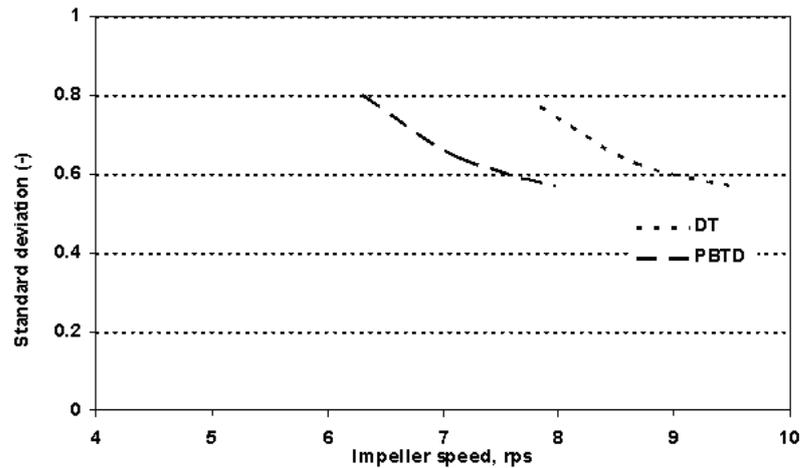


Figure 6.12. Variation of standard deviation values with respect to the impeller speed for DT and PBTD

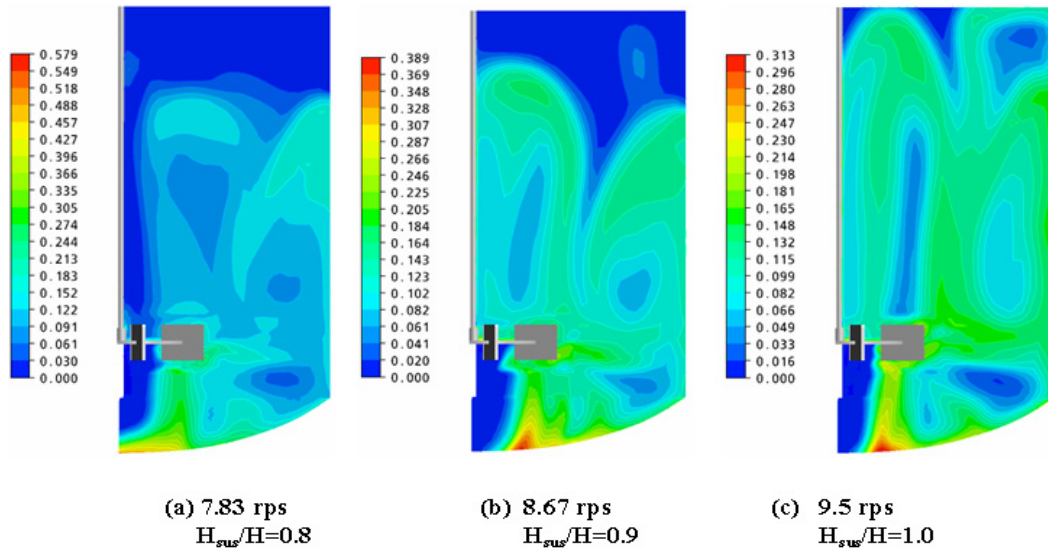


Figure 6.13. CFD prediction of cloud height with respect to the impeller speed for DT (gas flow rate = 0.5 vvm, particle size = 230 μm & particle loading = 30 wt.%)

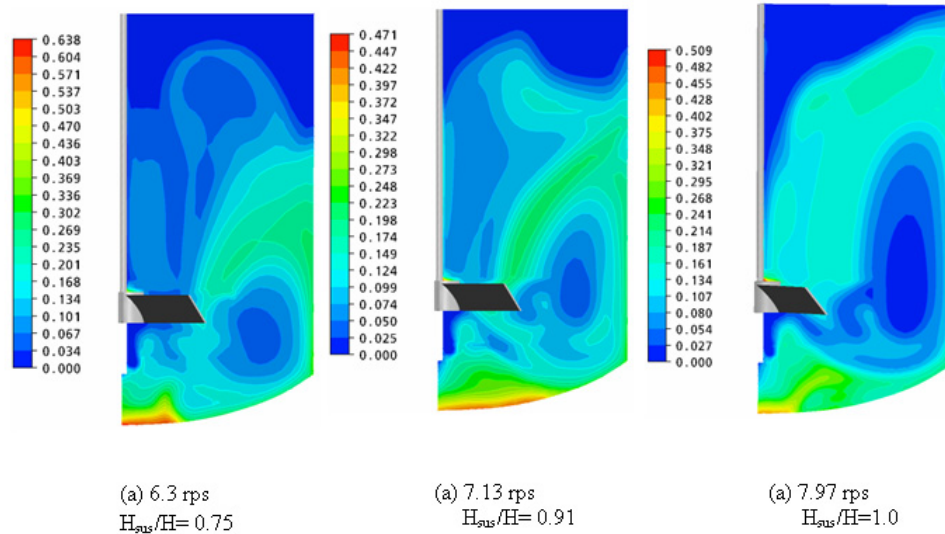


Figure 6.14. CFD prediction of cloud height with respect to the impeller speed for PBTD (gas flow rate = 0.5 vvm, particle size =230 μm & particle loading =30 wt %)

Figure 6.12 shows the variation of the standard deviation value with respect to impeller speed for DT and PBTD. The value of standard deviation decreases with increase in impeller speed for both the impellers. Figure 6.13 depicts the predicted cloud height for the three impeller rotational speeds (7.83, 8.67, and 9.5 rps) for DT and Figure 6.14 shows the predicted cloud height for PBTD for three different impeller speeds (6.3, 7.13, and 7.97 rps).

It can be seen clearly from these figures that there is an increase in the cloud height with an increase in the impeller rotational speed. Similar observations were also reported by Khopkar et al. (2006). The values of standard deviation and cloud height obtained by CFD simulation along with experimental values for both the type of impellers are presented in Table 6.6. Based on these two criteria, it is found that the critical impeller speed required for DT is 8.67 rps and for PBTD is 7.13 rps which

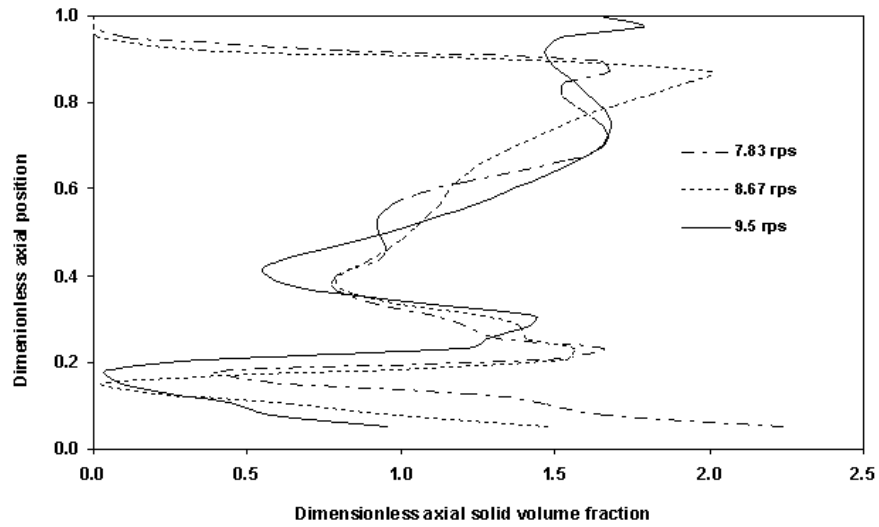
CFD Simulation of Gas-Liquid-Solid Mechanically Agitated Contactor

agrees very well with the experimental observation. It has to be noted again that both the criteria have to be satisfied for critical impeller speed determination.

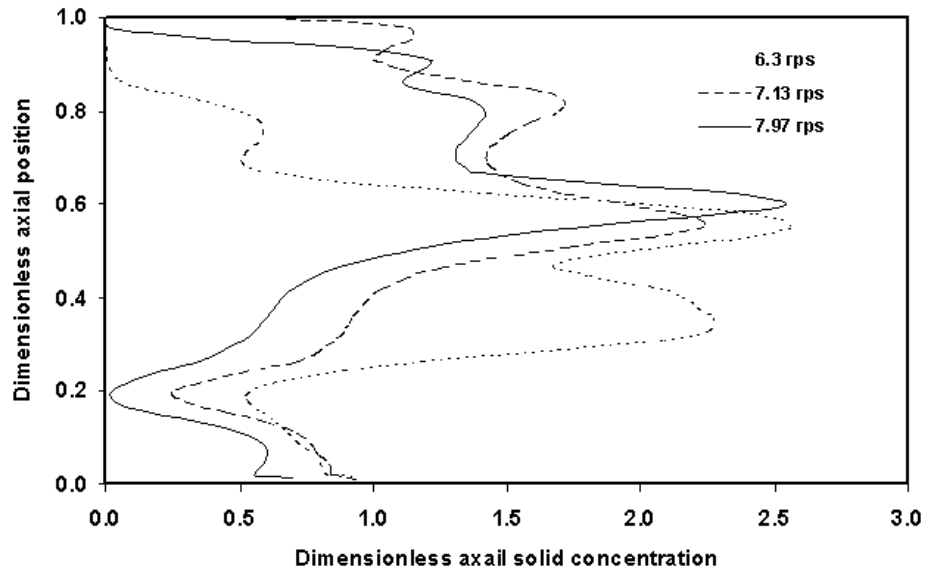
Table 6.6. Effect of impeller type on quality of suspension (gas flow rate =0.5 vvm, particle size = 230 μm , & particle loading = 30 wt %)

Type of impeller	Critical impeller speed, rps		Standard deviation, σ	Cloud height
	Experimental	CFD simulation		
DT	8.67	8.67	0.66	0.90
PBTD	7.13	7.13	0.64	0.91

Figures 6.15(a & b) show dimensionless axial concentration profiles for the DT and PBTD for various impeller speeds. The process conditions used are same as before. It can be seen that the amount of solid particles that settles at the bottom of the vessel decreases with increase in impeller rotational speed. The power required for DT is two times more than that of PBTD for the same operating conditions. For example, for solid loading of 30% wt, for the air flow rate of 0.5 vvm, DT requires 2.02 KW/m³ of power while PBTD requires only 0.91 KW/m³ of power. This lower power requirement for PBTD impeller can be attributed to the fact that travel length of fluid flow is lower for PBTD than for DT i.e., flow field generated by PBTD start from the tip of the impeller region and is directed towards the tank bottom which is responsible for solid suspension whereas liquid flow generated by DT travel in the radial direction and splits into two streams, one above and one below the impeller and only this lower stream of flow is associated with solid suspension. Hence DT requires more power.



(a)



(b)

Figure 6.15. Axial concentration profiles predicted by CFD simulation for different impellers of (a) DT (b) PBTD (gas flow rate = 0.5 vvm, particle size = 230 μm & particle loading = 30 wt %)

6.5.3.3.2. Effect of particle size

It has been reported in the literature that the critical impeller speed depends on the particle size. Hence, CFD simulations have been carried out for three different particle sizes viz, 125 μm , 180 μm and 230 μm at the solid loading of 30 % by wt. and a gas flow rate of 0.5 vvm with both DT and PBTD type impellers. From the CFD simulation, the standard deviation and cloud height values are also obtained and they are shown in Table 6.7.

Table 6.7. Effect of particle size on quality of suspension (gas flow rate = 0.5 vvm & particle loading 30 = wt %)

Particle diameter (μm)	(DT)				PBTD			
	Critical impeller speed, rps		Standard deviation, σ	Cloud height	Critical impeller speed, rps		Standard deviation, σ	Cloud height
	Experimental	CFD			Experimental	CFD		
125	5.67	5.67	0.50	0.90	5.42	5.42	0.46	0.91
180	6.25	6.92	0.75	0.89	5.77	6.0	0.62	0.88
230	8.67	8.67	0.66	0.90	7.13	7.13	0.64	0.91

It can be seen clearly that critical impeller speed predicted by CFD simulation based on the criteria of standard deviation and solid cloud height agrees very well with the experimental data. Further, from Figure 6.16 it can be observed that the critical impeller speed for solid suspension increases with an increase in the particle size for fixed set of operating conditions and impeller configuration. This is due to the fact that with increase in the particle size, the terminal settling velocity increases. This settling velocity of particle causes sedimentation which in turn affects the solids

suspension. Also it can be noted that an increase in particle size by two times results in an increase in critical impeller speed by approximately 1.5 times.

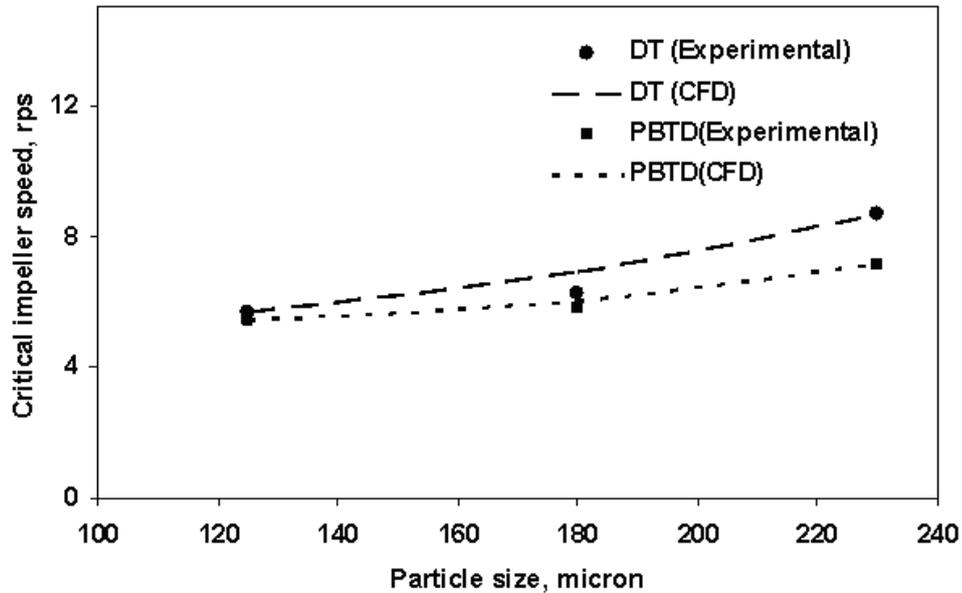


Figure 6.16. Effect of particle size on Critical impeller speed for different impellers (gas flow rate = 0.5 vvm & particle loading = 30 wt %)

6.5.3.3.3 Effect of air flow rate

CFD simulations have further been carried out to study the effect of air flow rate on the critical impeller speed for gas–liquid–solid mechanically agitated contactor. Figure 6.17 shows the comparison of CFD predictions with the experimental data on critical impeller speed for both the type of impellers at various gas flow rates (0 vvm, 0.5 vvm and 1.0 vvm). The values of the standard deviation and cloud height with respect to the impeller speed for different gas flow rates with different type of impellers are shown in Table 6.8.

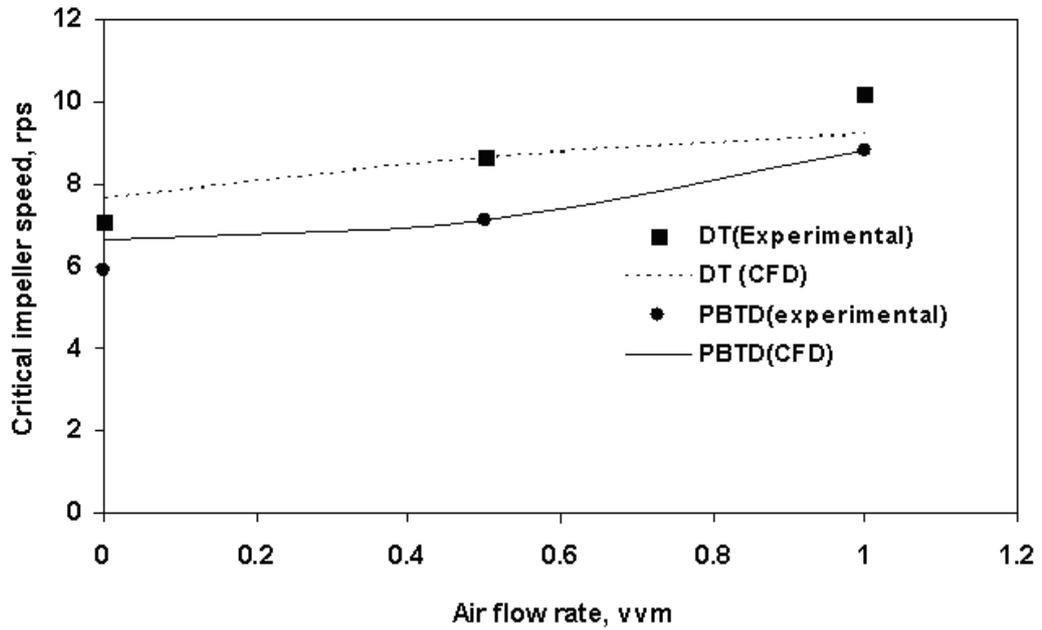


Figure 6.17. Effect of air flow rate on Critical impeller speed for different impellers (particle size= 230 μm & particle loading = 30 wt %)

Table 6.8. Effect of air flow rate on quality of suspension for different type of impellers (particle size = 230 μm & particle loading = 30 wt. %)

Air flow rate (vvm)	DT				PBTD			
	Critical impeller speed, rps		Standard deviation, σ	Cloud height	Critical impeller speed, rps		Standard deviation, σ	Cloud height
	Experimental	CFD			Experimental	CFD		
0	7.17	7.67	0.80	0.89	5.5	6.67	0.80	0.90
0.5	8.67	8.67	0.66	0.90	7.13	7.13	0.64	0.91
1.0	10.2	9.2	0.66	0.90	8.82	8.82	0.71	0.93

CFD Simulation of Gas-Liquid-Solid Mechanically Agitated Contactor

It can be observed that CFD simulation is capable of predicting the critical impeller speed in terms of standard deviation value and cloud height with an increase in gas flow rate for both types of impellers. Figure 6.18 shows solid volume fraction distribution predicted by CFD at the critical impeller speed for the solid loading of 30 % by wt. and particle size of 230 μm with different air flow rates (0, 0.5, 1.0 vvm).

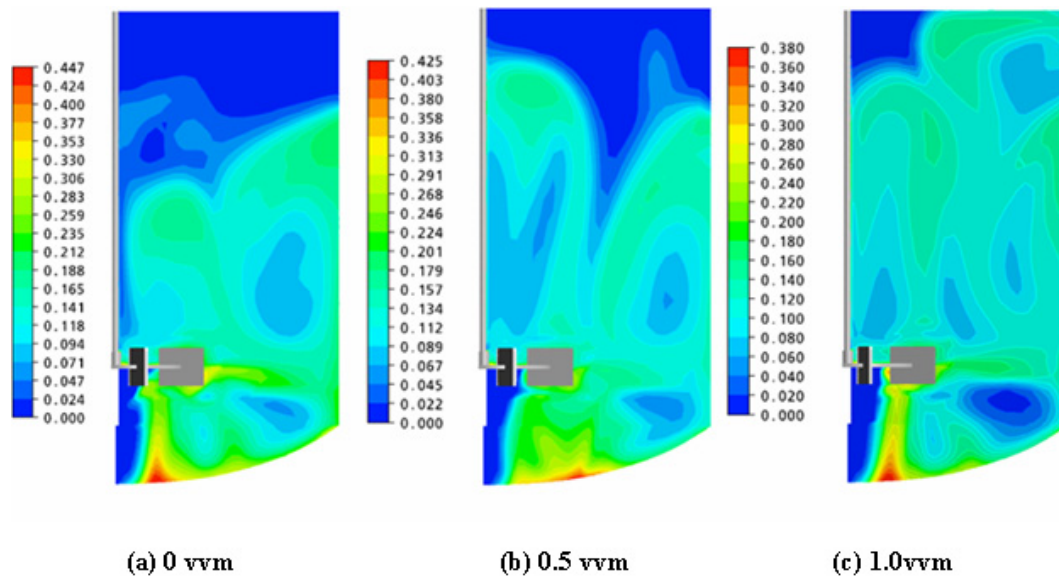


Figure 6.18. Effect of air flow rate on solid concentration distribution for DT by CFD simulations at the critical impeller speed (a) 0 vvm (b) 0.5 vvm (c) 1.0 vvm (particle size = 230 μm and particle loading = 30 wt. %)

Figure 6.19 shows the variation of standard deviation value with respect to the impeller speed. It can be seen that the reduction rate of standard deviation value in ungassed condition is more with increasing impeller speed when compared with gassed condition. Similarly for the case of higher gas flow rate, the reduction rate in the standard deviation value is much lower compared to lower gas flow rate. This is due to the presence of gas which reduces both turbulent dispersion and fluid circulation action of the impeller.

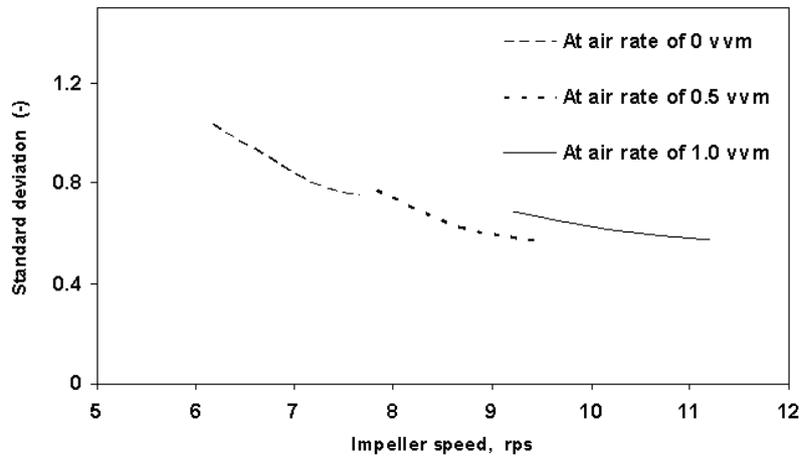


Figure 6.19. Effect of gas flow rate on the standard deviation value for different impeller speeds of DT (particle size= 230 μm & particle loading= 30 wt.%)

Since the quality of suspension is reduced due to decrease in impeller pumping capacity when gas is introduced in a suspended medium, there is a need to increase the impeller speed for re-suspension. This extent of increase in the impeller speed was found to depend upon gas flow rate (Q_g). In literature, various authors (Chapman et al., 1983; Nienow et al., 1985; Bujalski et al., 1988; Wong et al., 1987; Dutta and Pangarkar, 1995) have proposed a linear correlation between the difference in critical impeller speed for suspension with gas and without gas with the air flow rate as

$$\Delta N_{js} = N_{jsg} - N_{js} = aQ_g \quad \dots\dots\dots (6.34)$$

where a is a constant, N_{js} is the critical impeller speed without gas, while N_{jsg} is critical impeller speed under gas sparging conditions. Table 6.9 shows the value ‘ a ’ reported by various authors as well as by present CFD simulation. The operating conditions chosen for the present CFD simulation is solid particles of size 230 μm with solid loading of 30% by wt. and the impeller type chosen is DT.

Table 6.9. Reported values of constant ‘a’ of Equation (6.34) along with CFD prediction

Reference	Value of the parameter ‘a’ in equation (6.34)
Chapman et al.(1983) and Nienow et al.(1985)	0.94
Bujalski et al.(1988)	0.65
Wong et al.(1987)	2.03
Dutta and Pangarkar (1995)	3.75
Present CFD simulation	1.53

It can be shown that there is a significant variation in the parameter value ‘a’ between different studies. This may be due to the variation in operating conditions such as particle size, loading and impeller diameter. It varies from 0.94 to 3.75. The values obtained from Nienow et al. (1985) and Bujalski et al. (1988) show the smallest dependence of critical impeller speed on air flow rate while those by Dutta and Pangarkar (1995) and Chapman et al. (1983) show the largest dependence. The value predicted by CFD simulation is around 1.53.

The extent of increase in critical impeller speed with increasing air flow rate is also different for different type of impellers. The increase in N_{jsg} for PBTD is higher than DT. When gas flow increases from 0.5 vvm to 1.0 vvm, DT requires the lowest N_{jsg} which is approximately 5.7% more, whereas PBTD requires 19% times more in the increase in the N_{jsg} . This may be due to the instabilities due to the large fluctuations in impeller power at the higher gas flow rate for PBTD and also due to the flow generated by the PBTD impeller is directly opposite to the flow of gas. This observation is in agreement with those reported in literature (Chapman et al., 1983; Bujalski et al., 1988).

6.6. Conclusions

1. In this present work, Eulerian multi-fluid approach along with standard k- ϵ turbulence model has been used to study the solid suspension in gas-liquid-solid mechanically agitated contactor.
2. The results obtained from CFD simulations are validated qualitatively with literature experimental data (Guha et al., 2007; Spidla et al., 2005; Aubin et al., 2004) in terms of axial profiles of solid velocity in liquid-solid stirred suspension and liquid velocity in gas-liquid stirred suspension for different operating conditions. A good agreement was found between the CFD prediction and experimental data.
3. For gas-liquid-solid flows, the CFD predictions are compared quantitatively with our experimental data in terms of critical impeller speed based on the criteria of standard deviation method and cloud height in a mechanically agitated contactor. An adequate agreement was found between CFD prediction and experimental data.
4. The numerical simulation has further been extended to study the effect of impeller design (DT, PBTD), impeller speed, particle size (125–230 μm) and air flow rate (0–1.0 vvm) on the prediction of critical impeller speed for solid suspension in gas-liquid-solid mechanically agitated contactor.

Chapter 7

*A Comparative Study of Hydrodynamics and
Mass Transfer in Gas-Liquid-Solid
Mechanically Agitated
and Fluidised Bed Contactors using CFD*

7.1. Introduction

In earlier chapters, the validated CFD models for simulating the hydrodynamics of gas–liquid–solid mechanically agitated contactors and gas–liquid–solid fluidised beds are developed. Since the main objective of this work is to compare the performance of both these reactors in terms of hydrodynamics and transport phenomena in terms of gas–liquid mass transfer coefficient, this chapter focuses on this study. Similar studies have also been reported in the literature. In recent literature, Stitt (2002) discussed in detail the advantage of using alternate reactors like fluidised bed reactors, slurry bubble column and loop reactors instead of stirred tank reactors for intermediate scale and fine chemicals industries which involve reaction classes of type, oxidation, hydrogenation and carbonylation *etc.* Bouaifi et al. (2001) characterised the mass transfer parameters like volumetric mass transfer coefficient, and liquid side mass transfer coefficient in stirred multi impeller gas–liquid reactors and bubble columns and compared these parameters for both the reactors. They observed that for the same total power consumption, the volumetric mass transfer coefficient is higher for bubble column reactors than stirred reactors.

van Baten and Krishna (2003) used computational fluid dynamics (CFD) to compare the hydrodynamics and mass transfer of an internal airlift reactor with that of a bubble column reactor with an air–water system in the homogenous bubble regime. They observed that when compared at the same superficial velocity, the gas hold up is lower in the airlift reactors than in the bubble column reactors. Recently Balamurugan et al. (2007) studied hydrodynamics and mass transfer characteristics of gas–liquid ejector with different configurations and compared the performance of the ejector systems to other gas–liquid contacting systems like stirred tanks and bubble

Comparison study of Mechanically agitated and Fluidised Bed Contactors

columns and stated that the k_La values in the ejectors are very high compared to other conventional gas–liquid contactors.

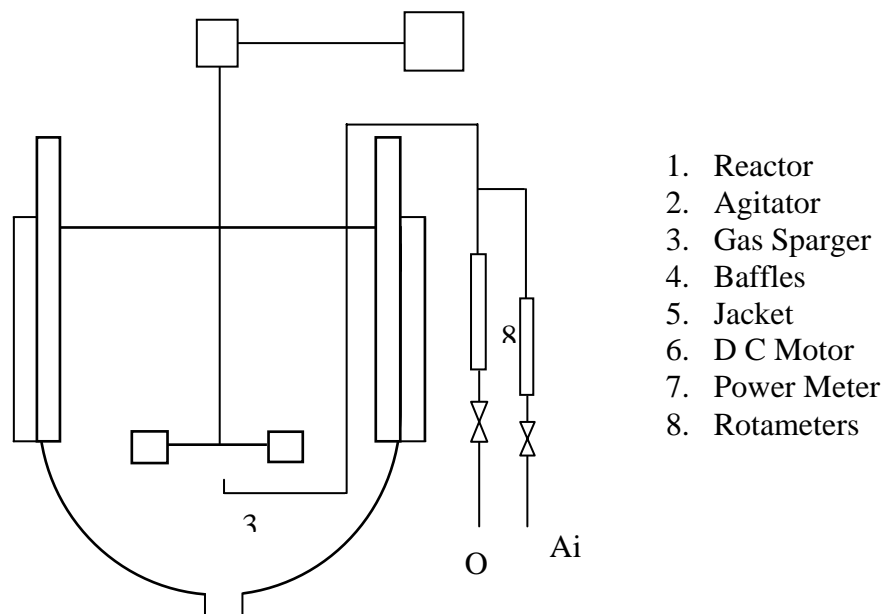
Thus, in the present Chapter, an attempt is made to compare the performance of gas–liquid–solid mechanically agitated contactor and fluidised bed contactor in terms of hydrodynamic parameters like gas holdup, power consumption and mass transfer characteristics in terms of volumetric mass transfer coefficient. In this work, CFD simulation is used as a tool to compare the performance between gas–liquid–solid mechanically agitated contactor and three-phase fluidised bed contactor. For the hydrodynamics, the comparison is based on the gas holdup prediction along with total power consumption (P/V) and for the mass transfer, the comparison is based on gas–liquid mass transfer coefficient along with total power consumption (P/V). CFD simulation is used to obtain the gas holdup profile and the turbulent energy dissipation rate for both the contactors under the same operating conditions. From these values, the mean bubble size and interfacial area are calculated and these values are used for predicting the mass transfer coefficient. The mass transfer coefficient is obtained theoretically using the equation based on the Higbie’s penetration theory (Higbie, 1935) and Kolmogoroff’s theory of isotropic turbulence.

7.2. Experimental details

7.2.1. Mechanically agitated contactor

7.2.1.1. Hydrodynamics

The mechanically agitated contactor which is used to carry out the experiments is shown in Figure 7.1. The configuration of agitated contactor and methodology used for the experiments are already given in detail in Chapter 6.



1. Reactor
2. Agitator
3. Gas Sparger
4. Baffles
5. Jacket
6. D C Motor
7. Power Meter
8. Rotameters

Figure 7.1. A schematic diagram of the experimental setup for mechanically agitated contactor

7.2.1.2. Mass transfer

Two methods are available in the literature for the determination of volumetric mass transfer coefficient *viz.*, sulphite oxidation method (SOM) and the gassing out method (GOM). For the present study, sulphite oxidation method is used for the determination of the volumetric mass transfer coefficient. When Na₂SO₃ solution is continuously supplied to a mechanically agitated aerated vessel, oxygen absorption accompanied by Na₂SO₃ oxidation occurs. The oxidation of sulphite to sulphate by oxygen is catalysed by the presence of either copper or cobalt ions, and is represented by



Steady-state determinations of the oxidation rate are usually made by titrimetric analysis of the residual Na₂SO₃ concentration in the contactor. In the slow

Comparison study of Mechanically agitated and Fluidised Bed Contactors

reaction regime, the rate of oxygen transfer through the gas–liquid boundary is equal to the rate of oxygen consumption through reaction in the bulk liquid and the concentration of oxygen in the bulk liquid is almost zero and the rate of transfer of oxygen r_{O_2} is given by the expression

$$r_{O_2} = k_{gl} a_g C_i \dots\dots\dots(7.2)$$

where $k_{gl} a_g$ is the volumetric gas–liquid mass transfer coefficient, C_i is the concentration of oxygen at the gas–liquid interface.

From Equation 7.1 we obtain,

$$r_{O_2} = r_{SO_3} / 2 \dots\dots\dots(7.3)$$

where r_{SO_3} is the rate of oxidation of sulphite, and is given by

$$r_{SO_3} = \frac{dC_{SO_3}}{dt} = 2k_{gl} a_g C_i \dots\dots\dots(7.4)$$

where C_{SO_3} is the concentration of sulphite in the contactor. Following the change in concentration of sulphite with time, volumetric gas–liquid oxygen mass transfer coefficient can be determined.

7.2.2. Fluidised bed contactor

7.2.2.1. Hydrodynamics

Figure 7.2 shows the schematic diagram of the experimental setup of the gas–liquid–solid fluidised bed contactor. The fluidised bed consists of a cylindrical column having an internal diameter 0.15m and an effective height 1.5 m. The bottom end of the fluidised bed is connected to a conical distributor and its top to an enlarged section. The conical distributor is packed with glass spheres for the purpose of distributing the liquid uniformly throughout the cross section of the column and a

Comparison study of Mechanically agitated and Fluidised Bed Contactors

perforated plate is kept above the conical distributor and it is used to retain the solids. A venturi mixer is used as the gas inlet for the three-phase fluidisation system, because of its ability to generate small size bubbles. It was provided between the discharge of the centrifugal pump and the inlet of the conical distributor. The outlet from the fluidised bed is connected to a solid-separator for recycling any entrained solids back to the fluidised bed through a recycling duct. The flow rate of the liquid is varied by adjusting the frequency of power supply to the motor coupled to a centrifugal pump. The piezometric pressure readings are noted as the flow rates are varied through the piezometer connected to the various pressure tapings located along the axial direction on the wall of the column. The variation of solid bed is monitored by visual inspection through transparent windows. The phase holdup of solid, liquid and gas are calculated using the following equations. The solid holdup is obtained using the following expression based on solid loading (W) of fluidised bed column

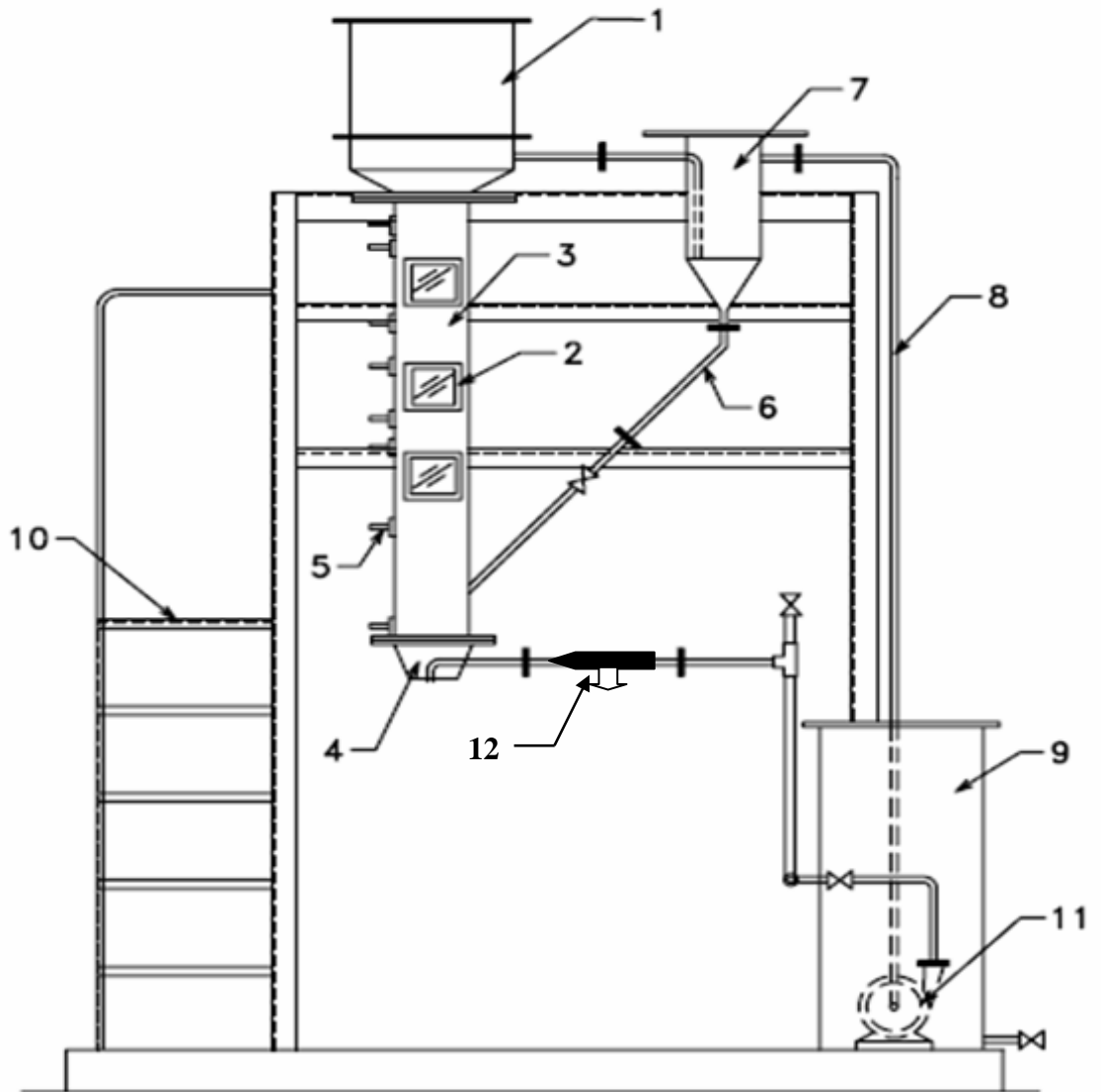
$$\epsilon_s = \frac{W}{\rho_s \frac{\pi}{4} D^2 H} \dots\dots\dots(7.5)$$

and the sum of the volume fractions of the individual phases is unity; thus,

$$\epsilon_l + \epsilon_g + \epsilon_s = 1 \dots\dots\dots(7.6)$$

The total axial pressure gradient at any cross section in the column under the steady-state condition represents the total weight of the bed consisting of the three phases per unit volume and it is given by

$$\frac{-dp}{dz} = (\epsilon_l \rho_l + \epsilon_g \rho_g + \epsilon_s \rho_s)g \dots\dots\dots(7.7)$$



- | | |
|-------------------------------|---------------------------|
| 1. Entrainment Section | 7. Liquid solid separator |
| 2. Glass window | 8. Liquid recycling duct |
| 3. Fluidised bed column | 9. Collecting tank |
| 4. Conical bottom distributor | 10. Platform |
| 5. Pressure tapping port | 11. Centrifugal pump |
| 6. Slurry recycling duct | 12. Venturi Mixer |

Figure 7.2. A schematic diagram of the circulating fluidised bed contactor used for experiments

7.2.2.2. Mass transfer

The determination of volumetric mass transfer coefficient is carried out using standard dynamic gassing out method. At the beginning of the experiment, oxygen present in the liquid is stripped out using nitrogen until minimum levels of dissolved oxygen is achieved. When the liquid is completely free of gas bubbles, air is sparged. The time dependent dissolved oxygen concentration is measured with a polarographic-membrane dissolved oxygen probe. The dissolved oxygen controller is provided with large dual display LCD for easy reading with clear multiple enunciators, alarm status operational and with memory recordable facility. Thus, oxygen mass balance is given by the following equation:

$$\frac{dC_{O_2}}{dt} = k_L a (C_{O_2}^* - C_{O_2}) \dots\dots\dots(7.8)$$

where $C_{O_2}^*$ is the saturation concentration of oxygen component in liquid phase in equilibrium with gas phase and C_{O_2} is concentration of oxygen in liquid phase.

The integration of above equation yields

$$\ln(C_{O_2}^* - C_{O_2}) = -k_L a . t \dots\dots\dots(7.9)$$

Thus, $k_L a$ can be evaluated from the slope of $\ln(C_{O_2}^* - C_{O_2})$ vs. time plot.

7.3. CFD model for hydrodynamics simulation

The gas-liquid-solid flows in mechanically agitated contactor and fluidised bed contactor are simulated using Eulerian multi-fluid approach. Each phase is treated as different continua which interacts with other phases everywhere in the computational domain. The motion of each phase is governed by respective Reynolds

Comparison study of Mechanically agitated and Fluidised Bed Contactors

averaged mass and momentum conservation equations. The model equations used in the present study are already given in Chapters 5 and 6. But the only difference is the usage of different drag force model for the momentum transfer between gas and liquid phases for the case of fluidised bed column. This drag coefficient is modified based on the following observation.

In the literature, different drag force models exist for the momentum transfer between gas–liquid phases (Schiller and Naumaan, 1935; Grace, 1973; Ishii and Zuber, 1979; Tomiyama, 1998; Zhang and Vanderheyden, 2002). Recently Tabib et al. (2008) studied the effect of various drag forces on the gas holdup and bubble rise velocity and reported that the drag law of the Zhang and Vanderheyden (2002) gives better prediction for various values of gas superficial velocities when compared to experimental results. Therefore based on their assumption, the drag law of the Zhang and Vanderheyden (2002) is used in the present study for the momentum transfer between gas and liquid phases and is represented by the following equation:

$$F_{D,lg} = C_{D,lg} \frac{3}{4} \rho_l \frac{\epsilon_g}{d_b} |\vec{u}_g - \vec{u}_l| (\vec{u}_g - \vec{u}_l) \quad \dots\dots\dots(7.10)$$

where $C_{D,lg}$ is the drag coefficient between liquid and gas and is given as

$$C_{D,lg} = 0.44 + \frac{24}{Re_b} + \frac{6}{1 + \sqrt{Re_b}} \quad \dots\dots\dots(7.11)$$

in which Re_b is bubble Reynolds number and it is given as

$$Re_b = \frac{d_b V_s \rho_l}{\mu_l} \quad \dots\dots\dots(7.12)$$

where V_s is axial slip velocity between gas and liquid. Inclusion of this drag coefficient has resulted in better prediction of averaged gas hold up.

7.4. Numerical Simulations

The commercial flow solver ANSYS CFX-10 was used for solving the governing equations of 3D hydrodynamic behavior of gas–liquid–solid flows in mechanically agitated and fluidised bed contactors. Tables 7.1 and 7.2 summarise the process and model parameters used for the present simulation for both the contactors. High-resolution discretisation scheme, which accounts for accuracy and stability, was chosen for obtaining the discretisation equations for all the governing equations. The discrete governing equations were solved by the element based finite volume method. Pressure–velocity coupling is based on the Rhie- Chow algorithm. For transient simulations, the second order backward Euler time scheme with time step of 0.001s is used. Other details of numerical methodology are already given in detail in the earlier Chapters.

Table 7.1. Model parameters used for the CFD simulations

Parameters	Fluidised bed contactor	Mechanically agitated contactor
Mode of simulation	3D	3D
Grid size	25000 nodes	200000 nodes
Time step	0.001 s	steady state
Inlet boundary	inlet velocity of gas and liquid	mass flow rate of gas
Outlet boundary	pressure (1atm)	degassing
Wall Boundary	no slip for all the phases	no slip for all the phases

Comparison study of Mechanically agitated and Fluidised Bed Contactors

Table 7.2. Process parameters used for the CFD simulations

Parameters	Fluidised bed contactor	Mechanically agitated contactor
Density of solid (kg/m ³)	4200	4200
Mean particle Size (µm)	230	230
Mean bubble size, mm	1	4
Initial bed height, m	0.35	
Solid volume fraction (solid loading = 5 kg)	0.6	0.1
Bed voidage (-)	0.4	0.32
Superficial liquid velocity U _l , m/s	0.01-0.04	-
Superficial gas velocity U _g , m/s	0.00566, 0.01132 m/s	0.5, 1.0 vvm

7.5. Results and Discussion

The dynamic characteristics of gas–liquid–solid flows using multi-fluid Eulerian approach for both the contactors are validated qualitatively with the data available in the literature and are presented in the Chapters 3, 4, 5 and 6. In this work, the main focus is on comparing the performance of both these contactors in terms of hydrodynamic and mass transfer characteristics.

7.5.1. Hydrodynamic parameters

The hydrodynamic parameters used in this work for comparing the performance of both the reactors are gas holdup, mean bubble size, interfacial area and power consumption. For comparing the performance, we have chosen equivalent processing conditions for both the reactors. Solid loading for both the contactors is 5 Kg and the particle size chosen is 230 µm. For the case of mechanically agitated contactor, the impeller speed is set above the critical impeller speed and the

Comparison study of Mechanically agitated and Fluidised Bed Contactors

simulation is carried out for both radial (disc turbine) and axial type (pitched blade turbine) impellers at two air flow rates viz., 0.5 and 1.0 vvm. CFD simulation of mechanically agitated contactor is carried out at the critical impeller speed of 520 RPM for the case of disc turbine (DT) impeller and at the critical impeller speed of 428 RPM for the case of pitched blade turbine with downward pumping (PBSD). For the case of fluidised bed contactor, liquid superficial velocity is varied from ($U_l=0.01-0.04$ m/s) which is above the minimum fluidisation velocity and gas superficial velocities is set to 0.00566 and 0.01132 m/s which is equivalent to the air flow rates used in mechanically agitated contactor.

7.5.1.1. Gas holdup

The gas holdup is one of the most important parameters for characterising the hydrodynamics and it depends mainly on the gas velocity and physical properties. The gas holdup obtained from the CFD simulation is compared for both the reactors at the same operating conditions. The gas holdup obtained from CFD simulation for both mechanically agitated reactor (radial and axial type impeller) and fluidised bed contactor are shown in Figures 7.3 (a, b, c). It can be seen from Figure 7.3a that the values of gas holdup is higher in lower regions of the tank and is lower in the upper regions of the tank. This is because the radial flow impellers discharge fluid radially outwards towards the wall. Also it can be observed that gas hold up is more near the tip of the impeller. This may be due to the breakage of bubbles by the high shear produced by the impeller. For the case of axial type impeller (PBSD, Figure 7.3b), the gas holdup is more or less distributed uniformly throughout the tank. The gas holdup obtained from the fluidised bed contactor is shown in Figure 7.3c. It can be seen from

Comparison study of Mechanically agitated and Fluidised Bed Contactors

Figure 7.3c that the time-averaged gas holdup in the fluidised bed contactor is in the range of 0.03–0.05.

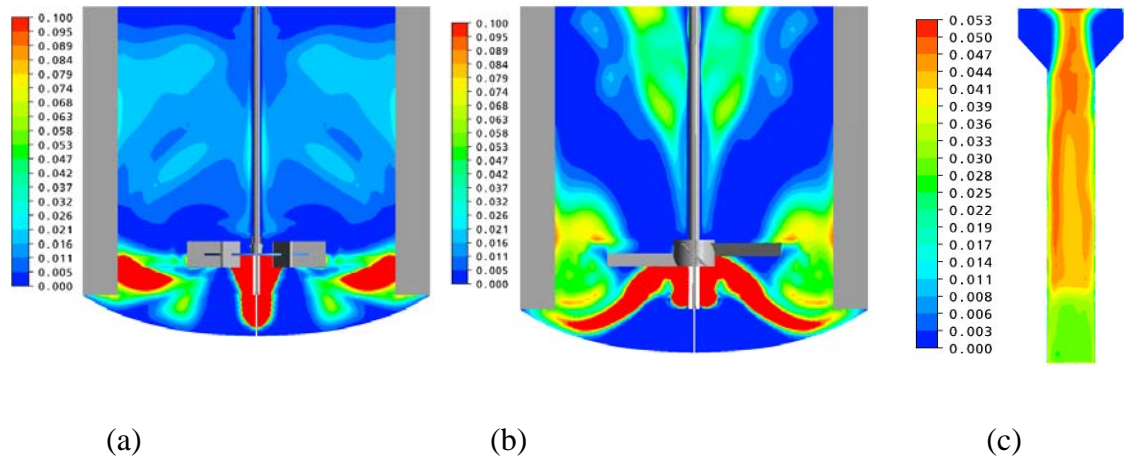


Figure 7.3. Contour plot of the fractional gas holdup, (a) mechanically agitated reactor with DT, (b) mechanically agitated contactor with PBTD (c) Fluidised bed contactor

7.5.1.2. Mean bubble size

Bubble size is a very important parameter in gas–liquid–solid reactor design. The distribution of bubble size in mechanically agitated and fluidised bed contactors are useful for a better understanding of gas dispersion mechanisms. Once the gas holdup and the turbulent energy dissipation rate are obtained from the CFD simulation, the local values of the average bubble diameter for mechanically agitated contactor are calculated using the following equation (Tatterson, 1991)

$$d_b = 4.15 \left(\frac{(\rho \epsilon)^{0.4} \rho^{0.2}}{\sigma^{0.6}} \right)^{-1} \epsilon_g^{0.5} + 0.0009 \dots\dots\dots(7.13)$$

For the case of fluidised bed contactor, Calderbank and Moo-Young (1961) reported the following equation for calculating the mean bubble diameter:

$$d_b = 1.90 \left(\frac{\sigma^{0.6} \epsilon_g^{0.65}}{(P_g / V)_l^{0.4} \rho_l^{0.2}} \right) \dots\dots\dots(7.14)$$

Comparison study of Mechanically agitated and Fluidised Bed Contactors

where ε and ε_g are the turbulent energy dissipation rate and the local gas holdup value and they are obtained from the CFD simulations for both the contactors. The energy dissipation rate is calculated by carrying out the volume integration of liquid phase energy dissipation. The local values of the average bubble diameter is shown in Figures 7.4 (a, b, c). It can be seen from Figure 7.4a that the average bubble diameter is lower and about 1mm near the tip of impeller region where there is a radial jet flow. In addition, this is a region where highest turbulent energy dissipation rate occurs. The mean bubble size increases with decrease in energy dissipation rates and this pattern is shown in the region away from the impeller. For the case of PBTD (Figure 7.4b), the mean bubble size is uniform and is around 3–4 mm. This is because PBTD impeller generates medium intensity turbulence, which gives better distribution of turbulence over the entire vessel of mechanically agitated contactor. The mean bubble size for the case of fluidised bed reactor is shown in Figure 7.4c and is in the range 1-2 mm.

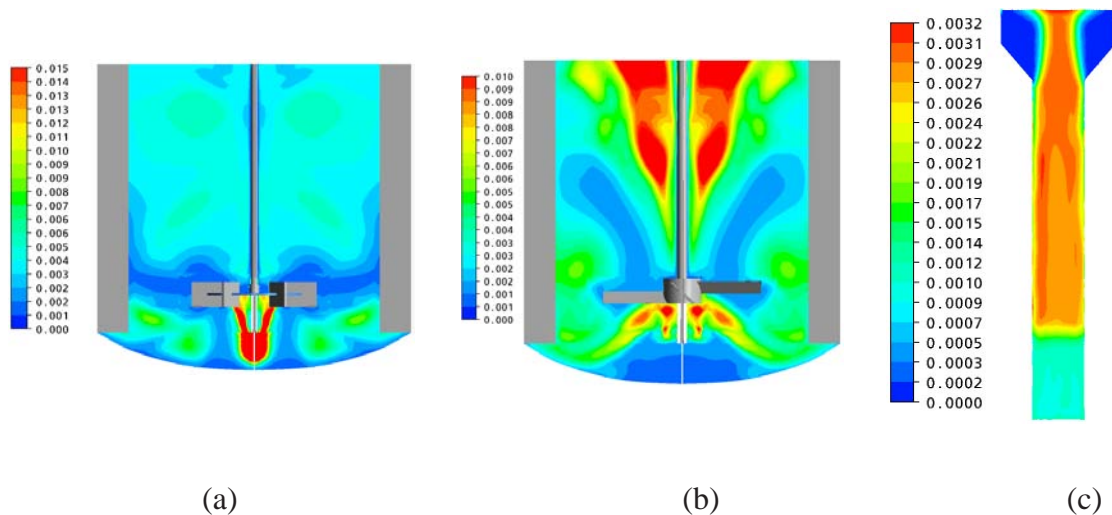


Figure 7.4. Contour plot of the mean bubble size (a) mechanically agitated contactor with DT, (b) mechanically agitated contactor with PBTD (c) Fluidised bed contactor

7.5.1.3. Interfacial area

Once the local mean bubble size is obtained, the local value of the interfacial area is obtained by using the following equation for both the contactors:

$$a = \frac{6 \epsilon_g}{d_b (1 - \epsilon_g)} \dots\dots\dots(7.15)$$

The local interfacial area obtained for both the contactors using equation (7.15) is shown in Figures 7.5 (a, b, c). It can be seen from Figure 7.5a that the interfacial area is higher (about 300 m²/m³) at the lower region of the mechanically agitated reactor for the case of DT and is lower (about 60 m²/m³) away from the impeller. This may be due to the lower value for the local mean bubble size. The volume averaged interfacial area within the contactor is 100 m²/m³. For the case PBTD impeller, the local interfacial area is higher (about 300 m²/m³) around the impeller and everywhere else it is lower value of around 50 m²/m³ (Figure 7.5b), but the value of overall volume averaged interfacial area for PBTD is 150 m²/m³. This value is more compared to that of the DT.

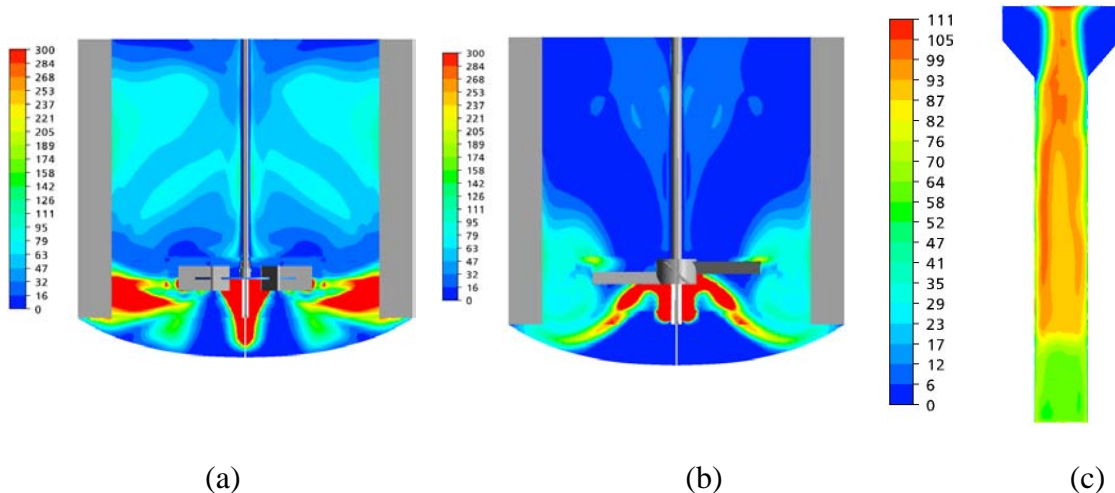


Figure 7.5. Contour plot of the interfacial area (m²/m³) (a) mechanically agitated reactor with DT ,(b) mechanically agitated reactor with PBTD (c) Fluidised bed reactor.

Comparison study of Mechanically agitated and Fluidised Bed Contactors

The volume averaged gas holdup and interfacial area for both the contactors are plotted against the power consumption per unit volume of contactor (P/V) under the fixed operating conditions. The other operating conditions remain the same as above. The total power consumption for both the contactors are obtained by making use of Equations (7.16) and (7.17) respectively.

$$\frac{P_g}{V_{tot}} = \frac{P_g}{V_l} + \rho_l g V_g \tag{7.16}$$

where V_l is the liquid volume, V_g is the superficial gas velocity and

$$P_g = \frac{\pi}{4} D^2 H g (U_l + U_g) (\epsilon_s \rho_s + \epsilon_l \rho_l + \epsilon_g \rho_g) \tag{7.17}$$

where U_l is the superficial liquid velocity, U_g is the superficial gas velocity

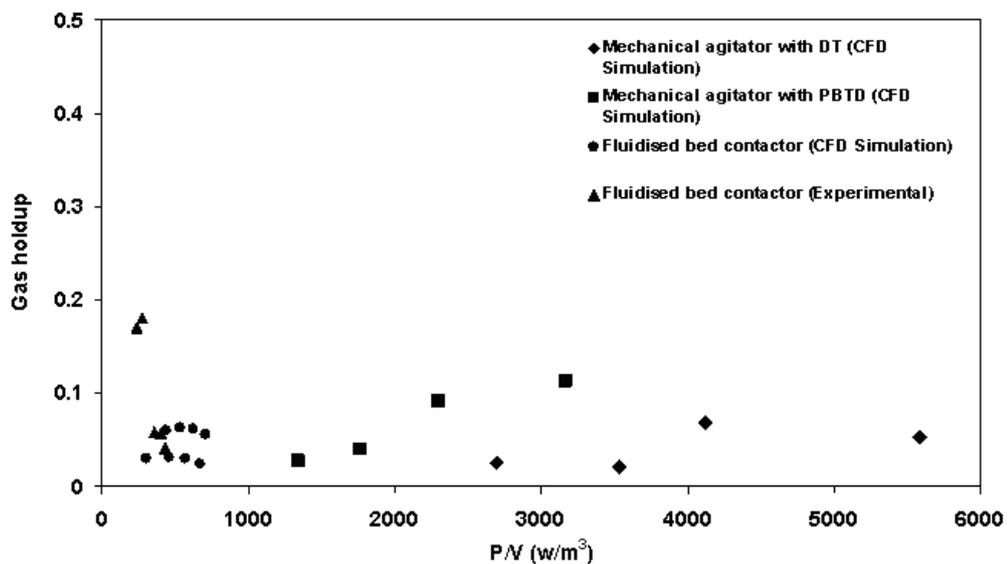


Figure 7.6. Gas holdup versus the total power consumption per unit volume of contactor (P/V)

Comparison study of Mechanically agitated and Fluidised Bed Contactors

It can be seen from Figure 7.6 that the gas holdup increases with increasing total power consumption per unit volume (P/V) for both the contactors. Figure 7.6 also shows that the fluidised bed contactor gives the gas holdup in the range of 0.03–0.07 at lower P/V values whereas the mechanically agitated contactor with DT and PBTB gives the same range of gas holdup at higher P/V values. This shows a typical mechanically agitated contactor requires around 1000–3000 W/m³ to obtain the same gas hold up (0.03–0.1).

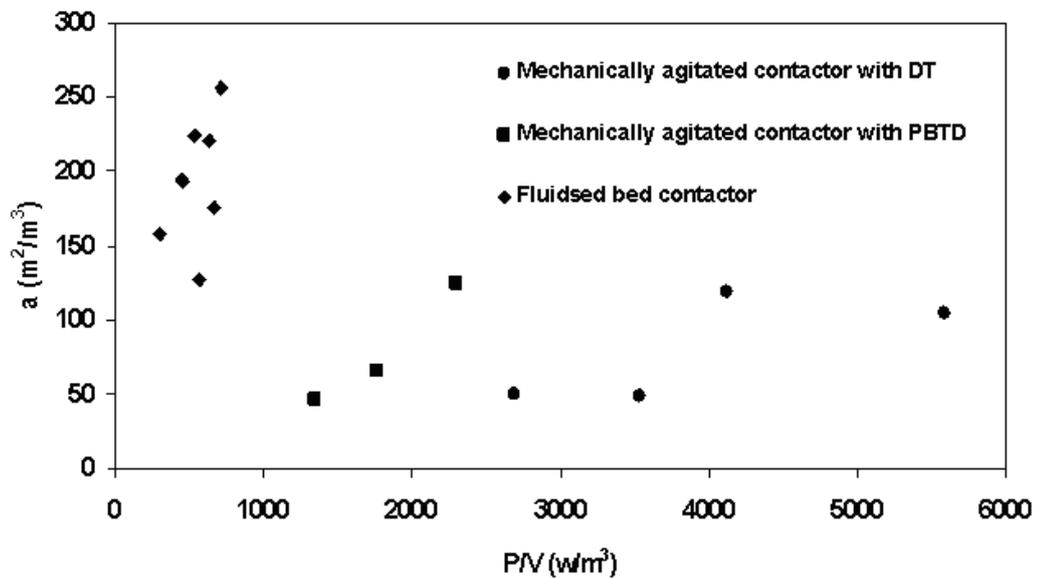


Figure 7.7. Interfacial area versus the total power consumption per unit volume of contactor (P/V)

The variation of the interfacial area with respect to the total power consumption per unit volume of the contactor (P/V) is shown in Figure 7.7. In fluidised bed contactor, the interfacial area ranges between 100 and 250 m²/m³ while the power consumption varies from 300 and 700 W/m³. In mechanically agitated contactor, the interfacial area ranges between 50 and 150 m²/m³ while the power consumption varies from 1000 and 4000 W/m³. Thus, fluidised bed contactor gives higher interfacial area at lower power

Comparison study of Mechanically agitated and Fluidised Bed Contactors

input than mechanically agitated contactor with DT and PBTB. In addition, it can be seen clearly from Figure 7.7 that the interfacial area generated by the fluidised bed contactor are about 50 % higher than those generated by the mechanically agitated contactor.

7.5.2. Mass Transfer Parameters

For comparing the performance of both the contactors in terms of mass transfer, the parameter chosen is gas–liquid mass transfer coefficient. The volumetric mass transfer coefficient (k_L) is calculated from theoretical mass transfer equation which is based on Higbie’s penetration theory (1935) and Kolmogoroff’s theory of isotropic turbulence (Tobajas et al., 1999) and is given by

$$k_L = \frac{2}{\sqrt{\pi}} \sqrt{\frac{D_L}{t}} \dots\dots\dots(7.18)$$

where t is the contact time, which is calculated based on Kolmogoroff’s theory of isotropic turbulence, $t = \sqrt{\frac{v}{\epsilon}}$.

Therefore,

$$k_L = \frac{2}{\sqrt{\pi}} \sqrt{D_L} \left(\frac{\epsilon}{v}\right)^{1/4} \dots\dots\dots(7.19)$$

where ϵ is the energy dissipation rate, (J/Kg) and v is the kinematic viscosity (m^2/s).

The volumetric liquid phase mass transfer coefficient ($k_L a$) can be calculated using Equations 7.15 and 7.19 and is given as

$$k_L a = \frac{2}{\sqrt{\pi}} \sqrt{D_L} \left(\frac{\epsilon}{v}\right)^{1/4} \frac{6 \epsilon_g}{d_b (1 - \epsilon_g)} \dots\dots\dots(7.20)$$

For the case of three phase reactors, the suspended solid particles influence the gas–liquid mass transfer. Various authors (Joosten et al., 1977; Oguz et al., 1987; Lee et al., 1978; Kojima et al., 1987) have developed different correlations for gas–liquid

Comparison study of Mechanically agitated and Fluidised Bed Contactors

mass transfer coefficient in the presence of solid particles for three phase systems.

Kojima et al. (1987) obtained the following equation for gas–liquid mass transfer in the presence of solid for the case of mechanically agitated contactor:

$$\frac{(k_L a)_s}{(k_L a)} = 1 - \phi_s \dots\dots\dots(7.21)$$

Geetha (1997) developed the following correlation for gas–liquid mass transfer in the presence of solid particles, which is given as

$$\frac{(k_L a)_s}{(k_L a)} = 1 - \frac{\phi_s}{0.45} \dots\dots\dots(7.22)$$

Nigam and Schumpe (1987) have developed the following relation for the gas–liquid mass transfer in the presence of glass spheres in three-phase fluidised beds:

$$\frac{(k_L a)_s}{(k_L a)} = 1 - \frac{\phi_s}{0.58} \dots\dots\dots(7.23)$$

In the present study, the above equations are used for calculating the gas–liquid mass transfer coefficient in the presence of suspended solid particles for both the types of contactors. In Figure 7.8, $(k_L a)_s$ values for the mechanically agitated contactor and fluidised bed contactor are plotted against power consumption per unit volume of contactor (P/V) for equivalent operating conditions. It can be seen from Figure 7.8 that, $(k_L a)_s$ value increases with increase in total power consumption per unit volume (P/V) for both the contactors. The value of $k_L a$ is in the range 0.05–0.2 s⁻¹ but the total power consumption per unit volume of contactor (P/V) varies between 300 and 700 W/m³ for fluidised bed contactor, whereas for mechanically agitated contactor the power consumption per unit volume of contactor (P/V) varies between 1000 and 4000 W/m³ for almost the same range of $(k_L a)_s$ (0.05–0.25 s⁻¹). It can be

Comparison study of Mechanically agitated and Fluidised Bed Contactors

concluded that the fluidised bed contactor gives better performance than the mechanically agitated contactor at lower power input.

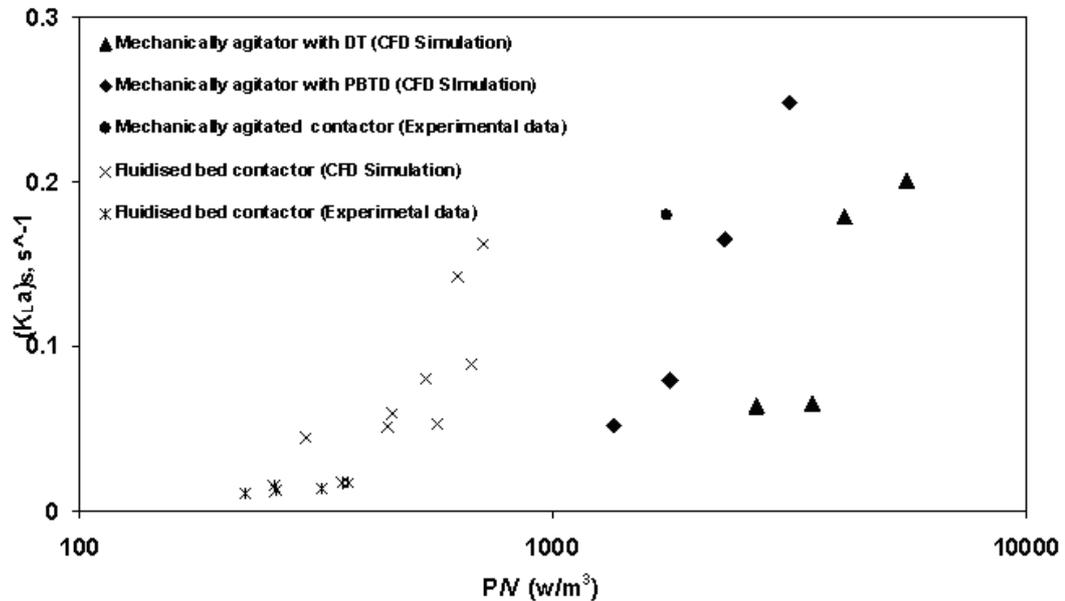


Figure 7.8. Gas–liquid mass transfer coefficient $(k_{La})_s$ prediction versus the total power consumption per unit volume of contactor for mechanically agitated and fluidised bed contactors

7.6. Conclusions

Using CFD, the performance of gas–liquid–solid mechanically agitated contactor and fluidised bed reactors are compared in terms of hydrodynamic parameters like gas holdup, mean bubble size and interfacial area and mass transfer parameters in terms of gas–liquid mass transfer coefficient in this work.

- For the case of gas–liquid–solid fluidised bed contactor, the gas holdup values are in the range 0.03–0.07 at lower P/V values (300–700 W/m^3) whereas three-phase mechanically agitated contactor with DT and PBT gives almost the same range of gas holdup (0.03–0.1) at higher P/V values (1000–3000 W/m^3).

Comparison study of Mechanically agitated and Fluidised Bed Contactors

- Similarly for the case of interfacial area, the values are in the range of 100 and 250 m^2/m^3 for the case of three-phase fluidised bed at lower P/V values (300–700 W/m^3). But for the mechanically agitated contactor the interfacial area values are in the range of 50 to 150 m^2/m^3 while P/V varies between 1000 and 4000 W/m^3 .
- The value of gas-liquid mass transfer coefficient $k_L a$ is in the range 0.05–0.2 s^{-1} but the total power consumption per unit volume of contactor (P/V) varies between 300 and 700 W/m^3 for fluidised bed contactor, whereas for the mechanically agitated contactor the power consumption per unit volume of contactor (P/V) varies between 1000 and 4000 W/m^3 for almost the same range of $(k_L a)_s$ (0.05–0.25 s^{-1}).
- It can be concluded that the gas–liquid–solid fluidised bed contactor gives better performance than the mechanically agitated contactor at lower total power consumption per unit volume of contactor (P/V) in terms of gas holdup, interfacial area and gas–liquid mass transfer coefficient $(k_L a)_s$.

Chapter 8

CONCLUSIONS AND FUTURE WORK

8.1. Conclusions

In this work, the validated computational fluid dynamic models that predict accurately the various flow behaviors in liquid–solid and gas–liquid–solid mechanically agitated reactor and fluidised bed reactor under various operating conditions was carried out. This chapter summarises all the major observations and the conclusions drawn from this study. The avenues for future work are also identified.

8.1.1. Mechanically agitated contactor

- ✓ The CFD simulation of solid suspension in a **liquid–solid and gas–liquid–solid mechanically agitated contactor** was carried out using Eulerian multi-fluid approach along with standard k- ϵ turbulence. The CFD prediction of critical impeller speed for solid suspension in both two-phase and three-phase mechanically agitated contactor based on the criteria of standard deviation method and cloud height are compared quantitatively with the experimental values reported in the literature. An adequate agreement was found between CFD predictions and the experimental data.
- ✓ CFD simulation was further extended to study the effect of impeller design (DT, PBTD and A-315 hydrofoil), impeller speed and particle size (360–650 μm) on the prediction of critical impeller speed for solid suspension in **liquid–solid mechanically agitated contactor**.
- ✓ The CFD simulation was further extended to study the effect of impeller design (DT, PBTD), impeller speed, particle size (125–230 μm) and air flow rate (0–1.0 vvm) on the prediction of critical impeller speed for solid suspension in **gas–liquid–solid mechanically agitated contactor**.

8.1.2. Fluidised bed reactor

- ✓ The CFD simulation of hydrodynamics of **liquid–solid and gas–liquid–solid fluidised bed** was performed using the Eulerian multi-fluid approach. The CFD predictions of solid phase hydrodynamics in terms of mean and turbulent velocities, and gas and liquid phase hydrodynamics in terms of phase velocities and holdup are validated with literature experimental data. An adequate agreement was demonstrated between CFD simulation results and experimental findings.
- ✓ The CFD simulation of **both solid–liquid and gas–solid-liquid fluidised bed** exhibits a single solid circulation cell for all the operating conditions, which is consistent with the observations reported by various authors.
- ✓ The predicted flow pattern of the averaged solid velocity profile from CFD simulation shows a higher upward velocity at the center region and a lower downward velocity at the wall region of the column for both two phase and three phase fluidised bed reactors.

8.1.3. Comparison of reactors

Based on validated CFD predictions, the performance of mechanically agitated reactor and fluidised bed reactor have been compared in terms of the following.

- Hydrodynamics, by comparing power per volume (P/V) for solid suspension in liquid–solid and gas–liquid–solid fluidised bed and solid suspension in liquid–solid and gas–liquid–solid mechanically agitated reactor.
- Transport phenomena, by comparing gas–liquid mass transfer in gas–liquid–solid fluidised bed and gas–liquid–solid mechanically agitated reactor.

Conclusions and Future work

- ✓ For the case of gas–liquid–solid fluidised bed contactor, the **gas holdup** values are in the range 0.03–0.07 at lower P/V values (300–700 W/m³) whereas three-phase mechanically agitated contactor with DT and PBTD gives almost the same range of gas holdup (0.03–0.1) values at higher P/V values (1000–3000 W/m³).
- ✓ Similarly for the case of **interfacial area**, the values are in the range of 100 and 250 m²/m³ for the case of three-phase fluidised bed at lower P/V values (300–700 W/m³). But for the mechanically agitated contactor the interfacial area values are in the range of 50 to 150 m²/m³ while P/V varies between 1000 and 4000 W/m³
- ✓ The value of gas–liquid mass transfer coefficient (k_{LA})_s is in the range 0.05–0.2 s⁻¹ but the total power consumption per unit volume of contactor (P/V) varies between 300 and 700 W/m³ for three-phase fluidised bed contactor, whereas for the mechanically agitated contactor the power consumption per unit volume of contactor (P/V) varies between 1000 and 4000 W/m³ for almost the same range of (k_{LA})_s (0.05–0.25 s⁻¹).

It can be concluded that the gas–liquid–solid fluidised bed contactor gives better performance than the mechanically agitated contactor at lower total power consumption per unit volume of contactor (P/V) in terms of gas holdup, interfacial area and gas–liquid mass transfer coefficient (k_{LA})_s.

8.2. Scope for Future work

- ✓ The present study covers the comparison of performance of mechanically agitated and fluidised bed contactors based on hydrodynamic and gas–liquid mass transfer parameters in hydrometallurgical applications through CFD. In future, the performance between these reactors is to be compared based on the kinetics of rusting process i.e., the percentage of removal of hydrated iron oxide from reduced ilmenite through hydrometallurgical aeration leaching.
- ✓ It has been observed that the drag force is an important term for interphase momentum exchange between the different phases. The existing models available in literature for the drag force between gas–liquid systems are actually based on the experiments on single bubbles in infinite stagnant liquids. Thus there is a need to obtain realistic models for the drag force over a wide range of operating conditions in gas–liquid systems.
- ✓ The numerical method used for turbulence also needs further development. The turbulence model used in the present study is k- ϵ model, which assumes isotropy. A systematic analysis is needed for understanding the physical significance of the turbulence parameters for multiphase flows where interface forces and interface energy transfer plays an important role. The future work should also include Reynolds stress modelling (RSM) and Large Eddy Simulation (LES) of turbulence.
- ✓ To further improve the accuracy of predictions of bubble rise velocity and gas–holdup in three-phase fluidized bed, the variation of bubble size due to bubble break-up and bubble coalescence should be incorporated in the CFD model.

Conclusions and Future work

- ✓ The physical significance of non-drag forces like virtual mass, Basset force and lift force has to be studied in detail for proper implementation in multiphase CFD model.
- ✓ Application of kinetic theory of granular flow (KTGF) approach for particle–particle interactions in the dense region of three-phase fluidised bed has to be considered and comparison should be made between KTGF and CVM approach.

REFERENCES

References

REFERENCES

Armenante, P.M., Nagamine, E.U., 1998. Effect of low off-bottom impeller clearance on the minimum agitation speed for complete suspension of solids in stirred tanks. *Chemical Engineering Science* 53, 1757-1775.

Aubin, J., Le Sauze, N., Bertrand, J., Fletcher, D.F., Xuereb, C., 2004. PIV measurements of flow in an aerated tank stirred by a down- and an up-pumping axial flow impeller. *Experimental Thermal and Fluid Science* 28, 447-456.

Auton, T.R., 1983. *The Dynamic of Bubbles, Drops and Particles in motion in liquids*. Ph.D. Thesis, University of Cambridge, UK.

Bahary, M., 1994. *Experimental and Computational Studies of Hydrodynamics in Three-Phase and Two-Phase Fluidised Beds*. Ph.D. Thesis, Illinois Institute of Technology, Chicago.

Bakker, A., Fasano, J.B., Myers, K.J., 1994. Effects of flow pattern on the solids distribution in a stirred tank. *Institution of Chemical Engineering Symposium Series* 136, 1-8.

Balamurugan, S., Lad, M.D., Gaikar, V.G., Patwardhan, A.W., 2007. Hydrodynamics and mass transfer characteristics of gas-liquid ejectors. *Chemical Engineering Journal* 131, 83-103.

Baldi, G., Conti, R., Alaria, E., 1978. Complete suspension of particles in mechanically agitated vessels. *Chemical Engineering Science* 33, 21-25.

Barigou, M., Greaves, M., 1992. Bubble size distribution in a mechanically agitated gas-liquid contactor. *Chemical Engineering Science* 47, 2009-2025.

Barrue, H., Bertrand, J., Cristol, B., Xuereb, C., 2001. Eulerian simulation of dense solid-liquid suspension in multi-stage stirred vessel. *Journal of Chemical Engineering Japan*. 34, 585-594.

Becker, S., Sokolichin, A., Eigenberger, G., 1994. Gas-liquid flow in bubble columns and loop reactors: Part II. Comparison of detailed experiments and flow simulations. *Chemical Engineering Science* 49, 5747-5762.

Bertola, F., Baldi, G., Marchisio, D., Vanni, M., 2004. Momentum transfer in a swarm of bubbles: estimates from fluid-dynamic simulations. *Chemical Engineering Science* 59, 5209-5215.

Bohnet, M., Niesmak, G., 1980. Distribution of solids in stirred suspension. *General Chemical Engineering* 3, 57-65.

References

- Bouaifi, M., Hebrard, G., Bastoul, D., Roustan, M., 2001. A comparative study of gas hold-up, bubble size, interfacial area and mass transfer coefficients in stirred gas–liquid reactors and bubble columns. *Chemical Engineering and Processing* 40, 97-111.
- Bouillard, J.X., Lyczkowski, R.W., Gidaspow, D., 1989. Porosity distribution in a fluidised bed with an immersed obstacle. *A.I.Ch.E. Journal* 35, 908-922.
- Briens, L.A., Ellis, N., 2005. Hydrodynamics of three-phase fluidised bed systems examined by statistical, fractal, chaos and wavelet analysis methods. *Chemical Engineering Science* 60, 6094-6106.
- Brownstein, A.M., Greene, M.I., Gartside, R.J., Roby, A.K., 1996. Proceedings of the 21st Annual Dewitt Petrochemical Review, Houston, TX.
- Brucato, A., Ciofalo, M., Grisafi, F., Micale, G., 1994. Complete numerical simulation of flow fields in baffled stirred vessels: the inner-outer approach. *Institution of Chemical Engineering Symposium Series* 136, 155-162.
- Brucato, A., Grisafi, F., Montante, G., 1998. Particle drag coefficient in turbulent fluids. *Chemical Engineering Science* 53, 3295-3314.
- Bujalski, W., Konno, M., Nienow, A.W., 1988. Scale-up of 45° pitch-blade agitators for gas dispersion and solid suspension. *Proceeding of 6th European Conference on Mixing, Italy*, 389-398.
- Bujalski, W., Takenaka, K., Paolini, S., Jahoda, M., Paglianti, A., Takahashi, K., Nienow, A.W., Etchells, A.W., 1999. Suspension and liquid homogenization in high solids concentration stirred chemical reactors. *Chemical Engineering Research and Design* 77, 241-247.
- Bunner, B., Tryggvason, G., 1999. Direct numerical simulations of dispersed flows. *In: Proceedings of the Ninth Workshop on Two-Phase Flow Predictions, Germany*, 13-19.
- Buwa, V.V., Ranade, V.V. 2004. Characterization of dynamics of gas–liquid flows in rectangular bubble columns. *A.I.Ch.E. Journal* 50, 2394-2407.
- Calderbank, P. H., 1967. Gas Absorption from Bubbles. *The Chemical Engineers* CE209-CE233.
- Calderbank, P.H., Moo-Young, M.B., 1961. The continuous phase heat and mass transfer properties of dispersions. *Chemical Engineering Science* 16, 39-54.
- Chapman, C.M., Nienow, A.W., Cooke, M., Middleton, J.C., 1983a. Particle–gas–liquid mixing in stirred vessels, part I: particle–liquid mixing. *Chemical Engineering Research and Design* 61a, 71-81.

References

Chapman, C.M., Nienow, A.W., Cooke, M.; Middleton, J.C. 1983b. Particle–gas–liquid mixing in stirred vessels, part III: three-phase mixing. *Chemical Engineering Research and Design* 61a, 167-181.

Chen, R.C., Reese, J., Fan, L.-S., 1994. Flow structure in a three-dimensional bubble column and three-phase fluidised beds. *A.I.Ch.E. Journal* 40, 1093-1104.

Chen, Z., Zheng, C., Feng, Y., Hofmann, H., 1995. Distributions of flow regimes and phase holdups in three-phase fluidised beds. *Chemical Engineering Science* 50, 2153-2159.

Chen, C. Fan, L.-S., 2004. Discrete simulation of gas–liquid bubble columns and gas–liquid–solid fluidized beds. *A.I.Ch.E. Journal* 50, 288-301.

Cheng, Y., Zhu, J.X., 2005. CFD modeling and simulation of hydrodynamics in liquid- solid circulating fluidised beds. *The Canadian Journal of Chemical Engineering* 83, 177-185.

Cheung, S.C.P., Yeoh, G.H., Tu, J.Y. 2007. On the numerical study of isothermal vertical bubbly flow using two population balance approaches. *Chemical Engineering Science* 62, 4659-4674.

Chudacek, M.W., 1986. Relationships between solids suspension criteria, mechanism of suspension, tank geometry, and scale-up parameters in stirred tanks. *Industrial and Engineering Chemistry Fundamentals* 25, 391-401.

Clift, R., Grace, J.R. Weber, M.E., 1978. *Bubbles, Drops, and Particles*. Academic press, New York.

Delnoij, E., Lammers, F.A., Kuipers, J.A.M., van Swaaij, W.P.M. 1997a. Dynamic simulation of dispersed gas-liquid two-phase flow using a discrete bubble model. *Chemical Engineering Science* 52, 1429-1458.

Delnoij, E., Kuipers, J.A.M., van Swaaij, W.P.M. 1997b. Dynamic simulation of gas-liquid two-phase flow: effect of column aspect ratio on the flow structure. *Chemical Engineering Science* 52, 3759-3772.

Delnoij, E., Kuipers, J.A.M., van Swaaij, W.P.M. 1999. A three-dimensional CFD model for gas–liquid bubble columns. *Chemical Engineering Science* 54, 2217-2226.

De Swart, J.W.A. Krishna, R., 2002. Simulation of the transient and steady state behaviour of a bubble column slurry reactor for Fischer-Tropsch synthesis. *Chemical Engineering and Processing* 41, 35-47.

Devanathan, N., Moslemian, D., Dudukovic, M.P., 1990. Flow mapping in bubble columns using CARPT. *Chemical Engineering Science* 45, 2285-2291.

References

Di Felice, R., 1994. The voidage functions for fluid–particle interaction system. *International Journal of Multiphase Flow* 20, 153-159.

Di Felice, R., 1995. Hydrodynamics of liquid fluidisation. *Chemical Engineering Science* 50, 1213-1245.

Dohi, N., Matsuda, Y., Itano, N., Shimizu, K., Minekawa, K., Kawase, Y., 1999. Mixing characteristics in slurry stirred tank reactors with multiple impellers. *Chemical Engineering communications* 171, 211-229.

Dohi, N., Takahashi, T., Minekawa, K., Kawase, Y., 2004. Power consumption and solidsuspension performance of large-scale impellers in gas–liquid–solid three-phase stirred tank reactors. *Chemical Engineering Journal* 97, 103-114.

Doroodchi, E., Galvina, K.P., Fletcher, D.F., 2005. The influence of inclined plates on expansion behaviour of solid suspensions in a liquid fluidised bed—A computational fluid dynamics study. *Powder Technology* 16, 20-26.

Dudukovic, M. P., Devanathan, N., Holub, R., 1991. Multiphase reactors: Models and experimental verification. *Revue de l'Institut Francais du Petrole* 46, 439-465.

Dudukovic, M.P., Larachi, F., Mills, P.L., 1999. Multiphase Reactor—Revisited. *Chemical Engineering Science* 54, 1975-1995.

Dutta, N.N., Pangarkar, V.G., 1995. Critical impeller speed for solid suspension in multi-impeller three-phase agitated contactors. *The Canadian Journal of Chemical Engineering* 73, 273-283.

Dylag, M., Talaga, J., 1994. Hydrodynamics of mechanical mixing in a three-phase liquid-gas-solid System. *International Chemical Engineering* 34, 539-551.

Einenkel, W.G., 1979. Description of fluid dynamics in stirred tanks. *VDI Forschungsheft No. 595*.

Epstein, N., 2003. Application of liquid–Solid fluidisation. *International Journal of Chemical Reactor Engineering* 1, R1.

Epstein, N., Leclair, B.P., Pruden, B.B., 1981. Liquid fluidization of binary particle mixtures-I, Overall bed expansion, *Chemical Engineering Science*, 36, 1803-1809.

Ergun, S., 1952. Fluid flow through packed columns. *Chemical Engineering and Processing*. 48, 89-94.

Essemiani, K., Ducom, G., Cabassud, C., Line, A., 2001. Spherical cap bubbles in a flat sheet nanofiltration module: Experiments and numerical simulation. *Chemical Engineering Science* 56, 6321-6327.

References

Feng, W., Wen, J., Fan, J., Yuan, Q., Jia, X., Sun, Y., 2005. Local hydrodynamics of gas–liquid–nano particles three-phase fluidization. *Chemical Engineering Science* 60, 6887-6898.

Fraguío, M.S., Cassanello, M.C., Larachi, F., Chaouki, J., 2006. Flow regime transition pointers in three-phase fluidised beds inferred from a solid tracer trajectory. *Chemical Engineering and Processing* 45, 350-358.

Frijlink, J.J., Bakker, A., Smith, J.M., 1990. Suspension of solid particles with gassed impellers. *Chemical Engineering Science* 45, 1703-1718.

Gamwo, I.K., Halow, J.S., Gidaspow, D., Mostofi, R., 2003. CFD models for methanol synthesis three-phase reactors: Reactor optimization. *Chemical Engineering Journal* 93, 103-112.

Garside, J., Al-Dibouni, M.R., 1977. Velocity–voidage relationship for fluidisation and sedimentation. *Industrial and Engineering Chemistry Process Design and Development* 16, 206-214.

Geetha K.S., 1997. Investigations on Iron Removal Process by Oxygen Leaching in a Mechanically Agitated Contactor, Ph.D. Thesis, Kerala University, India.

Geetha, K.S., Surender, G.D., 1997. Modelling of ammoniacal oxygen leaching of metallic iron in a stirred slurry reactor. *Hydrometallurgy* 44, 213-230.

Geetha, K.S., Surender, G.D., 2001. Intensification of iron removal rate during oxygen leaching through gas–liquid mass transfer enhancement. *Metallurgical and Materials Transactions B* 32b, 961-963.

Gibilaro, L.G., Hossain, I., Foscolo, P.U., 1986. Aggregate behaviour of liquid fluidised beds. *The Canadian Journal of Chemical Engineering* 64, 931-938.

Gidaspow, D., 1994. *Multiphase Flow and Fluidisation: Continuum and Kinetic Theory Descriptions*. Academic Press, San Diego.

Godfrey, J.C., Zhu, Z.M., 1994. Measurement of particle liquid profiles in agitated tanks. *A.I.Ch.E. Symposium Series* 299, 181-185.

Grace, J.R., 1973. Shapes and velocities of bubbles rising in infinite liquids. *Chemical Engineering Research and Design* 51a, 116-120.

Grevet, J. H., Szekeley, J., El-Kaddah, N., 1982. An experimental and theoretical study of gas bubble driven circulation systems. *International Journal of Heat and Mass Transfer*, 25, 487-497.

Grevskott, S., Sannæs, B.H., Dudukovic, M.P., Hjarbo, K.W., Svendsen, H. F., 1996. Liquid circulation, bubble size distributions, and solids movement in two- and three-phase bubble columns. *Chemical Engineering Science* 51, 1703-1713.

References

- Grienberger, J., Hofmann, H., 1992. Investigations and Modeling of bubble columns. *Chemical Engineering Science* 47, 2215-2220.
- Guha, D., Ramachandran, P.A., Dudukovic, M.P., 2007. Flow field of suspended solids in a stirred tank reactor by Lagrangian tracking. *Chemical Engineering Science* 62, 6143-6154.
- Guha, D., Ramachandran, P.A., Dudukovic, M.P., Derksen, J.J., 2008. Evaluation of large eddy simulation and Euler–Euler CFD Models for solids flow dynamics in a stirred tank reactor. *A.I.Ch.E. Journal*, 54, 766-778.
- Higbie, R., 1935. The rate of absorption of a pure gas into a still liquid during a short time of exposure. *Transactions of the American Institute of Chemical Engineering* 31, 365-389.
- Hillmer, G., Weismantel, L. Hofmann, H., 1994. Investigations and modelling of slurry bubble columns. *Chemical Engineering Science* 49, 837-843.
- Hirt, C.W. Nichols, B.D., 1981. Volume of Fluid (VOF) method for the dynamics of free boundaries. *Journal of Computational Physics* 39, 201-225.
- Ibrahim, S., Nienow, A. W., 1996. Particle suspension in the turbulent regime: the effect of impeller type and impeller/vessel configuration. *Chemical Engineering Research and Design* 74a, 679-688.
- Ishii, M., Zuber, N., 1979. Drag coefficient and relative velocity in bubbly, droplet or particulate Flows, *A.I.Ch.E. Journal* 25, 843-855.
- Jakobsen, H.A., Sanns, B.H., Grevskott, S., Svendsen, H.F., 1997. Modeling of vertical bubble-driven flows. *Industrial and Engineering Chemistry Research* 36, 4052-4074.
- Jianping, W., Shonglin, X., 1998. Local hydrodynamics in a gas–liquid–solid three-phase bubble column reactor. *Chemical Engineering Journal* 70, 81-84.
- Jiradilok, V., Gidaspow, D., Breault, R.W., 2007. Computation of gas and solid dispersion coefficients in turbulent risers and bubbling beds. *Chemical Engineering Science* 62, 3397-3409.
- Joosten, G.E.H., Schilder, J.G.M., Janssen. J.J., 1977. The influence of suspended solid material on the gas-liquid mass transfer in stirred gas–liquid contactors. *Chemical Engineering Science* 32, 563-566.
- Joshi, J.B., 1980. Axial mixing in multiphase contactor – A unified correlation. *Chemical Engineering Research and Design* 58a, 155-165.

References

- Joshi, J. B., 2001. Computational flow modelling and design of bubble column reactors. *Chemical Engineering Science* 56, 5893-5933.
- Kawase, Y., Moo-Young, M., 1989. Mixing time in bioreactors. *Journal of Chemical Technology and Biotechnology* 44, 63-75.
- Kawase, Y., Shimizu, K., Araki, T., Shimodaira, T. 1997. Hydrodynamics in three-phase stirred tank reactors with non-newtonian fluids. *Industrial and Engineering Chemistry Research* 36, 270-276.
- Kee, N.C.S., Tan, R.B. H., 2002. CFD simulation of solids suspension in mixing vessels. *The Canadian Journal of Chemical Engineering* 80, 1-6.
- Khopkar, A.R., Aubin, J., Xureb, C., Le Sauze, N., Bertrand, J. and Ranade, V.V., 2003. Gas-liquid flow generated by a pitched blade turbine: PIV measurements and CFD simulations. *Industrial and Engineering Chemistry Research*, 42, 5318-5332.
- Khopkar, A.R., Rammohan, A.R., Ranade, V.V., Dudukovic, M.P., 2005. Gas-liquid flow generated by a Rushton turbine in stirred vessel: CARPT/CT measurements and CFD simulations. *Chemical Engineering Science* 60, 2215-2229.
- Khopkar, A.R., Kasat, G.R., Pandit, A.B. and Ranade, V.V., 2006, Computational fluid dynamics simulation of the solid suspension in a stirred slurry reactor. *Industrial and Engineering Chemistry Research* 45, 4416-4428.
- Kiared, K., Larachi, F., Cassanello, M., Chaouki, J., 1997. Flow structure of the solids in a three-dimensional liquid fluidised bed. *Industrial and Engineering Chemistry Research* 36, 4695-4704.
- Kiared, K., Larachi, F., Chaouki, J., Guy, C., 1999. Mean and turbulent particle velocity in the fully developed region of a three-phase fluidised bed. *Chemical Engineering & Technology* 22, 683-689.
- Kmiec, A., 1982. Equilibrium of forces in a fluidised bed-experimental verification. *The Chemical Engineering Journal* 23, 133-136.
- Kojima, H., Uchida, Y., Ohsawa, T., Iguchi, A., 1987. Volumetric liquid-phase mass transfer coefficient in gas-sparged three-phase stirred vessels. *Journal of Chemical Engineering of Japan* 20, 104-106.
- Kolar, V., 1967. Contribution to the theory of suspension and dissolution of granular solids in liquids by means of mechanically mixed liquids. *Collection of Czechoslovak Chemical Communications* 32, 526-534.
- Kraume, M., 1992. Mixing times in stirred suspension. *Chemical Engineering and Technology* 15, 313-318.

References

Krishna, R., Sie, S.T., 1994. Strategies for multiphase reactor selection. *Chemical Engineering Science* 49, 4029-4065.

Krishna, R., De Swart, J.W.A., Ellenberger, J., Martina, G.B., Maretto, C. 1997. Gas holdup in slurry bubble columns: Effect of column diameter and slurry concentrations. *A.I.Ch.E. Journal* 43, 311-316.

Krishna, R., van Baten, J.M., 1999. Rise characteristics of gas bubbles in a 2D rectangular column: VOF simulations vs experiments. *International Communications in Heat and Mass Transfer* 26, 965-974.

Krishna, R., van Baten, J.M., Urseanu, M.I., 2000b. Three-phase Eulerian simulations of bubble column reactors operating in the churn-turbulent regime: A scale up strategy. *Chemical Engineering Science* 55, 3275-3286.

Kulkarni, A.A., Ekambara, K., Joshi, J.B., 2007. On the development of flow pattern in a bubble column reactor: Experiments and CFD. *Chemical Engineering Science* 62, 1049-1072.

Lai, K.Y.M, Salcudean, M., 1987. Computer analysis of multi-dimensional, turbulent, buoyancy-induced two phase flows in gas-agitated liquid reactors. *Computers and Fluids*, 15, 281-295.

Lain, S., Broder, D., Sommerfeld, M., 1999. Experimental and numerical studies of the hydrodynamics in a bubble column. *Chemical Engineering Science* 54, 4913-4920.

Lain, S., Broder, D., Sommerfeld, M., Goz, M. F., 2002. Modelling hydrodynamics and turbulence in a bubble column using the Euler-Lagrange procedure. *International Journal of Multiphase Flow* 28, 1381-1407.

Lapin, A., Paaschen, T., Junghans, K., Lübbert, A., 2002. Bubble column fluid dynamics, flow structures in slender columns with large-diameter ring-spargers. *Chemical Engineering Science* 57, 1419-1424.

Larachi, F., Cassanello, M., Chaouki, J., Guy, C., 1996. Flow structure of the solids in a 3-D gas-liquid-solid fluidised bed. *A.I.Ch.E. Journal* 42, 2439-2452.

Latif, B.A.J., Richardson, J.F. 1972. Circulation patterns and velocity distributions for particles in a liquid fluidised bed. *Chemical Engineering Science* 27, 1933-1949.

Lee, E.C., Lawson, F., Han, K.N., 1978. Effect of precipitant surface roughness on cementation kinetics. *Hydrometallurgy* 3, 7-21.

Lee, S.L.P., De Lasa, H.I., 1987. Phase holdups in three-phase fluidised beds. *A.I.Ch.E. Journal* 33, 1359-1370.

Lewis, E.W., Bowerman, E.W., 1952. Fluidisation of solid particles in liquids. *Chemical Engineering Progress* 48, 603-611.

References

- Li, Y., Zhang, J., Fan, L.-S., 1999. Numerical simulation of gas–liquid–solid fluidization systems using a combined CFD–VOF–DPM method: bubble wake behavior. *Chemical Engineering Science* 54, 5101-5107.
- Limtrakul, S., Chen, J., Ramachandran, P.A., Dudukovic, M.P., 2005. Solids motion and holdup profiles in liquid fluidised beds. *Chemical Engineering Science* 60, 1889-1900.
- Liu, Z., Zheng, Y., Jia, L., Zhang, Q., 2005. Study of bubble induced flow structure using PIV. *Chemical Engineering Science* 60, 3537-3552.
- Ljungqvist, M., Rasmuson, A., 2001. Numerical simulation of the two-phase flow in an axially stirred vessel. *Chemical Engineering Research and Design* 79, 533-546.
- Lopez de Bertodano, M., 1992. Turbulent Bubbly Two-Phase Flow in a Triangular Duct. Ph.D. Thesis, Rensselaer Polytechnic Institute, Troy, New York.
- Luo, J. Y., Issa, R. I. and Gosman, A. D., 1994. Prediction of impeller-induced flows in mixing vessels using multiple frames of reference. *Institution of Chemical Engineers Symposium Series* 136, 549-556.
- Matonis, D., Gidaspow, D., Bahary, M., 2002. CFD simulation of flow and turbulence in a slurry bubble column. *A.I.Ch.E. Journal* 48, 1413-1429.
- Mei, R. 1993. History force on a sphere due to a step change in the free stream velocity. *International Journal of Multiphase Flow* 19, 509-525.
- Micale, G., Montante, G., Grisafi, F., Brucato, A., Godfrey, J., 2000. CFD simulation of particle distribution in stirred vessels. *Chemical Engineering Research and Design* 78, 435-444.
- Michelletti, M., Nikiforaki, L., Lee, K.C., Yianneskis, M., 2003. Particle concentration and mixing characteristics of moderate-to-dense solid–liquid suspensions. *Industrial Engineering Chemistry Research* 42, 6236-6249.
- Michelletti, M., Yianneskis, M., 2004. Study of fluid velocity characteristics in stirred solid–liquid suspensions with a refractive index matching technique. In: *Proceeding of Institutions of Mechanical Engineers* 218, Part E: *Journal of Process Mechanical Engineering*, 191-204.
- Mitra-Majumdar, D., Farouk, B., Shah, Y.T., 1997. Hydrodynamic modeling of three-phase flows through a vertical column. *Chemical Engineering Science* 52, 4485-4497.
- Montante, G., Magelli, F., 2005. Modeling of solids distribution in stirred tanks: Analysis of simulation strategies and comparison with experimental data. *International Journal of Computational Fluid Dynamics* 19, 253-262.

References

- Mudde, R.F. Simonin, O., 1999. Two-and three-dimensional simulations of a bubble plume using a two-fluid model. *Chemical Engineering Science* 54, 5061-5069.
- Muroyama, A., Fan, L.-S., 1985. Fundamentals of gas-liquid-solid fluidization. *A.I.Ch.E. Journal* 31, 1-34.
- Murthy, B.N., Ghadge, R.S., Joshi, J.B., 2007. CFD simulations of gas-liquid-solid stirred reactor: Prediction of critical impeller speed for solid suspension. *Chemical Engineering Science* 62, 7184-7195.
- Narayanan, S., Bhatia, V.K., Guha, D.K., Rao, M.N., 1969. Suspension of solid by mechanical agitation. *Chemical Engineering Science* 24, 223-230.
- Nienow, A.W., 1968. Suspension of solid particles in turbine agitated baffled vessel. *Chemical Engineering Science* 23, 1453-1459.
- Nienow, A.W., Konno. M., Bujalski, W., 1985. Studies on three-phase mixing: A review and recent results. *Proceeding of 5th European Conference on Mixing*, Wurzburg, Germany, 1-12.
- Nigam, K.D.P., Schumpe. A., 1987. Gas-liquid mass transfer in a bubble column with suspended solids. *A.I.Ch.E.Journal* 33, 328-330.
- Ochieng, A., Lewis, A.E., 2006. CFD simulation of solids off-bottom suspension and cloud height. *Hydrometallurgy* 82, 1-12.
- Oguz, H., Brehm. A., Deckwer. W.-D., 1987. Gas/liquid mass transfer in sparged agitated slurries, *Chemical Engineering Science* 42, 1815-1822.
- Olmos, E., Gentric, C., Vial, C., Wild, G., Midoux, N. 2001. Numerical simulation of multiphase flow in bubble column reactors. Influence of bubble coalescence and break-up. *Chemical Engineering Science* 56, 6359-6365.
- Padial, N.T., VanderHeyden, W.B., Rauenzahn, R.M., Yarbrow, S.L., 2000. Three-dimensional simulation of a three-phase draft-tube bubble column. *Chemical Engineering Science* 55, 3261-3273.
- Pan, Y., Dudukovic, M.P., Chang, M., 1999. Dynamic simulation of bubbly flow in bubble columns. *Chemical Engineering Science* 54, 2481-2489.
- Pan, Y., Dudukovic, M.P., Chang, M., 2000. Numerical investigation of gas-driven flow in 2-D bubble columns. *A.I.Ch.E. Journal* 46, 434-449.
- Pantula, P.R.K., Ahmed, N., 1998. Solid suspension and gas hold-up in three phase mechanically agitated reactors. *Proceedings of the 26th Australian Chemical Engineering Conference (Chemica 98)*, Port Douglas, Australia.

References

Patil, D.J., van Sint Annaland, M., Kuipers, J.A.M., 2005. Critical comparison of hydrodynamic models for gas–solid fluidised beds–Part I: bubbling gas–solid fluidised beds operated with a jet. *Chemical Engineering Science* 60, 57-72.

Perng, C.Y., Murthy, J.Y., 1993. A moving-deforming mesh technique for the simulation of flow in mixing tanks. *A.I.Ch.E. Symposium Series*. 89 (293), 37-41.

Pfleger, D., Gomes, S., Gilbert, N., Wagner, H.G., 1999. Hydrodynamic simulations of laboratory scale bubble columns fundamental studies on the Eulerian–Eulerian modelling approach. *Chemical Engineering Science* 54, 5091-5099.

Pfleger, D., Becker, S., 2001. Modeling and simulation of the dynamic flow behaviour in a bubble column. *Chemical Engineering Science* 56, 1737-1747.

Picart, A., Berlemont, A. Gouesbet, G. 1982. De l'influence du terme de Basset sur la diepersion de particules discrettes dans le cadre de la theorie de Tchen, *C.R. Acad. Sci., Paris, Series II*, T295, 305.

Pinelli, D., Nocentini, M., Magelli, F., 2001. Solids distribution in stirred slurry reactors: Influence of some mixer configurations and limits to the applicability of a simple model for predictions. *Chemical Engineering Communications* 188, 91-107.

Rafique, M., Chen, P., Dudukovic, M., 2004. Computational modeling of gas–liquid flow in bubble columns. *Reviews in Chemical Engineering* 20, 225-375.

Raghava Rao, K.S.M.S., Rewatkar, V.B., Joshi, J.B., 1988. Critical impeller speed for solid suspension in mechanically agitated contactors. *A.I.Ch.E Journal* 34, 1332-1340.

Rampure, M. R., Buwa, V. V. Ranade, V.V., 2003. Modelling of gas–liquid/ gas–liquid–solid flows in bubble columns: Experiments and CFD simulations. *The Canadian Journal of Chemical Engineering* 81, 692-706.

Ranade, V.V., 1992. Flow in bubble columns: Some numerical experiments. *Chemical Engineering and Science* 47, 1857-1869.

Ranade, V.V., 1997. Modelling of turbulent Flow in a bubble column reactor. *Chemical Engineering Research and Design* 75A, 14-23.

Ranade, V.V., 2002. *Computational Flow Modeling for Chemical Reactor Engineering*. Academic Press, New York.

Ranade, V.V., Tayaliya, Y., Choudhury, D., 1997. Modeling of flow in stirred vessels: Comparison of snapshot, multiple reference frame and sliding mesh approaches. Presented at 16th NAMF Meeting, Williamsberg.

Raw, M.J., 1994. A coupled algebraic multigrid method for the 3-D Navier Stokes equations. *Proceedings of the Tenth GAMM-Seminar, Notes on Numerical Fluid Mechanics* 49, 205-215.

References

- Rewatkar, V.B., Raghava Rao, K.S.M.S., Joshi, J.B., 1991. Critical impeller speed for solid suspension in mechanically agitated three-phase reactors. 1. Experimental part. *Industrial and Engineering Chemistry Research* 30, 1770-1784.
- Rhie, C. M., Chow, W. L., 1982. A Numerical study of the turbulent flow past an isolated airfoil with trailing edge separation. *A.I.A.A. Journal* 21, 1525-1532.
- Richardson, J.F., Zaki, W.N., 1954. Sedimentation and fluidisation, Part I. *Chemical Engineering Research and Design* 32a, 35-53.
- Rieger, F., Dittl. P., 1994. Suspension of solid particles. *Chemical Engineering Science* 49, 2219-2227.
- Rigby, G.R., Van Brokland, G.P., Park, W.H., Capes, C.E., 1970. Properties of bubbles in three-phase fluidised bed as measured by an electroresistivity probe. *Chemical Engineering Science* 25, 1729-1741.
- Roy, S., Dudukovic, M.P., 2001. Flow mapping and modeling of liquid–solid risers. *Industrial and Engineering Chemistry Research* 40, 5440-5454.
- Roy, S., Kemoun, A., Al-Dahhan, M.H., Dudukovic, M.P., 2005. Experimental investigation of the hydrodynamics in a liquid–solid Riser. *A.I.Ch.E. Journal* 51, 802-835.
- Rudman, M., 1997. Volume-tracking methods for interfacial flow calculations. *International Journal of Numerical Methods in Fluids* 24, 671-691.
- Sardeing, R., Aubin J., Xuereb, C., 2004. Gas–liquid mass transfer a comparison of down-and up pumping axial flow impellers with radial impellers. *Chemical Engineering Research Design* 82, 1589-1596.
- Sato, Y., Sadatomi, M., Sekoguchi, K., 1981. Momentum and Heat Transfer in Two-Phase Bubbly Flow- I. Theory. *International Journal of Multiphase Flow* 7, 167-177.
- Schallenberg, J., Enß, J.H., Hempel, D.C., 2005. The important role of local dispersed phase hold-ups for the calculation of three-phase bubble columns. *Chemical Engineering Science* 60, 6027-6033.
- Schijung, B., 1983. Numerische Simulation Teilchenbeladener Vertikaler Rohrströmungen. Ph.D. Thesis, University Karlsruhe.
- Schiller, L., Naumaan, Z., 1935. A drag coefficient correlation, *Z. Ver. Deutsch. Ing.* 77, 318-320.
- Sha, Z., Palosaari, S., Oinas, P., Ogawa, K., 2001. CFD simulation of solid suspension in a stirred tank. *Journal of Chemical Engineering of Japan* 34, 621-626.

References

- Shamlou, P.A., Koutsakos, E., 1989. Solids suspension and distribution in liquids under turbulent agitation, *Chemical Engineering Science* 44, 529-542.
- Sharma, R.N., Shaikh, A.A., 2003. Solids suspension in stirred tanks with pitched blade turbines. *Chemical Engineering Science* 58, 2123-2140.
- Sokolichin, A., Eigenberger, G., 1994. Gas-Liquid Flow in bubble columns and loop reactors: Part 1. Detailed modelling and numerical simulation. *Chemical Engineering Science* 49, 5735-5746.
- Sokolichin, A., Eigenberger, G., 1999. Applicability of the standard $k-\varepsilon$ turbulence model to the dynamic simulation of bubble columns: Part I. Detailed numerical simulations. *Chemical Engineering Science* 54, 2273-2284.
- Sokolichin, A., Eigenberger, G., Lapin, A., 2004. Simulation of buoyancy driven Bubbly flow: Established simplifications and open questions. *A.I.Ch.E. Journal* 50, 24-45.
- Song, G., Fan, L.-S., 1986. Rheological behavior of a gas-liquid-solid fluidised bed. *World Congress III of Chemical Engineering* 3, 504-507.
- Spidla, M., Sinevic, V., Jahoda, M., Machon, V., 2005a. Solid particle distribution of moderately concentrated suspensions in a pilot plant stirred vessel. *Chemical Engineering Journal* 113, 73-82.
- Spidla, M., Sinevic, V., Machon, V., 2005b. Effect of baffle design on the off-bottom suspension characteristics of axial-flow impellers in a pilot-scale mixing vessel. *Chemical and Biochemical Engineering Quarterly* 19, 333-340.
- Stitt, E.H., 2002. Alternative multiphase reactors for fine chemicals: A world beyond stirred tanks?. *Chemical Engineering Journal* 90, 47-60.
- Syamlal, M., O'Brien, T.J., 1988. Simulation of granular layer inversion in liquid fluidised beds. *International Journal of Multiphase Flow* 14, 473-481.
- Tabib, M.V., Roy, S.A., Joshi, J.B., 2008. CFD simulation of bubble column-An analysis of interphase forces and turbulence models. *Chemical Engineering Journal* 139, 589-614.
- Taghipour, F., Ellis, N., Wong, C., 2005. Experimental and computational study of gas-solid fluidized bed hydrodynamics. *Chemical Engineering Science* 60, 6857-6867.
- Takahashi, K., Fujita, H., Yokota, T., 1993. Effect of size of spherical particle on complete suspension speed in agitated vessels of different scale. *Journal of Chemical Engineering of Japan* 26, 98-100.

References

- Tatterson, G.B., 1991. Fluid Mixing and Gas Dispersion in Agitated Tanks. McGraw Hill Publishing Co., New York.
- Tobajas, M., García-Calvo, E., Siegel, M.H., Apitz, S.E., 1999. Hydrodynamics and mass transfer prediction in a three-phase airlift reactor for marine sediment biotreatment. *Chemical Engineering Science* 54, 5347-5354.
- Tomiya, A., 1998. Struggle with computational bubble dynamics. In: Third International Conference on Multiphase Flow, ICMF'98, Lyon, France.
- Tsuji, Y., Kawaguchi, T., Tanaka, T., 1993. Discrete particle simulation of two-dimensional fluidized bed. *Powder Technology* 77, 79-87.
- van Baten. J.M., Krishna, R., 2002. CFD simulations of a bubble column operating in the homogeneous and heterogeneous flow regimes. *Chemical Engineering and Technology* 25, 1081-1086.
- van Baten, J.M., Ellenberger. J., Krishna, R., 2003. Scale-up strategy for bubble column slurry reactors using CFD simulations. *Catalysis Today* 79-80, 259-265.
- van Baten, J.M., Krishna, R., 2003. Comparison of hydrodynamics and mass transfer in airlift and bubble column reactors using CFD. *Chemical Engineering and Technology* 26, 1074-1079.
- van der Westhuizen, A.P., Deglon, D.A., 2007. Evaluation of solids suspension in a pilot-scale mechanical flotation cell: A critical impeller speed. *Mineral Engineering* 20, 233-240.
- van der Westhuizen, A.P., Deglon, D.A., 2008. Solids suspension in a pilot-scale mechanical flotation cell: A critical impeller speed correlation. *Mineral Engineering* 21, 621-629.
- van Sint Annaland, M., Deen, N.G., Kuipers, J.A.M., 2005. Numerical simulation of gas bubbles behaviour using a three-dimensional volume of fluid method. *Chemical Engineering Science*, 60, 2999-3011.
- van Wachem, B.G.M. Almstedt, A.E., 2003. Methods for multiphase computational fluid dynamics. *Chemical Engineering Journal* 96, 81-98.
- Wang, F., Mao, Z.S., Wang, Y., Yang. C., 2006. Measurement of phase holdups in liquid-liquid-solid three-phase stirred tanks and CFD simulation. *Chemical Engineering Science* 61, 7535-7550.
- Warmoeskerken, M.M.C.G., van Houwelingen, M.C., Frijlink, J.J., Smith, J.M., 1984. Role of cavity formation in stirred gas-liquid-solid reactors. *Chemical Engineering Research and Design* 62, 197-200.

References

- Warsito, W., Fan, L.-S., 2001. Measurement of real-time flow structures in gas–liquid and gas–liquid–solid flow systems using electrical capacitance tomography (ECT). *Chemical Engineering Science* 56, 6455-6462.
- Warsito, W., Fan, L.-S., 2003. ECT imaging of three-phase fluidised bed based on three-phase capacitance model. *Chemical Engineering Science* 58, 823-832.
- Wen, C.Y., Yu, Y.H., 1966. Mechanics of fluidisation. *Chemical Engineering Progress Symposium Series* 62, 100-111.
- Wong, C.W., Wang, J.P. Haung, S.T., 1987. Investigations of fluid dynamics in mechanically stirred aerated slurry reactors. *The Canadian Journal of Chemical Engineering* 65, 412-419.
- Wu, Y., Gidaspow, D. 2000. Hydrodynamic simulation of methanol synthesis in gas-liquid slurry bubble column reactors. *Chemical Engineering Science* 55, 573-587.
- Yamazaki, H., Tojo, K., Miyanami, K. 1986. Concentration profiles of solids suspended in a stirred tank. *Powder Technology* 48, 205-216.
- Yang, J., Renken, A., 2003. A generalized correlation for equilibrium of forces in liquid–solid fluidised beds. *Chemical Engineering Journal* 92,7-14.
- Yu, Y.H., Kim, S.D., 1988. Bubble characteristics in the radial direction of three-phase fluidised beds. *A.I.Ch.E. Journal* 34, 2069-2072.
- Yu, Y.H., Kim, S.D., 2001. Bubble-wake model for radial velocity profiles of liquid and solid phases in three-phase fluidised beds. *Industrial and Engineering Chemistry Research* 40, 4463-4469.
- Zhang, X., Ahmadi, G., 2005. Eulerian–Lagrangian simulations of liquid–gas–solid flows in three-phase slurry reactors. *Chemical Engineering Science* 60, 5089-5104.
- Zhang, D.Z., vanderheyden, W.B., 2002. The effects of mesoscale structures on the macroscopic momentum equations for two-phase flows. *International Journal of Multiphase Flow* 28, 805-822.
- Zhu, Y., Wu, J., 2002. Critical impeller speed for suspending solids in aerated agitation tanks. *The Canadian Journal of Chemical Engineering* 80, 1-6.
- Zlokarnik, N.W., Judat, P., 1969. Tubular and propeller stirrers—an effective stirrer combination for simultaneous gassing and suspending, *Chemie Ingenieur Technik* 41, 1270-1277.
- Zwietering, T.N., 1958. Suspending of solid particles in liquid by agitators. *Chemical Engineering Science* 8, 244-253.

List of Publications

List of Publications

1. **Panneerselvam, R.,** Savithri, S., Surender, G.D., 2007. CFD based investigations of hydrodynamics and energy dissipation due to solid motion in liquid fluidised bed. *Chemical Engineering Journal* 132, 159-171.
2. **Panneerselvam, R.,** Savithri, S., Surender, G.D., 2008. CFD modeling of gas-liquid-solid mechanically agitated contactor. *Chemical Engineering Research and Design* 86 1331-1334.
3. **Panneerselvam, R.,** Savithri, S., Surender, G.D., 2009. CFD simulation of hydrodynamics gas-liquid-solid fluidised bed reactor. *Chemical Engineering Science* 64, 1119-1135.
4. **Panneerselvam, R.,** Savithri, S., Surender, G.D., 2009. CFD simulation of solid suspension in gas-liquid-solid mechanically agitated contactor. *Industrial Engineering and Chemistry Research* 48, 1608-1620.
5. **Panneerselvam, R.,** Savithri, S., Surender, G.D., A Comparative study of hydrodynamics and mass transfer in gas-liquid-solid mechanically agitated and fluidised bed contactors using CFD, *Chemical Engineering and Technology*, under review.
6. **Panneerselvam, R.,** Savithri, S., CFD simulation of solid suspension in liquid–solid mechanically agitated contactor. (Communicated to *International Journal of Chemical Reactor Engineering*).

List of Publications

International/National Conference Presentation

1. **Panneerselvam, R.,** Savithri, S., Surender, G.D., Local hydrodynamic behavior of gas–liquid–solid three phase slurry reactors. ANSYS India Conference on Convergence 05, Dec 2005, Bangalore
2. **Panneerselvam, R.,** Savithri, S., Surender, G.D., CFD Simulations of Suspension of Solids in a Stirred Reactor. ANSYS India Conference on Engineering Innovation 06, Dec 2006, Bangalore.
3. **Panneerselvam, R.,** Savithri, S., Surender, G.D., Hydrodynamics of Gas–Liquid–Solid Three Phase Fluidised Bed - A CFD Study. Proceedings of CHEMCON-06, Dec 2006.
4. **Panneerselvam, R.,** Savithri, S., Surender, G.D., CFD based Investigation of Solid Suspension in Liquid–Solid and Gas–Liquid–Solid Agitated Contactors. ANSYS India Conference on Elevating Innovation 07, Oct 2007
5. **Panneerselvam, R.,** Savithri, S., Surender, G.D., CFD based Investigation of Solid Suspension in Liquid–Solid and Gas–Liquid–Solid Agitated Contactors. Proceedings of CHEMCON-07, Dec 2007.
6. **Panneerselvam, R.,** Savithri, S., Surender, G.D., CFD modeling of gas–liquid–solid mechanically agitated contactor. International Symposium on Mixing in Industrial Processes (ISIMP-VI), Canada, 2008. Aug 17-21.